

University of Nottingham
UK | CHINA | MALAYSIA

In Situ Generated Biopolymers Towards a Reverse Prodrug Therapy for Hard-to-Treat Cancers

Isobel Josephine Jobson, MChem

Thesis submitted to the University of Nottingham
for the degree of Doctor of Philosophy

November 2024

Abstract

Glioblastoma (GBM) is a highly aggressive form of brain tumour with poor patient prognosis. There is, therefore, a clinical need to find novel approaches to treat the disease. Tumour treating fields (**TTFields**) are low-intensity, intermediate-frequency, alternating electric currents that are licensed for the treatment of GBM. While they increase patient survival as compared to the standard treatment, expensive treatment costs and small improvements in life expectancy mean there is a need to enhance the efficacy of this cancer therapy.

Cell-induced polymerisation is a potential new approach to treat cancer. It follows a 'prodrug' strategy, where a biocompatible monomer is chemically transformed to a polymer that can induce cell death. An alternative method instead follows a 'reverse prodrug' strategy, where a cytotoxic monomer induces an effect on the cells; the subsequent polymerisation then curtails this toxicity.

This thesis explores the potential to combine a conductive polymer formed by a 'reverse prodrug' approach with TTFields as a dual modality to induce cancer cell death.

An effective strategy for the characterisation of the polymer in two glioblastoma cell lines was first found. Solid state nuclear magnetic resonance was shown to be most suitable for identifying the presence of polypyrrole in samples that also contained cell debris. The mechanism of cell death was also investigated, with a combination of apoptotic and necrotic death observed in both cell types. Variation in the degree of cell death between cell types indicates the potential to tailor this 'reverse prodrug' treatment for cancer therapy.

To understand the mechanism of the 'reverse prodrug' polymerisation in a more complex organism, the *Caenorhabditis elegans* (***C. elegans***) *in vivo* model was used. Raman spectroscopy proved a valuable tool for the identification of both

polymer and iron initiators in the presence of nematodes. Evidence was found that polypyrrole was formed *in situ* in samples containing monomer and *C. elegans*. This is the first time that polypyrrole has been synthesised *in situ* with *C. elegans*. The toxicity of the starting materials was also investigated, with effects on acute survival and nematode development assessed. These results showed that at concentrations less than or equal to 20 mM, pyrrole did not induce nematode death, however growth was arrested. Toxicity was also compared in two mutated *C. elegans* cancer models, with similar profiles observed.

To combine the cell-induced polymerisation with TTFields, a high-throughput platform capable of generating electric fields was designed. This electrode setup was then coupled with the 'reverse prodrug' approach, and the combination of both electrical stimulation with cell-mediated formation of polypyrrole resulted in a significant decrease in cell viability of 79% compared to the stimulation-only control. The results from this work indicate the potential to combine the two treatments in a dual approach to treat glioblastoma. By combining TTFields with inorganic nanoparticles, the efficacy of treatment *in vitro* was also shown to be enhanced, with metabolic activity decreased by between 12 – 18%.

As the prognosis for GBM is so poor, it is essential that novel alternative therapies are explored to better treat the disease. This thesis paves the way for further research in combining TTFields with conductive materials formed by a 'reverse prodrug' approach as a potential dual approach to treat cancer.

Acknowledgements

There are many people who have supported me over the past four years, so being concise is a challenge. Firstly, I would like to thank my supervisors Dr. Frankie Rawson, Dr. Veeren Chauhan and Professor Snow Stolnik for all your guidance: Frankie, your enthusiasm has kept me motivated; Veeren, thank you for introducing me to the 'worm community' and helping me with all things *C. elegans*; and Snow, I am grateful that you pushed me to be a better scientist.

A huge thank you also goes to Dr Graham Rance, who assisted with the Raman spectroscopy data collection and analysis, and helped me better understand this area of research. Also, thank you to the following people for their help with analytical techniques: Dr Huw Williams (Solid State Nuclear Magnetic Resonance); Dr Michael Fay (Transmission Electron Microscopy); and Lorelei Robertson (Scanning Electron Microscopy). Thank you to Dr Kate Nguyen for collaborating with me to design the high-throughput 96-well plate for electrical stimulation, and to Edward Kujawinski for manufacturing the plate.

Often overlooked, I am very grateful to the division technicians, Teresa Marshall, Ann Williams and Charlie Allen, for all the ways they kept the lab running - the PhD would have been much harder without all of the work you do behind the scenes.

I would also like to thank the Rawson Group, particularly Dr Akhil Jain for your guidance and encouragement over the years, my 'amigo' Dr Dominic Mosses for your constant entertainment, and Fleur Groualle for your willingness to go for coffees with me and be a good friend throughout the PhD. Thank you also to the Regenerative Medicine and Cellular Therapies Division, and particularly to Dr Ami Nash and Dr Derek Hardie for putting up with my long-winded stories and distracting me when the PhD got hard. Also, thank

you to Dr Joshua Jones for all the research 'food-for-thought' you gave me, as well as for checking I was still semi-sane while writing up, and for Roizza So and Zachary Muda for your friendship.

I am grateful to the CDT in Transformative Pharmaceutical Technologies for accepting me onto the PhD programme, and for my fellow cohort, in particular to Lewis O'Shaughnessy and Graziamarina Sinatra for our 'Teams call' lunches and exploits in other areas of the country.

Outside of the university, I am very grateful for my church family for the ways you have encouraged me and prayed for me, reminding me that this PhD is not everything. Thank you also to my flatmate Emily who has been very gracious when I have been stressed, been a good listener, and also been a wonderful friend.

Lastly, I cannot write these acknowledgements without mentioning my wonderful family, without whom I would not be who I am today. Thank you to my big sister, Rachel, who has provided me with much wisdom and constantly pointed me to Jesus. Thank you also for proof-reading large parts of my thesis, and repeatedly asking me what this 'this' was referring to. Also thank you to my little brother, Andrew, for making me laugh and keeping me up-to-date on both the news and good songs. Your LaTeXprowess was also very useful during the writing of this 'nitid' thesis. Finally, thank you to my Mum and Dad. Both of you have supported me in almost every way possible, be it practically, monetarily , mentally or spiritually, and I am so grateful to God for you.

Publications and Conferences

Publications:

- Jobson, I., Vo, N. T. N., Kujawinski, E., Denning, C., Stolnik, S., Chauhan V. M., & Rawson, F. J., (2025). Advancing cancer therapy with custom-built alternating electric field devices. *Bioelectronic Medicine*, 11 (2). https://doi.org/10.1186/s42234-024-00164-3.
- Jain, A., Jobson, I., Griffin, M., Rahman, R., Smith, S. & Rawson, F. J., (2022). Electric field responsive nanotransducers for glioblastoma. *Bioelectronic Medicine*, 8 (17). https://doi.org/10.1186/s42234-022-00099-7.

Oral Presentations:

- November 2024: Early Career Researchers (ECR) Society Seminar; Nottingham, UK.
- August 2024: 32nd International Materials Research Conference (IMRC); Cancún, Mexico.
- November 2023: School of Pharmacy Postgraduate Seminar; Nottingham, UK.
- November 2023: Centre for Doctoral Training (CDT) in Transformative Pharmaceutical Technologies - Autumn Colloquium; Nottingham, UK.
- May 2023: Regenerative Medicines and Cellular Therapies (RMCT) Divisional Seminar; Nottingham, UK.
- October 2022: Molecular Therapeutics and Formulation (MTF) Divisional Seminar; Nottingham, UK.

Flash Presentations:

- June 2024: Tissue Culture and Engineering Society (TCES) 2024; Glasgow, UK. **- Award for Best Flash Presentation.**
- April 2023: Centre for Doctoral Training (CDT) in Transformative Pharmaceutical Technologies - Spring Colloquium; London, UK.
- May 2022: Future Investigators in Regenerative Medicine (FIRM); Darlington, UK. **- Award for Best Flash Presentation.**

Poster Presentations:

- April 2023: CDT in Transformative Pharmaceutical Technologies - Spring Colloquium; London, UK.
- January 2023: Allied Health Professionals (AHPGR) Conference; Nottingham, UK.
- September 2022: Asilomar Bioelectronics Symposium; Monterey, USA.
- April 2022: CDT in Transformative Pharmaceutical Technologies - Spring Colloquium; London, UK. **- Award for Best Poster.**

Contents

Abstract **i**

Acknowledgements **iii**

Publications and Conferences **v**

Abbreviations **xxiii**

1 Introduction **1**

1.1 Glioblastoma 1

1.1.1 Background 1

1.1.2 Glioblastoma Treatment 3

1.2 Tumour Treating Fields 11

1.2.1 Background 11

1.2.2 Mechanism of Action 12

1.2.3 Limitations of Tumour Treating Fields 15

1.2.4 Enhancement of TTField 16

1.3 Cell-Induced Polymerisation 17

1.3.1 Overview to Cell-Induced Polymerisation 18

1.4 Polypyrrole as a Material for Bioelectronic Applications 29

1.5 *Caenorhabditis elegans* 34

1.5.1 Background and Life Cycle 34

1.5.2 Mutating *C. elegans* 36

1.6 Thesis Overview 37

2 Cell-Induced Polymerisation 41

2.1 Introduction 41

2.2 Experimental Aims and Objectives 43

2.3 Experimental Design 44

2.3.1 General information 44

2.3.2 Viability Studies 44

2.4 Results and Discussion 45

2.4.1 *In vitro* Polymerisation of Pyrrole - Initial Studies and Characterisation 45

2.4.2 Toxicity studies 56

2.5 Conclusions 67

3 Polymerisation of Pyrrole in Living Systems 71

3.1 Introduction 71

3.2 Experimental Aims and Objectives 74

3.3 Experimental Design 75

3.3.1 Brightfield Microscopy 75

3.3.2 Raman Spectroscopy 75

3.3.3 Toxicity Studies 76

3.4 Results and Discussion 77

3.4.1 Visualising the Polymerisation of Pyrrole 77

3.4.2 Raman Spectroscopy as a Tool for Polymer Analysis . . 81

3.4.3 Toxicity Studies - Bristol N2 Wild Type 94

3.4.4 Toxicity studies - *C. elegans* Mutant Models 99

3.5 Conclusions 103

4 Enhancing Tumour Treating Fields 105

4.1 Introduction 105

4.2 Aims 109

4.3 Methodology 110

4.3.1 Disclaimer 110

4.3.2 Cell Culture 110

4.4 Results and Discussion 115

4.4.1 Initial Plate Layout 115

4.4.2 Designing a High Throughput Platform 116

4.4.3 Combining Tumour Treating Fields with the Reverse Prodrug Approach 123

4.4.4 Electric field responsive nanotransducers for glioblastoma 125

4.5 Conclusions 138

5 Methods **141**

5.1 Materials 141

5.1.1 Cell, Culture Media and Passaging Components 141

5.1.2 *C. elegans* Maintenance Components 142

5.1.3 Biological Strains 143

5.1.4 Consumables 143

5.1.5 Other Reagents 145

5.1.6 Equipment 145

5.1.7 Locations 146

5.2 Cell Culture 148

5.2.1 Routine Cell Culture 148

5.2.2 Routine Freezing and Revival of Cell Stocks 150

5.2.3 Trypan Blue Exclusion 151

5.2.4 Cell Seeding 152

5.2.5 Presto Blue™ Cell Viability Assay 153

5.2.6 *In Vitro* Toxicity Studies 154

5.2.7 Flow Cytometry for Apoptosis Study 156

5.3 Cell-Induced Polymerisation 158

5.4 *Caenorhabditis elegans* 159

5.4.1 Preparation of Stock Solutions 159

5.4.2 Preparation of Growth Media 161

5.4.3 Culturing *C. elegans* 162

5.4.4 Synchronising the Worm Life Cycle 163

5.4.5 Counting *C. elegans* 164

5.4.6 Imaging *C. elegans* 165

5.4.7 *C. elegans* Life Cycle Study 166

5.4.8 *In vivo* Toxicity Study 166

5.4.9 Nematode Length Measurements 167

5.4.10 *In vivo* Polymerisation of Pyrrole 167

5.5 Tumour Treating Fields 169

5.5.1 Initial Well Plate Layout 169

5.5.2 High Throughput 96-Well Design 169

5.5.3 Tumour Treating Field Enhancement with Nanoparticles 171

5.6 Analytical Methods 174

5.6.1 Fourier Transform Infra-Red Spectroscopy 174

5.6.2 Ultraviolet-Visible Spectroscopy 175

5.6.3 Dynamic Light Scattering 175

5.6.4 Zeta Potential 175

5.6.5 Solid State Nuclear Magnetic Resonance 176

5.6.6 Raman Spectroscopy 176

5.6.7 Scanning Electron Microscopy 178

5.6.8 Transmission Electron Microscopy 178

5.7 Statistical Analysis 179

5.8 Software 179

6 Future Work and Perspectives **181**

6.1 Polypyrrole Can Be Synthesised Using Adherent Cells 182

6.2 *C. elegans* Can Generate Polypyrrole *In Situ* 184

6.3 Tumour Treating Fields Can Be Enhanced 187

6.4 Final Conclusions 190

Appendices **193**

A Introduction **193**

B Cell-Induced Polymerisation **198**

C Polymerisation of Pyrrole in Living Systems **201**

Bibliography **203**

List of Tables

1.1 List of the hallmarks of cancer. 2

1.2 List of polymerisation reactions mediated by human cells. 22

3.1 The strains of *C. elegans* and the corresponding human homologue. 99

5.1 Biological strains and full genotype. 143

5.2 Clinical and molecular features of GIN and GCE 28/ 31 cell pairs. 148

5.3 Volume of cell stock added to different culture plates or flasks. . 153

5.4 List of controls for flow cytometry experiment. 156

5.5 Treatments of *C. elegans* for *in situ* polymeristaion of pyrrole. . 168

5.6 Conditions used for tumour treating fields and 'reverse prodrug' combined study. 171

5.7 Conditions tested for tumour treating field-enhancement study. . 174

5.8 Grids used for TEM analysis of nanoparticles. 178

A.1 List of clinical trials in the past five years using a device-based treatment for GBM. 194

C.1 Assignment of pyrrole Raman peaks from Figure 3.4 201

C.2 Assignment of ferrocyanide and ferricyanide Raman peaks from Figure 3.5. 202

C.3 Assignment of *C. elegans* Raman peaks in Figure 3.8. 202

List of Figures

1.1 Clinical TTField device. 11

1.2 Antimitotic effects of tumour treating fields on cancerous cells. . 13

1.3 Band gaps of insulators, semi-conductors and conductors. 19

1.4 Cell-induced polymerisation concept. 21

1.5 Cell-induced polymerisation, comparing the 'prodrug' and 'reverse prodrug' approaches. 27

1.6 Chemical synthesis of pyrrole from furan. 30

1.7 Polymerisation mechanism of pyrrole. 31

1.8 Living polymerisation of pyrrole to polypyrrole in eukaryotic cells. 33

1.9 Life cycle of *C. elegans* at 25℃ 35

1.10 Research Overview: Combination approach of 'reverse prodrug' polymerisation and tumour treating field therapies. 38

2.1 Mechanism of the PrestoBlue™ assay. 45

2.2 Brightfield images of GIN 31 and GCE 31 after cell-mediated polymerisation (500 mM pyrrole and 2 mM ferrocyanide). 47

2.3 Colour change of culture medium after incubation with pyrrole and ferricyanide/ ferrocyanide in the presence or absence of GIN 31 or GCE 31 cells. 49

2.4 Scanning electron microscopy, dynamic light scattering and UV-Vis characterisation of polypyrrole. 50

2.5 FTIR characterisation of pyrrole, ferrocyanide and polypyrrole. . 53

2.6 Chemical structures of pyrrole and polypyrrole. 54

2.7 ^{13}C Solid State NMR of polypyrrole. 55

2.8 Effects of DMSO on GCE 31 and GIN 31 cells. 57

2.9 Live/ dead staining of GIN and GCE 31 cells with pyrrole. . . . 59

2.10 Effect of ferricyanide and ferrocyanide on the PrestoBlue^{TM} assay. 60

2.11 Toxicity curves of ferricyanide, ferrocyanide and pyrrole on GIN 31 and GCE 31 cells. 61

2.12 The Fenton Reaction 62

2.13 GIN 31 and GCE 31 representative flow cytometry quadrants showing apoptosis and necrosis. 64

2.14 GIN 31 and GCE 31 quadrant analysis 65

2.15 Percentage of cells at each gating stage to remove doublets and debris from flow cytometry data. 66

3.1 Estimation plot of worm length calculated using WormSizer vs manual measurements on ImageJ. 77

3.2 Brightfield images of N2 Bristol wild type *C. elegans* with Ppy. . 79

3.3 Simultaneous vs delayed treatment of N2 Bristol wild type *C. elegans* treated with pyrrole and potassium ferrocyanide. 81

3.4 Raman spectrum of the pyrrole monomer. 82

3.5 Raman spectra of iron initiators. 84

3.6 Comparison between A_{1g} and E_g stretching modes. 85

3.7 Raman spectra of Ppy. 86

3.8 Comparison of microscopes for analysis of *C. elegans*. 87

3.9 Raman analysis of *C. elegans* and polypyrrole. 89

3.11 Raman intensity map of *C. elegans* incubated with iron initiators. 93

3.12 Dose-response curve of *C. elegans* treated with iron initiators and pyrrole. 95

3.13 Effect of pyrrole concentration on size and larval production of *C. elegans*. 96

3.14 Percentage survival and worm length measurements of N2 Bristol wild type nematodes. 98

3.15 Percentage survival and worm length measurements of CE1255 and FAS46 nematodes. 101

3.16 Brightfield images of N2, CE1255 and FAS46 *C. elegans* strains from egg to L1 stage. 103

4.1 Initial setup for the tumour treating field optimisation study. . . 112

4.2 Diagram of the 96-well plate design. 114

4.3 Effects of electrode shape on tumour treating field efficacy. . . . 117

4.4 Initial study of 96 well-plate electrode platform. 118

4.5 Relative metabolism of GCE 31 cells ± tumour treating fields (TTFields), ± current. 119

4.6 Relative metabolism of GIN 31 and GCE 31 cells ± ZnO nanoparticles, ± tumour treating fields, ± current. 120

4.7 Relative metabolism of D425 cells ± ZnO nanoparticles, ± tumour treating fields, ± current. 121

4.8 Illustration of electric field distribution of two different electrode setups. 122

4.9 Enhancement of tumour treating fields or currents with the 'reverse prodrug' approach. 124

4.10 Aggregation of polypyrrole. 125

4.11 Chemical characterisation of Au, ZnO and SiO_2 nanoparticles. . 127

4.12 Transmission electron microscopy images of nanoparticles. . . . 128

4.13 Colloidal characterisation of Au, ZnO and SiO_2 nanoparticles. . 130

4.14 Toxicity profile of inorganic nanoparticles on patient-derived GBM cells after prolonged exposure. 132

4.15 4 hour *in vitro* toxicity of inorganic nanoparticles on patient derived GBM cells. 133

4.16 TTField enhancement with inorganic nanoparticles. 135

4.17 TTField enhancement with increased Au nanoparticle concentration on patient-derived GBM cells. 136

5.1 Gating strategy for negative control GCE 31 cells stained with both Caspase 3/7 and Zombie-NIR. 158

5.2 Graphical illustration of preparing agarose slides for imaging nematodes. 165

5.3 Novocure® Plate Layout. 172

5.4 Schematic for the removal and NP replacement for cells on a coverslip. 172

5.5 Schematic for using the ceramic dishes with the base plate and coverslips. 173

B.1 Live/ dead staining of GIN 31 cells exposed to increasing concentrations of pyrrole. 198

B.2 Live/ dead staining of GCE 31 cells exposed to increasing concentrations of pyrrole. 199

B.3 Example flow cytometry gating of cell events (FSC v SSC). . . . 200

Abbreviations

The following abbreviations are used in this manuscript:

5-ALA	5-Aminolevulinic Acid
AC	Alternating Current
ANOVA	Analysis of Variance
BBB	Blood-Brain Barrier
BEV	Bevacizumab
BTNP	Barium Titanate Nanoparticles
C. elegans	*Caenorhabditis Elegans*
CE1255	*C. elegans* strain - *cep-1* mutant
cep-1	TP53 homologue in *C. elegans*
CNS	Central Nervous System
Curr	Current
D425	Semi-Adherent Medulloblastoma Cell Line
DMEM	Dulbecco's Modified Eagle Medium
DLS	Dynamic Light Scattering
E. coli	*Escherichia Coli*

EPR	Enhanced Permeation and Retention Effect
FAS46	*C. elegans* strain - *his-72* mutant
FDA	United States Food and Drug Administration
FIC	Potassium Ferricyanide; Fe (III)
FOC	Potassium Ferrocyanide; Fe (II)
FSC	Forward Scatter
FTIR	Fourier Transform Infra-Red Spectroscopy
GBM	Glioblastoma
GCE	Glioma Core Enhanced - Cell Line
GIN	Glioma INvasive Margin - Cell Line
GRAS	Generally Recognised as Safe
GSH	Glutathione
HGA	Homogentisic Acid
his-72	Histone homologue in *C. elegans*
IC	Inhibitory Concentration
L1, 2, 3, 4	Larval stage 1, 2, 3, 4
LDH	Lactodehydrogenase
MCR	Multivariate Curve Resolution
MGMT	O6-Methylguanine-DNA Methyltransferase
MRI	Magnetic Resonance Imaging
MVA	Multivariate Analysis
N2	*C. elegans* strain - Bristol wild type

NP	Nanoparticle
PANI	Polyanaline
PBS	Phosphate-Buffered Saline
PDT	Photodynamic Therapy
PEDOT	Poly(3,4-Ethylenedioxythiophene)
Ppy	Polypyrrole
PSS	Polystyrene Sulfonate
PTT	Photothermal Therapy
Py	Pyrrole
ROS	Reactive Oxygen Species
S.E.M.	Standard Error of Mean
S.D.	Standard Deviation
SEM	Scanning Electron Microscopy
SiO_2	Silica/ Silicon Dioxide
SSC	Side Scatter
TEG-Br	Tetra(Ethylene Glycol) Bromoisobutyrate
TEM	Transmission Electron Microscopy
TMZ	Temozolomide
TTFields	Tumour Treating Fields
UV-Vis	Ultraviolet-Visible Spectroscopy
UVA	Univariate Analysis
ZnO	Zinc Oxide

Chapter 1

Introduction

This thesis aims to address the clinical need for new therapies to tackle hard-to-treat cancers such as glioblastoma (**GBM**). The focus in this work is on a combined approach of cell-induced polymerisation and electrical stimulation. It is hypothesised that the *in situ* polymerisation can first be used to induce cell death, accompanying the formation of a conductive polymer, which can then be enhanced using tumour treating fields (**TTFields**).

1.1 Glioblastoma

1.1.1 Background

Tumours that affect the brain and central nervous system (**CNS**) account for 3% of all new cancer cases in the United Kingdom (**UK**)[1]. GBM is the most aggressive and second most common primary brain tumour in adults behind meningioma, affecting an average of 2, 149 people every year in the UK alone [2]. 14% of all brain and CNS tumours, and 50% of malignant ones are classed

as GBM [3]. The median survival of patients with GBM is the lowest out of all the malignant brain and CNS tumours at just eight months. In the UK, the peak incidence age for GBM is between 65 - 74 years old [4], and men are 1.6 times more likely to be affected than women by the disease [5]. These statistics point to a clear clinical need for new and improved therapies for the treatment of GBM.

To understand how to develop effective therapies, it is first important to acknowledge the behaviour of cancer cells compared to healthy cells, as this affects how different cancers respond to treatment. There are eight hallmarks of cancer: sustaining proliferative signalling; evading growth suppression; inducing or accessing vasculature; replicative immortality; reprogramming cell metabolism; avoiding immune destruction; activating invasion and metastasis; resisting cell death [6] (Table 1.1). Out of all of the hallmarks of cancer, enabling replicative immortality, inducing angiogenesis, reprogramming cellular energetics and evading immune destruction are seen as the best ways to target GBM [7].

Table 1.1: **List of the hallmarks of cancer and how they affect cell behaviour.**

Hallmark	Traits	Mechanism	Ref.
Sustaining Proliferative Signalling	Maintain cell proliferation.	Production of own growth factors. Growth factors received from inflammatory cells e.g. macrophages.	[8]
Evading Growth Suppression	Uncontrollable cell proliferation.	Tumour protein (**TP**) 53 gene mutation leads to loss of tumour-suppression function.	[9, 10]
Inducing or Accessing Vasculature	Continued oxygen and nutrient supply from blood.	Angiogenesis induced by cancer cells, or healthy vessels are co-opted by invasion or metastasis.	[6, 11]

Table 1.1: **List of the hallmarks of cancer and how they affect cell behaviour.** (Continued)

Hallmark	Traits	Mechanism	Ref.
Replicative Immortality	Indefinite cell growth and division.	Telomerase enzyme is activated to add telomere segments onto DNA. Alternative telomere lengthening to maintain telomere length.	[12–14]
Reprogramming Cell Metabolism	Rapid growth rate and proliferation.	Increased aerobic glycolysis; acidic pH maintained through pH deregulation; enhanced reactive oxygen species (**ROS**) production; increased lipid biosynthesis for new cell growth.	[15, 16]
Avoiding Immune Destruction	Evasion of the immune system.	Immune checkpoint evasion; inhibition of antigen presentation; suppression of T cell activation and migration.	[17]
Activating Invasion and Metastasis	Migration of cancer to other organs/ tissues.	Cells invade surrounding tissues then migrate to distant sites through the blood/ lymphatic system, establishing new tumours in distant organs.	[12]
Resisting Cell Death	Continued proliferation of cells with damaged DNA.	TP53 mutation prevents the activation of a p53-dependent apoptotic cascade. Cancer cells inactivate pro-apoptotic proteins and overexpress anti-apoptotic proteins.	[18–20]

1.1.2 Glioblastoma Treatment

1.1.2.1 Standard Treatment

The gold standard of care follows the "Stupp protocol", utilising a combination of surgical resection, radiotherapy and chemotherapy [21, 22]. In this procedure, the tumour is first located using magnetic resonance imaging (**MRI**) or

5-aminolevulinic acid (**5-ALA**) fluorescence-based imaging. Next, gross total resection is carried out to safely remove as much of the tumour without compromising neurological function. Three to five weeks after surgical resection, the patient receives a combination of concomitant and adjuvant therapy of radiotherapy and chemotherapy with the chemotherapeutic agent temozolomide (3,4-dihydroimidazo[5,1-d][1,2,3,5] tetrazine; **TMZ**) [23]. Stupp *et al.* showed that the combination of TMZ with concomitant and adjuvant radiotherapy increased overall survival from 12.1 months (radiotherapy alone) to 14.6 months [21].

TMZ is an oral chemotherapeutic, and is able to cross the blood-brain barrier (**BBB**). As it is both lipophilic in nature and has a molecular weight of 194 daltons, it is able to achieve a bioavailability of 100% [24, 25]. Despite this positive bioavailability, over 50% of patients treated with TMZ are found to be resistant to the chemotherapeutic agent [26]. Alongside this, as with many chemotherapeutics, common side effects include headaches, nausea, vomiting, fatigue and muscle weakness, affecting between 20 - 100% of all patients [27]. These, plus the low overall survival of GBM patients, have driven the hunt for alternative therapies for GBM and other hard-to-treat cancers.

1.1.2.2 Difficulties with Treatment

Tumour recurrence in GBM is common, with more than 80% occurring at the sight of the original tumour [28]. The reasons for this are complex, however they can be broadly grouped into the following areas: inter-tumour heterogeneity, invasive cell population, rapid growth rate, resistance to treatment.

1. **Inter-Tumour Heterogeneity.** One of the major hurdles in the treatment of GBM surrounds inter-tumour heterogeneity, with cell plastic-

ity leading to a variation in the levels of multiple cell sub-populations throughout treatment which affects how the tumour behaves [29]. To address the differences in the cells at the invasive edge of the tumour, Smith *et al.* isolated cell populations from both the core region and the invasive margin [30]. These have since been isolated from a range of GBM patients to create a library of patient-derived GBM cells [31].

2. **Invasive Cell Population.** While surgery is standard treatment of care for GBM, the invasive nature of the tumour into healthy brain tissue prevents total resection, leading to tumour recurrence at the site of the invasive cells [32]. Brain tissue is highly vascularised in nature, so just three to six GBM cells are needed to reach and traverse neighbouring micro vessels, providing the glioma with a continuous blood supply [33, 34].
3. **Rapid Growth Rate.** GBM tumours have been shown to have a specific growth rate of 1.4% per day, taking on average 49.6 days to double the size of the tumour [35]. It has also been found that after the tumour has been surgically resected, the remaining tumour grows at a more rapid rate compared to non-resected tissue, believed to be triggered by changes to the tumour microenvironment after traumatic injury from surgical resection [36]. Despite this increase in aggressive growth, tumour resection still increases overall life expectancy.
4. **Treatment Resistance.** The main cause of drug resistance in GBM is due to a mutation in the DNA-repair enzyme O^6-methylguanine-DNA methyltransferase (**MGMT**). In its native state, this enzyme transfers a methyl at the O^6 site of guanine to cystine residues, preventing mutations that could lead to cancer. When it is overexpresssed in GBM, however, this enzyme is a key factor in responsiveness to methylating chemother-

apeutics such as temozolomide, countering the drug's methylation-based cytotoxic effects [37].

5. ***In Vitro* Models.** There are a range of models for *in vitro* GBM research. 2D cell line culture allows for the testing of homogeneous cell populations from easily-accessible sources; however the geno- and phenotypical features are least representative of GBM [38, 39]. One of the most common cell lines for 2D research into GBM is the U-87 MG cell line. Despite widespread use, the cell line purchasable from American Type Culture Collection was found to be genetically different from the original tumour, raising questions into the use of cell lines that are not linked to a patient [40]. For this reason, there is a movement within 2D work to use cells that are more clinically relevant, such as those isolated from GBM patients by Smith *et al.* [30].
6. **The Blood-Brain Barrier.** Within the highly vascularised central nervous system, the BBB is a semi-permeable barrier that restricts the movement of ions and molecules, protecting the brain from most-blood borne viruses and other substances. It is made up of both physical tight epithelial junctions and metabolic barriers such as efflux transporters [41]. As such, delivery of therapeutics for diseases within the CNS is greatly challenging as, in general, only small lipophilic, positively charged molecules smaller than 400 - 600 daltons can passively diffuse through [42, 43].

There are clearly many obstacles in the treatment of GBM and other gliomas. Therefore, when investigating alternative therapies, it is necessary to take into account these challenges to ensure that the proposed practice fits the requirements of the disease.

1.1.2.3 Other Drug or Biological-Based Treatments

Shortly after the approval of TMZ as a chemotherapeutic for GBM, a formulation of the chemotherapeutic carmustine, known as Gliadel® wafers, were approved in 2003 by the United States Food and Drug Administration (**FDA**) as a GBM therapy [44]. Carmustine, like TMZ, is a DNA and RNA alkylating agent, however it acts by cross-linking the DNA, preventing strand separation [45]. Due to the challenges associated with BBB drug delivery, carmustine was formulated with a biodegradable co-polymer into thin wafers that could be applied directly to the brain cavity after surgical resection. When exposed to the aqueous environment, hydrolysis of the co-polymer releases carmustine to the invasive cells remaining after surgery. The maximum serum concentration is reached three hours after insertion, and over 70% of the polymer degrades within three weeks of administration [44]. Initial studies suggest that the combined treatment of Gliadel® wafers and TMZ (plus radiotherapy) improves the therapy and overall patient survival, with a clinical trial study (registration number: jRCT1031190035) currently underway to directly compare these approaches [46, 47].

Following the concept of intracavity application, work has been carried out to formulate other drug-delivery platforms for the direct application of chemotherapeutics to the invasive cell margin. One example of this approach is the development of a paste formulated with two chemotherapeutics - TMZ and etoposide [48]. As with the wafers, the drug can be applied directly to the tumour microenvironment, bypassing challenges associated with the short half-life of TMZ (1.24 hours), while also better moulding to the irregular cavity compared to Gliadel® wafers allows for better targeting of the drugs. By using a cocktail of chemotherapeutics, it is proposed that treatment efficacy will be improved as more of the heterogeneous sub-populations of GBM can be treated [48].

The other main type of drug used for the treatment of GBM is bevacizumab, a monoclonal antibody VEGF inhibitor that addresses the cancer hallmark 'inducing or accessing vasculature'. It is a recombinant humanized monoclonal antibody that acts as an angiogenesis inhibitor, and has been shown to increase progression-free survival in patients with recurrent GBM [49].

While these drugs increase overall survival or progression-free survival, there is still a need to further improve the prognosis of patients who are treated for GBM. Therefore, alongside chemotherapeutic and other targeted cancer drugs, there has been increased interest in device-based treatments of GBM, which are discussed below.

1.1.2.4 Device-Based Treatments

In the past five years (October 2019 - October 2024), there has been an increase in the use of devices as alternative treatments for GBM, with 44 interventional trials listed on ClinicalTrials.gov for the treatment of glioblastoma using a device-based intervention (excluding three terminated and four withdrawn trials). The full list of these trials can be found in Appendix A.1. These approaches can be summarised as: phototherapy; magnetic therapy; ultrasound; radiotherapy; or electric therapy.

Radiotherapy: Radiotherapy is commonplace in the treatment of GBM, with high-energy x-rays (known as external beam radiotherapy) being one of the key components in the 'Stupp protocol' [21]. Recent work has looked at utilising other devices to apply targeted radiotherapy directly to the tumour site, such as yttrium-90 formulated in FDA-approved microsphere devices [50]. These microparticles have been shown to selectively affect tumours of the liver, providing a useful alternative for tumours where surgical resection is not suitable

[51]. A clinical trial is currently underway looking at the feasibility of transferring this technology to the treatment of GBM [52].

Phototherapy: Phototherapy utilises light of a specific wavelength to induce an effect and can be divided into two sub-therapies: photodynamic (**PDT**) and photothermal (**PTT**) therapy. PDT relies on photosensitisers, such as the FDA-approved 5-ALA, to generate reactive oxygen species when a specific light wavelength is applied [53]. PTT, on the other hand, uses light to thermally target areas where the photothermal agent is located. This then triggers a hyperthermic effect, providing a localised effect at the cancer cells. The main limitation of this type of therapy is to do with penetration depth - best effects are seen when the tumour is less than 1 cm deep in tissues [54].

Ultrasound Therapy: Ultrasound therapy relies on high-frequency sound waves (> 20 kHz) that can be precisely delivered to the brain to either transiently disrupt the BBB, helping to improve the delivery of a drug to the tumour site, or exerting a thermal effect on tumour cells [55]. To assist with opening the BBB, contrast agents or microbubbles are also used in the treatment. These components are excited by the ultrasound and due to the oscillation of the particles they are able to disrupt the tight junctions. This disruption allows the movement of chemotherapeutics or biologics that usually would not be able to cross the BBB [56].

Magnetic Field Therapy: There are two uses of magnetic-based therapy. The first approach treats cancer cells by the localised increase of temperature. In this approach, magnetic nanoparticles are applied at the tumour site, or guided to the tumour site by high-precision magnetic resonance navigation. Then an alternating magnetic field is applied to generate heat, resulting in tightly controlled cell hyperthermia at the tumour site [57]. The second approach relies on low frequency (< 30 kHz) magnetic fields to themselves have

an effect on the cancer cells, affecting the cell cycle and inducing calcium ion influx into GBM cells. Electron transport in the mitochondria is also disrupted, leading to a build-up of ROS and subsequent cell death [58]. These magnetic fields are applied using either a headband containing an electromagnetic coil, or a helmet comprising of three spinning magnets to generate the magnetic fields [59, 60].

Electric Field Therapy: Electric field therapy utilises electric currents to kill cancer cells. Electrochemotherapy, licensed for the treatment of skin-based tumours in the UK by the National Institute of Health and Care Excellence since 2013, is one such example of this therapy [61]. In this approach, cell membranes are temporarily permeabilised when exposed to high-voltage (400-1000 V) electric pulses delivered by needle-electrodes to the tumour site [62]. Locally-delivered chemotherapeutics can then enter the cancer cell, where they are trapped as the temporary pores close. This results in a targetted, localised cytotoxic effect [63].

An alternative therapy, known as TTFields, is one of the most promising non-invasive treatments for hard-to-treat cancers, particularly GBM. This treatment consists of low intensity ($1 - 3$ V/ cm), intermediate frequency ($100 - 300$ kHz) alternating electric currents [64]. Contrary to electrochemotherapy, the electric fields themselves influence cell behaviour and target the cancer cells. An FDA-approved system, known as Optune®, is licensed in a clinical setting, where they are applied through four transducer arrays each containing nine ceramic-coated electrodes [65]. It will be discussed in more detail in Section 1.2.

1.2 Tumour Treating Fields

1.2.1 Background

A landmark study showed that combining the Stupp protocol with TTFields increased overall survival of patients with new/ recurrent GBM by a median of 4.9 months from 16 to 20.9 months, with this increasing further to 24.9 months when the device was worn for 18 or more hours per day [66, 67]. As such, TTFields were approved by the FDA as a treatment to be used in conjunction with TMZ in 2011 [68].

The Optune® setup by Novocure Limited was first approved by the FDA in 2011 as a wearable and portable device for the treatment of GBM [69]. Adhesive patches containing insulated ceramic discs known as transducer arrays are placed on the shaved area of the body where the tumour is present, in the case of GBM this is the head (Figure 1.1). The layout of the transducer arrays is determined using MRI measurements to ensure maximal electric field intensity and direction to the tumour site [70].



Figure 1.1: Clinical TTField device.
The contents of the Optune® device used for clinical application of TTFields [71].

While this treatment does not provide an alternative to the chemotherapeutic agents previously discussed, additional side effects are limited to mild to moderate dermatitis (grades one and two) at the site of the transducer arrays in 16% of patients, which can be treated using topical corticosteroids [72].

1.2.2 Mechanism of Action

The modes of action of TTFields have been shown to be complex and not fully understood, however they can be broadly categorised into seven distinct modalities [64]:

1. **Antimitotic Effects.** The most understood and prominent TTField mechanism lies around interference with mitosis, targeting rapidly diving cancer cells. Within the broader effect of mitotic inhibition, cell division is limited through the mechanisms of dipole alignment and dielectrophoresis.

   In dipole alignment, microtubules involved in the formation of the mitotic spindle during the telophase of cellular division are influenced by the presence of electric fields (**EF**) due to their polar nature. Microtubles then align with the direction of the EF, preventing spindle formation and subsequent mitosis, and inducing apoptosis (Figure 1.2 A) [73].

   Dielectrophoresis utilises molecules that are inherently polar, or can become polarised, in the presence of an electric field. During metaphase, an inhomogeneous EF distribution within the cell results in the movement of polar molecules to regions with higher EF intensities, once again causing cell death (Figure 1.2 B) [74].

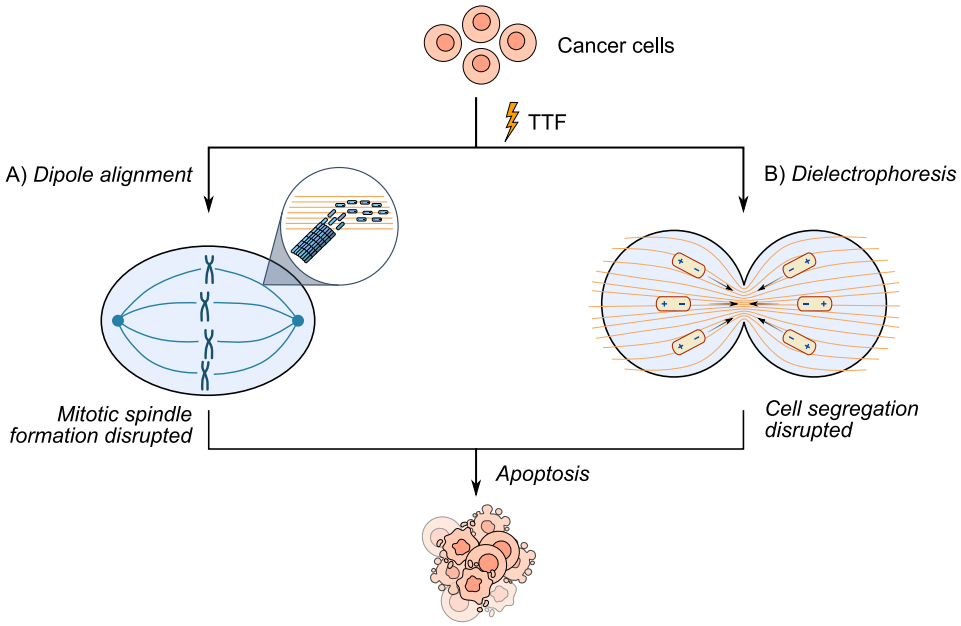


Figure 1.2: Antimitotic effects of tumour treating fields (TTFields) on cancerous cells.
Schematic to show effect of TTFields on cell division by (A) dipole alignment and (B) dielectrophoresis.

2. **Cell Membrane Permeability.** The ability of TTFields to transiently increase membrane permeability of cancer cells was first postulated when cells exposed to both TTFields and luciferase had increased bioluminescence [75]. Scanning electron microscopy showed significantly larger holes compared to untreated cells, with cell membranes returning to pre-TTField morphology after treatment was stopped [75]. This allows for more drug to enter the cell, allowing chemotherapeutics to be better targeted to cancer cells [76].

3. **Blood Brain Barrier.** Tight junctions at the blood-brain barrier restrict the movement of molecules into the brain, protecting it from blood-borne pathogens, but also increasing the challenges of treating diseases affecting the brain [41]. It has been found that when alternating currents (**AC**) at a low frequency of 100 kHz are applied, EFs can temporarily disrupt the BBB. This disruption allows enhanced drug delivery

of molecules normally unable to pass the BBB. After the low frequency EFs are applied, a higher frequency of 200-300 kHz can be used to target the tumour cells. The BBB disruption is reversible, and repeated cycles switching TTFields on/ off had no effect on the cells at the BBB [77, 78].

4. **Cell Migration.** As already discussed, the highly invasive nature of GBM is a reason for poor patient survival. Angiogenesis, the formation of new blood vessels, is a key component in cancer metastasis [79]. TTFields have been shown to inhibit cell migration and subsequent cell invasion and metastasis [80, 81].

5. **Replication Stress and DNA Repair.** Glioma-sensitisation to radiotherapy occurs when TTFields are used with radiotherapy. It was found that repair to the DNA is slowed down when TTFields are used, in part due to the decrease in expression of activators involved in DNA repair [82]. Chromatid-type aberrations induced by TTFields also show evidence for replication stress caused by TTFields [83].

6. **Induction of Autophagy.** TTField-treated cells have been shown to exhibit characteristic features associated with autophagy, such as double-membraned autophagosomes and increased cell granularity [84]. Genes related to autophagy have also shown to be upregulated in cells exposed to TTFields, however whether this is as a means of cell survival or death is not fully understood [84, 85].

7. **Immune Response.** Genes linked to the immune system and inflammatory environment can be modulated using TTFields [86, 87]. The secretion of ROS, nitric oxide and proinflammatory cytokines by macrophages have also shown to be promoted by TTFields [88].

It has previously been shown that the efficacy of TTFields can be adjusted by controlling the frequency of the EFs depending on the type of cells [74, 89]. The

glioblastoma cell line, U87, has the highest percentage of cell death when exposed to TTFields at a frequency of 200 kHz, while for patient-derived glioblastoma cells 'Glioma INvasive margin' (**GIN**) 31 and 'Glioma Core Enhanced' (**GCE**) 31 cells, a frequency of 200 - 300 kHz was most effective. The optimal frequency for TTField treatment is variable, however it is hypothesised to be inversely linked to cell size and the dielectric properties of different cell types [74, 90]. The duration of EF application also influences the efficacy of TTFields, with improved outcomes seen in patients who use the device for more than 18 hours per day [91]. This is because cell division is only disrupted when the cells are exposed to the TTField.

1.2.3 Limitations of Tumour Treating Fields

Whilst there is clear evidence for the benefit of using TTFields alongside standard radio- and chemo-therapeutic regimes, there are also challenges. The orientation of the setup is highly important in the clinical outcome, as TTFields only affect cells when the EF is parallel to cell axis for division [74]. While overall patient survival is shown to be significantly improved when TTFields are combined with the 'Stupp protocol', GBM is still a fatal disease, with the overall prognosis unchanged by treatment. TTFields alone do not have a substantial effect on cancer cells, with a chemotherapeutic agent needed alongside treatment. This hints at a lack of understanding of the exact mechanism of action.

It is also worth noting the expensive total cost of using this delivery system, which is approximately $21,000 per month. This covers the physical TTField platform including transducer arrays, EF generator and batteries, guidance on the transducer array layout based on tumour location, and training to both the patient and physician [92, 93]. TTFields are licensed in the United

States, Austria, France, Germany, Sweden, Switzerland, Japan and Israel after the incremental cost-effectiveness ratio was calculated and found to be positive [94]. Conversely, in healthcare systems that focus heavily on cost-effectiveness, such as the National Health Service in the United Kingdom, or equivalent systems in Australia and Canada, this therapy has yet to be approved as a clinical tool for GBM treatment as the costs of this therapy outweigh the associated benefits [64].

Consequently, it is of clinical importance to better understand the mechanisms of action and identify ways to enhance the outcomes seen with TTFields. This would ultimately be seen by increasing patient survival.

1.2.4 Enhancement of TTField

Work is being carried out on ways to improve the efficacy of TTFields. As TTFields have been shown to have an immunostimulatory effect, one way this is being carried out is by a combination therapy of TTFields with immunotherapy to enhance the immune response [95]. There are currently three clinical trials (phase I-III) investigating this dual approach for GBM treatment [96–98]. Other current work is looking at the application of TTField by either combining the treatment with radiotherapy, or investigating the optimum point for treatment to be started in relation to standard surgical and radiotherapeutic treatments [99, 100].

An alternative approach to TTField enhancement is through nanoparticles as TTField-responsive sensitisers. Nanoparticles are often used to hijack leaky vasculature found around tumour cells, caused by the rapid tumour growth, through the enhanced permeation and retention effect [101]. This effect is where particles passively accumulate at the site of the tumour through the

more permeable vasculature. Typically, NPs are formulated to be less than 100 nm for maximal accumulation and retention [102]. The types of nanoparticles used are varied, with different materials used depending on the tuneable properties at the NP surface to also allow for active tumour targeting [103]. Yoon *et al.* (2020) showed that barium titanate nanoparticles (**BTNPs**) could be used as TTField-responsive sensitisers [104]. Here, BTNPs (100 or 200 nm in size) were chosen as a ferroelectric nanomaterial which, without TTField treatment, were found to be biocompatible. They were shown to accumulate in the cytoplasm of breast cancer cells, and, when exposed to TTFields, exert anticancer activity on breast cancer cells, inducing cell-cycle arrest and modulating cancer signalling pathways.

Despite this early-stage work investigating ways to enhance TTFields, there is clearly a gap in this research that needs to be addressed. While BTNPs were shown to act as TTField-sensitisers, they are not approved by the FDA for the treatment of GBM, creating a barrier to clinical translation. It is also necessary to better understand the underlying mechanism of action for TTField-enhancement, as this is essential to choosing the best approach to improve the current therapy.

1.3 Cell-Induced Polymerisation

The aim of this thesis is to identify ways to enhance TTFields. One route to achieve this is by using a conductive polymer. It was hypothesised that this polymer could be formed by a cell-mediated approach as discussed below, as alongside the TTField enhancement an effect from the polymerisation may also be seen, creating a dual approach for cancer treatment.

1.3.1 Overview to Cell-Induced Polymerisation

The electrical conductivity of a material, recorded in Siemens per meter (S/m), is a measurement that determines the ability of a material to transport an electric charge. It is the reciprocal of resistivity, recorded in Ohm-meter s(Ω·m), which measures the resistance of electric current through a material [105]. Depending on the ability of a material to conduct an electrical charge they are classed as: 1) insulators; 2) semi-conductors; or 3) conductors.

Insulators have a band gap between the valence and conduction bands greater than 3.0 eV. This large gap prevents the promotion of an electron to the conduction band, resulting in low electrical conductivity (Figure 1.3 a). While semi-conductors also have a band gap, this is typically between 0.1 - 3.0 eV. Consequently, electrons can be promoted to the conduction band, resulting in some conductive properties (Figure 1.3 b). In metals, the valence and conductive bands overlap, resulting in a band gap of 0 eV. Here, the electrons are free to move into the conduction band, resulting in high conductivity (Figure 1.3 c) [106]. When in an un-doped state, conjugated polymers have large band gaps and act as insulators or semi-conductors. When doped, however, bipolaronic states form intermediate doping bands, which allow for the movement of electrons to the conduction bands, thus giving the polymer conductive properties (Figure 1.3 d) [107].

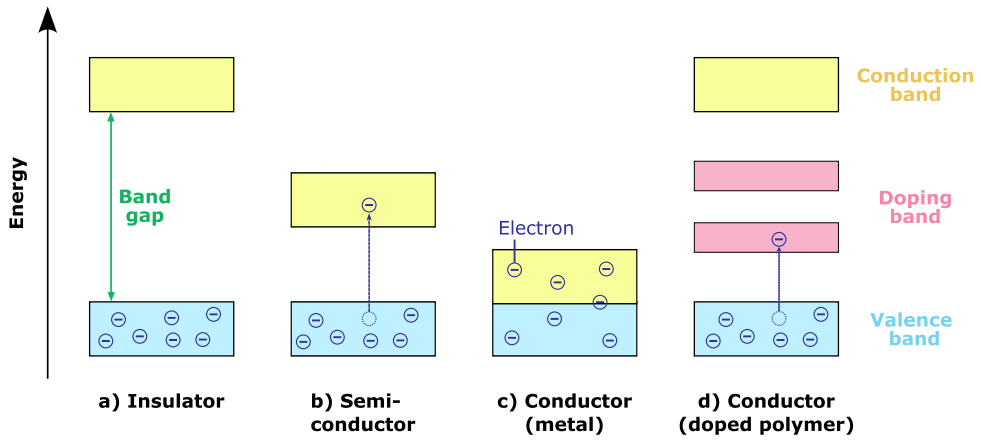


Figure 1.3: Band gaps of a) insulators, b) semi-conductors, c) conductors (metal) and d) conductors (doped polymer).
The valence bands are shown in light blue, the conduction bands in yellow, the valence bands in pink and the band gap in green. The promotion of an electron from the valence to the conduction band is shown in dark blue.

As scientific research is often inspired by naturally-occurring reactions, there has been much research into the biosynthesis of polymers such as actin, DNA and collagen [108]. A class of these molecules, known as conjugated polymers, is also found within the body. These molecules contain overlapping p-orbitals, enabling the delocalisation of electrons [109]. Conjugated molecules have narrow gaps between filled and empty orbitals, allowing for the absorption of longer-wavelength light. Consequently, these compounds are highly pigmented.

Within the human body, the most well-known of these is melanin, which controls the pigmentation of skin, hair and neurons. This molecule class can further be divided into: 1) eumelanin; 2) pheomelanin; and 3) neuromelanin [110]. Both eumelanin and pheomelanin are responsible for hair and skin pigmentation, the former of which causes black or brown pigmentation and acts as a photo-protectant, while the latter, a photosensitiser, causes lighter yellow and red pigmentation, and is also responsible for the colour of lips and other

pink/ red features of the human body [111]. Neuromelanin is black-brown in colour and is involved in neuroprotection [112].

The rare genetic disease alkaptonuria, or 'black urine disease' is caused by a mutation to a gene responsible for the removal of homogentisic acid (**HGA**). This mutation results in the build-up and subsequent polymerisation of HGA, and results in melanin-like structures that have a black pigmentation [111, 113].

This understanding of native polymerisation reactions has paved the way for capitalising on cell environments to drive the formation of synthetic polymers. Within this field, the biological system can be broadly broken down into prokaryotic or eukaryotic living systems, which will be discussed in Sections 1.3.1.1 and 1.3.1.2 respectively.

1.3.1.1 Prokaryotic Polymerisation

There are many examples of utilising the cellular microenvironment to functionalise the surface of bacteria. For example, the reducing capabilities of bacteria have been shown to convert copper (**Cu**) (II) to Cu (I). This then drives the polymerisation of a synthetic polymer from its monomer at the surface of the bacteria, with the polymers later separated from the cells to generate templated polymers with a specific monomer sequence [114]. Alternatively, other metals, such as palladium (II) can be reduced at the surface of bacteria to drive the Sonogashira polymerisation of an aryl halide to an alkyene as a tool to kill *E. coli* [115]. To transfer this technology to a disease-based target, work has also shifted to focus on using eukaryotic cells.

1.3.1.2 Eukaryotic Polymerisation

The interest in using *in situ* cell-mediated polymerisation reactions has been fuelled by a need to better track and target diseased human cells. This approach delivers monomers to the cells and the polymerisation occurs either at the cell surface, intracellularly or extracellularly (Figure 1.4). A full list of polymerisation approaches that use human cells can be found in Table 1.2.

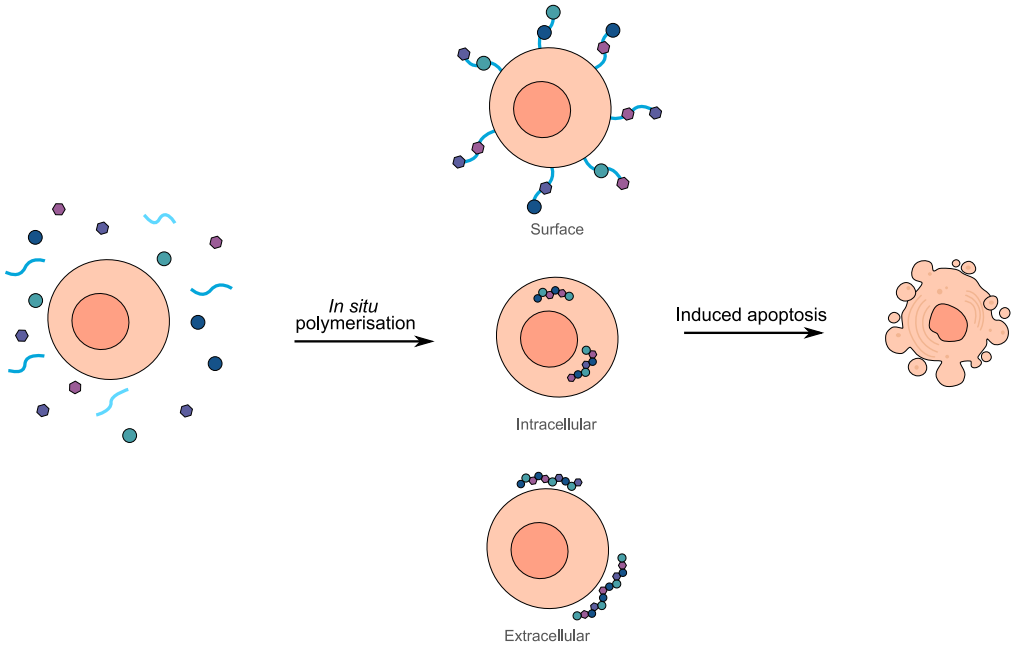


Figure 1.4: Cell-induced polymerisation concept.

Table 1.2: **List of polymerisation reactions mediated by human cells.**

Monomer	Initiator	Reaction Conditions	Type	Cell(s)	Results	Ref
AAm	APS/ TMEDA	Acryloylation of amino acids at cell membrane using NAS for 2 h. *In situ* polymerisation of polymer with GDMA as cross-linker for 2 h. Carried out at 4-8℃.	FRP	HeLa; BAC; hMSC	Single cell encapsulation to protect cells from environmental stressors.	[116]
PEGDA	SA-EITC	Labelled sequentially with biotinylated CD45 antibodies and initiator 10 min llumination (hv = 530 nm, 30 mW/ cm^2)	FRP; PI	Jurkat	Nanofilm formation on single cell. Protects cells from environmental stressors.	[117, 118]
MF-CD20-M	APS	1 h incubation of cells with macromer at 37℃. Washed with PBS, then incubated with initiator for 30 min.	FRP	Raji	Apoptosis induced by CD20-receptor clustering.	[115]
PEGA-Sn	Eosin Y/ TEA (co-catalyst)	BTPA used as chain transfer agent, non-covalently attached to cells using a lipid analogue. 465 nm irradiation, 5 mW/ cm^2	PET-RAFT	Jurkat	Polymers formed on cell membrane without disrupting metabolic activity.	[119]

Surface

Table 1.2: **List of polymerisation reactions mediated by human cells.** (Continued)

	Monomer	Initiator	Reaction Conditions	Type	Cell(s)	Results	Ref
Intracellular	HEA; FMMA; Acr-PTX	TEG-Br/ Cu-His	2 h incubation with monomer, then initiator added and incubated for 2 h. Polymerisation driven by reduction of Cu (II) using NaAsc and endogenous GSH.	AGET-ATRP	HepG2; HeLa; HPF	Polymerisation driven by the cell microenvironment to dictate cell fate.	[120]
	PA-NH2	ROS	4 hour incubation with monomer. Polymerisation occurs due to endogenous ROS.	FRP	HeLa	Polymerisation induces cytotoxicity.	[121]
	SPA	H_2O_2/ HRP	Overexpressed H_2O_2 catalysed by exogenous HRP to produce ·OH radicals and drive polymerisation of analine dimer.	FRP	4T1; HeLa	Formed pSPA NPs can be used for photoacoustic imaging and PDT.	[122]
	B3-Te	ROS	Hyperbranched polymerisation triggered by intracellular ROS in cancer cells.	FRP	A549; MCF-7	Polymers are resistant to cellular efflux and induce apoptosis.	[123]

Table 1.2: **List of polymerisation reactions mediated by human cells.** (Continued)

	Monomer	Initiator	Reaction Conditions	Type	Cell(s)	Results	Ref
Intracellular	ELP	TGase	Endogenous TGase used to create a covalent bond between the -NH_2 of lysine and the -C(=O)NH_2 of glutamine	Con	HeLa	Homogeneous cross-linked network of polypeptides within cytoplasm of cells that are rich in TGase.	[124]
	D2P1/ 3CBT	Cathepsin B	Simultaneous reduction and enzymatic *in situ* cleavage of D2P1 with endogenous GSH and Cathepsin B. Exposed cysteine then polymerises with 3CBT.	Con	MDA-MB-231; HT-29	Disrupts cancer cell motility and cell proliferation. Polymer accumulation allows for use as photosensitiser.	[125]
	DFY	TYR	Polymerisation only occurred in cells overexpressing TYR.	Ox	B16	Polymerisation induces protein cross-linking and subsequent necrotic cell death.	[126]
	Te-O	[O]	Reaction driven by intracellular ROS from cancer microenvironment.	Ox	HepG2	Polymerisation self-amplified by generation of ROS. Induces ROS-related apoptosis.	[127]

Table 1.2: **List of polymerisation reactions mediated by human cells.** (Continued)

	Monomer	Initiator	Reaction Conditions	Type	Cell(s)	Results	Ref
Extracellular	Py	FOC	48 h incubation with monomer and initiator.	Ox	K562	tPMETs and cellular exudate oxidises Fe (II), driving polymerisation of Py. 'Reverse prodrug' approach to induce cancer cell death and subsequent self-inactivation.	[128]

Monomers: 3CBT = cyanobenzothiazole-cysteine; AAm = acrylamide; Acr-PTX = acryloyl-paclitaxel; D2P1 = aggregation-induced emission fluorogen-peptide conjugate; DFY = Asp-Phe-Tyr tripeptide; ELP = elastin-like polypeptide; FMMA = ferrocenylmethyl methacrylate; HEA = 2-hydroxyethyl acrylate; MF-CD20-M = Maleimide-functionalized anti-CD20 aptamer-modified macromer; PEGA-Sn = ω-biotin-PEG acrylamide; PEGDA = poly(ethylene glycol) diacrylate; Py = pyrrole; Te-O = organotelluride.

Initiators: APS = ammonium persulphate; Cu-His = Cu(II)-histidine; FOC = potassium ferrocyanide (Fe (II)); SA-EITC = streptavidin-eosin isothiocyanate; TEA = triethanolamine; TEG-Br = tetra(ethylene glycol) bromoisobutyrate; TGase = transglutaminase; TMEDA = N,N,N',N'-tetramethylethylenediamine; TYR = tyrosinase; [O] = intracellular oxidative species.

Other materials: BTPA = 2-(butylthiocarbonothioyl) propionic acid; GDMA = glycerol dimethacrylate; GSH = glutathione; NAS = N-acryloxysuccinimide.

Polymerisation type: AGET-ATRP = activator generated by electron transfer - atom transfer radical polymerization; Con = condensation (step-growth) polymerisation; FRP = free-radical polymerisation; Ox = oxidative polymerisation; PET-RAFT = photoinduced electron transfer-reversible addition-fragmentation chain-transfer polymerization; PI = photo-initiated.

Differing microenvironments present in tumour cells allow for the selective polymerisation of biocompatible monomers based on the redox capabilities of the cell [120, 127]. The resulting polymers then induce apoptosis of the cancer cells. Shen *et al.* sought to exploit the overexpression of glutathione (**GSH**) found in many cancer microenvironments, testing the possibility of cell-induced polymerisation in liver and cervical cancer (HepG2 and HeLa) cells, and lung fibroblast (HPF) cells [120]. To limit cytotoxicity of the metal catalyst, a Cu(I) catalyst was generated *in situ* from a Cu(II)-complex by the endogenous reducing agent GSH and exogenous sodium ascorbate. Alongside the initiator tetra(ethylene glycol) bromoisobutyrate, a variety of monomers, including a derivative of the chemotherapeutic agent paclitaxel, were shown to be polymerised [120] by a cell-induced mechanism. As larger polymeric molecules cannot be effluxed from the cell due to their size, the polymeric paclitaxel drug remains at a higher level in cancer cells for longer. Drug efficacy is therefore improved, along with the subsequent extent of apoptosis.

A study by Dai *et al.* instead focused on the presence of intracellular ROS to oxidatively polymerise telurium (**Te**)-based nanoreservoirs to Te-O polymers [127]. Here, a self-amplification polymerisation mechanism occurs due to the disruption of the cell metabolism and subsequent hampering of intracellular antioxidant systems, resulting in oxidative stress which can then result in further oxidative polymerisation. This approach is aimed at activating the ROS-related apoptosis pathway [127].

Many of these cell-induced polymerisations loosely follow the concept of a prodrug, where the starting compound has little effect on the cells until it has been chemically transformed [129]. In these cases, a biocompatible monomer is given to the cells. Upon polymerisation, the formed material induces an effect on the cells (Figure 1.5 (i)). A counter approach, coined the ‘reverse

prodrug' approach was discussed by Sherman *et al.*, as the starting compound induces an effect on the cells, but after chemical transformation the formed polymer has no pharmacological effect [128]. In this method, the monomer pyrrole (**Py**) is used to induce cell death. Cellular exudate then oxidises the biocompatible initiator. Simultaneously, Py is converted to the biocompatible conductive polymer, polypyrrole (**Ppy**), via an intermediate radical species [130] (Figure 1.5 (ii)).

Conductivity of healthy and malignant tissue is different, with the latter generally being higher due to an increased water and salt content caused by leaky vasculature and poorly functioning lymphatic system [131]. The electrical conductivity of the surrounding tissue has also been shown to have a significant impact on the efficacy of electric field therapy, such as TTFields [132]. The 'reverse prodrug' approach has opened new potential avenues for cancer treatment, with the resulting polymer's conductive nature providing the opportunity for a combined therapy with TTFields.

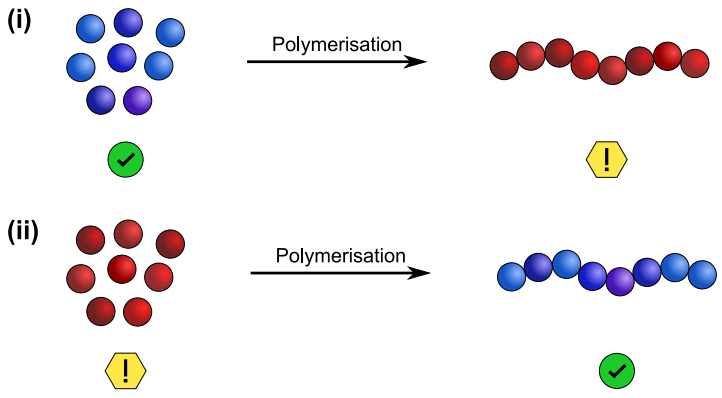


Figure 1.5: Cell-induced polymerisation, comparing the 'prodrug' and 'reverse prodrug' approaches.
(i) 'Prodrug' and (ii) 'reverse prodrug' polymerisation approaches. The green tick icons indicate biocompatibility while the hexagonal exclamation marks indicate cytotoxicity.

There has been increasing interest in transferring the application of conductive polymers from *in vitro* to an *in vivo* system, with Berggren *et al.* showing examples of *in situ* generated poly(3,4-ethylenedioxythiophene) (**PEDOT**) systems in the roots of living plants [133–135]. PEDOT has also been made in an *ex vivo* system, using the monomer and an electrochemical polymerisation approach to create an implantable biomedical electronic device [136].

Following on from this, Strakosas *et al.* polymerised an organic trithiophene-based monomer (**ETE**) derivative in an *ex vivo* zebrafish (*Danio rerio*) brain. Here, tissue metabolites were converted into hydrogen peroxide (**H_2O_2**) by oxidase enzymes, with horseradish peroxidase used as a catalyst to form the radical monomer and subsequent conductive polymer [137]. Next, this polymerisation was moved into an *in vivo* model, with the zebrafish chosen due to reduced ethical concerns. Also their optical transparency allows for easy observation of the formed black polymerised gel [138]. ETE-based polymeric gels were formed in both the tail and brain of the fish at the site of injection. As this reaction was catalysed by the metabolites glucose and lactate, the relative concentrations of these components in different organs dictated the amount of polymer that formed. No polymerisation occurred in the brain when the glucose oxidase enzyme was used, as glucose levels are very low in this organ [137].

Polymerisation *in situ* has also been shown within the nematode *Caenorhabditis elegans* (*C. elegans*), genetically modified to express ascorbate peroxidase which is involved in H_2O_2 metabolism. Liu *et al.* suggested that polyaniline could form locally at the pharyngeal muscle cells after mutated nematodes were soaked in a mixture of the monomer, dimer, and hydrogen peroxide. Here, H_2O_2, when activated by the peroxidase enzyme, acts as a catalyst, enabling the polymerisation of aniline monomers/ dimers. This process had

little effect on overall survival of the worm, but changes in the worm movement and pharyngeal pumping were observed [139]. This approach highlights an alternative method of identifying polymerisation *in situ*. Liu *et al.* found it was not possible to visually observe small quantities of polymer within *C. elegans*, and instead relied on clear changes to physical movement to indicate polymerisation in an *in vivo* model.

There have been some examples of polymerisation in living systems, both *ex vivo* and *in vivo*. However harsh polymerisation conditions alongside difficulties in controlling the reaction in a more complex environment have made the transfer of this technology from *in vitro* models challenging. Therefore, further investigation into the polymerisation approach in both a simple 2D *in vitro* model and the subsequent application to *in vivo* is necessary.

1.4 Polypyrrole as a Material for Bioelectronic Applications

Py (C_4H_5N) is a five-membered aromatic heterocyclic small molecule consisting of carbon, nitrogen and hydrogen with a molecular weight of 67.09 g mol^{-1} [140]. The most common commercial route of synthesis is through the treatment of furan with ammonia and an alumina catalyst at 400℃ (Figure 1.6) [141]. While Py itself is not a naturally occurring molecule, the substructure is found in many natural and pharmaceutical agents [142, 143].

Py forms the polymer, Ppy, which can be fabricated by one of two routes: chemical or electrochemical polymerisation. Within chemical polymerisation, Py is combined with an oxidising agent, commonly $FeCl_3$ [130, 144] to initiate the reaction. With electrochemical polymerisation, Py is dissolved in

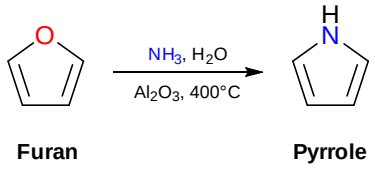


Figure 1.6: Chemical synthesis of pyrrole from furan.

an appropriate solvent, usually acetonitrile, containing an anionic doping salt. Oxidisation then occurrs at the surface of an electrode [145–147].

The most widely accepted mechanism, described by Diaz *et al.* [145] begins with the oxidation of the monomer Py, either at an electrode surface, or using an oxidising agent to form a radical cation (**1**), with resonance structures (**2**, **3**, **4**) (Scheme 1) (Figure 1.7). The coupling of two radicals forms a charged dihydromer (**5**), which then loses two protons to form a Py dimer (**6**) (Scheme 2). This dimer is then oxidised to a cation radical dimer (**7**) with three resonance structures (**8**, **9**, **10**) (Scheme 3), which can react with a radical cation monomer and, upon subsequent deprotonation, form a Py trimer (**11**) (Scheme 4). This sequence continues until the final polymer (**12**) is formed (Scheme 5) [148].

Ppy is a well-used polymer within the bioelectronic field due to its biocompatibility and conductive nature [149]. The conductivity is due to the π-π conjugated backbone, with charge transfer possible from the oxidation of Ppy resulting in polaron and bipolaron states [150]. By varying the oxidant, solvent, dopants and technique, it is possible to create a range of structures such as nanoparticles, nanosheets and nanofibers for different biomedical applications [151–153]. It is also possible to generate soft, flexible materials incorporating Ppy, allowing for significant use of the polymer within bioelectronic research [154].

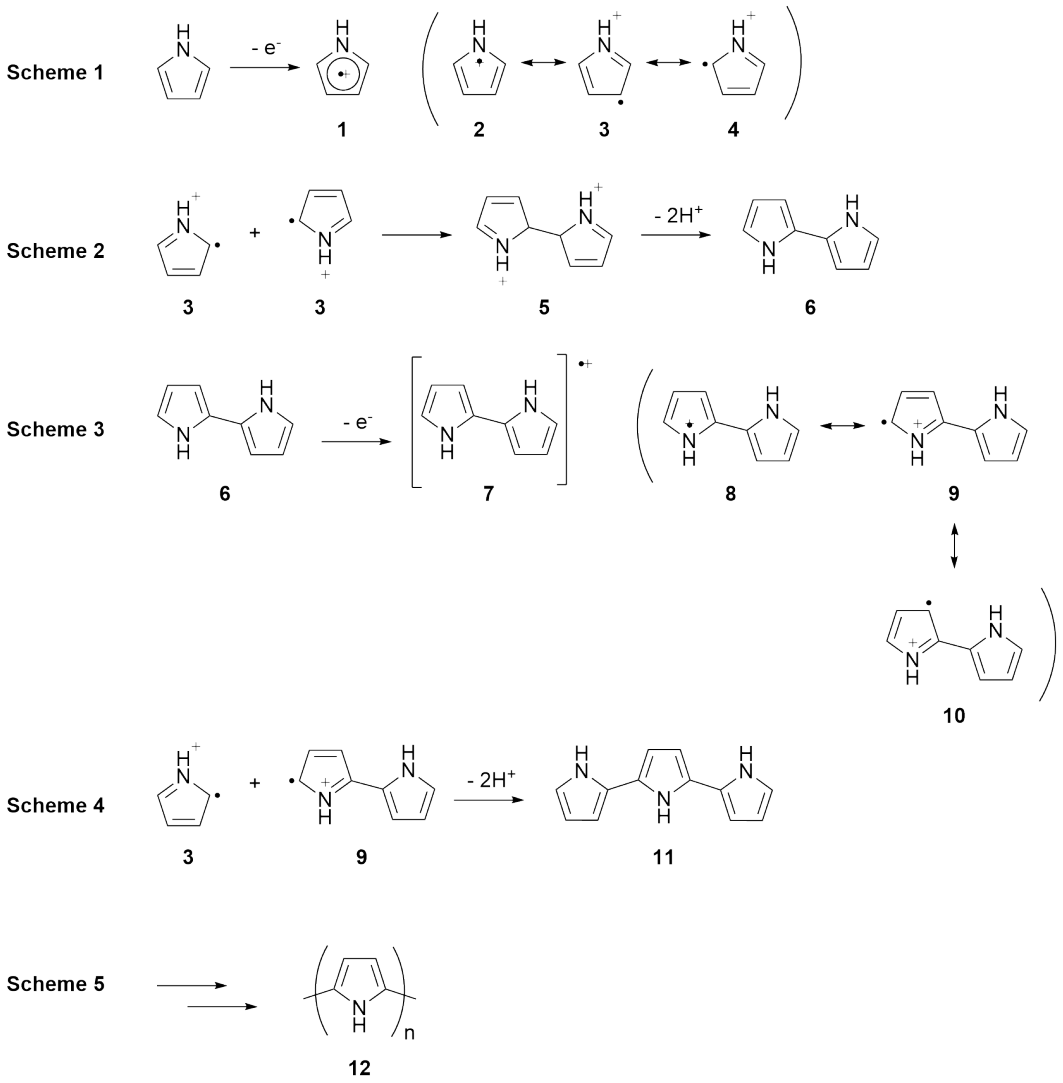


Figure 1.7: Polymerisation mechanism of pyrrole.

Ppy has been used as a controlled release platform for drug delivery, where Ppy is doped with the drug of interest, which upon electrical reduction, is then released from the structure. This was shown by Esrafilzadeh *et al.* who used the antibiotic ciprofloxacin as a dopant of Ppy. This was layered over a PEDOT:PSS-chitosan fibre core, and electrical stimulation of the fibres caused drug release [155]. Alternatively, the corticosteroid dexamethasone has been used to dope Ppy nanowires, which again was released from the system as Ppy was reduced electrochemically [156].

There has been much work combining conductive materials such as Ppy with external electrical stimulation to affect cell behaviour, with a significant portion of this investigating using Ppy as a tool for tissue regeneration. There have been examples of Ppy scaffolds coupled with electrical stimulation promoting neurite growth and orientation, as well as cell differentiation [157–159].

To build on combining Ppy with cells for enhanced electrical stimulation, Ppy has been generated using a living polymerisation approach. This has been achieved using surface modification of *Shewanella oneidensis* and *Escherichia coli* bacteria by Song *et al.*, using Fe (III) as the oxidative initiator to polymerise Py to Ppy [160]. In this way, the bacteria could be used as microbial fuel cells, enhancing the extracellular electron transfer of the system by the conductive polymer surface coating. There has also been work creating artificially conductive biofilms using polymers such as Ppy [161]. This area of research aims to capitalise on the conductive nature of Ppy, allowing a more efficient transfer of electrons from the bacteria to an anode.

The first example of utilising a eukaryotic system was by Ramanavicius *et al.* in 2016 [162]. Here potassium ferrocyanide, ($K_4[Fe(CN)_6]$); (**FOC**), acts as a catalyst and drives the oxidative polymerisation of Py to Ppy. Plasma membrane oxido-reductases then reduce the $[Fe(CN)_6]^{4+}$ ions back into $[Fe(CN)_6]^{3+}$ ions, which can then re-oxidise Py to Ppy, as shown in Fig 1.8 A.

The work using yeast cells was then built on by Sherman *et al.* in 2019, showing the first example of using mammalian cells for cell-driven polymerisation [128]. In this method, the suspension leukaemia cell line K562 was used to polymerise Py. The hypothesis for this reaction was that polymerisation was driven by the trans plasma membrane electron transport system – a network of oxidoreductases that facilitate redox reactions at the outer surface of the cell [163]. It was initially suggested that FOC was oxidised to potassium fer-

ricyanide (**FIC**), where it accepts an electron from Py, driving the radical polymerisation reaction. This hypothesis was found to be incorrect after an electrochemical assay showed that the K562 cells did not have any oxidative capacity, even though FOC was being oxidised to FIC. The proposed mechanism, therefore, suggests instead that the polymerisation of Py to Ppy was driven by cellular exudate upon cell death due to the cytotoxicity of the monomer. This is shown in Figure 1.8 B.

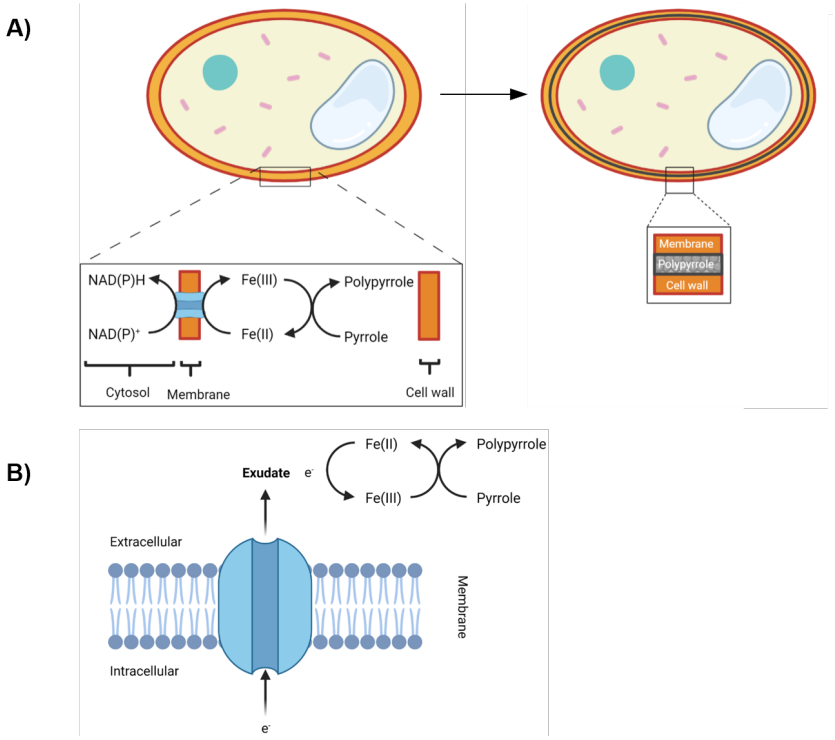


Figure 1.8: Living polymerisation of pyrrole (Py) to polypyrrole (Ppy) in eukaryotic cells.
A) Oxidative polymerisation of Py to Ppy between yeast cell wall and cell membrane. Based on a figure by Ramanavicius *et al.* [162]. B) Redox polymerisation of Py to Ppy in mammalian cells. Based on a figure by Sherman *et al.* [128]. Reproduced with permission. Created with biorender.com.

A potential opportunity to capitalise on the tumour microenvironment has been highlighted, allowing the polymerisation of Py by a cell-mediated polymerisation approach. Further investigation into the characterisation of the polymer, as well as expanding the cell types used for this reaction, is necessary. There is also a need to better understand the polymerisation in a more

complex living system to identify its potential as a tool for cancer therapy by a 'reverse prodrug' mechanism.

1.5 *Caenorhabditis elegans*

1.5.1 Background and Life Cycle

Caenorhabditis elegans, more commonly referred to as ***C. elegans***, belong to the phylum Nematoda, or roundworm. They are small (approximately 1 mm in length), non-hazardous and non-parasitic organisms that freely live in the soil. *C. elegans* are also transparent, which means that biological transformations can be observed in situ with conventional brightfield or with fluorescence microscopy [164]. One of the most common strains, the naturally occurring Bristol N2 'wild-type', was isolated by Nicholas *et al.* in 1959 from mushroom compost near Bristol, England [165].

The are a variety of reasons why *C. elegans* are seen as an attractive alternative to other traditional *in vivo* models. Firstly, the genome of *C. elegans* was mapped in 1973 by Brenner [166], allowing for much research into how genetics can be altered upon changes to environmental and chemical stimuli.

Secondly, *C. elegans* are typically self-fertilising hermaphrodites (0.1% of the population is spontaneously male), allowing for the rapid generation of clones [167].

Thirdly, the life cycle is short, and can easily be controlled by adjusting the temperature, with *C. elegans* progressing from embryo to adult in 3 - 5 days at a temperature of 15 - 20°C (Figure 1.9). The adults then live for a further 2 - 3 weeks assuming favourable conditions (sufficient food, space and an appropri-

ate temperature) [168]. In the case of unfavourable conditions, *C. elegans* do not progress from larvae to adults, but instead undergo dauer arrest [169]. In this state, the body of the worm is constricted, intake is arrested, there is an increased storage of lipids and the worms undergo a state of dormancy. Upon the return of favourable conditions, dauer rapidly revert to Larval stage (**L**) 3/ L4 and then progress to adulthood, with no effects on the overall lifespan of the adult nematodes [169, 170].

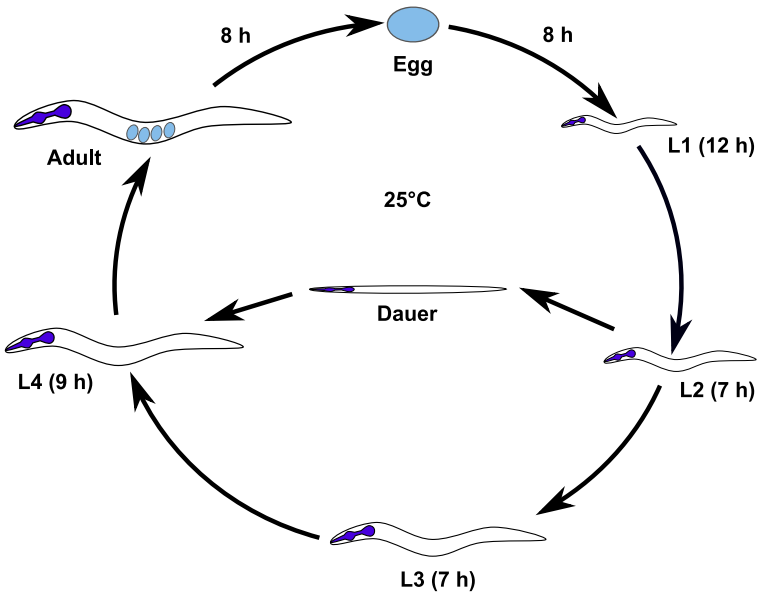


Figure 1.9: Life cycle of *C. elegans* at 25℃. Adapted from Pandey & Pandey 2014 [171]

Lastly, *C. elegans* comply with the UK National Centre for the **R**eplacement, **R**eduction and **R**efinement (**NC3Rs**), which aim to replace *in vivo* testing of sentient animals with those that, based on current scientific understanding, are not capable of experiencing suffering [172, 173].

C. elegans are increasingly being utilised as a model for toxicity testing [174–177]. There are a variety of endpoint studies that can be undertaken to determine the toxicity of a compound. Firstly, survival rates of nematodes can be used to measure the effect of a compound over the lifespan of the worm [176].

Secondly, a growth and development assay can be employed to observe variations in the phenotype of *C. elegans* when exposed to a toxin. Here, changes in size, metabolomics, genetics, developmental delays or morphological abnormalities can be shown to indicate toxicity [178]. Reproduction assays may also be used to assess the impact of a substance on the reproductive capacity of *C. elegans* [179]. Other tests include behavioural assays, studying changes in locomotion, feeding and chemotaxis (showing potential neurotoxicity), bioaccumulation studies, and molecular and genetic assays, investigating changes in gene expression and DNA damage at the molecular or genetic level [174, 180].

1.5.2 Mutating *C. elegans*

Of the hallmarks of cancer, the only two that cannot be investigated using *C. elegans* are: 1. avoiding immune destruction; and 2. affecting vasculature. These nematodes are therefore an attractive model for cancer [181]. *C. elegans* is commonly used in genetic research since the genome was sequenced, with over 83% of *C. elegans* proteome having an equivalent human homologue [182].

As discussed previously, specific genes are known to play a role in cancer progression and therapeutic outcomes. Mutated *C. elegans* are being increasingly used in disease models as changes to genes can be monitored, as well as changes to the phenotype and nematode behaviour. For example, a loss-of-function mutation to the *ced-3* gene, involved in programmed cell death, was used to identify the mechanism of action of the protease inhibitor bortezomib in the treatment of non-melanoma skin cancer [183]. By treating nematodes that can undergo apoptosis and mutated nematodes that cannot, it was possible to compare the number of apoptotic corpses and changes in expression of specific proteins of interest. This helped provide valuable information as to the effects of a specific treatment on a living system [183].

This highlights the advantages of using a simple *in vivo* model in cancer research, as effects of specific treatments can be compared between mutated *C. elegans* and the Bristol N2 wild-type. The range of experiments that can be carried out is also expansive, with effects of a treatment on survival, worm size, phenotype, motility, and the genome all possible.

1.6 Thesis Overview

Cell-mediated polymerisation is a growing area of research. This approach allows a unique ability to capitalise on the cellular microenvironment, enabling the polymerisation to occur in conditions unique to cancer cells. There is little research on utilising this approach to make conductive polymers in both *in vitro* and *in vivo* systems which can then be used with electric stimulation to provide a further effect. For example, organic conductive biopolymers could be coupled with TTFields, potentially enhancing the TTField effect and improving the treatment.

The main aim of this thesis, as illustrated in Figure 1.10, is:

To investigate the enhancing tumour treating fields with cell-mediated polymerisation as a dual approach for a possible treatment of hard-to-treat cancers, such as glioblastoma.

This thesis is comprised of three results chapters - Chapters 2, 3 and 4, as well as a methods chapter - Chapter 5, and a perspectives future work chapter - Chapter 6. The rationale and brief aims for the results chapters are as follows:

Chapter 2 - Cell-Induced Polymerisation: This chapter aims to expand on initial studies by Sherman *et al.* on using Py in a 'reverse prodrug' approach with two patient-derived cancer cell lines [128]. The aims of this chapter are:

- to identify key methods to characterise the polymer formed in an *in vitro* system; and
- to investigate the cytotoxicity of the starting materials on the cells.

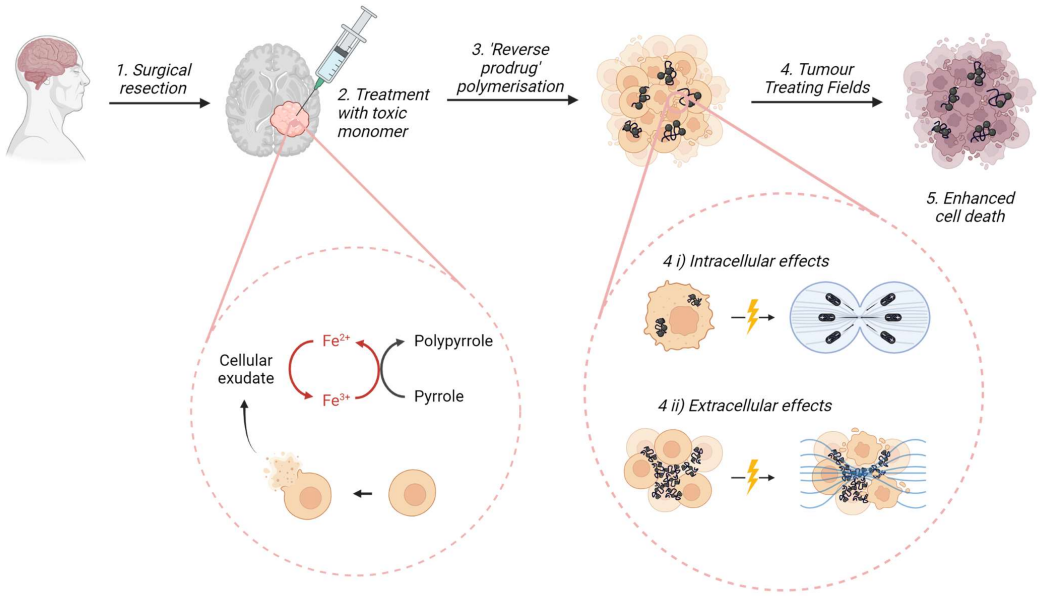


Figure 1.10: Research Overview: Combination approach of 'reverse prodrug' polymerisation and tumour treating field therapies.

Chapter 3 - Polymerisation of Pyrrole in Living Systems: *C. elegans* is beginning to be used more as a cancer model due to its transparent nature, short life cycle, sequenced genome and the range of ways toxicity can be assessed. Therefore, the overall aim of this section is to investigate the 'reverse prodrug' approach using *C. elegans* as the *in vivo* model. As it is possible to use genetic mutants as cancer models, this also creates the opportunity to apply this approach on two modified nematode models that better represent the mutated p53 and H3.3 proteins found in some gliomas.

The aims of this chapter are:

- to characterise the formation of Ppy within wild-type *C. elegans*; and
- to investigate the cytotoxicity of the starting materials on wild-type *C. elegans* and mutated nematodes.

Chapter 4 - Enhancing Tumour Treating Fields: TTFields are an increasingly important modality in the treatment of glioblastoma and other hard-to-treat cancers. Despite an increased overall survival when used alongside standard chemo- and radio-therapy procedures, there is still a long way to go to improve overall prognosis of the disease. It is therefore of interest to investigate potential ways to enhance the TTField effect, capitalising on the modes of action dielectrophoresis and dipole alignment by using molecules that are conductive, polar or dielectric.

The aims of this chapter are:

- to design and test a high throughput plate for the application of TTFields *in vitro*; and
- to investigate the enhancement of TTFields using nano-sensitisers and the 'reverse prodrug' approach.

Chapter 2

Cell-Induced Polymerisation

2.1 Introduction

Cell-induced polymerisation is a growing area of research, utilising the localised cell environment to dictate the chemistry of polymerisation [184]. Such reactions can occur either at the cell surface [119, 185–187] or intracellularly, and result in the formation of smaller polymers [127, 188] or supramolecular structures such as hydrogels or nanoparticles [189–191]. The potential application of this technology is vast, ranging from cell tracking, cancer therapy and cell behaviour modulation.

Alongside this, in recent years there has been increased understanding of the effects of bioelectricity on cell behaviour. This can be used to specifically address cancer, by hijacking bioelectricity within the cancer cell microenvironment, taking advantage of both ionic currents (from ion movement across a cell membrane) and faradaic currents (from redox systems) [192].

Polypyrrole (**Ppy**) is a typically used polymer within this field, due to its biocompatibility and conductive nature [149]. Ppy has been coupled with electrical stimulation for tissue engineering applications such as neurite cell growth stimulation and controlled release [156, 157, 193]. However, due to its long, conjugated chain and weak polymer-solvent interactions, Ppy is poorly soluble [194]. This creates a challenge in characterising the material, as purification is harder, and standard characterisation methods that rely on analysing a sample in solution are not possible.

There is a variety of analytical methods in literature that are used to characterise Ppy, with multiple different approaches used to holistically understand the chemical composition and morphology of the polymer. To investigate the physical form, scanning electron microscopy (**SEM**) is routinely used, as the starting materials and polymerisation method can greatly affect the structure, which can, in turn, influence the conductivity of the material [195, 196].

To analyse the chemical structure, Fourier-transform infrared spectroscopy (**FTIR**) is often used due to the distinct peaks associated with Ppy, while X-ray diffraction may be employed to show the amorphous nature of the polymer [197]. Ultraviolet-visible (**UV-Vis**) spectroscopy is also commonly utilised due to an absorption peak at approximately 446 nm for Ppy [197]. Other techniques used include differential scanning calorimetry to assess the glass transition temperature, and conductivity measurements [198].

While these techniques can successfully be used to characterise Ppy produced either chemically or electrochemically, the polymerisation of pyrrole (**Py**) using a cell-induced approach is inherently more complex due to the unique chemical fingerprints of all additional cellular components [199]. Therefore, multiple characterisation methods must be employed to provide a detailed understanding as to how to characterise polymers formed in a more complex environment,

as well as the physicochemical properties of the Ppy formed in a cell-induced approach.

2.2 Experimental Aims and Objectives

The overall aims for this chapter are:

- to identify key ways to characterise the polymer formed in an *in vitro* system; and
- to investigate the cytotoxicity of the starting materials on the glioblastoma (**GBM**) cells.

To assess polymer formation using an adherent cell line, the first objective is to use patient-derived cells from the core and invasive margin of a GBM tumour to synthesise Ppy using Py and the inactive initiator potassium ferrocyanide (**FOC**; Fe (II)). It is hypothesised that the cellular exudate oxidises Fe (II) to Fe (III), which drives the polymerisation mechanism. After forming the polymer, it is necessary to investigate the most suitable method for polymer characterisation, such as brightfield microscopy, greyscale analysis, FTIR spectroscopy, UV-Vis spectroscopy and solid state nuclear magnetic resonance (**SS NMR**). To probe polymer morphology, dynamic light scattering (**DLS**) and SEM can be used.

After this, the next objective is to understand the toxicity of the starting materials on the cells. This can be achieved using live/ dead fluorescence and metabolic assays, alongside flow cytometry to gain insight into the mechanism of cell death. As a result, the optimum concentrations of the starting materials for the polymerisation reaction can be determined.

2.3 Experimental Design

2.3.1 General information

In the following text these abbreviations are used: samples are labelled as Py for pyrrole, FIC for potassium ferricyanide and FOC for potassium ferrocyanide. The concentration used is expressed in mM and recorded in subscript with the abbreviation, for example 'FOC_2' denotes 2 mM FOC solution. Samples that contain cells are denoted with a 'C' at the end of the abbreviation, for example $Py_{500}FOC_{40}C$.

2.3.2 Viability Studies

There are numerous assays that can be used for *in vitro* toxicity testing. They can broadly be summarised into the following assays [200]:

A. Colorimetric e.g. 3-[4,5-dimethylthiazol-2-yl]-2,5-diphenyl tetrazolium bromide (**MTT**) or lactate dehydrogenase (**LDH**);

B. Fluorometric e.g. resazurin-based assays.

Resazurin-based assays have much less inter- and intra-variation than LDH assays, and have also shown greater sensitivity to cell numbers than MTT assays, therefore they were chosen as an appropriate assay for the viability study in this work [200, 201]. The assay detects the number of living cells within a sample by the following mechanism: first, the non-fluorescent molecule, resazurin, is taken into healthy cells. The co-enzyme nicotinamide adenine dinucleotide (**NADH**) and other reducing agents then reduce this into the strongly fluorescent pink molecule resorufin, as shown in Figure 2.1 [202]. The fluorescence

can then be recorded using a plate reader at 560/ 590 nm (excitation/ emission) and the percentage viability determined from the fluorescence of negative (healthy) and positive (dead) cells.

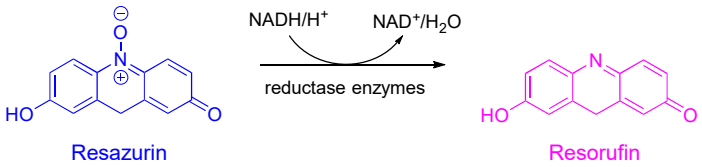


Figure 2.1: Mechanism of the PrestoBlue™ assay.
Mechanism of metabolic assay. Blue, non-fluorescent resazurin is reduced to pink, fluorescent resorufin by reductase enzymes and NADH.

2.4 Results and Discussion

2.4.1 *In vitro* Polymerisation of Pyrrole - Initial Studies and Characterisation

To select a monomer for this reaction, the following criteria was used: the starting material must exert cytotoxicity on the cells, and this toxicity must be curtailed upon formation of the polymer; the reaction must be able to occur in physiological conditions i.e. in an aqueous solution at a biological pH between 6.8 - 7.2; the formed polymer must have a conjugated backbone and exhibit good electrical conductivity; the polymer must have good long-term electrochemical stability and be biocompatible. Polypyrrole is easily synthesised in aqueous solutions, has an intense brown-black colour, is biocompatible without an inflammatory effect *in vivo* and has good long-term stability [149, 203]. Therefore pyrrole was chosen as the monomer for this work investigating the 'reverse prodrug' approach.

'Glioma Core Enhanced' (**GCE**) 31 and 'Glioma INvasive margin' (**GIN**) 31, originating from the core and invasive margin of a glioblastoma patient respectively, were chosen as the adherent cell lines used here [30]. As the cell-mediated polymerisation is inherently uncontrolled, with purification of the resulting polymer time-consuming, it was of interest to investigate a range of characterisation techniques that could provide insight into the physicochemical properties of Ppy.

To first determine the potential of this cell-induced polymerisation approach, high concentrations of the toxic monomer Py and the active/ inactive initiator FIC (Fe (III))/ FOC (Fe (II)) were used to treat the GBM cells. These cells were then imaged using a brightfield microscope to observe visual changes in the cell morphology, and identify the formation of any black polymer.

In the case of cells treated with FOC (Fe (II); 2 mM), the cell morphology of GIN 31 was the same as that of the untreated negative control (Figure 2.2 A (i, ii)). FOC is licensed by the European Food Safety Authority as food additive E536 at a level of 20 mg/ kg in food for adults, with no concerns about genotoxicity and carcinogenicity [204]. Cells treated with Py (500 mM) in both the presence and absence of FOC (Fe (II); 2 mM) had a different morphology to that of the negative control, with an enlarged shape and flattened cytoplasm, akin to the shape of a fried egg (Figure 2.2 A (iii, iv)). This shape is commonly associated with cellular senescence, which can be induced as a cell is exposed to a stressor [205]. Both the sample containing Py with the inactive initiator (Fe (II)), and the sample with just the monomer, Py, showed the presence of black dots within the cells. These were also observed with GCE 31 cells (Figure 2.2 B (iii, iv)). While this may be indicative of the formation of black Ppy, this may be due to cell blebbing or the formation of apoptotic bodies [206].

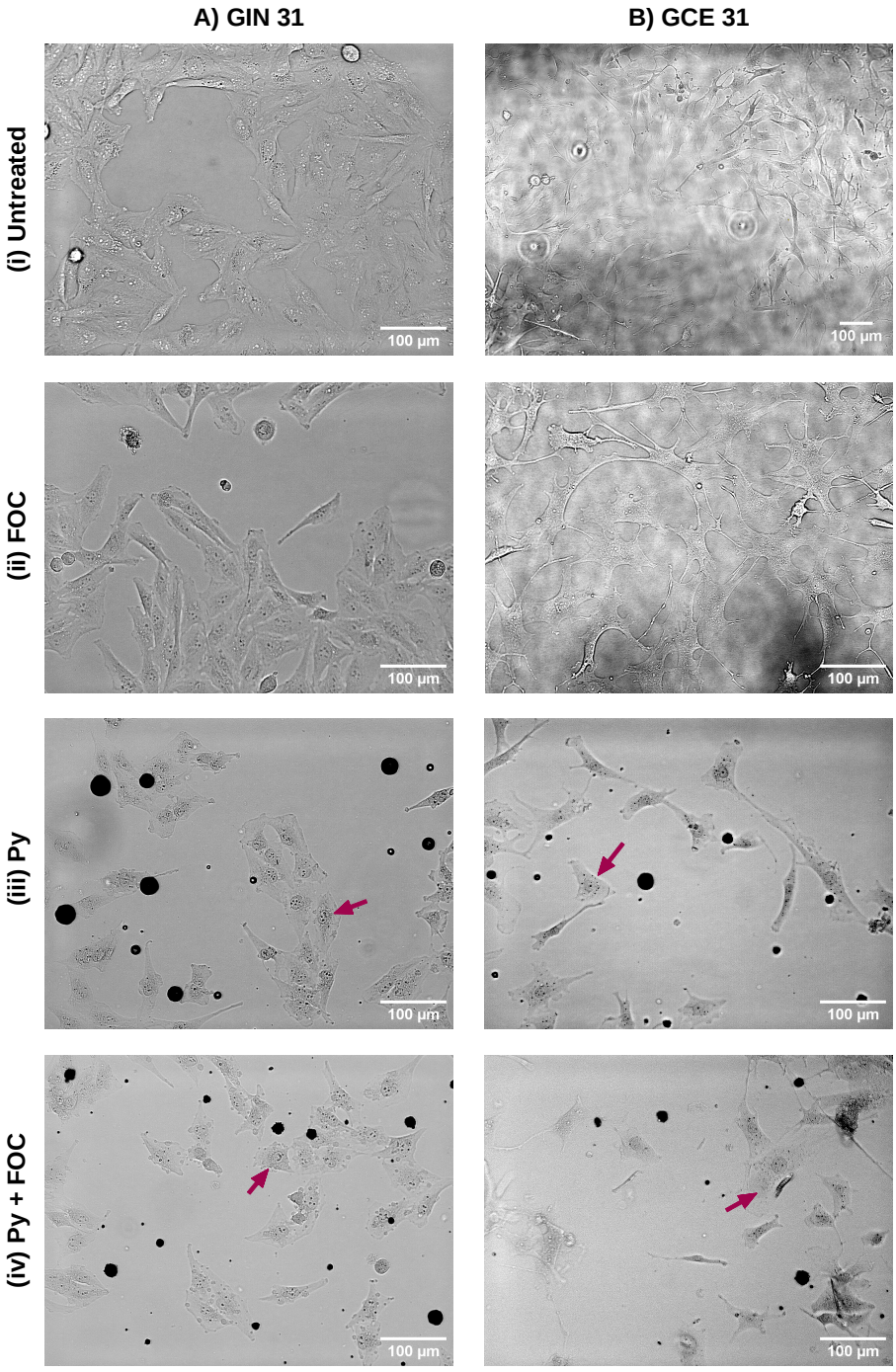


Figure 2.2: Brightfield images of (A) GIN 31 and (B) GCE 31 morphology 48 hours after cell-mediated polymerisation at 500 mM pyrrole (Py) and 2 mM ferrocyanide (FOC; Fe (II)).
Microscope images of cells (i) untreated, or treated with FOC (2 mM) (ii), Py (500 mM) (iii), or Py and FOC (iv). Scale bar is 100 μm. Arrows show 'fried egg' morphology.

To confirm the formation of Ppy, an alternative characterisation approach focused on capitalising on the dark colour of the polymer. This was achieved by comparing the colour intensity of samples with or without the monomer, cells and the initiator in both its active and inactive form (Figure 2.3 A and B (i)). The pixel intensity was determined using ImageJ, where a lower pixel intensity, i.e. a darker colour, indicated the presence of more Ppy (Figure 2.3 A and B (ii)). The positive control, consisting of Py and the active initiator, FIC (Fe (III)), had the lowest pixel intensity, corresponding to the instantaneous polymerisation of Py. This value was then compared to samples containing Py and FOC (Fe (II)) in the presence and absence of cells.

For this polymerisation to occur, it is necessary for Fe (II) to first be oxidised to Fe (III) before the reaction can proceed. It is hypothesised that this oxidation is caused by the release of cellular exudate from the cells and is due to the electron transport through cell plasma membrane by trans-plasma membrane electron transfer. In both cases, cells are required to drive this oxidation, and so it was hypothesised that polymer should only form in the presence of cells.

Therefore, it was anticipated that samples containing Py, FOC (Fe (II)) and cells would appear darker in colour than samples of Py and FOC in the absence of cells (Figure 2.3 A, B (i)). However, the pixel intensity was very similar for both samples (Figure 2.3 A, B (ii)) and was more noticeable with GIN 31 cells compared to GCE 31 cells (Figure 2.3 A), suggesting the flask may contain more reducing components than the GCE 31 sample. This suggests that some components present in the cell culture medium may also have oxidative capabilities, and the GIN 31 flask may have contained more reducing components than the GCE 31 flask.

A lower pixel intensity compared to the negative control was also seen in the samples containing Py in the presence or absence of cells without initiator. This was not seen in samples containing only initiator. Therefore, this darker colour may be, in part, due to some auto-polymerisation as Py oxidises [207].

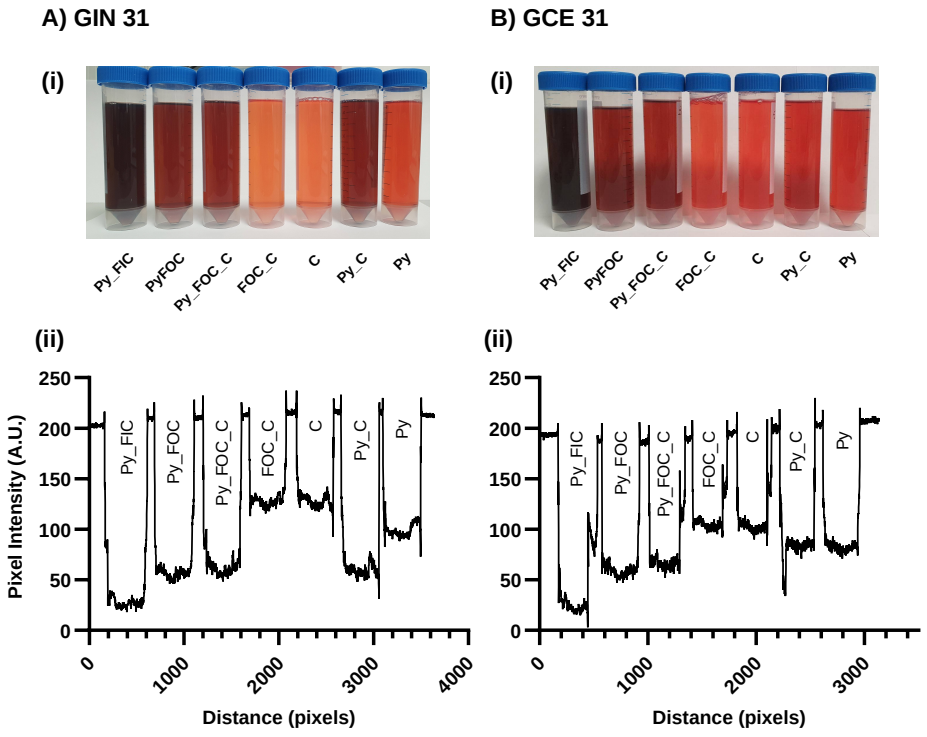


Figure 2.3: Colour change of culture medium after incubation pyrrole (Py) and/ or ferricyanide (FIC; Fe (III)) and/ or ferrocyanide (FOC; Fe (II)) in the presence or absence of (A) GIN 31 or (B) GCE 31 cells after 48-hour incubation.
(i) Tubes containing cell-culture medium plus treatment in the presence or absence of cells 'C'. Concentrations used: Py - 500 mM; FIC - 40 mM; FOC - 40 mM. Image (i) translated to greyscale and pixel intensity values of each tube determined using ImageJ (ii).

Size, shape and charge of particles influence both the conductivity of a material and how it is taken up by cells [195, 208, 209]. Following previous work by Sherman *et al.* that used SEM to characterise Ppy [128], this approach was adopted here. Good quality high magnification images of the cell-induced polymer were acquired, but the morphologies of the sample exhibit differences compared to previous literature [128, 210] with the polymer here formed in sheets, compared to the aggregated structures recorded by others (Figure 2.4 A).

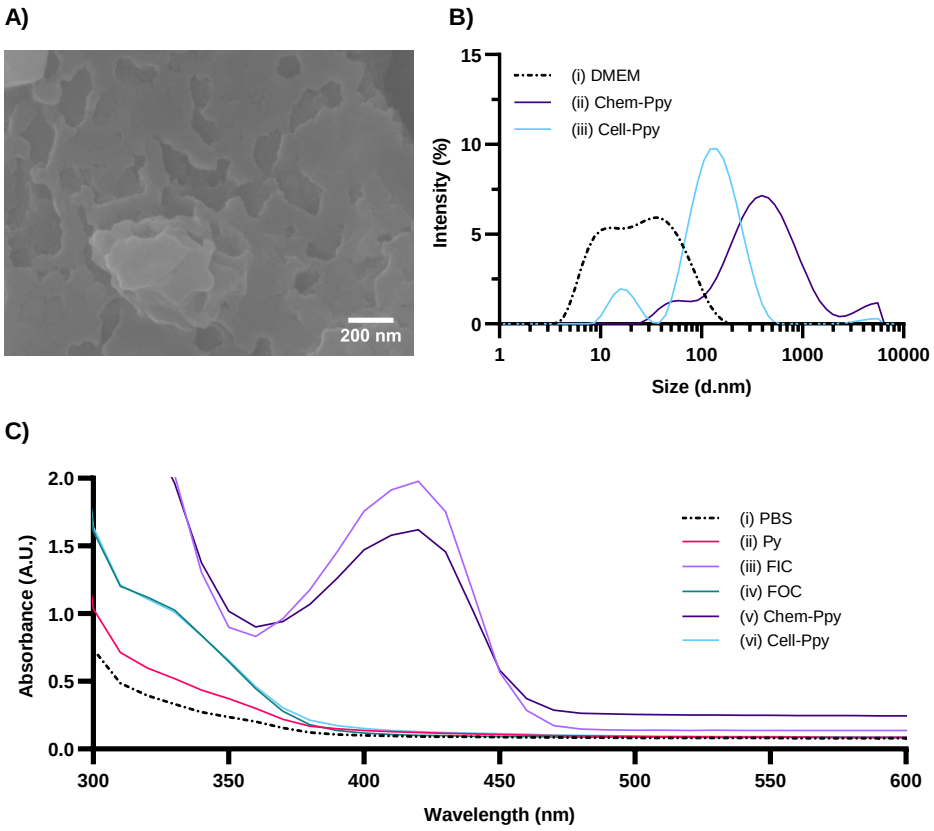


Figure 2.4: Scanning electron microscopy (SEM), dynamic light scattering (DLS) and UV-Vis characterisation of polypyrrole (Ppy).
(A) SEM images of solid at a magnification of ×70 000; scale bar = 200 nm. (B) DLS of (i) complete cell-culture medium, (ii) chemically-synthesised Ppy ($Py_{500}FIC_{40}$) or cell-mediated Ppy ($Py_{500}FOC_{40}C$ (GCE 31)). (C) UV-Vis spectroscopy of starting materials ((i) PBS, (ii) Py, (iii) FIC_{20}, (iv) FOC_{20}) and polymer formed by (v) chemical-synthesis ($Py_{500}FIC_{20}$) or (vi) cell-induced polymerisation ($Py_{500}FOC_{20}C$).

Next, DLS was investigated as a tool to report the size of the polymer particles. Average sizes for particles obtained from chemically-synthesised Ppy ($Py_{500}FIC_{40}$) experimental conditions were recorded as 411 ± 41 nm, compared to 133 ± 9 nm for cell-mediated Ppy ($Py_{500}FOC_{40}C$) (Figure 2.4 B). The results are affected by broad particle size distribution, skewing results towards the larger particle sizes due to the intensity of light scattered [211, 212]. Here, a narrower particle size distribution was recorded for the cell-induced polymerisation. As this reaction can only occur when Fe (II) is converted to Fe (III), the rate of reaction is slower, and so the polymer will form more gradually. This will have resulted in a more controlled polymerisation with shorter chains formed.

Previous works reported in the literature have shown that Ppy can be characterised using UV-Vis, with the neutral polymer having a peak at 387 - 413 nm, the bipolaron with two peak at 886 - 1240 nm and the polaron with two peaks at 539 - 590 and 1550 - 1771 nm [213, 214]. Ferricyanide (**FIC**) can easily be identified in a sample due to its absorbance at a wavelength of 420 nm due to the transfer of an electron from the ligand to the Fe (III) core [215–218]. In contrast, this absorption is not seen with FOC.

In this work, spectra for the starting materials and medium (PBS) were first obtained to identify peaks indicative of each material (Figure 2.4 C (i - iv)). A positive control of chemically-synthesised Ppy ($Py_{500}FIC_{20}$) was next measured, and showed an absorbance peak at 420 nm, with any absorbance from Ppy masked by the $[Fe(CN)_6]^{3-}$ ion (Figure 2.4 C (v)). There was no peak associated with the cell-induced polymerisation between 400 - 500 nm, and no peak above 500 nm for the chemically synthesised or cell-induced polymer sample (Figure 2.4 C (vi)). The absence of a peak at 420 nm also suggests that minimal FOC (Fe (II)) was oxidised by the cells to FIC (Fe (III)), potentially

limiting the polymerisation reaction. In this experiment, a lower concentration of FOC was used compared to previous experiments (20 mM instead of 40 mM) to reduce the overlap or hiding of Ppy peaks, however this may have also lowered the rate of polymerisation. To identify distinct peaks associated with Ppy, other chemical characterisation methods were employed.

FTIR was used because the peaks associated with Py and FOC occur at different wavenumbers and peak intensities [219, 220]. Peaks associated with the sample from cell-mediated synthesis ($Py_{500}FOC_{40}C$) (Figure 2.5 B (iv)) were compared to spectra the starting materials - Py (Figure 2.5 A and B (i)) and FOC (Figure 2.5 A and B (ii)), as well as the chemically synthesised Ppy ($Py_{500}FIC_{40}$) in the same supplemented cell-culture medium ('Dulbecco's modified eagle medium'; **DMEM**) as for the cell-mediated polymerisation reaction, but in the absence of cells (Figure 2.5 B (iii)).

In the chemically synthesised Ppy, a shoulder at 3080 cm^{-1} and a peak at 1647 cm^{-1} are indicative of the respective N-H stretch and bend of a secondary amine (Figure 2.5 A and B (iii)) [197, 221, 222].The peak at 1530 cm^{-1} most likely shows ring vibrations, while those at 1453 and 1236 cm^{-1} are typical of C-N stretching, as in line with other literature [197, 221–223].

Finally, the peaks at 1029 and 741 cm^{-1} are proposed to be N-H in-plane deformations and C-H out-of-plane deformations correspondingly [221, 223]. These peaks can be seen in the sample from cell-mediated synthesis at 3060 (N-H stretch) and 1646 (N-H bend), 1185 (C-N stretch) and 1049 (N-H in-plane deformation) cm^{-1} (Figure 2.5 B (iv)). A peak indicative of C≡N from FOC (Figure 2.5 A) can be seen in the FOC spectrum at 2047 cm^{-1} (Figure B (ii)), and at 2043 and 2048 cm^{-1} in the chemically-synthesised (Figure 2.5 B (iii)) and cell-mediated (Figure 2.5 B (iv)) samples respectively.

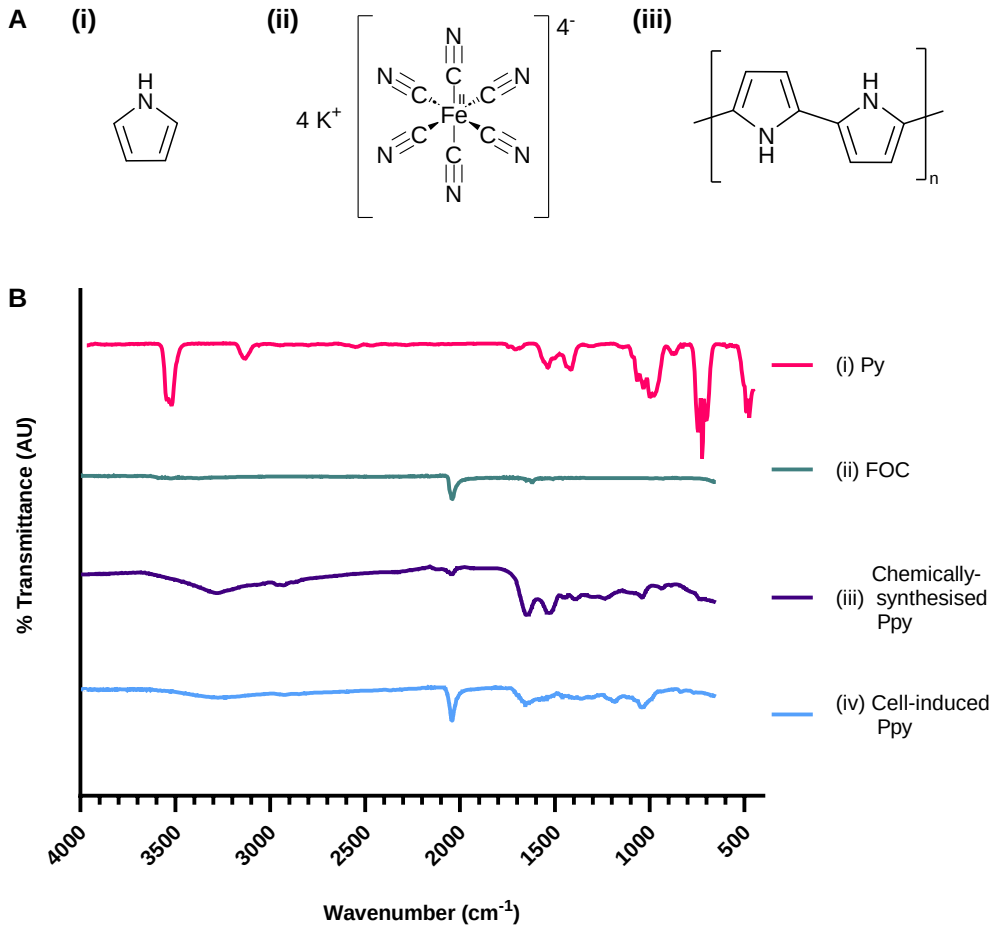


Figure 2.5: FTIR characterisation of pyrrole (Py), ferrocyanide (FOC) and polypyrrole (Ppy). (A) Chemical structures of (i) Py, (ii) FOC, (iii) PPy. (B) Stacked FTIR spectra of (i) Py; (ii) FOC; (iii) chemically-synthesised Ppy ($Py_{500}FIC_{40}$); (iv) cell-induced Ppy ($Py_{500}FOC_{40}C$). Py spectrum obtained from NIST [224].

To support this FTIR work, carbon 13 SS NMR was also employed to determine the formation of Ppy, as this polymer has been extensively characterised by NMR in literature [225–227]. The Py monomer is known to have two key peaks at 119 and 108 ppm for the α and β carbons respectively (Figure 2.6 A), while the α-α' linkages of neutral Ppy can be found around 125 ppm (Figure 2.6 B). Finally, evidence of the oxidised polaron and bipolaron forms of the polymer (Figure 2.6 C and D) can be identified by a peak at approximately 143 ppm. The positive charges present on the (bi)polaron are deshielded when exposed to a magnetic field, leading to high-frequency chemical shifting.

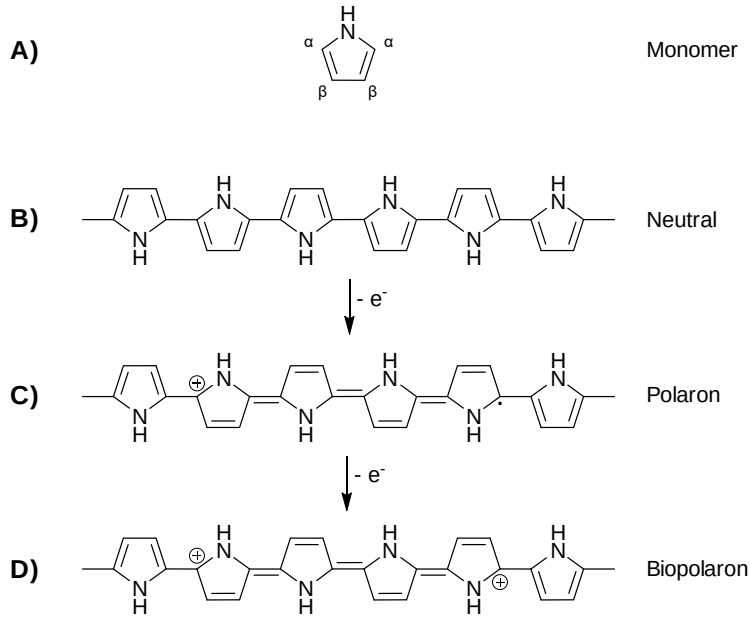


Figure 2.6: Chemical structures of pyrrole (Py) and polypyrrole (Ppy) (A) Py with α and β carbons labelled; neutral Ppy (B), oxidised polaron (C), and bipolaron states (D).

First, a control of Ppy and carbon black was analysed to identify unique peaks associated with the polymer (Figure 2.7 A). The peaks at 123 and 125 ppm were consistent with the chemical shifts of carbon in the neutral and partially oxidised forms of Ppy, with the broad peak at 146 ppm indicating some of the polymer was in the quinoid form (due to its handling in air) [225].

Next, a chemically-synthesised sample of Ppy using Py and FIC (Fe (III)), prepared in deionised water, was analysed (Figure 2.7 B), with peaks at 120 - 130 ppm again indicating the presence of Ppy. A slight peak at 145 ppm once again was indicative of the (bi)polaron structure of Ppy. This sample still contained traces of Py, as evidenced by the peak at 106 ppm.

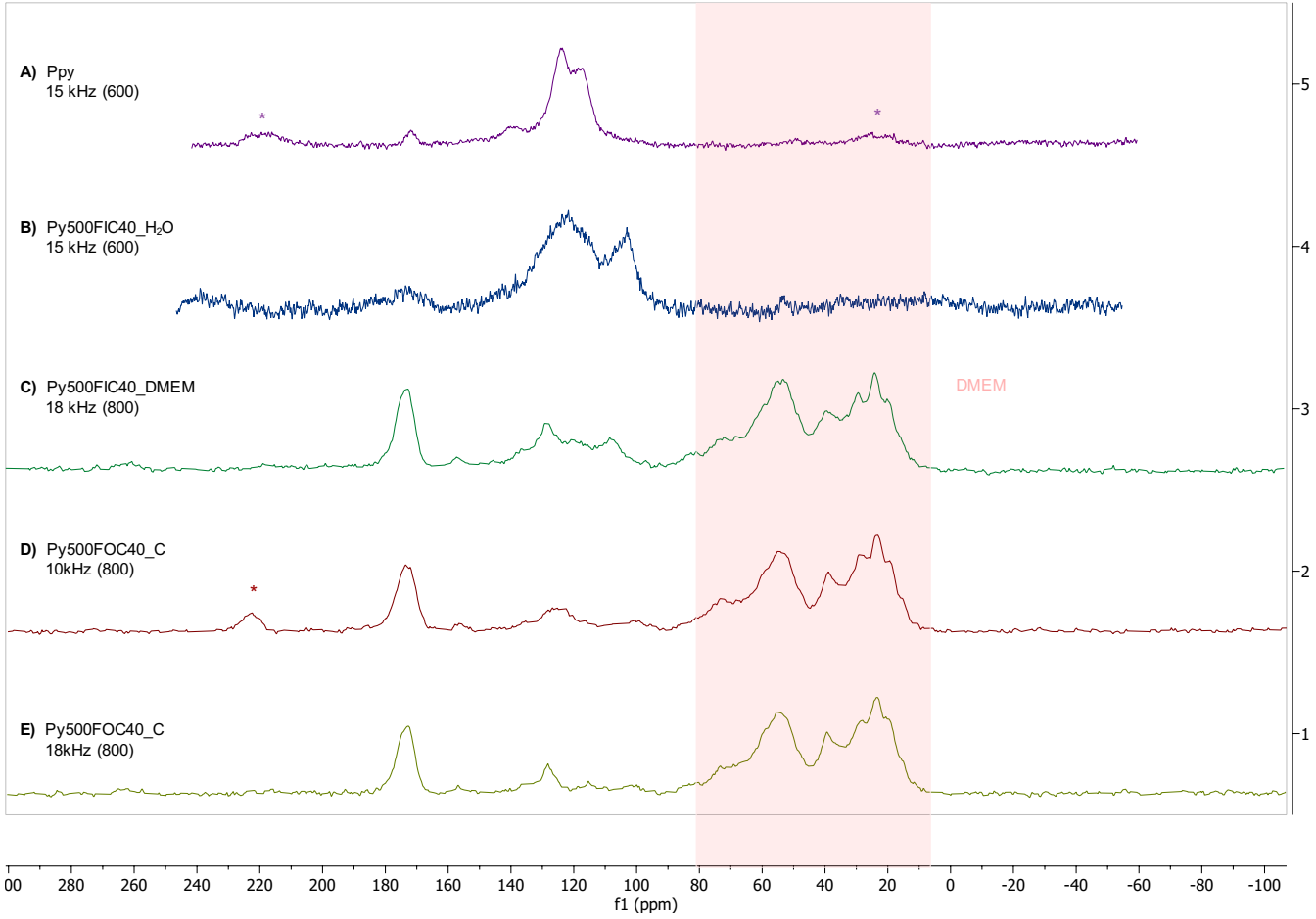


Figure 2.7: ^{13}C Solid state NMR of polypyrrole.

Figure 2.7: (A) 'Control' Ppy (Sigma); (B) Chemically-synthesised Ppy in H_2O; (C) Chemically synthesised Ppy in complete DMEM; (D and E) Cell-mediated Ppy carried out at different magic angle spin frequencies. Number in brackets represents the magnet used (600 or 800 MHz). * = spinning side band. Peaks associated with the cell-culture medium 'DMEM' are highlighted in pink.

To identify peaks associated with the cell-culture medium, which would be present in the cell-mediated synthesis sample, Ppy was next chemically-synthesised in DMEM (Figure 2.7 C). Due to a relatively poor signal-to-noise ratio seen for the sample in water (Figure 2.7 B), the analysis of the sample in DMEM was carried out using an 800 MHz magnet and 3.5 mm probe. Similar peaks between 120 - 130 and 158 ppm were observed, with peaks between 6 - 81 ppm likely arising from components in the cell-culture medium.

Lastly, a sample of the cell-mediated synthesis ($Py_{500}FOC_{40}C$) conducted in DMEM was analysed. To confirm that the peaks associated with Ppy were not hidden by sidebands, this sample was run at both 10 and 18 kHz MAS (Figure 2.7 D, E). The peak in the cell-mediated sample at 222 ppm (also appearing in the Ppy/ carbon black control sample at 223 ppm) was shown to be a sideband, as when this was rerun at 18 kHz this band disappeared. The opposing sideband is hidden beneath the DMEM peaks. Once again, peaks at 123 - 129 ppm indicate the formation of Ppy, with a peak at 157 ppm suggesting the presence of the quinoid form. A small peak at 102 ppm indicated Py impurities not fully removed from this sample.

2.4.2 Toxicity studies

As the cell mediated polymerisation was carried out at toxic concentrations of Py and FIC or FOC, it was necessary to better understand the toxicity profile of these starting materials on GBM cells. This is important, as a tailored concentration that maximises polymerisation while minimising the side-effects

will be required to transfer this therapy into a clinical setting. Therefore dose-response curves and apoptosis studies were carried out to optimise these concentrations.

As Py has limited solubility in water [140, 207, 228], it was preferential to solubilise Py in dimethylsulfoxide (**DMSO**), however cell line sensitivity to this solvent greatly varies [229–231]. GCE 31 cells were exposed to 0.2% DMSO for 48 hours and clear signs of toxicity were observed, with cells exposed to DMSO showing a significant decrease in metabolic activity compared to untreated cells (Figure 2.8 A). Preliminary findings also show that GIN 31 cells were similarly affected by this concentration of DMSO (Figure 2.8 B). Therefore, it was decided that the GBM cells should be treated with Py that was not solubilised in DMSO.

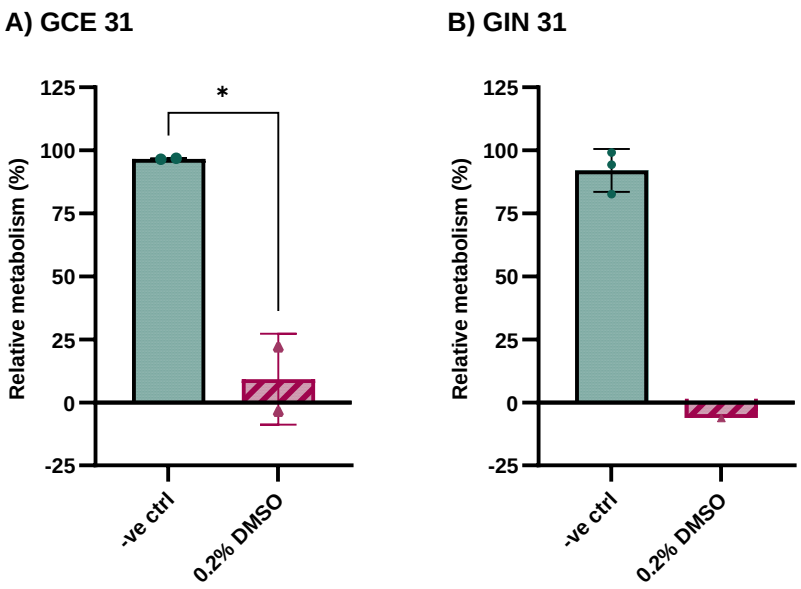


Figure 2.8: Effects of 0.2 % DMSO on GCE 31 and GIN 31 cells.
Relative change in metabolism for (A) GCE 31 cells (N = 2, n = 3); *P = 0.0332 vs control obtained using an unpaired t-test. (B) GIN 31 cells (N = 1, n = 3). Both results are graphed as mean ± S.D.

To image changes in the proportion of live and dead cells at increasing concentrations of Py on GIN and GCE 31 cells, live/ dead fluorescent staining was used. Individual fluorescence channels can be found in the appendix (Appendix B.1, B.2). For both GIN and GCE 31, there were similar cell numbers and morphology up to 20 mM Py (Figure 2.9). Past this concentration, the proportion of dead cells increased, and the cells became less elongated, indicating a treatment-induced response [232]. Despite this providing more understanding on the effects of Py on cytotoxicity, it was necessary to use a quantitative assay. This allowed the inhibitory concentration (**IC**) of Py and FOC to be determined and compared between the two cell types.

Based on the hypothesis of the polymerisation mechanism, a non-toxic concentration of FOC (Fe (II)) and a slightly-toxic concentration of Py is required for the polymerisation to be initiated. PrestoBlue^{TM} and other resazurin-based metabolic assays rely on the reduction of blue, non-fluorescent resazurin to pink, fluorescent resorufin (Figure 2.1). It is possible for resazurin to be reduced by compounds other than reductase enzymes found within cells [233], and given that FOC (Fe (II)) is a well-known reducing agent, before PrestoBlue^{TM} could be used to generate metabolic viability curves it was first important to test for the reducing capabilities of Fe (II) and Fe (III) on this assay (Figure 2.10 A).

Despite slight changes in the relative fluorescence of PrestoBlue^{TM} at higher concentrations of both FIC and FOC, when compared to the relative fluorescence of untreated GCE 31 cells, this change was found to be minimal (Figure 2.10 B, C). As such, the effects of reducing FOC were considered negligible, so toxicity experiments using PrestoBlue^{TM} could be carried out.

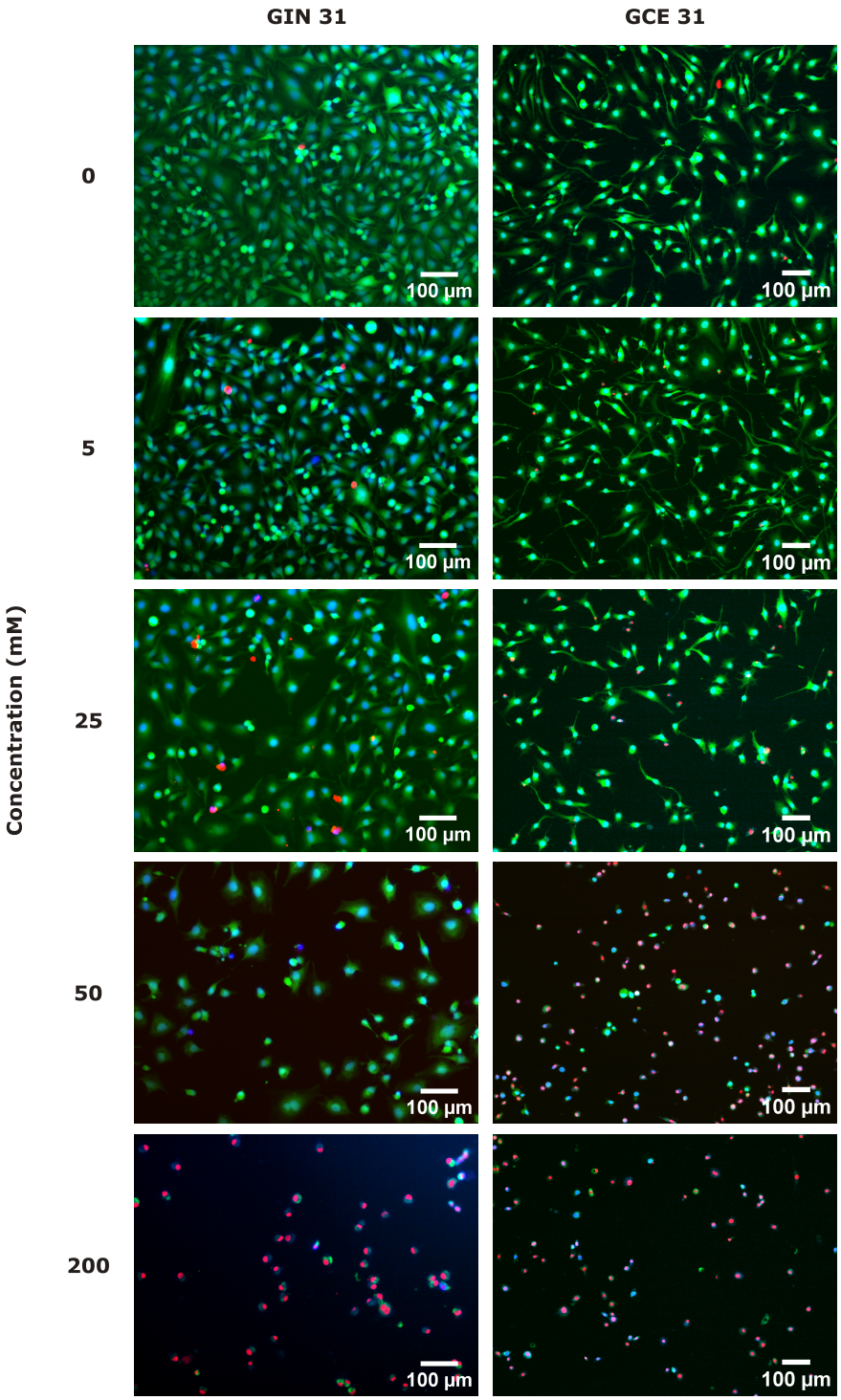


Figure 2.9: Live/ dead staining of GIN and GCE 31 cells with pyrrole (48-hour treatment).
Merge of live (green fluorescence - Calcein AM), dead (red fluorescence – propidium iodide) and nuclei (blue fluorescence – Hoechst 33342) channels. Scale bar 100 μm. Independent channels (brightfield, live, dead, nuclei shown separately in Appendix B.1, B.2.

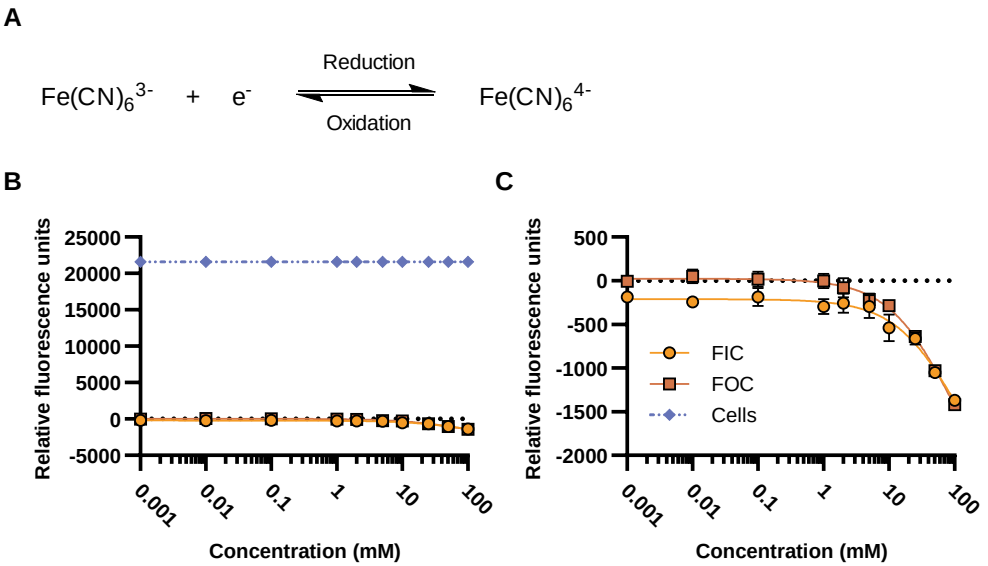


Figure 2.10: Effect of ferricyanide (FIC) and ferrocyanide (FOC) on the PrestoBlue assay.
(A) One electron redox equation of FIC (Fe (III)) to FOC (Fe (II)). (B) Comparison of average relative fluorescence of PrestoBlue^{TM} assay from untreated GCE 31 cells (blue diamond line) to 10% PrestoBlue^{TM} mixed with FIC (yellow circle line) or FOC (orange square line). (C) Focused view of graph (B) highlighting the change in fluorescence of the FIC and FOC samples.

To generate a dose-response curve to identify the toxicities of FIC, FOC and Py, GIN 31 and GCE 31 cells were treated with increasing concentrations of the starting materials and changes in the metabolic activity of the cells against an untreated negative control were plotted. Metabolic activity was used as a proxy for cell viability, where 100% metabolic activity was considered biocompatible, while 0% was considered toxic.

In the case of FIC (Fe (III)), GCE 31 cells were shown to be more sensitive, with an 80% IC ($\mathbf{IC_{80}}$) of 4 mM compared to 13 mM for GIN 31 cells (Figure 2.11 A). Both cell types were slightly more tolerant to FOC (Fe (II)), with IC_{80} values of 19 and 15 mM for GIN 31 and GCE 31 cells respectively (Figure 2.11 B).

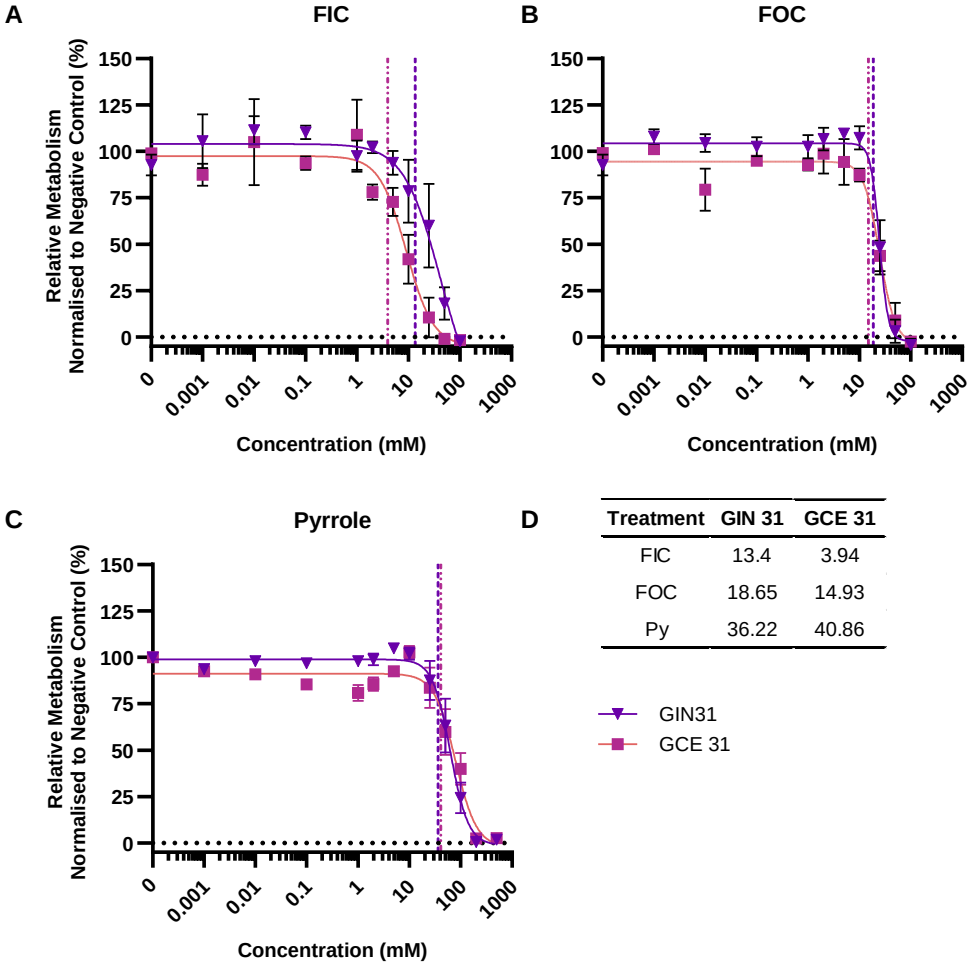


Figure 2.11: Toxicity curves of ferricyanide (FIC; Fe (III)), ferrocyanide (FOC; Fe (II)) and pyrrole (Py) on GIN 31 and GCE 31 cells.
Relative metabolic activity of cells treated with increasing concentrations of (A) FIC, (B) FOC and (C) Py 48 hours post-treatment. GIN 31 samples shown by diamond, purple line; GCE 31 samples shown by square, pink line. IC_{80} values for GIN 31 and GCE 31 shown in dashed purple and dash-dot pink lines respectively and listed in (D). Error bars show mean ± S.E.M.

In literature Fe (II) is well-known to induce toxicity in cells due to the ability of the ferrous ion to induce the Fenton reaction (shown in Figure 2.12), which generates hydroxyl radicals, capable of damaging cell membranes [234]. Less work has been undertaken to understand the toxicity of Fe (III), however Chamnongpol *et al.* showed that toxicity is induced by an oxygen-independent mechanism, by disrupting cell membranes [235]. Based on the IC_{80} values of

FIC on GIN 31 and GCE 31, variation in cell sensitivities to this mechanism can be seen.

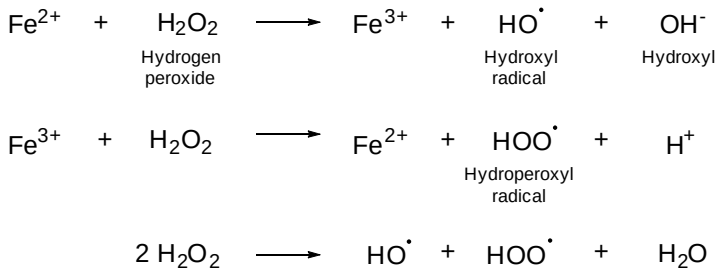


Figure 2.12: The Fenton Reaction

The toxicity of Py was also assessed, with similar effects seen on both cell types (IC_{80} of 36 and 41 mM for GIN 31 and GCE 31 cells respectively) (Figure 2.11 C). The IC_{80} values for each chemical and both cell types are listed in Figure 2.11 D. These results are in line with previous results showing the difference in the responsiveness of core and invasive GBM cells depending on the treatment [236].

Following the identification of the cytotoxicity profile, it was pertinent to identify if the mechanism of cell death was by apoptosis or necrosis. Traditionally apoptosis was seen as the 'desired' mode of cell death as the process is controlled and ordered, removing cells without having an inflammatory effect. In apoptosis, cells break apart by membrane blebbing to form apoptotic bodies which can be removed by phagocytosis. In the case of necrosis, cells swell rather than shrink, and the plasma membrane ruptures, releasing cellular contents [237, 238].

In recent years, targeting cancer cells by a necrotic death mechanism has become of interest, as the apoptotic pathway found here is often dysregulated or bypassed by tumour cells [239–241]. As cellular exudate is generated by the necrotic pathway, for the work in this thesis it would be advantageous for

cells to die in this manner. This is because the mechanism of cell-induced polymerisation is hypothesised to occur as Fe (II) is converted to Fe (III) by ions found in the exudate [128].

To understand the mechanism of cell death induced by Py and FOC, flow cytometry was employed using a caspase 3/ 7 reagent and a dead cell stain. Cells in quadrant 1 were considered healthy, those in quadrant 2 were undergoing early-stage apoptosis, those in quadrant 3 late-stage apoptosis, and those in quadrant 4 necrosis. Cells were either untreated, or treated with Py (20 mM), FOC (2 mM) or Py and FOC (20 mM and 2 mM, respectively).

For both cell types, there was no significant difference between the percentage of untreated cells and those treated with 2 mM FOC (Fe (II)) in quadrants 1 - 4 (Figure 2.13 A and B (i, ii); Figure 2.14) ($P \geq 0.9590$ in all cases). This showed that at a concentration of 2 mM, FOC does not induce any toxicity in either GIN 31 or GCE 31 cells.

For GIN 31 cells, there was no significant change in the percentage of gated cells in each quadrant for cells treated with 20 mM Py compared to the negative control (Figure 2.13 A (iii); Figure 2.14) ($P \geq 0.9888$ for all quadrants). Contrasting this, GCE 31 cells were found to be much more sensitive to treatment with Py (Figure 2.13 B (iii); Figure 2.14 (i, iv)). The percentage of non-apoptotic cells reduced significantly by 54% ($P = 0.0001$) and the percentage of necrotic cells increased by 37% ($P = 0.0168$). The percentage of cells that underwent apoptosis remained low (Figure 2.14 (ii, iii)). There was a significant difference between the number of non-apoptotic cells that had been treated with Py compared to FOC ($P = 0.0002$), or FOC compared to $Py_{20}FOC_2$ ($P = 0.0121$), confirming that Py induces cell death.

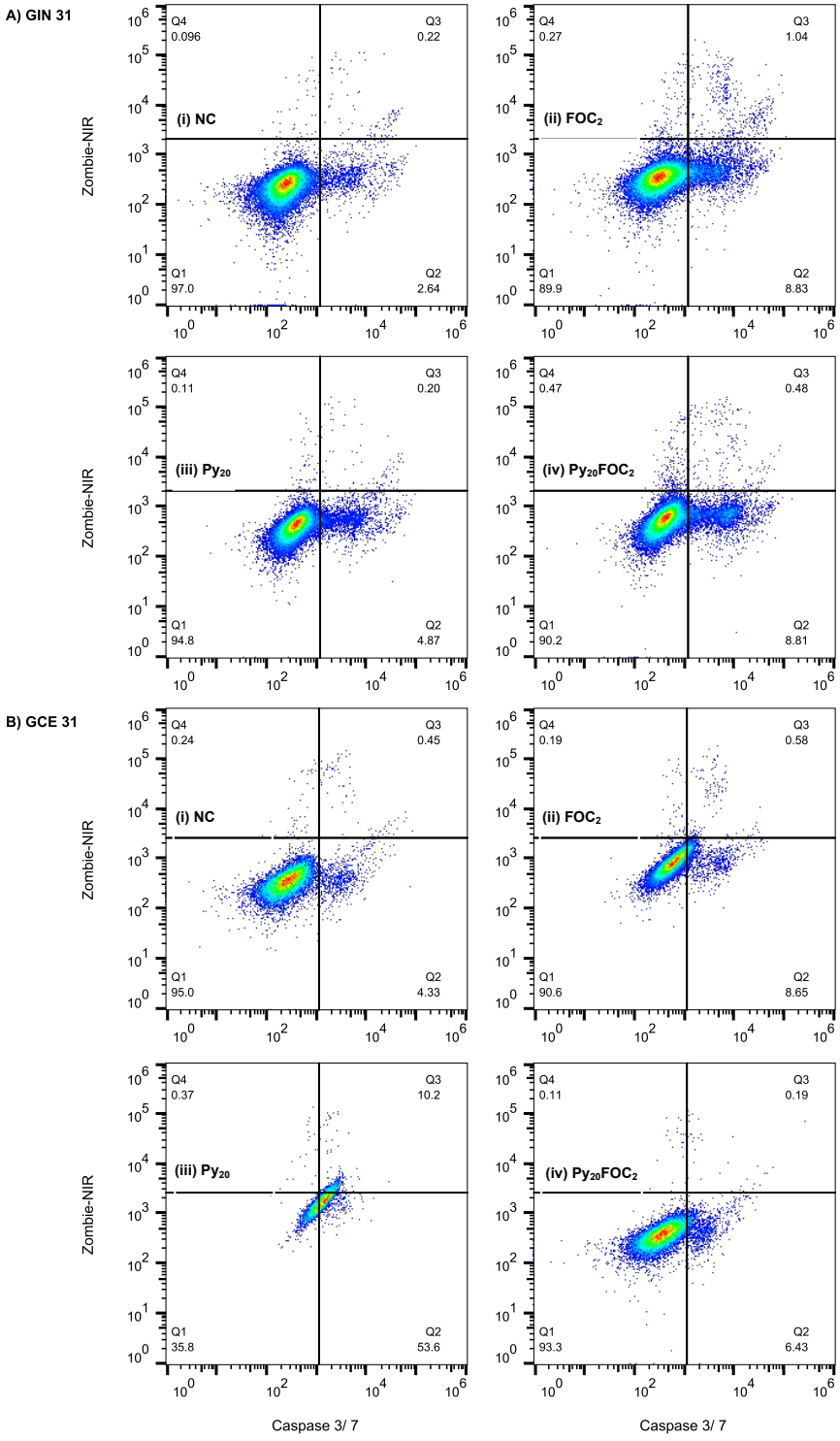


Figure 2.13: (A) GIN 31 and (B) GCE 31 representative flow cytometry quadrants (Q) showing apoptosis and necrosis. (i) Negative control (**NC**); (ii) potassium ferrocyanide (**FOC**) - 2 mM; (iii) pyrrole (**Py**) - 20 mM; (iv) Py and FOC combined treatment. Caspase 3/ 7 (**C**) and Zombie-NIR (**Z**) stains used. Q1: C- Z- (live cells); Q2: C+ Z- (early-stage apoptosis); Q3: C+ Z+ (late-stage apoptosis); Q4: C- Z+ necrosis. Fraction of cells in each quadrant recorded as a percentage.

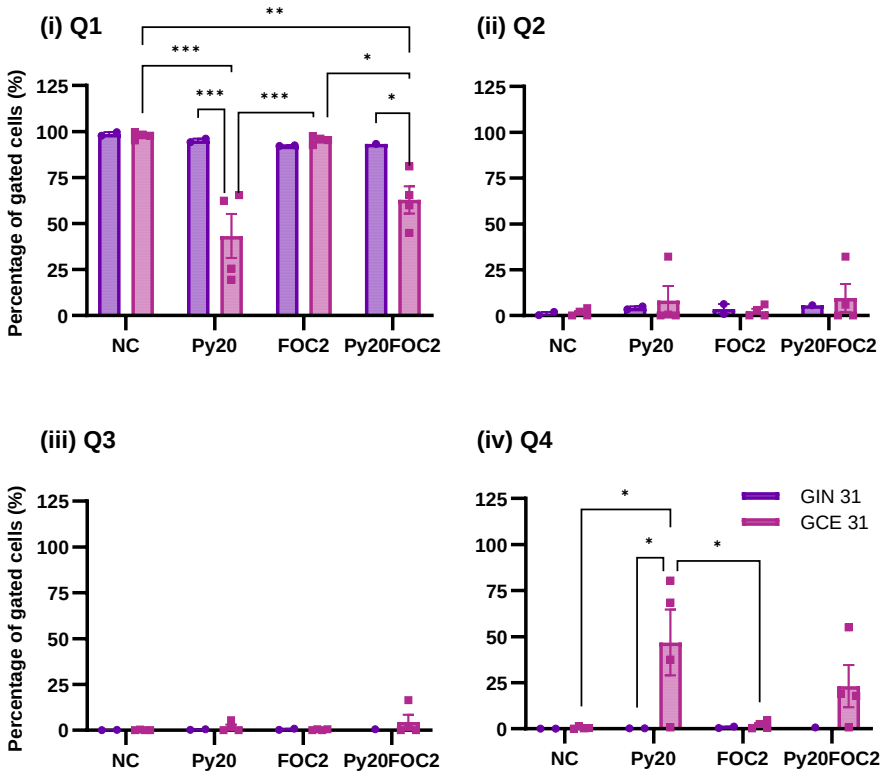


Figure 2.14: GIN 31 and GCE 31 quadrant analysis
Percentage of gated cells in quadrants 1-4 after no treatment (NC), or treatment with pyrrole (Py; 20 mM) and/ or ferrocyanide (FOC; 2 mM). Caspase 3/ 7 (C) and Zombie-NIR (Z) stains used. (i) Q1: C- Z- (live cells); (ii) Q2: C+ Z- (early-stage apoptosis); (iii) Q3: C+ Z+ (late-stage apoptosis); (iv) Q4: C- Z+ necrosis. N = 3, n = 1. Error bars show mean ± S.E.M.

It was hypothesised that the toxicity of Py would be reduced by combining Py and FOC, deactivating the monomer by the formation of Ppy. While there was a higher percentage of non-apoptotic cells when they were treated with the 'reverse prodrug' ($Py_{20}FOC_2$) compared to Py alone (Py_{20}) (62.83% compared to 43.23%), this was not found to be significant (P = 0.1745) (Figure 2.14 (i)). The number of equivalents required for the polymerisation is approximately 1:2.5 Py to Fe (III)[242], however here Py was in excess (10:1). While this ensured the maximum production of Ppy, the effects of the 'reverse prodrug' would have been limited, resulting in no significant difference between samples treated with Py alone or Py and FOC.

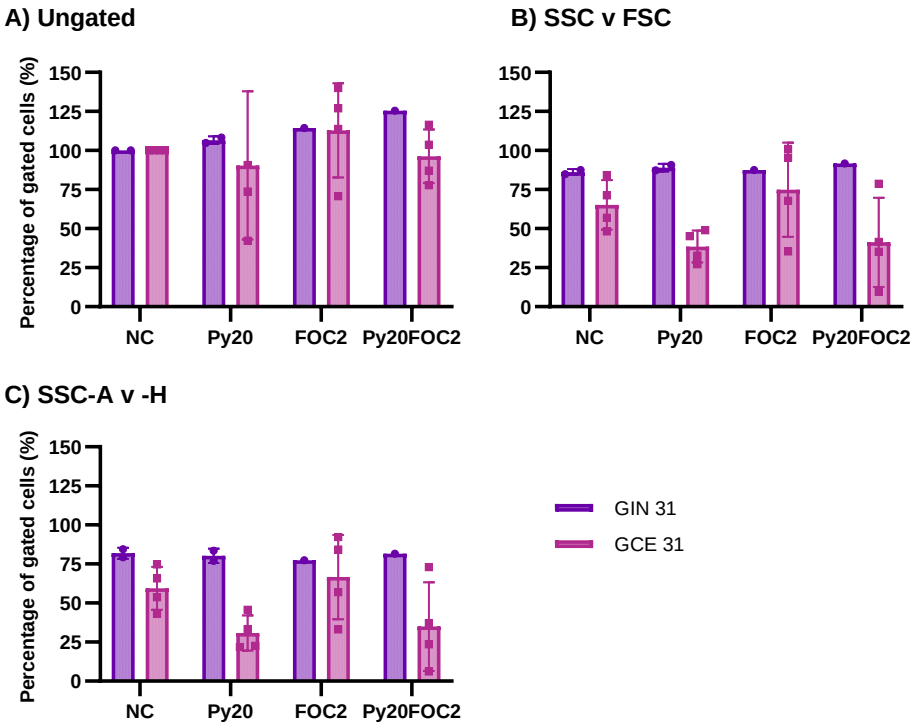


Figure 2.15: Percentage of cells at each gating stage to remove doublets and debris from flow cytometry data.
(A) Ungated, (B) side scatter (SSC) vs forward scatter (FSC) and (C) side scatter area vs height. N = 4, n = 1 for GCE 31; N = 1 or 2, n = 1 for GIN 31. No significant difference within each group and at each gating stage was found. Error bars show mean ± S.D.

To ensure the data was not skewed due to a lower number of events recorded when cells were exposed to Py, the percentage of gated cells at each stage was determined (Figure 2.15). There was no significant difference in the number of events for any treatment, indicating that changes in the percentage of apoptotic or necrotic cells was not caused by a reduced set of data points.

The focus of this area of work was to investigate the effects of the starting monomer Py and both the inactive and active initiator (FOC (Fe (II)) and FIC (Fe (III)), respectively) on two GBM cell types. The toxicity of Py was shown to cause similar metabolic changes to both GIN 31 and GCE 31 cells, however clear differences on the cytotoxicity were observed. While there was little change in the percentage of GIN 31 cells that underwent apoptosis or necrosis

when exposed to 20 mM Py, the percentage of GCE 31 cells that underwent necrosis was significantly increased compared to the untreated control.

The distinction between cell death between GIN 31 and GCE 31 cells indicates that different cells respond to the 'reverse prodrug' therapy to differing extents, and can be used to tailor the dosage of the starting materials to influence the extent of polymerisation. Not only does this highlight the importance of verifying a metabolic assay with a mechanistic study, but also addresses the underlying mechanism of action.

2.5 Conclusions

In this chapter, the aim was to synthesise and characterise Ppy in the presence of GBM cells. Firstly, the GBM cells were treated with high concentrations of Py and FOC (Fe (II)). It is hypothesised that the monomer initiates cell death, converting Fe (II) to Fe (III) by the presence of oxidising agents within cellular exudate. This results in the chemical polymerisation of Py, self-inactivating the monomer in a 'reverse prodrug' approach.

Characterisation of Ppy is complex due to the presence of cells, proteins, and other cell debris, alongside standard challenges associated with poor polymer solubility. As such, a multi-stage characteristic approach was assumed to verify the formation of Ppy using a cell-mediated approach.

To first characterise the polymer, brightfield microscopy, greyscale analysis, FTIR and UV-Vis were utilised. Despite the presence of black spots in samples containing cells exposed to Py and FOC, these were similar to the cells only exposed to Py, potentially indicating some auto polymerisation of the monomer when in the presence of the cells and cell culture medium. These findings were

supported by greyscale analysis of the solutions, with the pixel intensity of samples containing Py (Py_{500}) or Py and FOC ($Py_{500}FOC_{40}$) being similar in the presence ($Py_{500}FOC_{40}C$) or absence ($Py_{500}FOC_{40}$) of cells.

Literature has used UV-Vis to confirm the formation of Ppy, however due to the nature of this polymerisation, FIC masked any distinct peaks associated with Ppy. FTIR was also used to establish the formation of Ppy in both the chemically-synthesised and cell-mediated samples. In both cases, residual FOC was also observed, reinforcing the results found using UV-Vis.

Finally, SS NMR was employed, confirming the formation of Ppy, while also shedding light onto the oxidation states of the polymer, with evidence of both neutral and bipolaron states shown in the spectra. Again, evidence of incomplete conversion and removal of the starting materials was observed here.

To understand the morphology of the polymer, SEM and DLS were both used, showing the polymer formed was a range of sizes and shapes. Despite this, the reaction was more tightly-controlled than the chemically-synthesised polymer, with a narrower size distribution of particles formed by a cell-induced approach.

The second half of the work in this chapter aimed to investigate the toxicity of the starting materials, to provide information into the optimum reaction conditions for developing this work. Dose-response curves for Py, FIC and FOC directed the decision to investigate the effects of these starting materials at concentrations of 20 mM Py and 2 mM FIC or FOC, below the IC_{80} limit. With the GIN 31 cells, at these concentrations there was minimal effect on the proportion of cells that underwent apoptosis and necrosis. For the GCE 31 cells there was a significant increase in the number of cells dying by necrosis when exposed to Py. Effects of the 'reverse prodrug' could be seen here, with

this significant increase in necrotic cell death only occurring when the cells were not also treated with FOC.

While Ppy is a well-characterised polymer when made using traditional chemical and electrochemical techniques, or by the generation of consistent nanoparticles, the cell-mediated polymerisation is more complex, making characterisation challenging. The presence of unreacted monomer and initiator also created intricacy with using standard characterisation techniques such as UV-Vis to verify the presence of Ppy.

This chapter shows, for the first time, that Ppy can be formed by an adherent GBM cell-induced polymerisation approach. The redox capabilities of the cell were utilised to direct the conversion of Fe (II) to Fe (III), hypothesised to be driven by the release of cellular exudate upon cell death. This research lays the groundwork for understanding the synthesis and characterisation of polymers formed in the complex cell-induced polymerisation approach as a therapy for glioblastoma.

Chapter 3

Polymerisation of Pyrrole in Living Systems

3.1 Introduction

There is an increasing shift to harness the conductive properties of organic polymers within *in vivo* models to modulate the behaviour of a living organism in the presence of an electrical stimulus [133, 137, 139]. *Caenorhabditis elegans* (commonly referred to as ***C. elegans***) are small living organisms with a characterised genome. They require minimum maintenance, are free from ethical constraints so are compliant with the EU's "Three Rs" (replacement, reduction and refinement) and population studies can be completed in a couple of weeks compared to the lifetimes needed in humans [167, 243]. While they are typically used for studies on ageing and genetics, because of these advantages more work is being undertaken in other areas, such as cancer research. *C. elegans* are also transparent, a useful feature that allows for researchers to monitor internal behaviour, such as pharyngeal pumping (the action of the

pharynx that enables feeding), as well as allowing for visualisation of molecules that are fluorescent or otherwise high-contrast [164, 244].

To investigate the effects of polypyrrole (**Ppy**) nanoparticles on arrhythmia, *C. elegans* Srinivasan *et al.* used them as a bridge organism between *in vitro* models and vertebrates [244]. By capitalising on function similarities between the human heart and nematode pharynx, the use of Ppy nanoparticles as a treatment in cardiac arrhythmia was analysed. First, the nanoparticles were visualised using a brightfield microscope, with noticeable darkening of the intestinal tract indicative of Ppy nanoparticle ingestion. To assess the toxicity of the treatment, the body length of untreated and treated nematodes was compared - this is used to ascertain worm development. The production of progeny was also investigated to assess reproductive toxicity. Visual changes to the pumping rate of the pharynx were also observed, as were changes to lipid metabolism, which was monitored using Fourier transform infrared spectroscopy (**FTIR**) [244].

Other work identifying changes to the body composition of *C. elegans* has used Raman spectroscopy instead of FTIR [245]. This technique allowed Chen *et al.* to identify five distinct regions of interest within the nematode to compare the proportions of saturated and unsaturated lipids, as well as proteins present [245]. This work shows that Raman spectroscopy can be used to map the distribution of molecules within *C. elegans*.

Among the many genes researched in cancer, the *TP53* homologue, *cep-1* (from *C. elegans* p53-like–1), and the gene involved in coding for histone 3.3 (**H3.3**), *his-72* (from histone), have been used to provide a genetic model for gliomas, as established by both Ceron *et al.* and Delaney *et al.* [181, 246, 247]. These mutated strains of *C. elegans* can, therefore, be used as a proxy for an *in vivo* cancer model, allowing a more simplified approach into assessing cancer

therapies compared to more complex living systems. *Cep-1* regulates apoptosis caused by impaired DNA. To assess the conservation of the gene in *C. elegans*, *cep-1* was knocked out causing germ cell death by radiation to be inactivated [248, 249]. This mutation did not cause obvious changes to the phenotype. Therefore this mutated nematode can be used as a model organism for studying the p53 pathway, including how this is affected by cancer treatments [181].

A key mutation in paediatric high-grade gliomas is the H3.K27M mutation which occurs in histone H3.3, where lysine 27 is substituted with methionine on histone 3 [250]. To understand how this mutation affected the genome, Delaney *et al.* genetically modified *C. elegans* to form a *his-72* strain [247]. Through RNA sequencing, extensive gene dysregulation was observed. A link was found between the H3.3 mutation and a signalling pathway which, when dysregulated, is involved in the proliferation of glial cells and cancer stemness [251]. This highlights how mutated *C. elegans* can be utilised within cancer research. For example, to compare the effects of a treatment between different mutant and naturally occurring ('wild-type') models.

All of the above research demonstrates an increasing interest in transferring the application of conductive polymers from an *in vitro* to an *in vivo* system for a variety of applications [137, 139, 244]. Despite this development, there has been little work on the polymerisation of Ppy within a living system. There is the potential to combine this approach with another modality, such as tumour treating fields, to better investigate the effect of a conductive polymer on *C. elegans*.

3.2 Experimental Aims and Objectives

The overall aim of this chapter is to further the application of the polymerisation of pyrrole to Ppy from an *in vitro* system to an *in vivo* one, using *C. elegans* as a model organism. The objectives broadly fall into two categories:

1. to characterise the formation of Ppy within wild-type *C. elegans*; and
2. to investigate the cytotoxicity of the starting materials on wild-type *C. elegans* and mutated nematodes.

To gain insight into Ppy from the starting materials of pyrrole, potassium ferrocyanide and ferricyanide, the first objective is to use brightfield microscopy to visually identify changes in the *C. elegans* phenotype. After this, Raman spectroscopy can be performed as a complementary technique to verify the presence of specific compounds. The final objective is to carry out toxicity studies of these reagents on the Bristol 'N2' wild type and two cancer strains, to begin to optimise the concentrations for this polymerisation process.

3.3 Experimental Design

3.3.1 Brightfield Microscopy

Chen *et al.* have previously utilised the transparent nature of *C. elegans* to visualise Ppy within the intestinal tract of nematodes using a brightfield microscope [245]. As that experiment was carried out using 100 μg/ mL of Ppy nanoparticles, for this work the concentration of Ppy (commercial control) given to the worms was also 100 μg/ mL to match the experimental conditions as closely as possible.

3.3.2 Raman Spectroscopy

Raman spectroscopy has been shown to be a useful tool in identifying different areas of interest within *C. elegans* [245]. Ppy also has a distinct Raman fingerprint [252, 253]; the peaks of which occur in silent regions of the *C. elegans* spectrum. This property this could be used to establish polymer formation within a living system. Raman spectroscopy has two significant advantages over solid state nuclear magnetic resonance (**SS NMR**), which was used in Chapter 2.

Firstly, it is possible to analyse localised intensities of different molecules within the worm. Information can be gathered on how the starting materials are distributed within the worm and where polymerisation of pyrrole occurs. In addition, changes to the oxidation state of iron can be observed. Secondly, the technique only requires the imaging of a small number of worms, whereas SS NMR requires a large amount of sample for analysis.

An excitation energy of 785 nm was chose, as this is close to the energy of polaron and bipolaron electronic states of Ppy. Therefore, this wavelength, while not providing a spectrum representative of the entire sample, best matches the resonance conditions of Ppy [254].

3.3.3 Toxicity Studies

3.3.3.1 Length measurements

Phenotype assays are important in understanding the toxicity of a treatment on *C. elegans* as the development of nematodes can be monitored over a defined period [255]. In this work, to assess the toxicity of different treatments on nematodes, the average length of the worm was compared to that of a negative control (untreated) population. Worm length was determined using either the ImageJ plugin 'WormSizer' (v.1.2.5) [256] or manual measurement.

To ensure the WormSizer measurement matched those measured manually, untreated worms were imaged and analysed using WormSizer, then assigned an ID number up to 155. A random number generator from calculator.net was then used to select 16 integers, which were then manually measured using the 'segment' tool on ImageJ. These values were compared to the WormSizer results and plotted in Figure 3.1. No significant difference was found between the two approaches to determine length ($P = 0.2681$). Consequently, WormSizer was used as a tool for measurement. For worms that were lying at the edge of the well plate, issues with thresholding were seen, so they were measured manually.

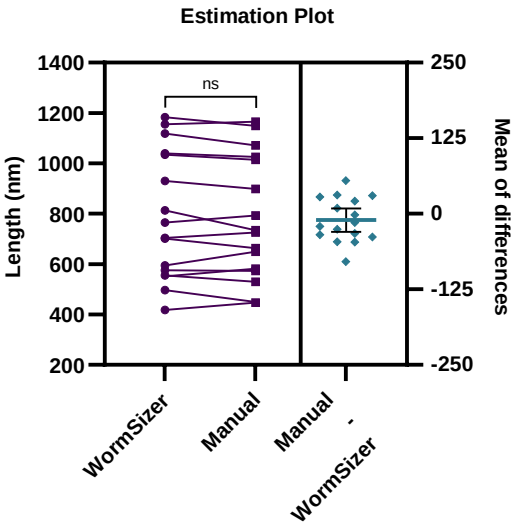


Figure 3.1: Estimation plot of worm length calculated using WormSizer vs manual measurements on ImageJ. Statistical analysis was carried out using a paired t-test.

3.4 Results and Discussion

3.4.1 Visualising the Polymerisation of Pyrrole

As pyrrole polymerised to Ppy, there was a dramatic shift in the colour of the solution, from a straw colour to blue/ black [257]. This optical property of Ppy, coupled with the transparent nature of *C. elegans* [168], has been utilised previously by Srinivasan *et al.* to observe the polymer in the gastrointestinal tract of nematodes [244]. It was therefore hypothesised that the formation of Ppy within the N2 worms could be observed.

In this work, *C. elegans* were imaged without treatment as a negative control. Distinct anatomical features of the nematode were seen, including the head, pharynx, vulva, intestine and lipid-containing fat granules (Figure 3.2 A) [258, 259]. Here, to identify differences with samples containing Ppy, two polymer controls were prepared.

The first consisted of nematodes treated with a pre-made polymer using an approach adapted from a previous study by Srinivasan *et al.* [244]. Signs of internalised polymer were seen in approximately 20% of the worms imaged (Figure 3.2 B). Zheng *et al.* showed the time taken for maximum drug absorption in *C. elegans* is 24 hours, with drug concentration gradually decreasing past this peak [260]. Therefore it is possible that the polymer in this work had already been excreted from other worms where polymer was absent as the worms were imaged 48 hours after treatment. This hypothesis is corroborated by location of the internalised polymer at the time of imaging; near the rectum.

It is also worth noting that approximately 50% of *C. elegans* imaged underwent a process known as faculative vivipary, or "worm bagging". This phenomenon occurs when worms are exposed to environmental stress; eggs hatch within the adult worm, preventing the usual egg laying process [261–263]. The observation of faculative vivipary in this work showed that Ppy induces some stress on the worms.

The second positive control consisted of nematodes treated with pyrrole and ferricyanide (Fe(III)) (Figure 3.2 C). Here, pyrrole can polymerise in the absence of *C. elegans* due to the presence of Fe (III), which initiates the reaction. As it was necessary to better visualise the nematodes with high concentrations of the polymer, high concentrations of these starting materials based on the initial experiments in Chapter 2 were used. The entire surface of the nematode was black, possibly due to adsorption of the polymer to the exoskeleton and *in situ* polymerisation [264, 265].

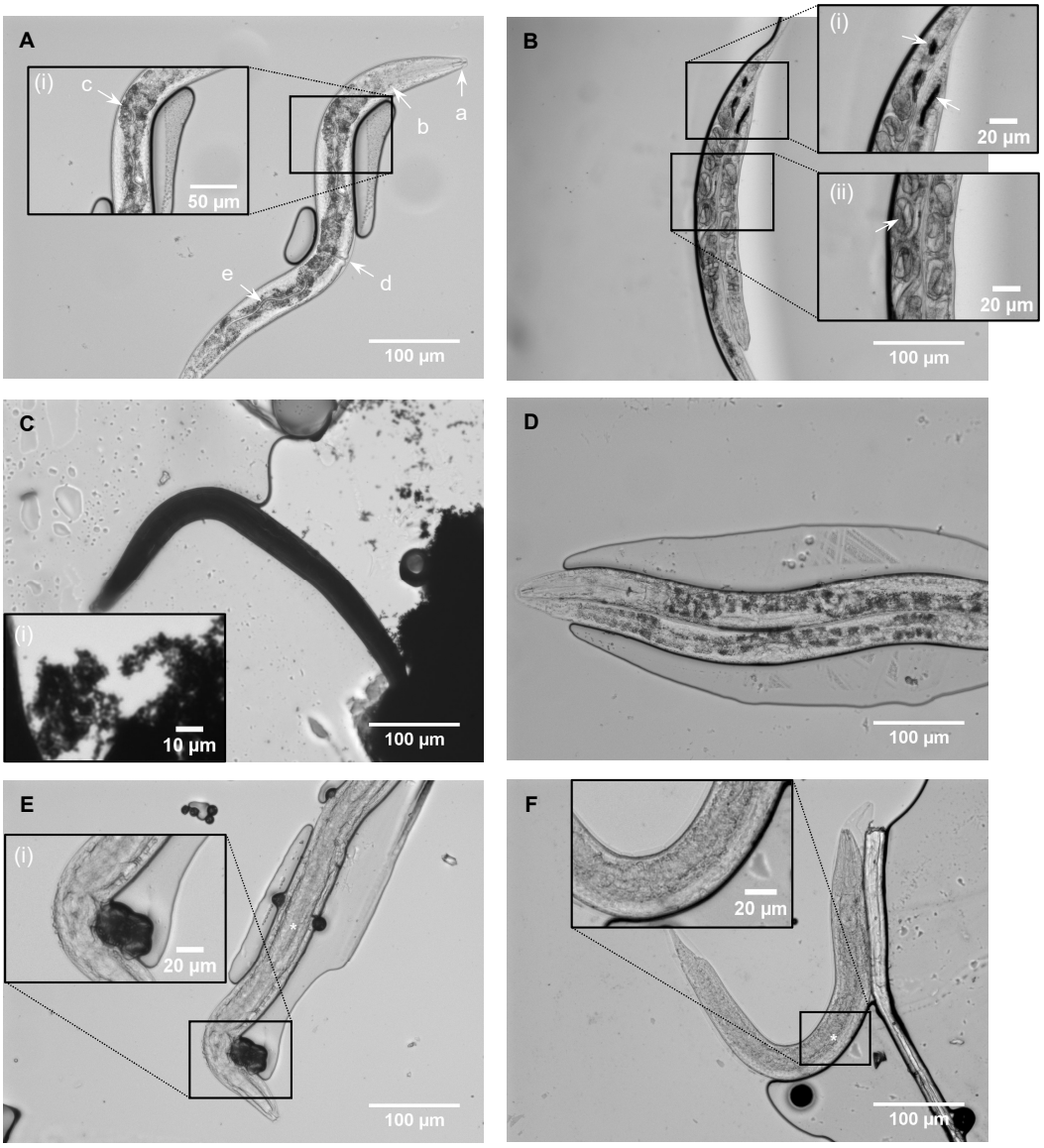


Figure 3.2: Images of N2 Bristol wild type *C. elegans* with Ppy.
(A) untreated nematode showing key anatomical features of (a) head, (b) pharynx, (c) lipids (expanded in the insert (i)), (d) vulva and (e) intestine. Nematodes were with (B) Ppy (100 μg/ mL) (i) insert shows locations of Ppy highlighted with arrows) (ii) insert showing faculative vivipary; (C) potassium ferricyanide (FIC) (40 mM) + pyrrole (Py) (500 mM) (positive control) (i) insert shows polymer formed outside of worm; (D) potassium ferrocyanide (FOC) (40 mM); (E) pyrrole (Py) (500 mM) (i) insert shows droplet; (F) Py (500 mM) + potassium ferrocyanide (FOC) (40 mM), (i) insert shows disorganised internal structure. * in (E) and (F) show disorganised structure. Solutions prepared in H_2O then imaged after 24-hour incubation at 20°C.

Following this, *C. elegans* were added to solutions containing the two starting materials, potassium ferrocyanide and pyrrole, in a manner previously demonstrated by Liu *et al.* [139]. The morphology of the worms treated with potassium ferrocyanide (**FOC**; Fe (II)) was similar to that of the untreated control (Figure 3.2 D), but 13% of the worms underwent faculative vivipary, suggesting that this concentration of FOC induced some environmental stress. Contrasting this, the internal structures of *C. elegans* treated with pyrrole were shown to be disorganised, lacking a clear intestinal track or fat deposits as previously described for untreated nematodes (Figure 3.2 E). This indicates cell disruption, as is commonly seen with other drugs that induce toxicity on nematodes [266, 267] .

Once the controls had been imaged, attention shifted to the treatment of *C. elegans* with both pyrrole and FOC (Figure 3.2 F). As expected, similar ultrastructural disorganisation was observed as with the pyrrole sample. While there were some dark spots, believed to be droplets of autopolymerised monomer, in the area imaged, these were also seen in the sample with pyrrole alone and therefore cannot be attributed to the formation of Ppy from the combination of the starting monomer, initiator and worm. Instead, this may be due to the conversion of pyrrole to its dimer form as it is readily oxidised in air [148, 268].

As the polymer could not be observed within the worms, it was hypothesised that pyrrole was causing internal structural damage and death before FOC (Fe (II)) could be ingested and converted to Fe (III) due to the toxicity of the monomer observed *in vitro* in Chapter 2. To account for this, *C. elegans* were treated with FOC (Fe (II)) for 24 hours before treatment with pyrrole to increase the likelihood of internal polymerisation. This change in treatment made no difference to the visual appearance inside of the worms, however

more black material could be seen surrounding the worms (Figure 3.3). This suggested that more polymer was formed *in situ* potentially due to more Fe (II) being converted to Fe (III).

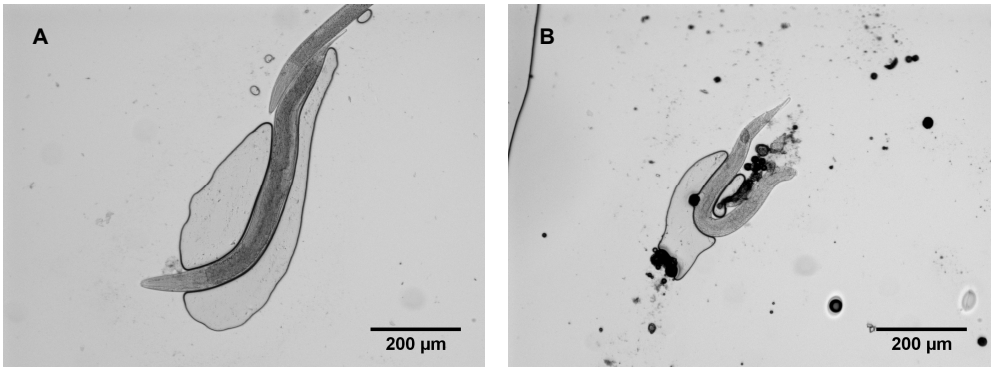


Figure 3.3: Simultaneous vs delayed treatment of N2 Bristol wild type *C. elegans* treated with pyrrole and potassium ferrocyanide.
(A) Simultaneous treatment with pyrrole (500 mM) and FOC (40 mM); (B) Delayed treatment – treatment with FOC for 24 hours then pyrrole added. Both samples in H_2O; imaged after 48 hours. Images taken at 10x magnification scale bar = 200 μm.

In this work morphological changes to the nematodes were observed, with differences in internal structures attributed to the treatment used. To better understand the chemical transformations involved in the *in situ* polymerisation, it was necessary to couple this work with an approach that could provide a molecular structural fingerprint. Given previous work by Chen *et al.* using Raman to identify regions of varying lipid intensity within *C. elegans*, this spectroscopic technique was chosen for this work [245].

3.4.2 Raman Spectroscopy as a Tool for Polymer Analysis

Beyond brightfield microscopy images, it was important to characterise the formation of Ppy chemically. Chen *et al.* showed distinct chemical features associated with *C. elegans* at 870, 1000, 1080, 1200 - 1500, 1650 and 1740 cm^{-1} attributed to the lipids present in this type of nematode [245]. As Ppy has

two characteristic peaks that are in opposing regions to the *C. elegans* spectra at 1545 cm^{-1} (C=C stretch) and 975 cm^{-1} (C-H out-of-plane deformation) [252, 253], it was postulated that Raman spectroscopy could be used as a tool for identifying the presence of Ppy in this *in vivo* model.

The starting monomer, pyrrole, was first characterised using Raman spectroscopy (Figure 3.4). The spectrum was shown to be consistent with previous literature [269], with the peaks between 3054 and 3136 cm^{-1} attributed to C-H stretching, the peaks at 1469, 1237, 1077 and 1048 cm^{-1} to C-H bending (in plane) and the peak at 842 cm^{-1} to C-H bending (out of plane). The peak at 1416 cm^{-1} was due to C-N stretching and N-H bending (out of plane), the peak at 1382 cm^{-1} to C-C stretching, and the peak at 559 cm^{-1} to N-H bending (out of plane). The other highlighted peaks were due to ring breathing and deformation (see Appendix C.1 for full peak assignment).

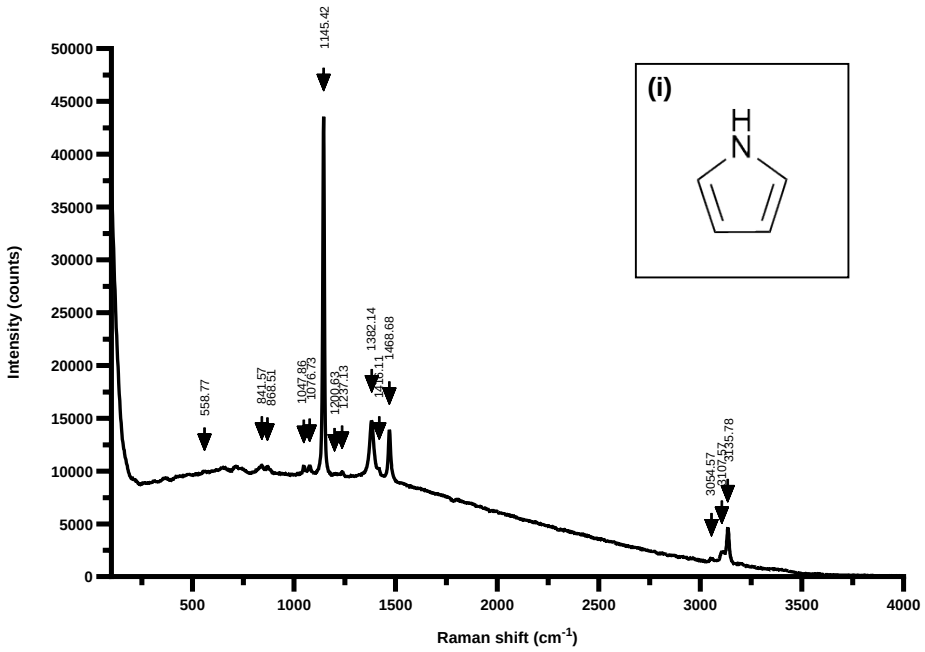


Figure 3.4: Raman spectrum of the pyrrole monomer. (i) Chemical structure shown in insert.

Weak background fluorescence of impurities in the pyrrole sample contributed to a non-zero baseline [270]. The fingerprint is as expected of pyrrole, and showed it was possible to identify peaks characteristic of the monomer using Raman spectroscopy. Therefore, it was confirmed that this spectrum could be used as a standard alongside biologically-loaded samples.

Next, it was necessary to characterise the iron initiator in both oxidation states, Fe (II) (FOC) and Fe (III) (FIC), to serve as standards. The Raman shift of the crystalline structures were analysed to locate key peaks at the highest intensity possible (Figure 3.5 A). In both samples, diagnostic C≡N stretching vibrations were used to confirm the presence of FIC (Fe (III)) and FOC (Fe (II)) in the sample.

Encouraged by these distinct peaks between the iron oxidation states, as the *in vivo* polymerisation will occur in solution, Raman spectra of aqueous solutions were also obtained (Figure 3.5 B). Once again, distinct peaks were observed at 2058 and 2093 cm^{-1} for FOC (Fe (II)) and a singular peak at 2131 cm^{-1} for FIC (Fe (III)). Full assignment of peaks in solid state and in solution can be found in Appendix C.2. Crucially, the spectra of the two initiators are different, as is well-documented in literature [271, 272].

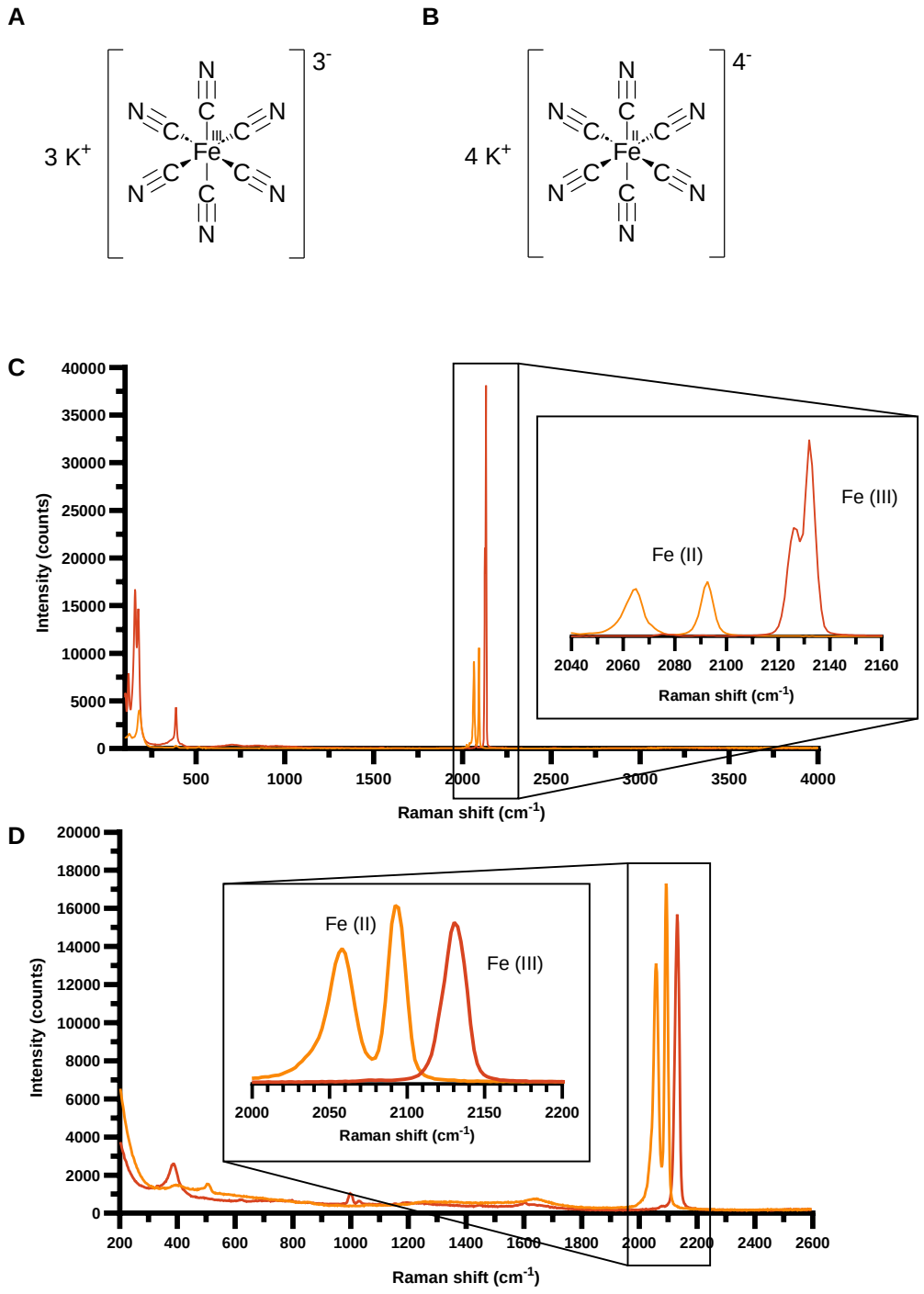


Figure 3.5: Raman spectra of iron initiators.
Chemical structures of (A) ferricyanide and (B) ferrocyanide. Raman spectra of potassium ferricyanide (Fe (III); FIC; dark orange) and potassium ferrocyanide (Fe (II); yellow) in (C) crystalline and (D) solution. C≡N stretch peaks (inset) shown.

Distinct peaks in each Fe sample were due to the different stretching modes of the C≡N functional group (A_{1g} and E_g; Figure 3.6) [272, 273].

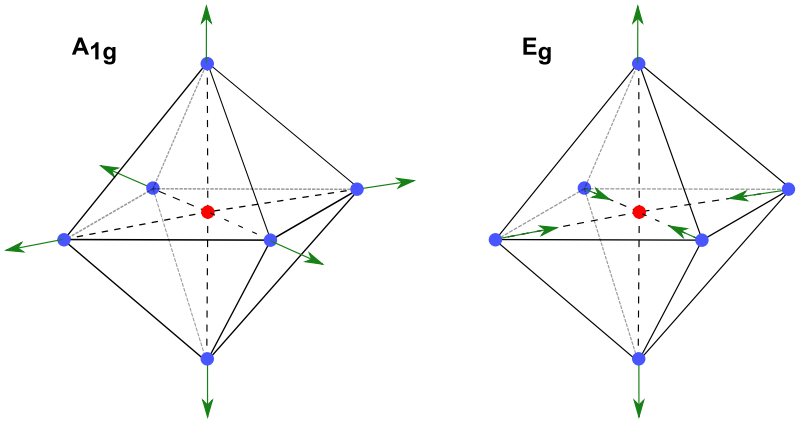


Figure 3.6: Comparison between A_{1g} (left) and E_g (right) stretching modes.

After identifying distinct Raman signals for the starting materials, it was next of interest to characterise the polymer. As a control, the Raman spectrum was first obtained from commercial doped Ppy (Figure 3.7 A). At a consistent wavelength of 785 nm, the effect of laser power was investigated from 0.1 - 10% (0.1 - 10 mW). Ppy seemed to be very sensitive to increases in laser power, as has been observed in literature [274, 275]. Consequently, to preserve both the polymer and the resulting peaks, all further Raman spectroscopy analysis involving Ppy was performed at 0.1% laser power.

The Raman spectrum of Ppy has been studied extensively, with the conformation and protonation states greatly altering Raman shift [254, 274, 276]. The 785 nm Raman spectra of both the commercial Ppy and chemically-synthesised sources were found to be similar, but there were differences in the baseline intensity due to fluorescence, and the position and intensity of some of the bands (notably around 1300 cm^{-1}) (Figure 3.7 B). This could indicate structural differences in the Ppy depending on the method of preparation, however it is possible that the differences were associated with impurities in the polymer.

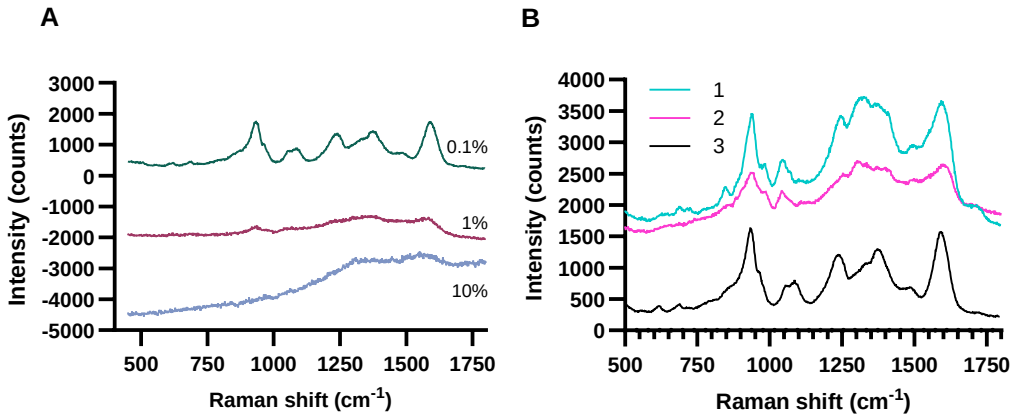


Figure 3.7: (A) Raman spectra of polypyrrole (Ppy) (0.1-10 % power), spectra offset. (B) Raman spectra of Ppy. Chemically-synthesised Ppy formed either in (1) H_2O or (2) cell-culture medium from 500 mM pyrrole + 40 mM ferricyanide (FIC; Fe (III)). (3) Commercial Ppy analysed as obtained.

To expand the characterisation of pyrrole from an *in vitro* system to an *in vivo* model, it was necessary to first determine which microscope produced the best signal-to-noise ratio to ensure that peaks unique to both the nematode and treatment could be identified. The same location on the same worm was analysed on both the XPlorA (inverted, higher grating of 600 lines/ mm) and LabRAM (upright, lower grating of 300 lines/ mm) microscopes (Figure 3.8 A). The signal-to-noise ratio at 5 second integration was found to be marginally better on the XploRA (Figure 3.8 B), the single window spectral range was wider ($\sim$ 200 - 3600 cm^{-1} vs $\sim$ 410 - 1800 cm^{-1}) and the samples could be readily inverted. Therefore, despite slightly worse spectral resolution ($>$ 1.6 cm^{-1} vs $>$ 3.0 cm^{-1}), all subsequent measurements were performed using the XploRA. The Raman shifts found were as previously recorded in literature [245, 277], with key peaks from DNA and RNA at 780 cm^{-1}, protein at 996, 1240, 1250, 1450 and 1662 cm^{-1}, and lipids at 1315 and 1450 cm^{-1}. Full peak assignment can be found in Appendix C.3.

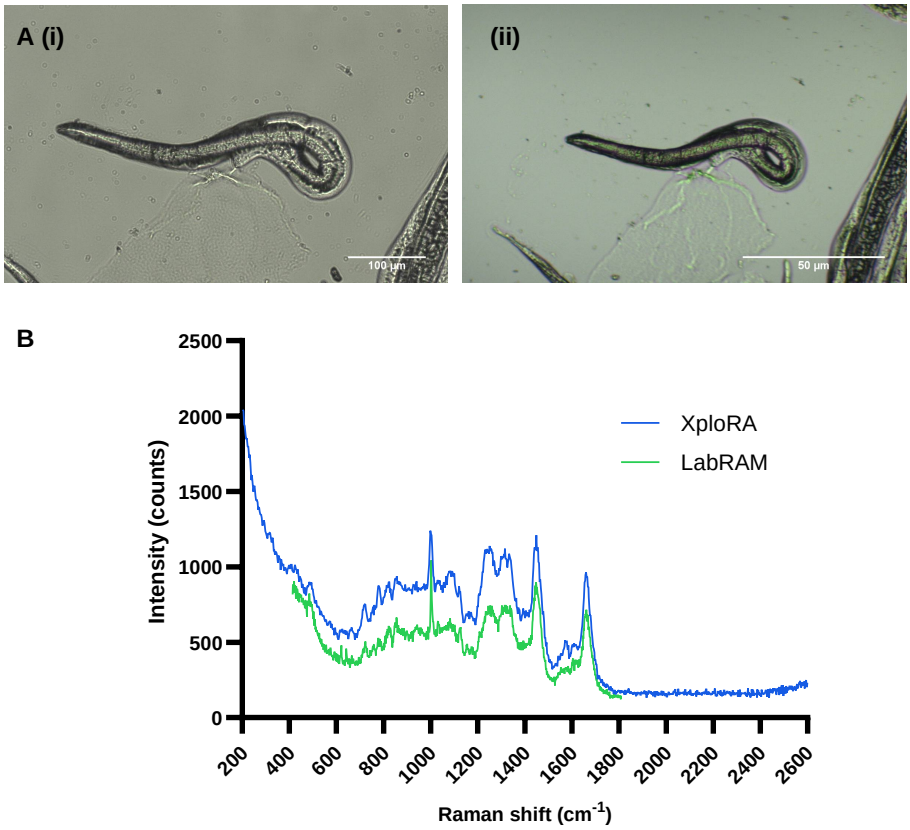


Figure 3.8: Comparison of microscopes for analysis of *C. elegans*.
(A) Optical image of N2 Bristol wild type *C. elegans* using (i) XploRA and (ii) LabRAM microscope. B) Raman spectra of N2 nematode. Spectrum obtained from XploRA in blue; spectrum obtained from LabRAM in green.

As hypothesised, there are two distinct regions where the peaks of *C. elegans* and Ppy do not overlap (Figure 3.9 A). Peaks from Ppy at 932 and 1591 cm^{-1} from C-H (out-of-plane) and C=C stretching, respectively, are found in quiet regions in the *C. elegans* spectrum. These exclusive peaks suggests that, if Ppy and *C. elegans* were combined, polymer could be observed within *C. elegans*.

Encouraged by the results from the separate components of the polymerisation reaction, next *C. elegans* were incubated with different chemical combinations to observe key peaks indicative of composition shifts.

To probe the oxidation state of Fe ((III) vs (II)) within the worm, the *C. elegans* model was treated with FIC (Fe (III)) or FOC (Fe (II)) (40 mM).

A small area of each of the worms was then mapped and the mean spectra extracted (Figure 3.9 B). Peaks unique to the iron initiators were seen in *C. elegans* treated with FIC (Fe (III)) at 2096 and 2132 cm^{-1}, blue-shifting to 2087 and 2125 cm^{-1} respectively for the sample treated with FOC (Fe (II)).

A peak at 2128 cm^{-1} for the FIC-treated worm, and a peak at 2130 cm^{-1} for the FOC-treated worm provides strong evidence for Fe (III) in both cases (Figure 3.9 B). These peaks closely match the position of the C≡N observed for FIC in solution (which was found at 2130 cm^{-1}) (Figure 3.5 D). A peak at 2096 cm^{-1} in the FIC-treated worm also provided evidence for Fe (II) (which was found at 2095 cm^{-1} in the FOC solution), but broader C≡N stretching modes were observed. These results potentially indicate changes to both the iron coordination environment as well as the redox state, as discussed previously in literature [278, 279].

There may be evidence for Fe (II) in the FOC-containing worm (Figure 3.9 B), but the position of the band at 2088 cm^{-1} did not precisely match either of the peaks observed in solution (2095 or 2060 cm^{-1}) (Figure 3.5 D). These results indicated that the nematodes modulated the oxidation state of iron without pyrrole needed to induce this. To understand this modulation better, future work carrying out Raman analysis over a period of 48 hours to monitor changes in the ratio of Fe (II) and Fe (III) peaks may provide more insight into the redox that occurs within *C. elegans*.

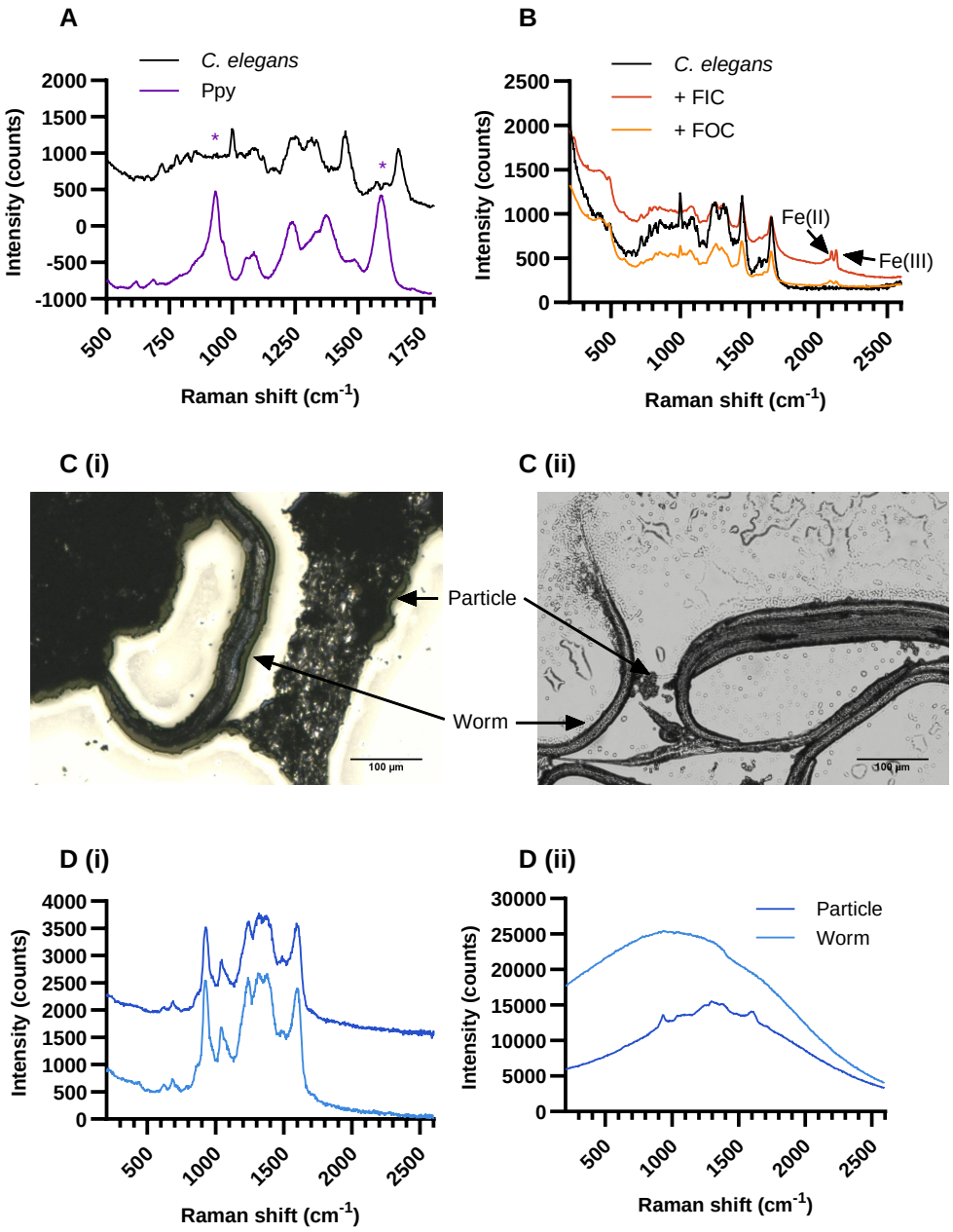


Figure 3.9: Raman analysis of *C. elegans* and Ppy.
A) Raman spectra of N2 Bristol wild type *C. elegans* (top purple line) and Ppy (commercial; bottom black line). Spectra offset. * to show Ppy diagnostic bands that don't strongly overlap with CE spectrum. (B) Raman spectra of *C. elegans* in the presence and absence of iron initiators in the two activation states. Untreated *C. elegans* shown in black. Potassium ferricyanide (Fe (III); FIC) in dark orange. Potassium ferrocyanide (Fe (II); FOC) in yellow). (C) Optical images of *C. elegans* treated with (i) Py + FIC or (ii) Py + FOC. (D) Raman spectra showing particle (dark blue) or worm (light blue) treated with (i) Py + FIC or (ii) Py + FOC.

Following this, *C. elegans* were treated with FIC (Fe (III)) and pyrrole. In the positive control (FIC and pyrrole), namely under the conditions that form Ppy irrespective of the addition of *C. elegans*, black particles and worms could be seen. The dramatic colour change strongly suggested the formation of Ppy, a black polymer (Figure 3.9 C (i)). This theory was corroborated by the Raman spectra, which showed a fingerprint indicative of Ppy in both the particle of polymer and the worm (Figure 3.9 D (i)).

Next the test condition of FOC (Fe (II)) and pyrrole combined was analysed. Both the worms and particles in solution were, again, a darker colour, but not as opaque as the positive control. The colour change strongly indicated the formation of Ppy (Figure 3.9 C (ii)). The Raman spectrum ((Figure 3.9 D (ii) 'Particle') of a particle in solution indicated the presence of Ppy by peaks at 934 and 1597 cm^{-1}. This indicates the formation of Ppy *in situ* in the presence of *C. elegans*.

To identify internal polymerisation within *C. elegans*, Raman spectroscopy of the worm was also performed ((Figure 3.9 D (ii) 'Worm'). This spectrum, however, was dominated by fluorescence, likely from unreacted pyrrole. Consequently, any peaks associated with the polymer were completely masked. These results are confirmation that Ppy was formed in the presence of pyrrole, FOC and *C. elegans*, however it is not possible to verify if Ppy can be formed within *C. elegans*.

To determine if the polymer was adsorbed on the exoskeleton or internalised in *C. elegans* for the sample treated with pyrrole and FIC (Fe (III)), the nematode was optically imaged (Figure 3.10 A), then multivariate curve resolution (**MCR**) was carried out (Figure 3.10 B). By using MCR, two loadings were generated corresponding to the polymer and the background (Figure 3.10 C). The maximum signal intensity of PPy was then imaged across the nematode,

and a heat map corresponding to polymer loading was obtained (Figure 3.10 D). The multivariate analysis showed that Ppy was co-localised with the worm. As the maximum Ppy concentration was found in the middle of the nematode, rather than at the edges, it is possible that some polymer was internalised, based on the assumption that the laser was able to penetrate through both the polymer and nematode.

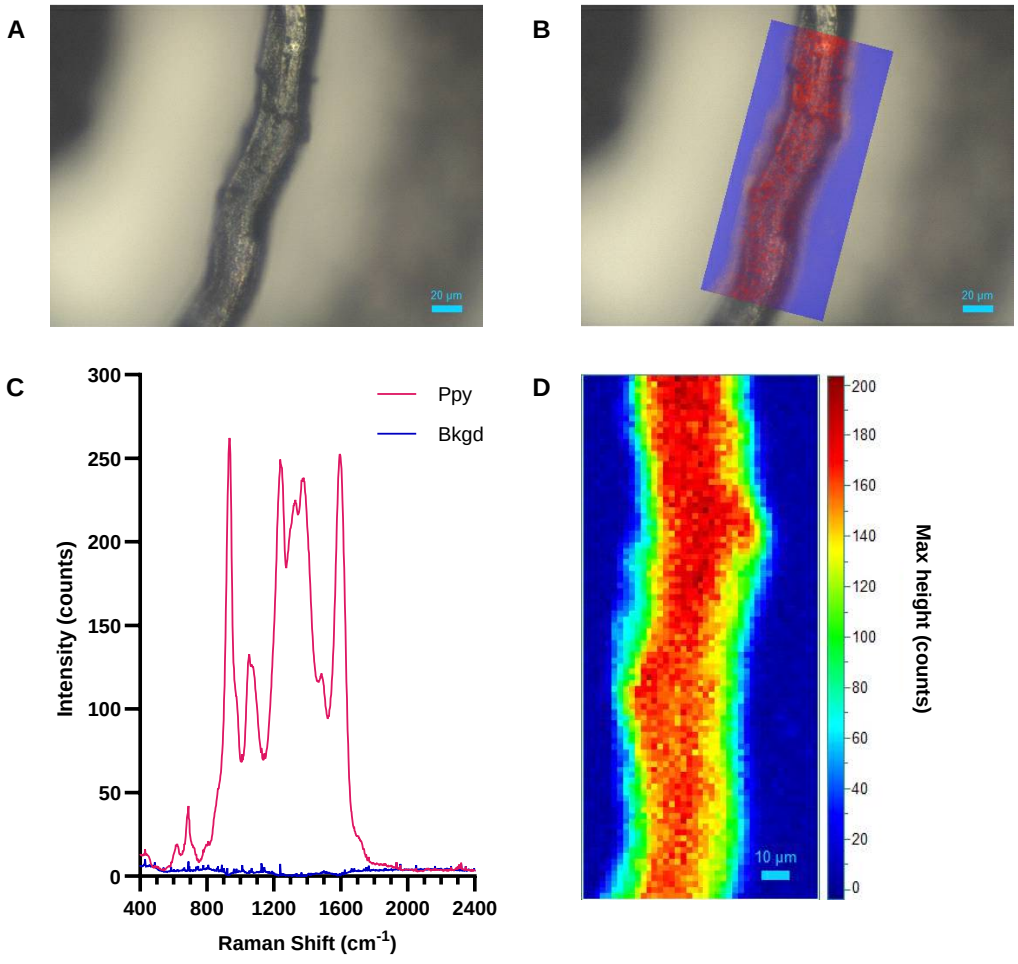


Figure 3.10: Multivariate analysis of co-localised polypyrrole with a N2 bristol wild type nematode.
(A) 20 × magnified surface of the polymer-coated nematode. (B) Multivariate curve resolution (MCR) maps of both polypyrrole (Ppy) (red) and substrate background (blue) overlayed on the optical image. (C) Raman spectra showing MCR loading of both Ppy and background (bkgd). (D) Heat map showing maximum signal intensity of Ppy across the nematode, where red is highest and blue is lowest.

To better understand the distribution of Fe (II) and Fe (III) across the worm, a heat map was produced (Figure 3.11). A homogeneous distribution of Fe (III) across the area selected can be seen (Figure 3.11 A - C). In contrast, the distribution of Fe (II) was found to be inconsistent, with hotspots only identifiable in specific regions (Figure 3.11 D - F). This suggests that Fe (II) is more localised than Fe (III), potentially limiting the amount of iron that is oxidised to drive the polymerisation reaction. These observations were supported by previous findings from McColl *et al.*, who showed that iron, alongside other metals, is highly compartmentalised in *C. elegans*, being mainly restricted to the cytoplasm of intestinal cells [280].

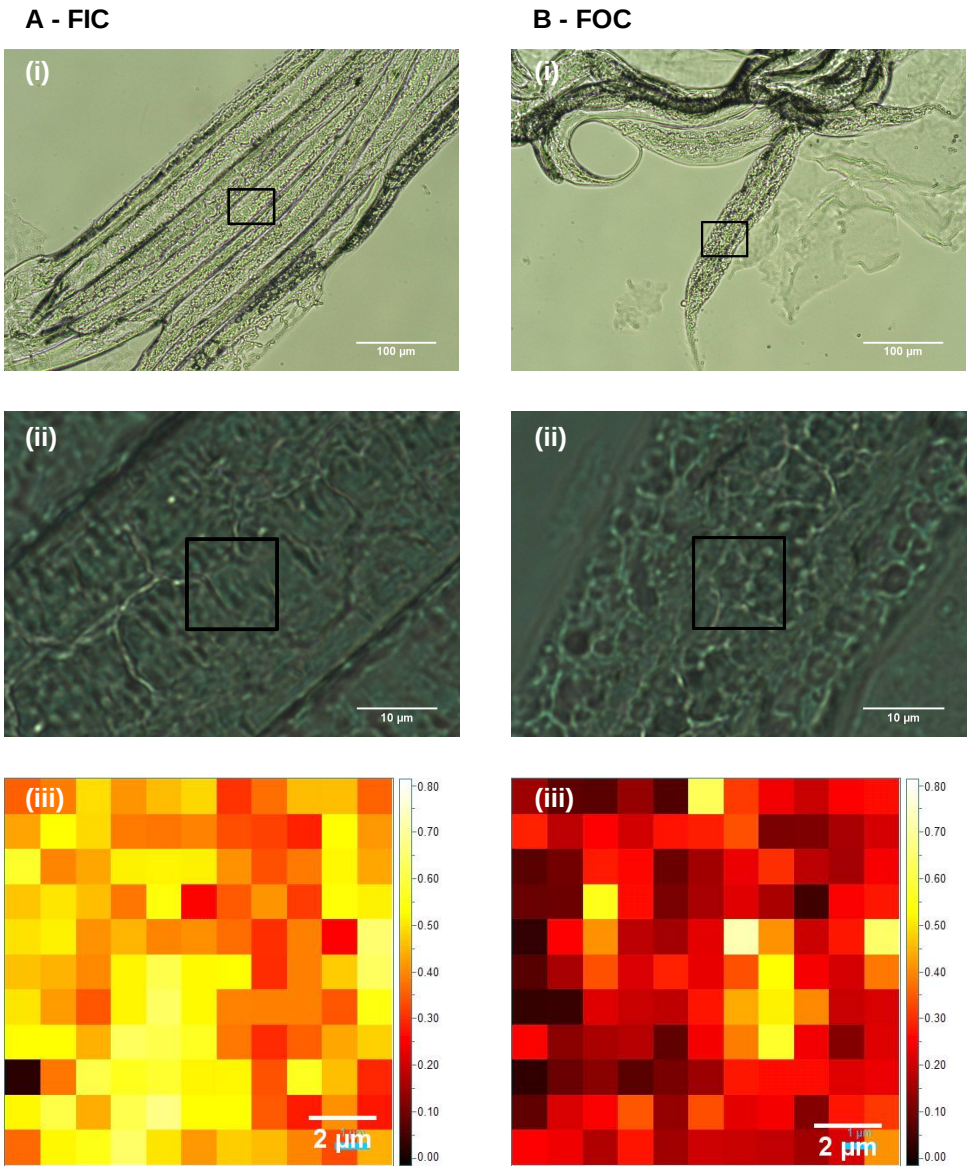


Figure 3.11: Raman intensity map of *C. elegans* incubated with iron initiators.
Raman analysis of *C. elegans* incubated with potassium ferricyanide (FIC) (A-C) and potassium ferrocyanide (D-F). Optical images of *C. elegans* at 10x (A, D) and 100x (B, E) magnification. Scale bar = 20 and 2 μm respectively. (C, F) Intensity map (as area) of bands of the initiator ($I2_{100}$, i.e., 2000-2200 cm^{-1}, C≡N stretching modes) with respect to bands of the worm ($I1_{660}$, i.e.,1520-1780 cm^{-1}, amide I) as a function of spatial location for the FIC- and FOC-loaded worms. Intensity measured across a 11.15 x 11.15 μm grid. Scale bar = 2 μm.

3.4.3 Toxicity Studies - Bristol N2 Wild Type

After investigating the polymerisation of pyrrole and FOC (Fe (II)) at high concentrations of 500 mM and 40 mM respectively, it was important to investigate what concentration induced toxicity in the N2 Bristol wild-type nematodes. As with the *in vitro* cell-induced polymerisation toxicity work, it was necessary to identify a concentration of FOC (Fe (II)) that is biocompatible and a concentration of pyrrole that induced slight toxicity due to the proposed mechanism discussed in Chapter 2.

Work found in literature has already been carried out to understand the effects of iron exposure on *C. elegans* [281–284]. These studies show that iron can induce oxidative stress due to the formation of reactive oxygen species which causes oxidative damage. The effects of iron toxicity can be passed down to progeny. To assess the toxicity of FIC (Fe (III)) and FOC (Fe (II)) on *C. elegans* in this work, percentage viability of nematodes after 24 or 48-hour treatment was investigated. A clear reverse-sigmoidal curve was observed with increasing concentrations of FIC (Fe (III)), and up to the concentration tested (100 mM) percentage survival was reduced (Figure 3.12 A). As incubation time increased from 24 to 48 hours, the 80% lethal concentration ($\mathbf{LC}_{80}$) value halved from 3.4 to 1.7 mM, highlighting the minor latent effect seen when *C. elegans* are treated with FIC (Fe (III)) for increasing periods of time [285].

Contrasting the reduction in N2 nematode survival when treated with FIC (Fe (III)), nematodes were found to be far more tolerant of FOC (Fe (II)) at the same concentrations (Figure 3.12 B), with percentage survival only decreasing to 64% when the nematodes were treated with the highest concentration of 100 mM. Due to the minimal effects of FOC on the N2 Bristol wild type nematodes, it was not possible to predict LC_{80} values with certainty. However it is clear

that survival at concentrations less than 25 mM will not be greatly impacted, as over 80% of the nematodes remained alive.

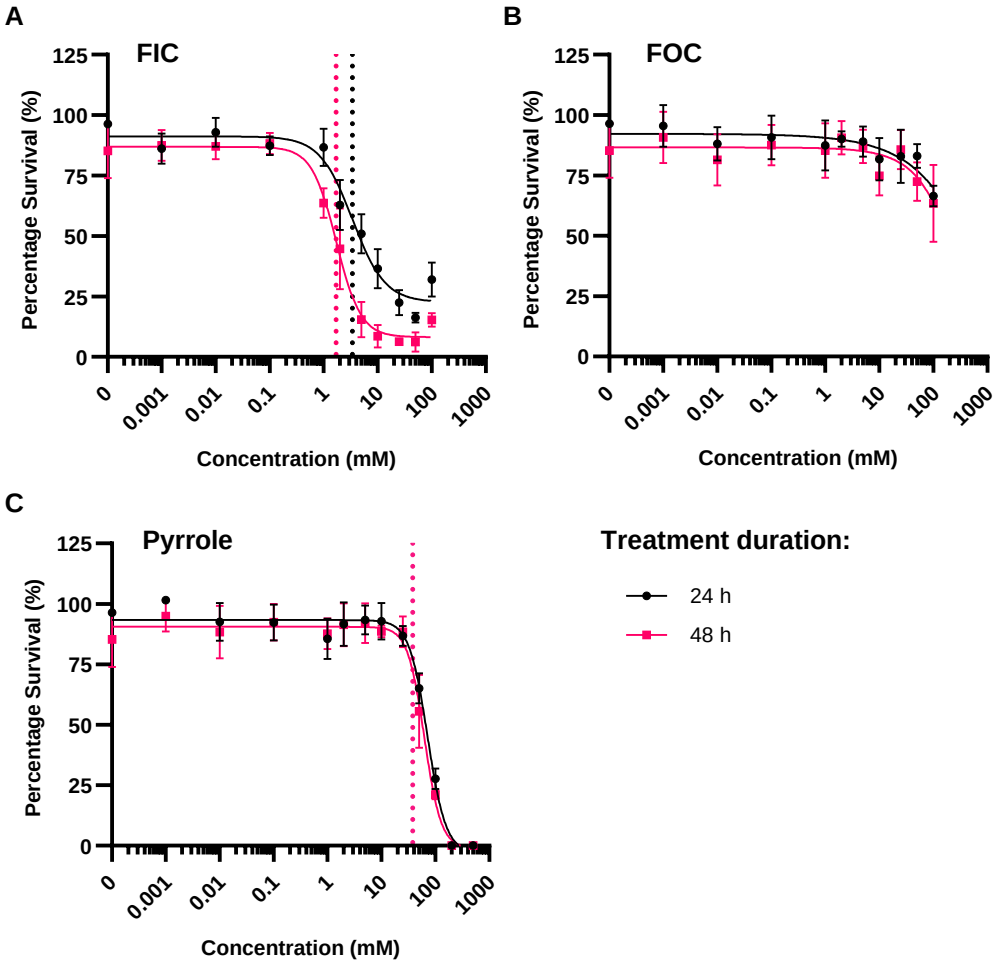


Figure 3.12: Dose-response curve of *C. elegans* treated with iron initiators and pyrrole.
Toxicity of increasing concentrations of (A) potassium ferricyanide (FIC), (B) potassium ferrocyanide (FOC) and (C) pyrrole on N2 Bristol wild type *C. elegans* 24 (black circle) and 48 (pink square) hours post-treatment. N = 3, n = 3; results represent mean ± S.E.M. Black dotted line represents LC_{80} (24 h) and pink dotted line represents LC_{80}(48 h). LC_{80} (FIC) = 3.4 mM (24 h), 1.7 mM (48 h). LC_{80} (Py) = 38 mM (48 h).

A concentration curve for pyrrole was also obtained (Figure 3.12 C). The length of time the samples were treated for (24 or 48 hours) had minimal effect on percentage survival, showing that pyrrole did not cause delayed death, as with

the samples exposed to FIC. The LC_{80} value for the 48-hour treatment was 38 mM.

Alongside this percentage survival, it was found that at concentrations greater than 10 mM, there was no larval production after 48 hours. Also, nematodes were visibly smaller, and lipid-containing fat deposits were not observed (Figure 3.13). These findings suggest that nematode development was inhibited above 10 mM.

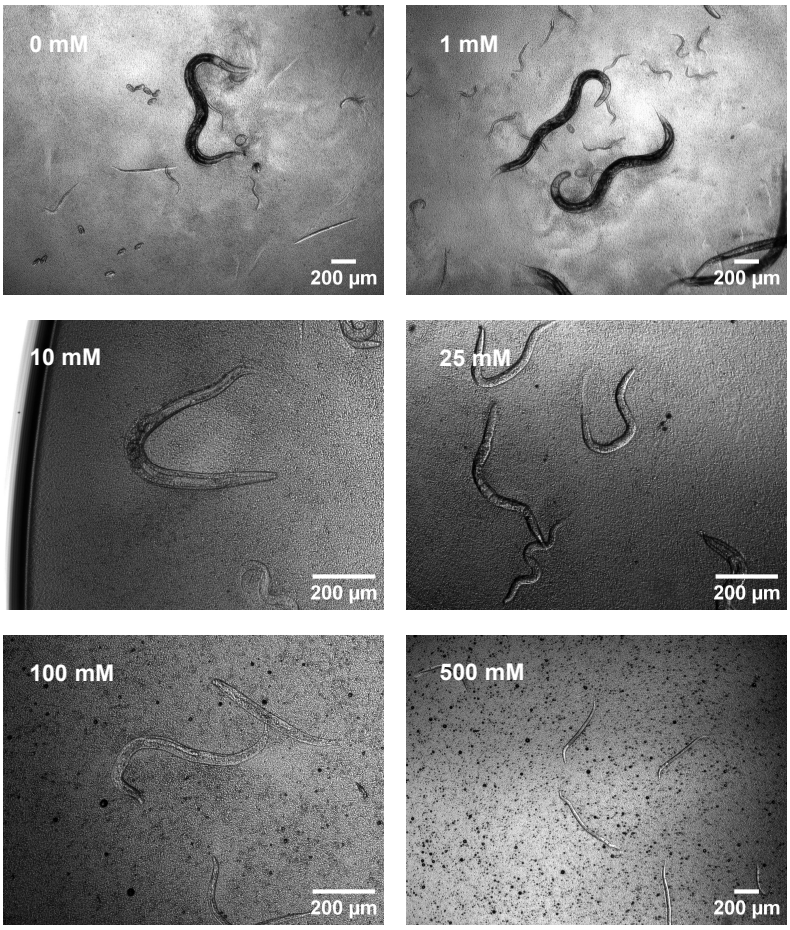


Figure 3.13: Effect of pyrrole concentration on size and larval production of *C. elegans*.

The cell-mediated polymerisation of pyrrole, is hypothesised to be driven, at least in part, by the oxidation of Fe (II) to Fe (III) as cellular exudate is released. In light of this hypothesis, a concentration of pyrrole that induced slight toxicity to the *in vivo* model was required. Consequently, based on the LC_{80} value and indications of developmental suppression for pyrrole, a concentration of 20 mM was selected. For both FIC (Fe (III)) and FOC (Fe (II)), non-toxic concentrations were preferred, so a concentration of 1 mM was deemed to be suitable.

To explore the effect of pyrrole on N2 nematodes further, it was of interest to determine if growth was arrested in the presence of pyrrole at 20 mM. Therefore, it was first necessary to identify the growth profile of untreated nematodes (Figure 3.14 B). Nematodes eggs were incubated at 20℃ for 52 hours to reach the stage of young adult ('Maturity Point'; time = 0 hours. All subsequent times were recorded from this point onwards). The average length of the nematodes was recorded using the WormSizer plugin in ImageJ [256]. Nematodes were then incubated for a further 24 or 48 hours, with the average length measured at each time point.

The median length increased from 738 nm at time 0 hours (Maturity Point), to 1056 nm after 24 hours and to 1176 nm at 48 hours (a total of 100 hours after worms initially hatched). This length increase was significant ($P < 0.0001$). Therefore, a hypothesis was formed: nematodes exposed to pyrrole will be smaller in length than when compared to an untreated control.

As expected, when nematodes were treated with FIC (Fe (III)) and FOC (Fe (II)) for both 24 and 48 hours, there was no significant difference in the percentage survival compared to the untreated control ($P = 0.7178$ (FIC) and $P > 0.9999$ (FOC) at both time points), indicating that this concentration has no effect on short-term survival of N2 nematodes (Figure 3.14 A). Despite

results from the concentration curve suggesting that slight toxicity could be seen at 20 mM pyrrole, when the N2 nematodes were treated for 24 and 48 hours with the monomer, there was no significant change in survival (P = 0.9138 at both time points).

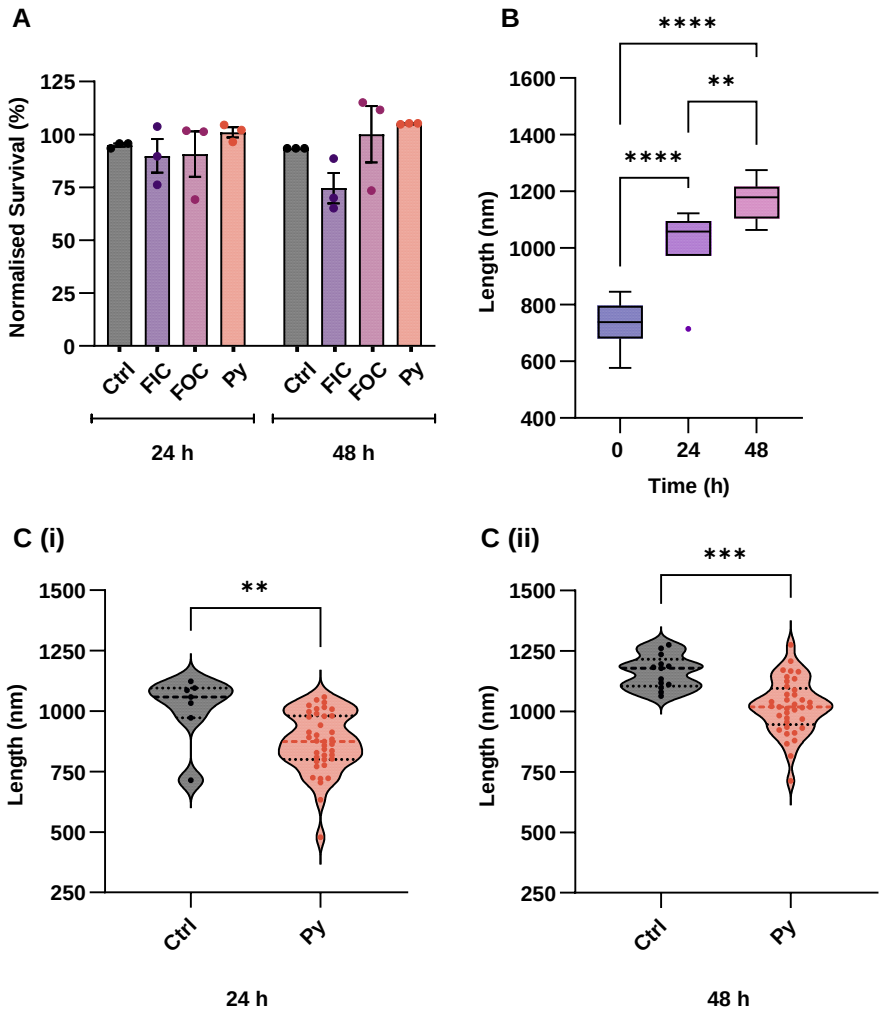


Figure 3.14: Percentage survival and worm length measurements of N2 Bristol wild type nematodes.
(A) Percentage survival after 24 and 48 hours of incubation with pyrrole (20 mM), potassium ferricyanide (FIC) (1 mM), potassium ferricyanide (FOC) (1 mM). N = 3, n = 3. B) Tukey box plot of untreated N2 Bristol wild type nematode length (nm) after 0, 24 or 48 hours. C) Violin plots of N2 Bristol wild type nematode length (nm) after treatment with pyrrole (Py; 20 mM) for (i) 24 or (ii) 48 hours. Results show mean and quartile lines. Data analysed using an unpaired t-test.

As with the untreated controls, the length of nematodes treated with 20 mM pyrrole was measured at 24 and 48 hours post-treatment and compared to the

equivalent untreated nematodes at that timepoint. Statistical analysis at both 24 hours (Figure 3.14 C (i)) and 48 hours (Figure 3.14 C (ii)) revealed that nematodes treated with pyrrole were significantly shorter in length. At 24 hours, the mean length was 1012 and 869.7 nm for untreated and treated worms, respectively (P = 0.0096). At 48 hours, the mean length was 1163 and 1021 nm for untreated and treated respectively (P = 0.0001). From this combined analysis, it is evident that, while the toxicity of pyrrole at this concentration is insufficient to cause death, it has an effect on the growth of the nematode.

3.4.4 Toxicity studies - *C. elegans* Mutant Models

There are many advantages to using a simpler *in vivo* model such as N2 Bristol wild type nematodes as discussed in Section 3.1. However, there are limitations in using this strain to model of diseases such as high grade gliomas. Consequently, attention was shifted using two *C. elegans* disease models that had specific genes involved in cancer knocked out. The mutants used are listed in Table 3.1.

Table 3.1: The strains of *C. elegans* and the corresponding human homologue.

Strain	Nematode Genotype	Human Genotype	Reference
CE1255	cep-1 (ep347)I	p53	[286]
FAS46	his-72 (uge30[gfp::his-72])	H3.3	[246, 247]

It was of interest to determine the toxicity of pyrrole, FIC and FOC on the mutant nematodes. Firstly, growth of the nematodes after treatment was investigated. For the CE1255 strain, average length at the Maturity Point (52 hours after eggs were incubated) was found to be smaller than the N2

wild type at 635 nm, increasing to 1038 nm 24 hours later, and finally 1170 nm at time = 48 hours. This increase between each time point was shown to be significant ($P< 0.0001$ and $P = 0.0002$ between 0 - 24 and 24 - 48 hours, respectively) (Figure 3.15 B). When the CE1255 strain was treated with FIC and FOC (1 mM), there was no significant difference in the length of the nematode compared to the untreated control after either 24 ($P = 0.9245$ (FIC) and 0.5630 (FOC)) or 48 ($P = 0.5384$ (FIC) and 0.9777 (FOC)) hours (Figure 3.15 C).

The lack of variance between worm length of the untreated and iron-treated nematodes was considered in tandem with the toxicity point measurements. Both results suggest that neither of the oxidation states of the initiator induce a toxicity level that affects overall survival or growth of this strain. Conversely, CE2155 treated with pyrrole with or without FOC resulted in significantly smaller worm lengths after 24 and 48-hour treatment ($P < 0.0001$ in all cases). The difference in worm lengths indicated that while the short-term survival of the nematodes was not affected by the presence of 20 mM pyrrole, it did affect the development of CE2155.

The percentage survival of CE1255 and FAS46 was then determined when treated with the different compounds (1 mM FIC or FOC; 20 mM pyrrole) (Figure 3.15 A, D). As with the N2 nematodes, for both mutant strains there was no significant difference between percentage survival of the untreated nematodes and those treated with any of the four conditions: 1. FIC (Fe (III); 2. FOC (Fe (II)); 3. pyrrole; or 4. pyrrole with FOC (Fe (II)) after either 24 or 48 hours ($P \geq 0.5125$ in all cases).

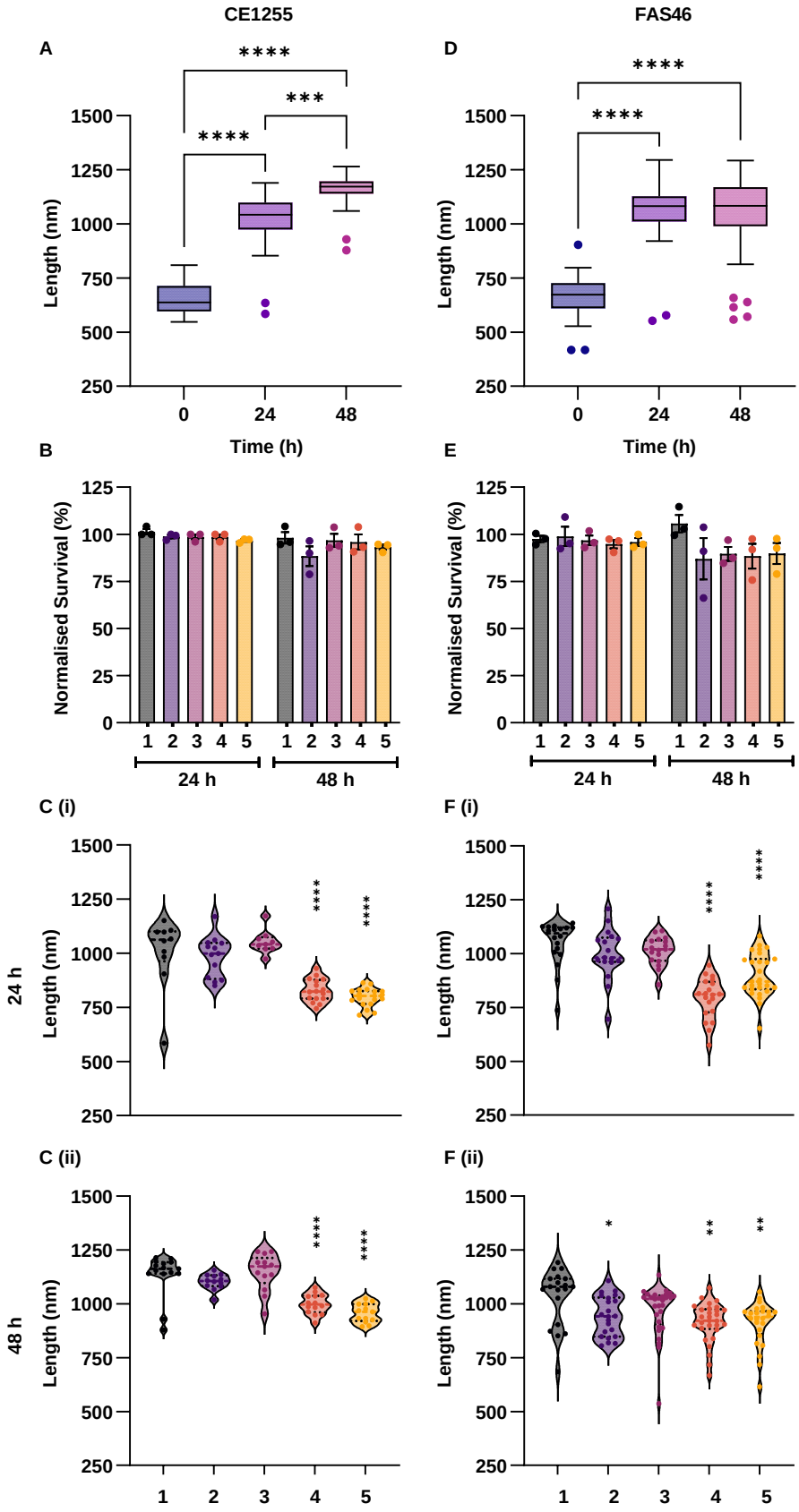


Figure 3.15: Percentage survival and worm length measurements of CE1255 and FAS46 nematodes.

Figure 3.15: Effect of treatment of (1) no treatment; (2) potassium ferricyanide (FIC; 1 mM); (3) potassium ferrocyanide (FOC; 1 mM); (4) pyrrole (Py; 20 mM) or (5) pyrrole + FOC (Py + FOC; 20 mM and 1 mM respectively) on (A-C) CE1255 and (D-F) FAS46 mutant nematodes. (A, D) Tukey box plot of untreated nematode length (nm) after 0, 24 or 48 hours. (B, E) Percentage survival of CE1255 and FAS46 mutant nematodes after 24 and 48 hours of incubation. N = 3, n = 3. (C, F) Violin plots of mutant nematode length (nm) for (i) 24 or (ii) 48 hours. Results show mean and quartile lines.

The FAS46 strain showed a similar survival profile, with, again, no significant change in percentage survival (Fig 3.15 D). The size at 0, 24 and 48 hours post-synchronisation was found to be similar to the CE1255 strain, with mean lengths of 670, 1078 and 1082 nm respectively. However, contrary to the CE1255 strain, while there was a significant increase in nematode length between 0 and 24 hours ($P < 0.0001$), there was no significant change in length between 24 and 48 hours ($P = 0.8910$). These findings indicated that the life cycle of the FAS46 strain was faster than the CE1255 strain (Fig 3.15 E).

As with the N2 and CE1255 strains, after both 24 and 48-hour exposure to pyrrole or pyrrole with FOC (Fe (II)), the FAS46 nematodes were found to be significantly shorter in length than the untreated samples (Figure 3.15 F) ($P < 0.0001$ (24 hours) or $P = 0.0010$ (48 hours)). The length of the FAS46 nematodes treated with FIC (Fe (III)) was also found to be significantly shorter than the untreated sample after 48 hours ($P = 0.0244$).

The hypothesis that FAS46 had a shorter lifecycle time was corroborated by initial observations that the maturation of the FAS46 strain was faster than that of the N2 or CE1255 strains. It was observed that some of the FAS46 nematodes entered larval stage 1 (**L1**) three hours post-synchronisation. In contrast, both N2 wild type and the CE1255 nematodes began to enter the L1 stage after nine hours (Figure 3.16).

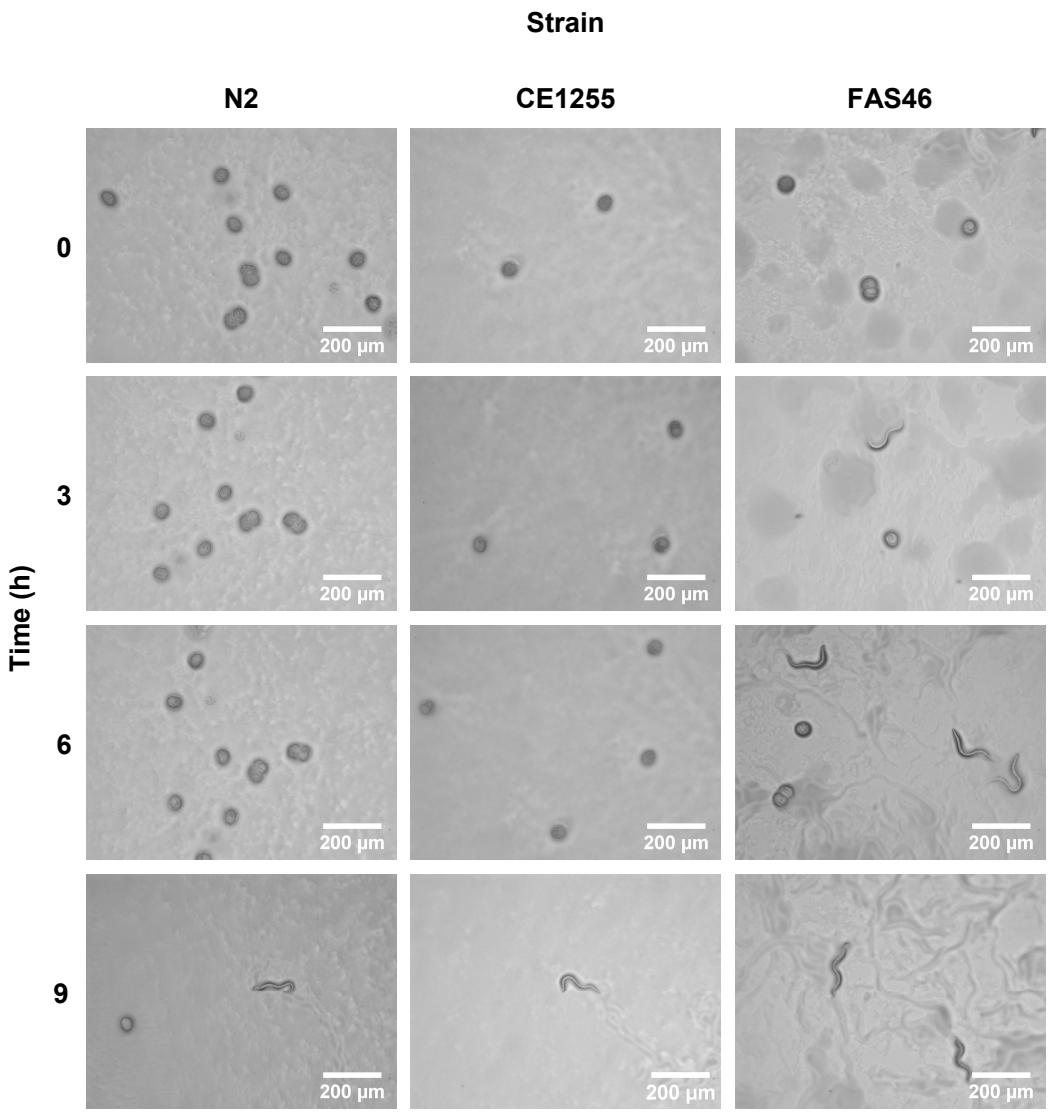


Figure 3.16: Brightfield images of N2, CE1255 and FAS46 *C. elegans* strains from egg to L1 stage. Images taken at time = 0, 3, 6 and 9 hours post-synchronisation. Scale bar = 200 μm.

3.5 Conclusions

The aim of the work in this chapter was to move from an *in vitro* to an *in vivo* system using *C. elegans* in the polymerisation of pyrrole to Ppy. The characterisation of this reaction was first achieved using brightfield microscopy. Despite clear signs of polymer in the nematodes treated with both commercial Ppy and the positive control of pyrrole with FIC (Fe (III)), the presence of

Ppy in the condition of interest (*C. elegans* treated with pyrrole and FOC (Fe (II))) could not be observed.

Research, therefore, shifted to using a semi-qualitative approach using Raman spectroscopy, to identify the unique fingerprints of the molecules of interest. After characterisation of the starting materials, the formation of Ppy was investigated. It was found that Ppy particles were formed in the presence of *C. elegans*. Despite the characteristic dark brown/ black appearance of Ppy clearly visible in the *C. elegans*, fluorescence of the sample made it difficult to validate the formation of polymer within the worms. Future work investigating the mechanism of polymerisation, alongside the polymerisation within the nematodes, is needed here.

Following this, it was necessary to assess the toxicity of the reagents on *C. elegans*, to ensure that future polymerisation studies are carried out at a concentration that is below the toxic threshold. A dose-response curve for the N2 wild type was therefore generated with further investigations into toxicity carried out by looking at percentage survival and the developmental growth of the wild type. This was then compared to two mutated *C. elegans* models to begin to assess differences in treatment responses between different strains.

This chapter has demonstrated that it is possible to move the 'reverse prodrug' polymerisation approach from an *in vitro* to an *in vivo* system. For the first time, it has been shown that Ppy can be formed *in situ* with *C. elegans*. These initial findings pave the way for a better understanding of the polymerisation in more complex organisms. Utilising mutated nematodes as cancer models could be the first step in applying this polymerisation technique in a cancer setting.

Chapter 4

Enhancing Tumour Treating Fields

This chapter is expanded from the following papers:

I. Jobson, Nguyen T. N. V., E. Kujawinski, C. Denning, S. Stolnik, V. M. Chauhan and F. Rawson, "Advancing cancer therapy with custom-built alternating electric field devices", *Bioelectronic Medicine*, vol. 3, no. 2, 2025. [Online]. Available: https://doi.org/10.1186/s42234-024-00164-3.

A. Jain, **I. Jobson**, M. Griffin, R. Rahman, S. Smith, and F. J. Rawson, "Electric Field Responsive Nanotransducers For Glioblastoma", *Bioelectronic Medicine*, vol. 8, no. 17, pp. 1–9, 2022. [Online]. Available: https://doi.org/10.1186/s42234-022-00099-7.

4.1 Introduction

The gold standard of treatment of glioblastoma (**GBM**) follows the 'Stupp protocol' [21], which consists of maximal safe surgical resection followed by

radiotherapy and chemotherapy using the alkylating chemotherapeutic, temozolomide (**TMZ**). Since this landmark change to the treatment of GBM in 2005, further advances in treatment have been slow. The most impactful development to GBM therapy has been through tumour treating fields (**TTFields**), developed by Novocure® [92]. TTFields are low intensity (< 4 V/ cm), intermediate frequency (100 - 500 kHz), alternating current (**AC**) electric fields (**EF**s) [66, 74]. When used alongside TMZ, TTFields have been shown to increase overall survival by a median of five months, a significant improvement in the context of GBM treatment [287].

While the biological and biophysical mechanisms of TTFields on cancer cells are extensive and varied, the most fundamental mechanism of action lies in the antimitotic effects of TTFields [64, 74]. During the metaphase of cell division, the alignment of molecular dipoles, such as microtubules involved in spindle formation, with the uniformly distributed EFs causes abnormal cell division and cell death by apoptosis. In anaphase, the non-uniform EF leads to dielectrophoresis of polarisable molecules. This results in the migration of the charged particles to the cleavage furrow, interfering with cytokinesis [73, 288].

For spherical cells, such as non-mitotic cells or cells in metaphase, the orientation of the cell with the EF is irrelevant. However, as the cell shape becomes irregular, the angle of the EF on the cells, and the divisional axis of the cell affects the efficacy of TTFields. Maximal intracellular field intensity is observed when the axis of division of a cell in telophase is parallel to the EF and decreases as the angle tends to 90°. When the cell is orthogonal to the EF, the maximal intracellular field intensity is lowest [90, 289].

To investigate the effects of TTFields *in vitro*, Novocure® designed the research system 'inovitro™', consisting of eight ceramic dishes housed in a base plate connected to a generator [290, 291]. Two pairs of electrodes are found

perpendicular to each other within the base of each dish ensure a maximum number of the cells are exposed to the EFs. By using a dual electrode system within each dish, cells are also more likely to be in the correct alignment with one set of EFs, resulting in maximum treatment efficacy.

Challenges associated with device cost, along with limited ability to track the effect of the TTFields in real time, due to the opaque base of the dish, has resulted in efforts to engineer additional platforms that can mimic the TTField effects shown by the inovitro^{TM} device [73, 292–295].

A significant amount of research focused on designing alternate electrical stimulation platforms has centred on intratumoral modulation therapy. This therapy uses electrodes implanted into the tumour to deliver EFs directly at the cancer [296, 297]. In addition, *in silico* modelling of EFs can map the intensity distribution profiles of different device setups [298–300].

In addition to designing a high throughput platform for *in vitro* TTField research, there is also a clinical need to improve the efficacy of TTFields. A study by Yoon *et al.* used inorganic biocompatible barium titanate nanoparticles (**BTNP**), which have a high dielectric constant, as potential TTField-sensitisers for breast cancer [104]. They showed that the BTNPs could accumulate in the cytoplasm and, when exposed to TTFields, become polarised by the inhomogeneous EF. This resulted in nanoparticle (**NP**) migration to the cleavage furrow, causing the cells to undergo apoptosis. While this study shows that BTNPs can be used to enhance the effects of TTFields, this type of NP is not approved by the United States Food and Drug Administration (**FDA**), creating a barrier to the translation of this therapy to a clinical setting.

Alternative NPs need to be investigated as potential tools to enhance TTFields. For example, gold (**Au**) NPs have been used considerably within cancer ther-

apy. Au NPs have been used to treat gliomas as, while biocompatible, surface conjugation and their conductive nature allows for wireless sensing of cell behaviour, and the treatment of the tumour by thermal ablation [301–303]. There are many clinical trials that have used Au to treat a variety of diseases, indicating its safety in patients [301, 304].

Similarly, the semi-conductive zinc oxide (**ZnO**) is listed as "generally recognised as safe" (**GRAS**) by the FDA, and is one of the most exploited NPs for drug delivery and cancer therapy [305]. The wide band gap of 3.37 eV is also thought to be linked to the ability of the NP to promote the generation of reactive oxygen species (**ROS**)[306]. ZnO NPs have been shown to exhibit targeted anti-cancerous activity on a range of different cancers [307–309].

Finally, silica (**SiO_2**) NPs are commonly employed in nanomedicine due to their easy synthesis, surface modification and drug loading capabilities [310, 311].

There is a need to broaden the research into the TTField mechanism and its enhancement by making the technology more widely accessible. By designing a high throughput platform, with separate control of frequency and voltage, a better assessment into the mechanism of action can be achieved.

Also, there is a gap in the literature on enhancing TTFields to make them more cost-effective and increase patient overall survival. It is hypothesised that this enhancement could be achieved by combining the electrical stimulation with the 'reverse prodrug' approach. This approach is where a toxic monomer is polymerised into a biocompatible polymer. Results from Chapters 2 and 3 have shown the potential to synthesise polypyrrole (**Ppy**) in this manner. By utilising the physicochemical properties of this conductive organic material,

or that of other inorganic NPs, better insight into the mechanism of TTField enhancement could be addressed.

4.2 Aims

The overall aims and objectives of this chapter can be broadly categorised into two areas:

- to design and test a high throughput plate for the application of TTFields *in vitro*; and
- to investigate the enhancement of TTFields using nano-sensitisers and the 'reverse prodrug' approach.

In the first area, electrode shape and orientation will be investigated to design an alternative platform to the *in vitro* system by Novocure®. Following this, optimising TTField therapy using a TTField enhancer will be researched. This is achieved using one of two methods - inorganic NPs or a 'reverse prodrug'. The inorganic NPs will be characterised physico-chemically, and their toxicity on patient-derived GBM cells will be assessed. Combining non-toxic concentrations of these NPs with TTFields to assess an enhanced TTField effect will then be assessed using a metabolic assay. Alternatively, the use of combining a 'reverse prodrug' synthesised and characterised in the Chapter "Polymerisation of Pyrrole in Living Systems" will be investigated for a dual therapy for cancer treatment.

4.3 Methodology

4.3.1 Disclaimer

The following work associated with research published by Jain *et al.* (2022) [312] was performed with A. Jain: NP characterisation (Figs. 4.11 A (Au NP only), 4.12 A, 4.13 A, B); toxicity of NP on GIN and GCE 28 cells (Figure 4.15); TTField enhancement using Au NPs (25 μg/ mL) (Figure 4.17 C).

4.3.2 Cell Culture

For this work, the 'Glioma INvasive margin' (**GIN**) and 'Glioma Core Enhanced' (**GCE**) 31 pair was first used as a continuation from the work carried out in Chapter 2. Additionally, the GIN 31 cells have been used in other TTField studies, making them a suitable *in vitro* model for this work [89]. To explore the greatest effects of enhancing TTFields with NPs, GIN and GCE 28 cells were selected because this pair have been shown to be more sensitive to other treatments [313]. Therefore, by using the GIN and GCE 28 cells instead of the GIN and GCE 31 pair, any TTField enhancement would potentially be amplified.

To examine the effects of TTFields on cells grown in different ways, a suspension or semi-adherent cell line was required to be tested alongside the adherent GIN and GCE cell lines. A semi-adherent paediatric medulloblastoma cell line, D425, has previously been used to investigate the effects of TTFields on medulloblastoma. Nitta *et al.* found that the optimum TTField frequency was 300 kHz [314]. As the parameters for the optimum TTField frequency for D425

cells align with the experimental approach of this work, D425s were selected as an appropriate cell line for comparison.

4.3.2.1 Initial Well Plate Layout

In the initial setup, two electrodes (either both straight or both bent) were positioned 20 mm apart in a 12-well plate, or 10 mm apart in a 24-well plate (Figure 4.1 A). Electrodes were either left as 'straight' or bent 4 mm from the bottom of the electrode to create a 90° angle (as shown in Figure 4.1 B). The electrodes were coated in dielectric ink (TiO_2, butyl lactate, SiO_2, carbon black & proprietary ingredients) to provide an insulated coating, mimicking the inovitro^{TM} electrode design [65]. The electrodes were then connected to a generator capable of producing AC EFs.

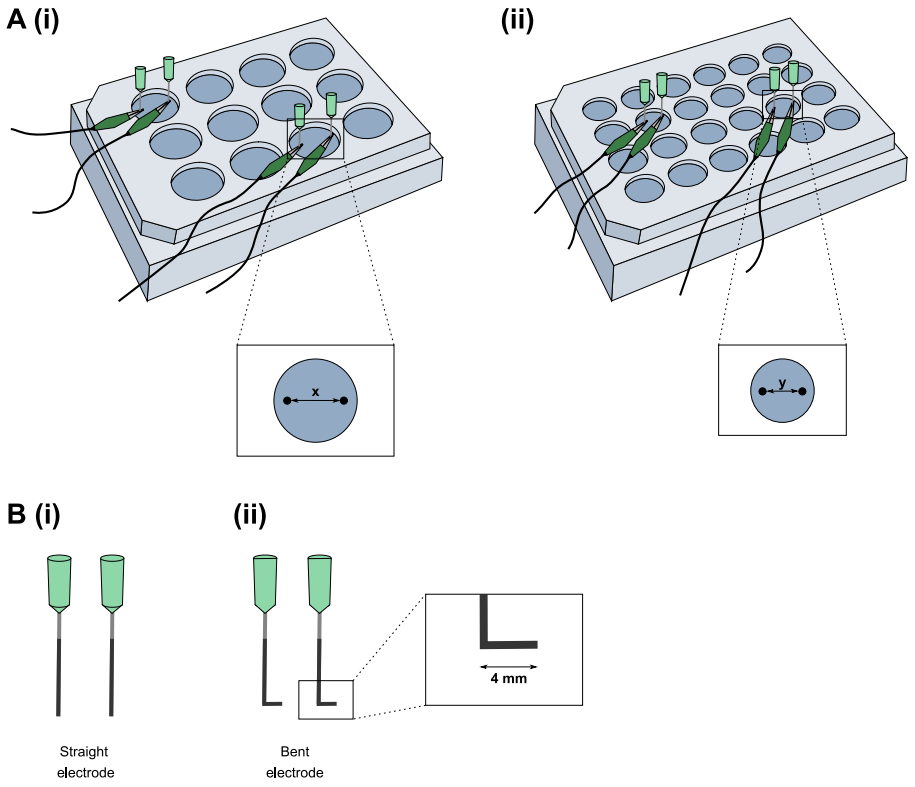


Figure 4.1: Initial setup for the tumour treating field optimisation study. (A) Positioning of the electrodes within a (i) 12-well; or (ii) 24-well plate. Birds-eye view of wells show electrode placement of both straight and bent electrodes where x is 20 mm (12-well plate) and y is 10 mm (24-well plate). (B) Electrode shapes: (i) Straight electrodes coated in dielectric ink; (ii) electrodes bent at a 90° angle 4 mm from the tip of the electrode.

4.3.2.2 96-Well Plate Layout

A high-throughput 96-well plate system for cardiomyocyte pacing (work unpublished) has been designed by Dr Nguyen Vo (School of Medicine, University of Nottingham), and made by Edward Kujawinski. This platform was modified in this work to generate TTFields.

A lid of a 96-well cell-culture treated plate was modified to contain a printed circuit board (PCB) housing electrodes (Figure 4.2 A). For each well that has a pair of electrodes, there was a hole in the PCB (Figure 4.2 A (i) - top insert) to allow for real-time monitoring of the cell behaviour (Figure 4.2 A (i)).

In the inovitro™ platform by Novocure®, the electrodes are coated in ceramic, preventing the movement of ions [65]. Therefore in this work, insulated wire was was chosen as the electrode material for the wells producing TTFields. The graphite electrodes were added to allow for comparison between field and current effects. Four sets of insulated copper wire electrodes, and four sets of conductive graphite electrodes were used (Figure 4.2 A (ii)).

To ensure the cut ends of the copper electrodes were not conductive, epoxy resin was added (shown in Figure 4.2 A (ii) insert). To guarantee the epoxy resin did not leech into the cell-culture medium, the electrodes were primed before first use – to achieve this, phosphate-buffered saline (**PBS**) was added to the wells and TTFields were applied for 24 hours. The toxicity of the electrodes on the cells without electrical stimulation was then assessed for 48 hours using a PrestoBlue™ assay. Primed electrodes were not found to exhibit any cytotoxic effects.

Two wedges were added to the underside of the lid to ensure the correct lid placement. The connection points between each electrode pair and the corresponding wire are shown in Figure 4.2 A (iii). These values corresponded to the connectors on the connector box (Figure 4.2). A rainbow wire from the 96-well plate connected to this connector box. Bayonet Neill–Concelman (**BNC**) cables then connected each well from the connector box to a generator. This meant there was the capacity to individually adjust the EFs for each well.

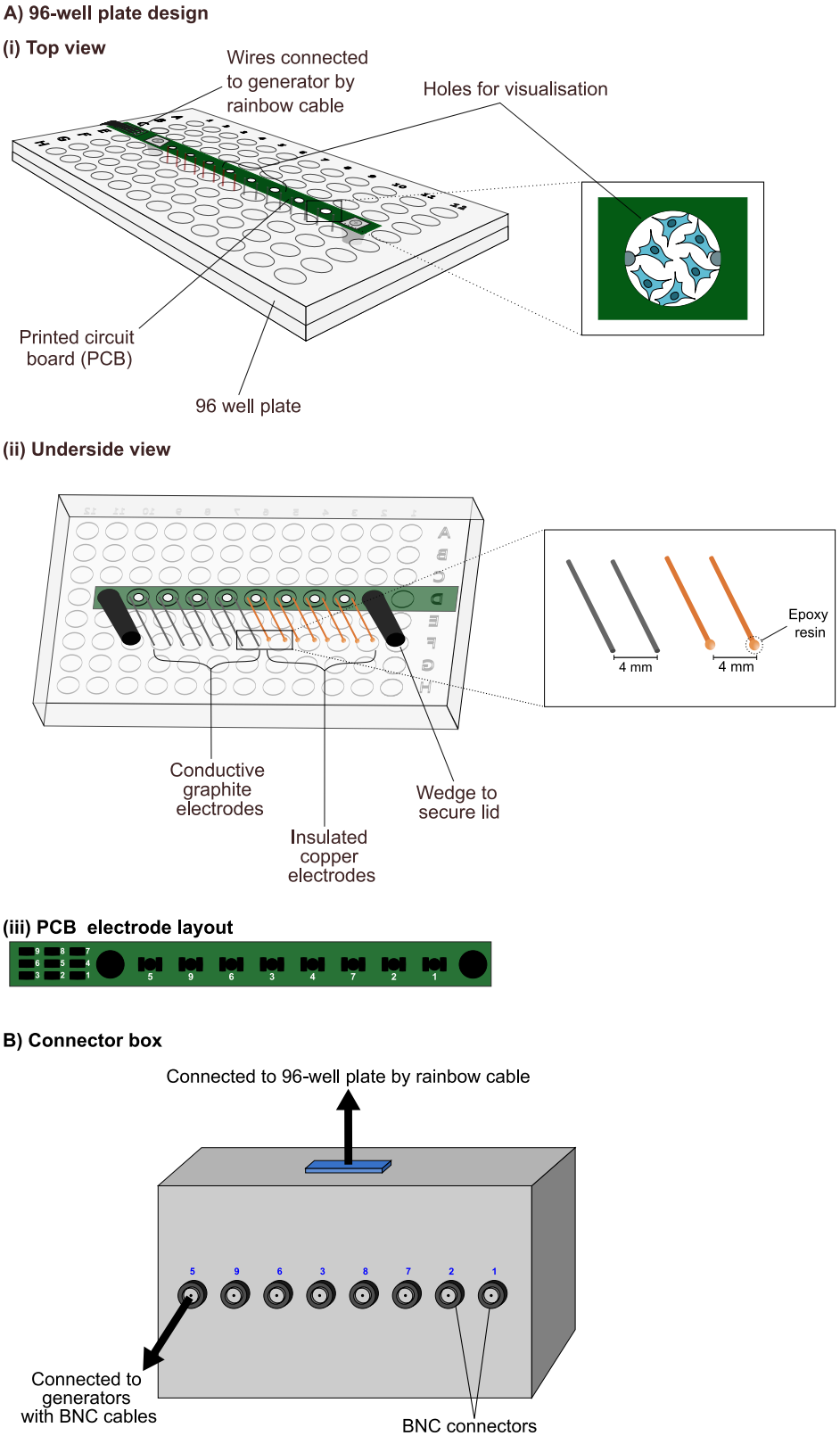


Figure 4.2: Diagram of the 96-well plate tumour treating field system. (A) 96-well plate design showing (i) top and (ii) underside views and (iii) PCB electrode layout. (B) Connector box between plate and generator.

4.3.2.3 Electrical Stimulation Parameters

Previous work has assessed variation in TTField frequency and voltage to optimise parameters for inducing cell death. The frequency used varies across cell lines but typically is most efficacious between 100 - 400 kHz [89]. Therefore, a frequency of 300 kHz was chosen for all the EF experiments. TTField intensity used in literature is between 1 - 4 V/ cm, and cell viability decreases with increasing field intensity, in this work an intensity of 3 V/ cm was used [74].

4.4 Results and Discussion

4.4.1 Initial Plate Layout

To begin understanding the most important features in preparing a plate suitable fir electrical stimulation, a simple plate was first prepared as described in Figure 4.1. This plate consisted consisting of a pair of electrodes in a cell culture plate. Cahalan *et al.* and Cho *et al.* have both showed that AC produced by conductive electrodes can depolarise the cell membrane, inducing the influx of calcium ions into cells [315, 316]. Cell depolarisation does not occur in the TTField setup licensed by Novocure® as the electrodes have a ceramic coating to prevent an ion concentration change within cells [74]. To replicate this insulated electrodes, in this work electrodes were coated in a dielectric ink before being used to generate EFs.

Cells were initially seeded in a 12-well plate to most accurately simulate the conditions used with other *in vitro* systems such as inovitro™ [89]. No significant change in metabolic activity was observed compared to an unstimulated

control (Figure 4.3). The lack of effect was hypothesised to be because the electrode tip was small, and so the area the EFs could effect would also be minimal. To address this challenge, electrodes were bent to create a flat surface on the bottom of the plate that could affect more cells as shown by Trueman *et al.* [317]. To counteract the effect that EF distribution becomes less homogeneous as the distance between an electrode pair increases [318], the expermient was carried out in a 24-well plate instead of a 12-well plate. The distance between the electrode pair was therefore halverd from 2 cm to 1 cm.

A significant decrease in metabolic activity was observed for cells that were exposed to EFs from both straight and bent electrodes in the 24-well plate (P = 0.0112 and 0.0209 respectively). However, a major drawback with this setup was the variation in metabolic change between biological repeats, ranging by 82% for the straight electrodes and 55% for the bent electrodes (Figure 4.3). This discrepancy was thought to be because the electrodes were not fixed to the plate lid, resulting the the movement of electrode positioning if the plate was knocked. Consequently, the actual distance between the electrode pair could fluctuate. In order to address this problem, an EF platform with fixed electrodes was prepared, as discussed in the next Section.

4.4.2 Designing a High Throughput Platform

To address the challenges with the simple plate - mainly associated with large inter- and intra-experiment variation, it was clear than a more robust platform needed to be designed for the TTField experiments. Subsequently, a high throughput 96-well plate was adapted from unpublished work by Nguyen Vo (School of Medicine, University of Nottingham). In this modified design, electrodes were attached to a PCB, preventing movement of the electrodes, which could alter the field strength exhibited on the cells. Also, copper wire

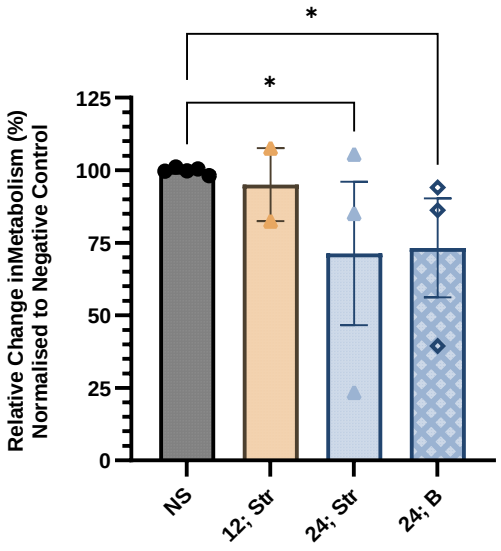


Figure 4.3: Effects of electrode shape on tumour treating field efficacy. Relative metabolism of GIN 31 cells seeded in either 12- or 24-well plates. In the 12-well plates, electrodes were placed 2 cm apart; in the 24-well plate, electrodes were placed 1 cm apart. Insulated electrodes used were either straight (Str) or bent (B) to increase contact with the base of the well. TTField (300 kHz, 3 V/ cm) applied for 24 hours. N = 2, n = 3 (12-well); N = 3, n = 3 (24-well plate). Results show mean ± S.E.M.; Analysed with two-way ANOVA with a Tukey post-test.

electrodes replaced the dielectric ink-coated electrodes in Section 4.3.2.1, reducing variation between the thickness of the insulating layer. Full information on the layout is described in Section 4.4.2 and shown in Figure 4.2.

The features of the 96-well plate were hypothesised to help reduce the experimental variation compared to the initial plate layout. To first test this design, changes to the relative metabolism of cells exposed to either electric field or currents at increasing durations were monitored. It was hypothesised that as the application time of TTFields increased, the relative cell metabolism would decrease as death occurs during mitosis. To test the optimum duration, alternating electric currents were therefore applied at a frequency of 300 kHz and 3 V/ cm for either 4, 24 or 48 hours (Figure 4.4) based on the optimum TTField conditions [89, 312].

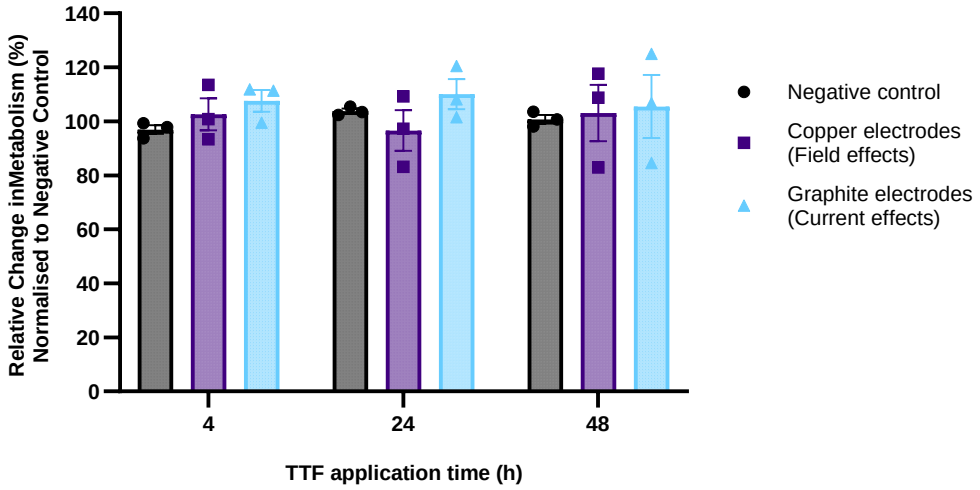


Figure 4.4: Initial study of 96 well-plate electrode platform.
GCE 31 cells were exposed to either no tumour treating fields (TTField) (negative control) or 300 kHz, 3 V/ cm alternating currents through either insulated copper electrodes to observe TTField effects, or conductive graphite electrodes to observe current effects. Metabolic activity of GCE 31 cells was monitored after 4, 24 or 48 hours of treatment. N = 3, n = 1; results represent mean ± S.E.M.

Interestingly, while the standard error of each control increased with lengthening TTField application time, there was no significant difference between the negative controls and cells electrically stimulated, or between the time exposed to electrical stimulation ($P \geq 0.7295$ for all comparisons). While it is well known that TTFields do not affect astrocytes or other non-cancerous cells [89], the lack of impact seen here with GBM contradicts the outcomes seen in many other *in vitro* platforms [95, 293].

Attention shifted to focus on ways to increase the rate of mitosis, as it was hypothesised that this would result in a more pronounced TTField effect (due to the TTField mechanism of action). Therefore, the TTFields were applied at an increased temperature of 37°C [288, 319]. However, at this higher temperature, evaporation of water occurred due to localised heat generated by the EFs [291]. In the case of electric fields, the increased salt concentration may have led to a decreased relative permittivity and increased EF strength [320]. Contrasting this, for the electric current, the increased salt concentration may

have resulted in a reduced electrical resistivity and increased current flow (Figure 4.5) [321].In both cases, cell metabolism was greatly impacted, and so all future experiments were conducted in an incubator set at 25℃.

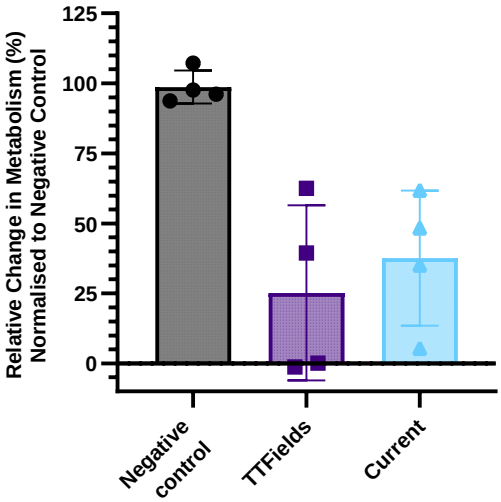


Figure 4.5: Relative metabolism of GCE 31 cells ± tumour treating fields (TTFields), ± current.
TTField (300 kHz, 3 V/ cm) applied for 48 hours. Cells incubated at 37℃ and 5% CO_2. Results show mean ± SD; N = 1, n = 4.

4.4.2.1 Tumour Treating Field Enhancement with Zinc Oxide Nanoparticles

As the high-throughput setup for electric fields alone did not cause a decrease in cellular metabolic activity, amplification of the TTField effect was investigated. ZnO NPs, which are charged semi-conductive particles, were chosen as the TTField amplifier for this study. They were selected because ZnO can become polarised under an electric field due to their semi-conductive nature [322]. As a result, they can migrate under the influence of an EF. It was hypothesised that ZnO NPs could interfere with spindle formation, and also build up at the cleavage furrow during mitosis, potentially causing apoptosis in both cases. Therefore, the TTField effect could be enhanced. Cells were incubated with the NPs at a non-toxic concentration of 5 μg/ mL for four hours to allow for

cellular uptake, after which the cell medium was replaced to remove any NPs in solution. TTFields were then applied for 48 hours to maximise any potential effects of the EF on the cells.

Despite the significant decrease in metabolic activity previously seen when using the inovitro^{TM} system with ZnO NPs [312], there was no significant change when GIN 31 cells were exposed to either TTFields or currents with or without ZnO NP (Figure 4.6 A). This indicated that the setup used here was not optimised for this work. Increasing metabolic activity trends were observed for GCE 31 cells for all treatments, however this was not shown to be statistically significant (Figure 4.6 B).

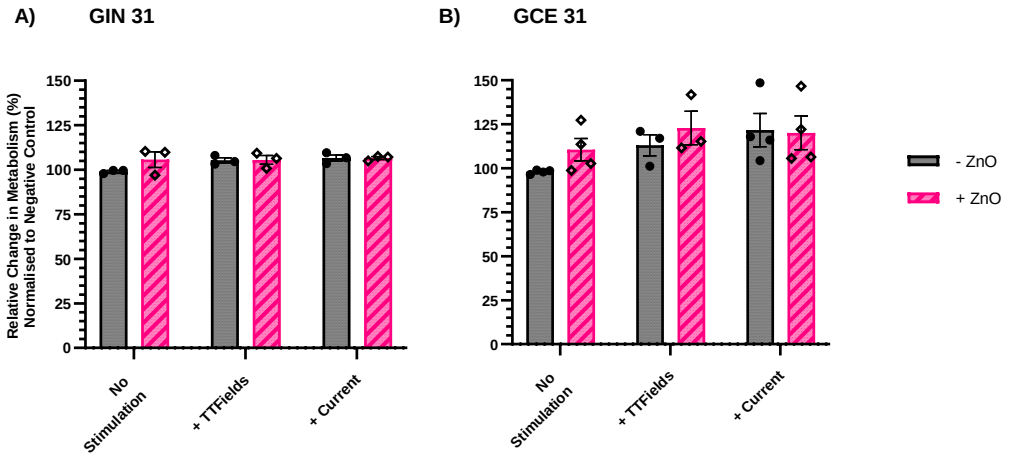


Figure 4.6: Relative metabolism of (A) GIN 31 cells and (B) GCE 31 cells ± ZnO nanoparticles (NP), ± tumour treating fields (TTFields), ± current.
TTField (300 kHz, 3 V/ cm, AC) applied for 48 hours. Cells treated with ZnO NP for 4 hours prior to treatment; NP removed and replaced with fresh Dulbecco's Modified Eagle Medium (DMEM). N = 4, n = 2 for all samples except TTField, where N = 3, n = 2 and TTField + ZnO, and Current + ZnO where N = 2, n = 2. Results show mean ± S.E.M.

It was postulated that the unilateral electrode orientation limited the proportion of cells exposed to the EFs and therefore this hypothesis was probed using a semi-adherent cell line. Using a protocol modified from the adherent cell lines, paediatric medulloblastoma (D425) cells were used to study the ef-

fects of TTFields or current with or without ZnO NPs (Figure 4.7). Here the relative metabolic activity of cells exposed to TTField was markedly increased to 177% of the unstimulated (negative) control. While there was an increase in the relative metabolism of TTFields with ZnO NPs, this was not found to be significantly different from cells solely treated with ZnO NP (P = 0.1417). Conversely, for cells stimulated with an electric current and treated with or without ZnO NP, there was a significant decrease in the relative metabolism (38% and 27% of the negative controls respectively).

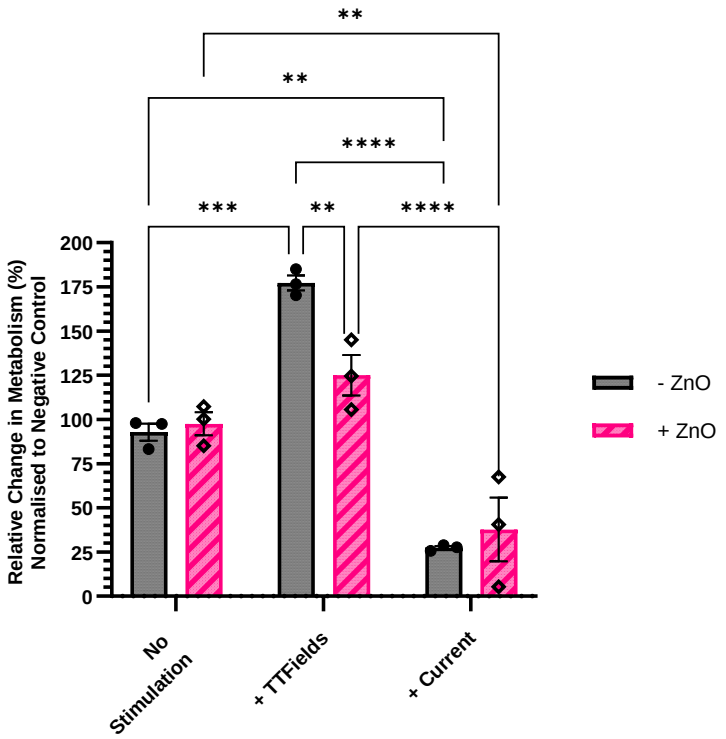


Figure 4.7: Relative metabolism of D425 cells ± ZnO nanoparticles (NP), ± tumour treating fields (TTFields), ± current.
TTField (300 kHz frequency, 3 V/ cm, AC) applied for 48 hours. Cells treated with 5 μg/ mL ZnO NP for 4 hours prior to treatment; NP removed and replaced with fresh Dulbecco's Modified Eagle Medium (DMEM). N = 3, n = 2. Results show mean ± S.E.M.

Given the lack of TTField effects observed with adherent cells and the enhanced metabolic effects with the semi-adherent cells, the work here highlights the importance of considering the orientation of the EFs in this platform, as

field directionality greatly impacts the TTField efficacy. As mitotic cells are only impacted by the presence of an EF when in they are aligned with the field, by only using one pair of electrodes to generate the TTFields, the number of cells affected will be limited to the number of cells in the correct orientation (Figure 4.8) [299, 323]. Low cell numbers per well may also limit the number of correctly orientated cells, further reducing any potential effects by TTFields on cell survival.

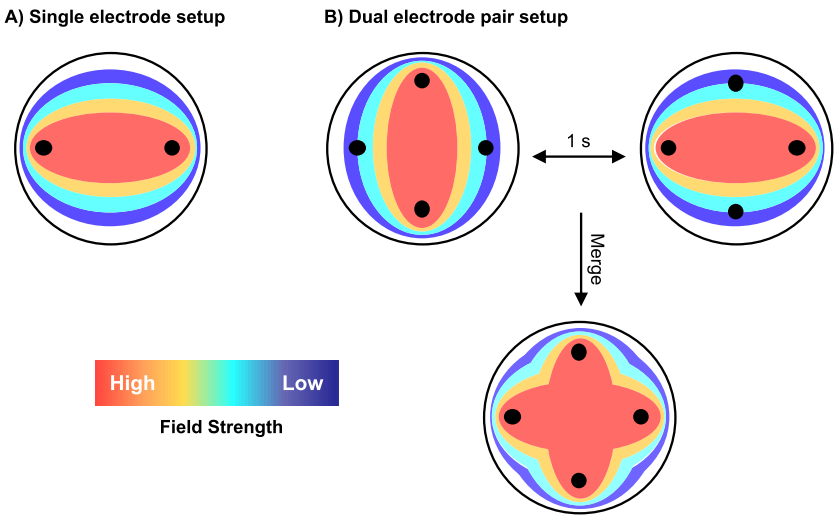


Figure 4.8: Illustration of electric field distribution of two different electrode setups. (A) Single electrode setup where electric field (EF) orientation remains constant between the single pair. (B) Dual electrode setup where field orientation changes orientation by 90° every 1 s. Merged EF distribution combining both orientations shown. Red represents the highest EF strength, dark blue represents the lowest field strength (V/ cm).

It is, therefore, recommended to use of at least two pairs of electrodes, perpendicular to one another, with a frequency phase shift as described by [297] to better replicate the TTField seen using the inovitro™ setup (Figure 4.8 B).

This study highlights the importance in considering the optimum parameters when designing an alternative *in vitro* platform to the inovitro™ (Novocure®) setup. A high-throughput modified 96-well plate consisting of one pair of electrodes per well was used to test a simple *in vitro* setup. After finding no significant difference in metabolic activity of a patient-derived GBM cell

type after TTField application for 4, 24 or 48 hours, the potential to improve the observed efficacy of the platform by combining TTFields with ZnO NPs was assessed. Contrary to previous literature, it was found that there was no significant change in the metabolic activity of GIN 31 and GCE 31 cells when treated with both 5 μg/ mL ZnO and AC electric currents at a frequency of 300 kHz and 3 V/ cm [312]. On the other hand, the semi-adherent D425 cells showed a significant increase in metabolic activity when exposed to TTField alone, and significant decreases in metabolic activity when exposed to current with or without ZnO NPs.

4.4.3 Combining Tumour Treating Fields with the Reverse Prodrug Approach

It was next hypothesised that combining the 'reverse prodrug' approach with TTFields may result in an enhanced TTField effect. Ppy formed by the 'reverse prodrug' approach is a conductive material, and so there was potential to hijack this physicochemical property of the material, as well as combine any effects seen from the TTField enhancemnet with increased cell death from the toxic monomer. Relating the approach to a clinical setting, by using a dual-approach to target GBM cells, a higher proportion of remaining infiltrative GBM cells could be targetted, thus increasing overall survival in patients [324, 325].

To achieve this, cells were treated in one of three ways based on the work performed in Chapter 2: 1. commercial Ppy (5 μg/ mL); 2. pyrrole (**Py**; 10 mM) and ferrocyanide (**FOC**; 2 mM); 3. Py (20 mM) and FOC (2 mM). Immediately after treatment, an EF or current was applied for 48 hours, then the metabolic activity was assessed. As work in Section 4.4.2 showed, cells exposed to just TTFields or current had no change in metabolic activity. Cells

treated with commercial Ppy were also not affected by the presence of electric stimulation (Figure 4.9).

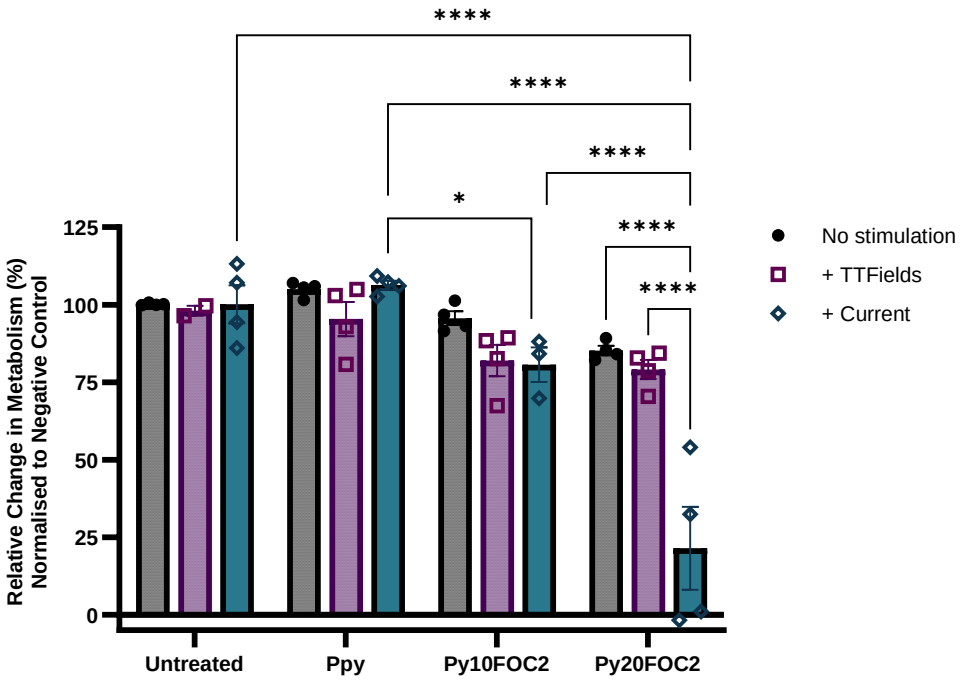


Figure 4.9: Enhancement of tumour treating fields (TTFields) or currents with the 'reverse prodrug' approach.
Relative metabolism of GIN 31 cells treated with either nothing (untreated), polypyrrole (Ppy) (5 μg/ mL), Py (10 mM) + FOC (2 mM) or Py (20 mM) + FOC (2 mM). Treated cells were then exposed to either no stimulation, TTFields or current (+ Curr)). TTFields (300 kHz, 3 V/ cm, AC) applied for 48 hours. N = 4, n = 1. For cells + TTField or Curr; N = 4, n = 2 for cells + no stimulation. Results show mean ± S.E.M.; analysed using two-way ANOVA with a Tukey post-test.

As Ppy was not formulated to be taken up by the cells, such as in NP form [326], the polymer tended to aggregate into clumps (Figure 4.10), decreasing the amount of polymer that could be taken in by the cells. It would therefore be of interest to investigate the effect of using a NP formulation of Ppy to identify if the current would have an effect.

In addition, cells treated with the lower concentration of the 'reverse prodrug' (Py (10 mM) and FOC (Fe (II); 2 mM)) were not affected. Conversely, cells treated with both a higher concentration of the 'reverse prodrug' (Py (20 mM) and FOC (Fe (II); 2 mM)) and electric currents showed a significant decrease

in metabolic activity compared to to current alone or cells treated with the 'reverse prodrug' without electrical stimulation (in both instances $P < 0.001$) (Figure 4.9).

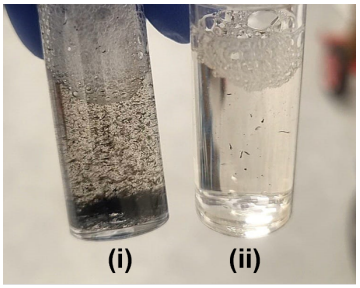


Figure 4.10: Aggregation of polypyrrole (i) 1.42 mg/ mL and (ii) 5 μg/ mL.

This showed that it is the combination of the two therapies (cell-induced polymerisation 'reverse prodrug' and electric stimulation) that caused the significant effect of cell metabolism. As this effect was only limited to stimulation from an electric current not electric field, the effect observed must be as a consequence of the movement of ions in culture medium, or linked to the depolarisation of the cell membrane.

4.4.4 Electric field responsive nanotransducers for glioblastoma

While the combination of the reverse prodrug and electric currents did cause a significant decrease in cellular metabolic activity, the mechanism of action of dual treatment was not clear. To investigate whether this change could be attributed to conductivity or dielectrophoresis, three types of inorganic NP were chosen as simple models to be used with the inovitro^{TM} system by Novocure®. The official TTField platform was used for this work to ensure any changes in cell metabolism were due to the combination of NPs, not due to the platform setup.

Conductive Au, semi-conductive ZnO, and insulating SiO_2 were chosen due to their differences in both conductivity and dielectric constants (where Au has the lowest dielectric constant and SiO_2 the highest [327–329]).

4.4.4.1 Nanoparticle Characterisation

Before enhancing the TTField with NPs, it was first necessary to characterise them. To confirm the chemical profile of Au and ZnO NPs, ultraviolet/ visible (**UV-Vis**) spectroscopy was employed (Figure 4.11 A). UV-Vis is a useful tool for determining a range of physico-chemical characteristics of Au NPs, due to to their optical properties. Surface plasmon resonance is an optical phenomenon which occurs when, at a specific wavelength of light, the electrons at the surface collectively oscillate, causing strong absorption and scattering of the light. NP size greatly effects the absorption wavelength, and colloidal stability of the NPs can be determined, as less stable solutions with greater aggregation have reduced absorbance intensities, broader bands, and a second peak at longer wavelengths [330, 331].

The NPs were shown to have a sharp absorption at 524 nm, which is seen in literature for NPs with a size of 30 - 50 nm [330, 332]. ZnO also had a strong peak at 362 nm, corresponding to a band gap of 3.4 eV as electrons are excited from the valence band (oxygen) to conductive band (zinc) [333]. The sharp singular peak is also indicative of a monodisperse population [334].

To characterise SiO_2 NPs, Fourier transform infrared-spectroscopy (**FTIR**) was used (Figure 4.11 B). Two peaks at 800 and 1050 cm^{-1} were indicative of Si-O-Si asymmetric stretching [335, 336]. A second shoulder under the peak at 1050 at 1142 cm^{-1} was likely to be from the C-N stretching of the amine from the triethoxylpropylaminosilane functionalisation of the NPs.

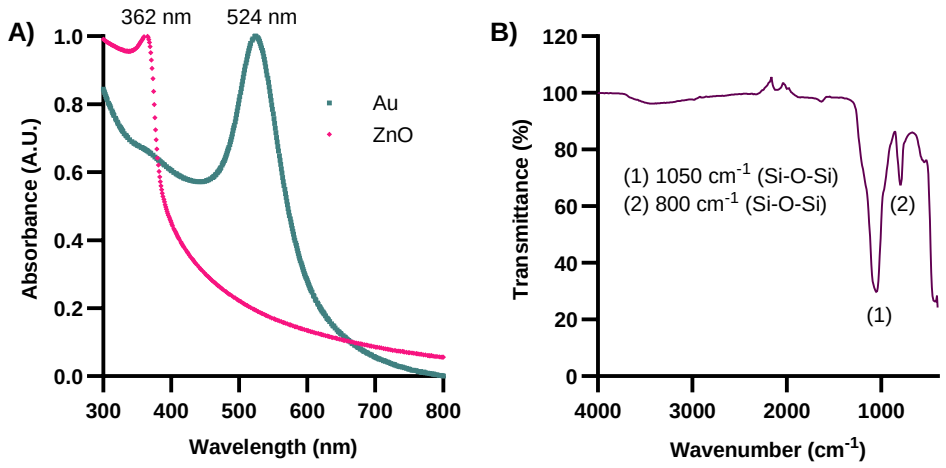


Figure 4.11: Chemical characterisation of Au, ZnO and SiO_2 nanoparticles (NPs).
(A) UV-Vis absorption spectrum of Au and ZnO NPs in PBS; (B) FTIR spectrum of SiO_2 NPs.

The size and shape of NPs is known to have an effect on their biodistribution and uptake due to the enhanced permeation and retention effect [337]. To observe the morphology of the NPs in this study, transmission electron microscopy (**TEM**) analysis was used (Figure 4.12 A - C).

Au NPs were found to have a homogeneous spherical shape, with a mean diameter of Au NPs of approximately 51 ± 8 nm. Contrasting Au, ZnO NPs were observed to be more angular in shape, with a wide variety of different morphologies and a tendency to agglomerate. The mean diameter was found to be smaller than Au NPs at approximately 21 ± 8 nm. SiO_2 NPs had a spherical morphology, however there was a greater disparity within the sample (Figure 4.12 D). The average size was 20 ± 14 nm.

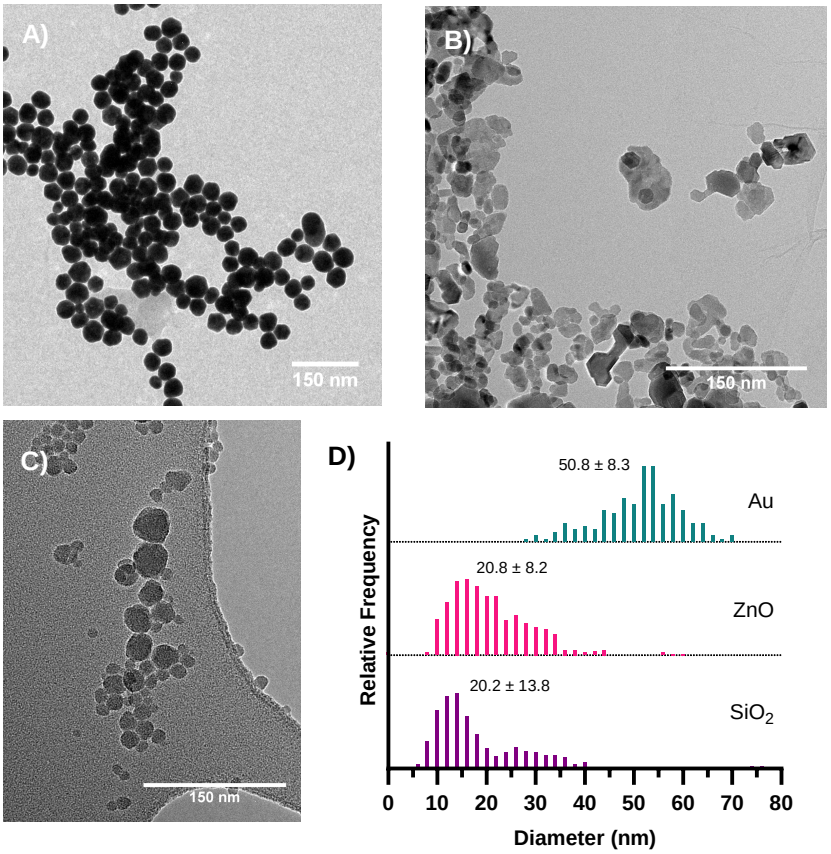


Figure 4.12: Transmission electron microscopy images of nanoparticles (NPs). (A) Au, (B) ZnO and (C) SiO_2 NPs. (D) Histogram showing size distribution of NPs.

Surface charge plays an important role in cellular uptake, with positively charged NPs more favourably taken up by cells, due to the electrostatic attraction between the NPs and the negatively charged cell membrane [338]. Colloidal stability can also be assessed using zeta potential, with with stability increasing as net surface charge (positive or negative) increases [339], whereby a charge of -10 $\leq \zeta <$ 10 mV is likely to be highly unstable, while ζ $\pm$ 20 mV is required for steric stabilisation and $\zeta > \pm$ 30 mV is likely to be highly stable [340]. As these NPs were going to be dispersed in solutions, understanding their colloidal behaviour was important. Zeta potential was used to determine the surface charge of the particles (Figure 4.13 A) and dynamic

light scattering was employed (**DLS**) to determine hydrodynamic diameter (Figure 4.13 B).

Both Au and ZnO NPs had negative surface charges of - 39.2 ± 2.2 mV and - 36.5 ± 1 mV respectively, attributed to the citrate ($C_6H_5O_7^{3-}$) (Figure 4.13 C) and oxide ions [341]. These large negative charges indicate that both of these NPs are highly stable in a colloidal system. There is also potential that they will be influenced by TTField and migrate to a region with higher EF intensity (the cleavage furrow), possibly enhancing the TTField effect. SiO_2 instead has a positive charge of 12.2 ± 0.9 mV, which can be ascribed to the amine ($-NH_2$) groups present from the triethoxylpropylaminosilane surface functionalisation (Figure 4.13 D). Some colloidal stability will be seen due to the weak repulsive forces between the protonated amine groups.

DLS results revealed monodisperse Au NPs with a hydrodynamic diameter (h_d) of 44 ± 3.2 nm, while ZnO NPs had an h_d of 69 ± 6.7 nm, and SiO_2 an h_d of 51 ± 5.5 nm (Figure 4.13 B). The increase in particle size for ZnO and SiO_2 can be attributed to some particle agglomeration, which aligns with the TEM data. DLS data also assumes the particles are spherical, and so other shapes, for example the angular ZnO NPs, will result in improper size calculations.

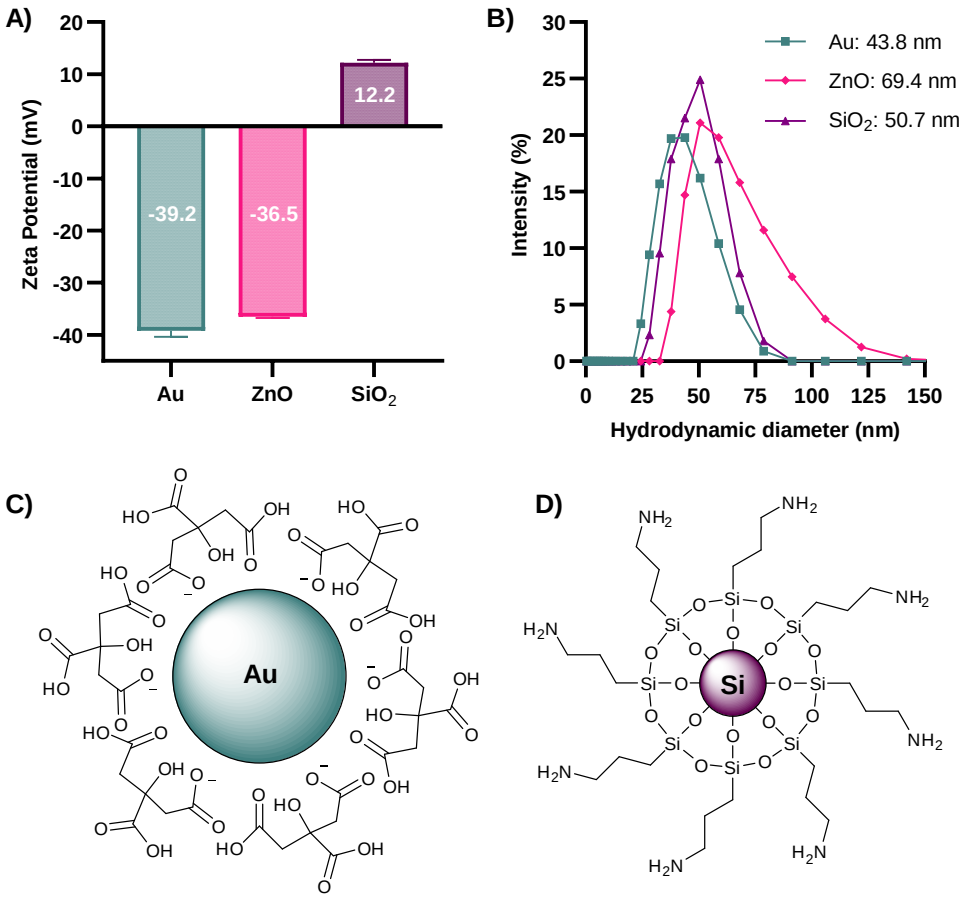


Figure 4.13: Colloidal characterisation of Au, ZnO and SiO_2 nanoparticles.
(A) Zeta potential and (B) hydrodynamic diameter obtained using DLS. Error bars represent the standard deviation of the mean.N = 3; n = 3. Chemical structures of (C) citrate capped gold NP and (D) triethoxylpropylaminosilane functionalised silica NP.

4.4.4.2 *In Vitro* Toxicity of Inorganic Nanoparticles

Next it was important to ascertain the toxicity of the different NPs on the core and invasive patient-derived glioblastoma cells. An experiment was therefore carried out to investigate the effect of increasing the NP concentration from 0 to 200 μg/ mL, by using a PrestoBlue^{TM} assay, which reports on the metabolic activity of cells as an indicator of cell viability. It should also be noted that,

while this is the concentration of NPs given to the cells, the percentage of these NPs internalised by the cells was not quantified.

In the cases of SiO_2 NPs, there was no effect on the relative metabolism of the cells across the concentration range tested after 24 or 48-hour treatment (Figure 4.14 A). From this, we can infer that these NPs are not toxic to the patient-derived cells used in this study at concentrations up to 200 μg/ mL for SiO_2 NPs. Contrasting, as the concentration of ZnO NPs increased, a clear effect on cellular metabolism was seen for both cell types, with relative metabolism significantly reduced at concentrations of 10 μg/ mL. In the case of both cell types at both 24 and 48 hours, a distinct peak can be seen between 10 - 20 μg/ mL and 200 μg/ mL, where the metabolic activity initially dropped, before increasing at around 50 μg/ mL, and then rapidly decreasing as the NP concentration continues to increase.

The limitation of a metabolic assay is that, while it is a rapid indicator of cell metabolism and can be used to infer cell viability, it does not rely on live or dead markers, like the lactodehydrogenase assay does [201]. As such, the data here that shows an increased metabolic activity was seen between 20 - 200 μg/ mL, not that the NPs were less toxic between these concentrations. Exocytosis is a way of moving intracellular components out of the cell by active transport [342]. This process is one of the main ways NPs are also removed from cells [343]. A suggestion for the 'shoulder' seen in this work is that as the concentration of NPs increases, the amount of exocytosis also increases and so the cellular metabolism increases. Once the NP concentration becomes toxic, cell death causes the decrease in metabolic activity.

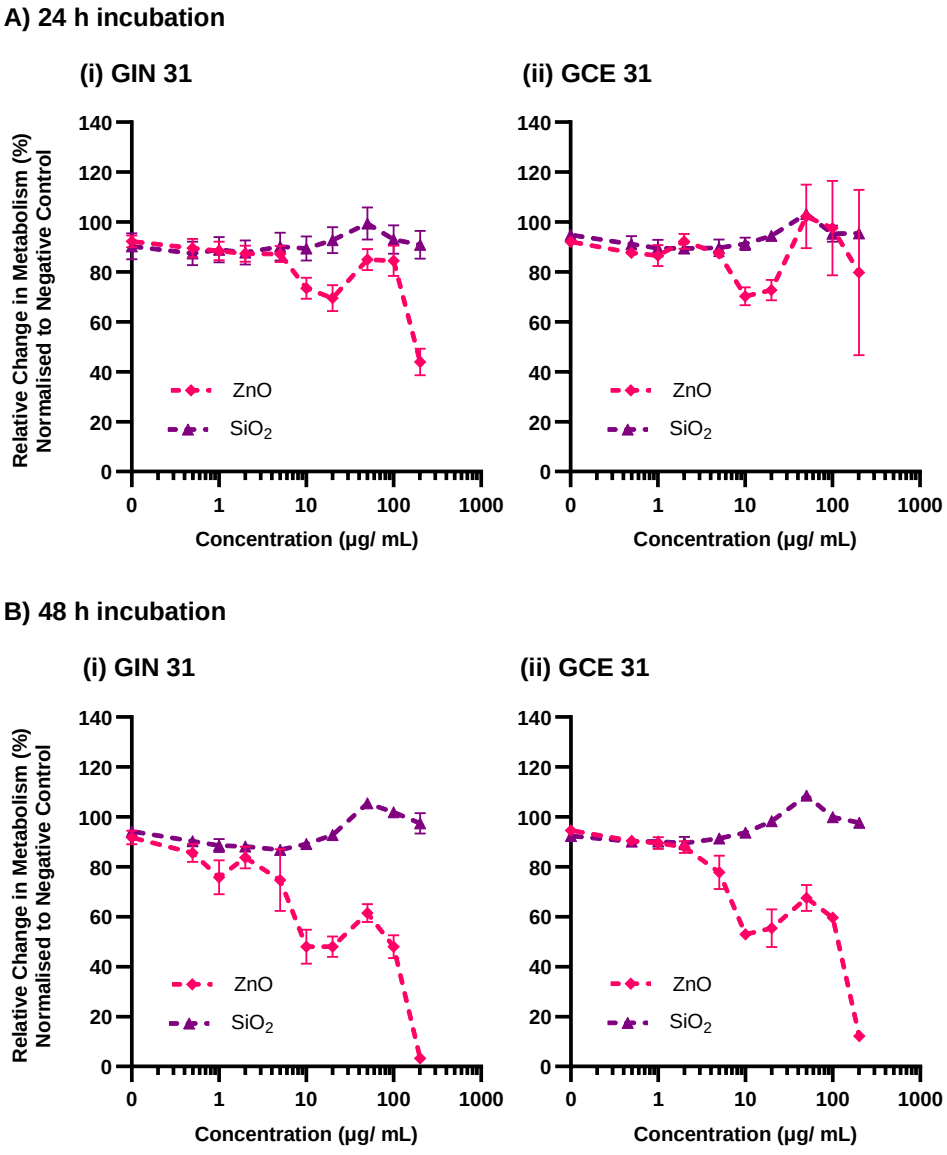


Figure 4.14: Toxicity profile of inorganic nanoparticles on patient-derived GBM cells after prolonged exposure.
(i) GIN 31 and (ii) GCE 31 cells after (A) 24 or (B) 48-hour exposure. Results show mean ± S.E.M. N = 2, n = 4

To ensure the treatment would be more suitable for translation to clinic, it was postulated that NPs should be given four hours before TTField treatment, as this would reduce the wait between NP treatment and TTField therapy. As such, it was necessary to optimise the dose of NPs by incubating the cells with increasing doses of NP for four hours, before the culture medium was replaced with fresh culture medium. Cells were then incubated for 48 hours, to match the duration of time TTField would be applied for. Here, both Au and SiO_2 NPs had no effect on metabolic activity of GIN 28 (Figure 4.15 A) and GCE 28 (Figure 4.15 B) cells up to a concentration of 50 μg/ mL. It was inferred that up to this concentration both Au and SiO_2 NPs were biocompatible with patient-derived GBM cells.

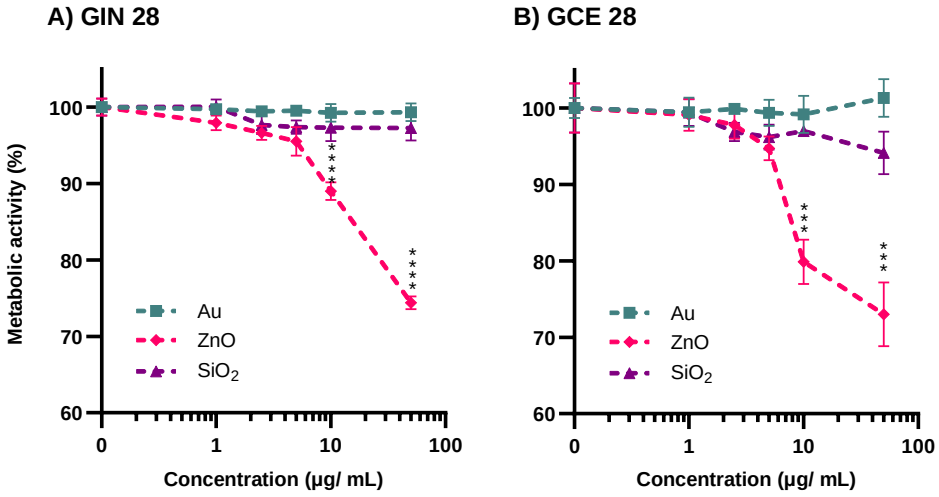


Figure 4.15: Four hour *in vitro* toxicity of inorganic nanoparticles (NPs) on patient derived GBM cells.
(A) GIN 28, and (B) GCE 28 were incubated with increasing concentration of Au, SiO_2 and ZnO NPs for 4 hours, before changing the media containing the NPs with fresh media. Metabolic activity was determined 48 hours after changing the media. Results are expressed as the mean ± S.D. Analysed using 2-way ANOVA with a Tukey post-test.

Conversely, clear signs of toxicity could be observed when GIN 28 and GCE 28 cells were incubated with ZnO NPs at concentrations of 10 μg/ mL or above (Figure 4.15). Toxicity of ZnO at higher concentrations is well-recorded in

literature to be due to the generation of ROS, however the FDA considers ZnO NPs as GRAS at lower concentrations [305, 306]. Based on the toxicity curves of all NPs, a non-toxic concentration of 5 μg/ mL was chosen as the optimum concentration for the *in vitro* TTField enhancement study.

4.4.4.3 Tumour Treating Field Nanoparticle Enhancement

After the toxicity profiles of the NPs had been assessed, research into enhancing TTField with inorganic NPs could be carried out. There are two main mechanisms associated with TTField: dipole alignment and dielectrophoresis (see Section 1.2 for more information). To make this work clinically relevant, and to continue on from the four hour toxicity study in Section 4.4.4.2, cells were first treated with the non-toxic concentration of NPs (5 μg/ mL) for four hours. After allowing for NP uptake, the cell culture medium was replaced and cells were treated with an *in vitro* system from Novocure® (inovitro™) that models the system used clinically (Optune™), and metabolic activity was assessed.

Both GIN and GCE 28 cells exposed to TTField (300 kHz, 1 V/ cm, AC) exhibited a significant decrease in metabolic activity compared to the negative control (Figure 4.16). Despite indications that results showing that 5 μg/ mL of ZnO NPs were not toxic to the cells, a statistically significant reduction in metabolic activity was seen in both cell lines (0.0343 and 0.0245 for GIN and GCE 28 respectively). This only resulted in less than a 12% metabolic decrease, and so this toxicity was limited. Both other NPs (Au and SiO_2) were not found to be toxic.

Most importantly, there was a significant decrease in metabolic activity of cells treated with both TTField and NPs compared to either TTFields or NPs. GIN

28 treated with ZnO had the biggest reduction in metabolic activity compared to TTField alone (approximately 25% decrease; $P < 0.0001$) followed by Au (approximately 19%; $P = 0.0007$) and the SiO_2 (approximately 13% decrease; $P = 0.0150$). The decrease in metabolic activity was also observed for GCE 28 cells, although here it was marginally less pronounced (decreases vs TTField alone of approximately 14% for ZnO ($P = 0.0033$), approximately 18% for Au ($P = 0.0003$) and approximately 12% for SiO_2 ($P = 0.0111$)).

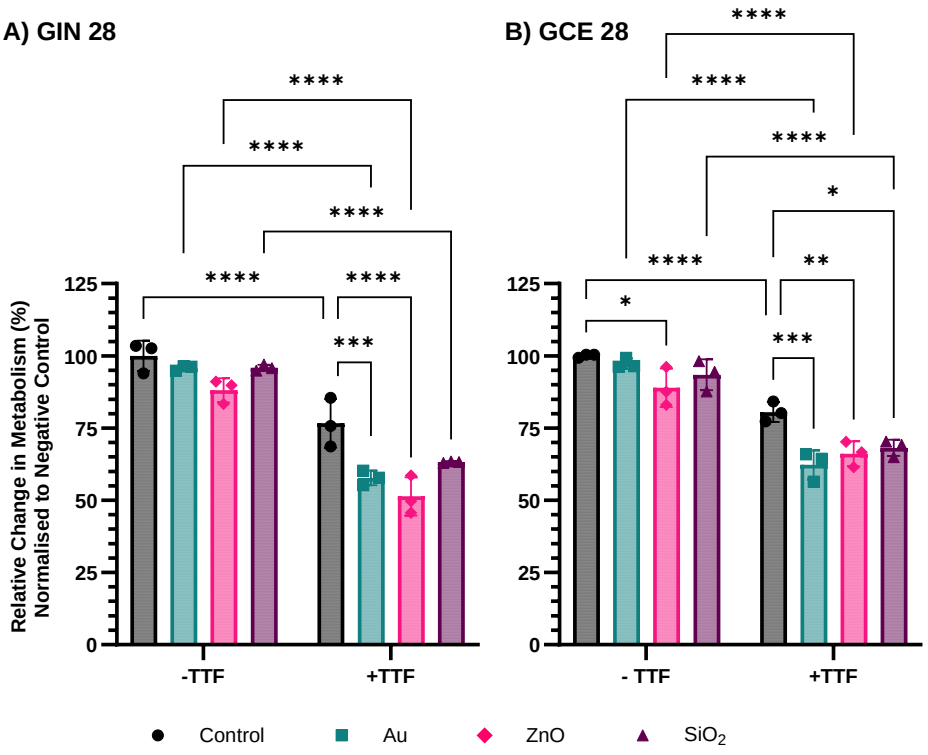


Figure 4.16: TTField enhancement with inorganic nanoparticles (Gold – Au; Zinc oxide – ZnO; Silica oxide – SiO_2) on patient-derived GBM cells. (A) GIN 28 cells and (B) GCE 28 cells treated with TTFields (300 kHz, 1 V/ cm, 48 hours) and 5 μg/ mL NPs. Error bar represents mean ± S.E.M.; N = 2, n = 3.

Next, it was postulated that this TTField enhancement could be improved further by increasing the concentration of NPs. The greatest enhancement effects were seen with either Au or ZnO NPs. As Au NPs had a more favourable toxicity profile it was decided that a concentration of 25 μg/ mL of Au NPs would be used for to further enhance the TTFields. As application time is also

known to greatly impact efficacy of TTFields both in a clinical setting and *in vitro* [89, 91], changes in cellular metabolic activity were also assessed after both 48 and 72 hours (Figure 4.17). One again, combining both TTFields and NPs resulted in an increased efficacy of the TTField treatment, decreasing metabolic activity compared to TTField alone by 24% after 48 hours, and 17% after 72 hours to 45% and 22% respectively. The combination therapy was therefore found to be even more effective at higher concentrations of Au NPs, providing further evidence that the addition of the NPs to the TTField system caused the decrease in metabolic activity.

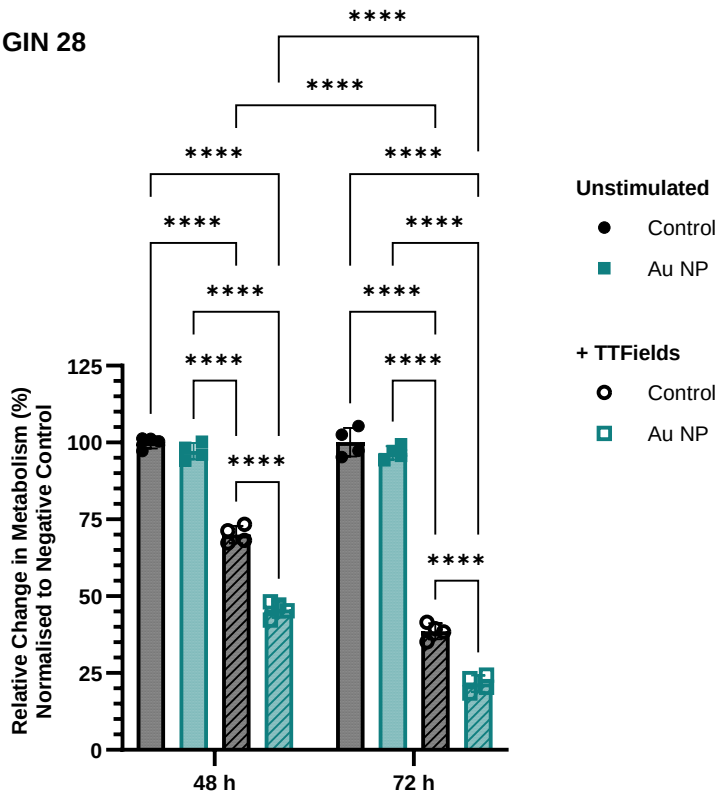


Figure 4.17: TTField enhancement with increased Au nanoparticle (NP) concentration on patient-derived GBM cells.
Metabolic activity measured after 48 and 72 hours TTField enhancement with a NP concentration of 25 μg/ mL. Error bar represents mean ± S.E.M.; N = 2, n = 4.

Application time also played an important role to this study, with cells exposed to TTField for 72 hours having a significant decrease in metabolic activity

compared to the same conditions at 48 hours for cells treated with TTFields in the presence or absence of NPs. Dipole alignment and dielectrophoresis both only occur when TTFields are applied. A such, increasing the application time from 48 to 72 hours is a simple yet positive strategy for the treatment of GBM with TTFields.

It has previously been shown that conductive and semi-conductive NPs can become polarised under an EF as bipolar nanoelectrodes [344, 345]. In this instance, both Au and ZnO NPs could have affected cells by the dipole alignment TTField mechanism, migrating within the cell and disrupting spindle formation. Additionally, both Au and ZnO NPs used here possess a strong negative charge, which may result in the NP movement towards the area of higher field intensity (the cleavage furrow) by bipolar electrophoresis [346]. SiO_2, on the other hand, is a well-known dielectric and so could move by dielectrophoresis when the TTFields within the cell are non-uniform. This could, again, result in a greater build-up of polar components at the cleavage furrow, restricting cell division further than when NPs are not used.

Based on the *in vitro* effects seen here, it is hypothesised that the inorganic NPs can enhance the TTField effect by bipolar electrophoresis (in the case of the conductive and semi-conductive Au and ZnO NPs) or dielectrophoresis (for SiO_2 NPs).

4.5 Conclusions

The aim of this chapter was to address using TTFields for hard-to-treat cancers, starting with the development of an *in vitro* platform. Following this, TTField enhancement was probed using both the conductive organic polymer Ppy in the form of a 'reverse prodrug' treatment and three inorganic NPs.

After initial studies using a simplified TTField setup, attention was switched to a more robust high throughput platform to investigate optimum design parameters. Given the importance of directionality of EFs on cell cycle arrest, the work here highlights electrode shape and orientation as key parameters when replicating an *in vitro* TTField setup. Modelling a platform using the recommendations will contribute to the improvement in understanding of GBM and ultimately an enhancement in TTField therapy and much needed patient outcomes.

The feasibility of combining the 'reverse prodrug' approach (the *in situ* cell-mediated polymerisation of pyrrole to Ppy) with TTFields has also been assessed. Here, cells exposed to both the monomer, inactive initiator and electric currents exhibited a decreased metabolic activity compared to the respective controls. This indicates there is the potential to combine these two treatments for a dual approach to treat hard-to-treat cancers, such as glioblastoma.

Finally three FDA-approved inorganic NPs with different conductivity (Au - conductive; ZnO - semi-conductive; SiO_2 - insulator) were selected to probe the mechanism for TTField enhancement. In all cases, TTFields were shown to be enhanced when combined with NPs *in vitro*, paving the way for further improvements to the TTField treatment.

It is hypothesised that the conductive, highly charged Au and ZnO NPs can migrate intracellularly, interfering with the process of spindle alignment, as well as moving to the cleavage furrow under the presence of a non-homogeneous EF. It is proposed that the dielectric NP SiO_2 may undergo dielectrophoresis, again migrating to the cleavage furrow as the cells undergo mitosis, interfering with cell division.

The work in this chapter shows the importance in not only understanding the underlying mechanism behind TTFields, but also highlights the gap in research to improve the efficacy of this treatment for patients with GBM and other hard-to-treat cancers.

Chapter 5

Methods

5.1 Materials

5.1.1 Cell, Culture Media and Passaging Components

Material	Code	Supplier
Antibiotic-antimycotics	15240062	ThermoFisher
Calcein AM	C1430	ThermoFisher
Caspase-3/7 Green	R37111	ThermoFisher
Dimethyl Sulfoxide (DMSO; $(CH_3)_2SO$)	D2438	Sigma Aldrich
Dulbecco's Modified Eagle Medium, high glucose, HEPES	12430054	ThermoFisher
Dulbecco's Modified Eagle Medium, high glucose, HEPES, no phenol red	21063045	ThermoFisher
Fetal Bovine Serum	F9665	Sigma Aldrich

(Continued)

Material	Code	Supplier
Hanks' Balanced Salt solution	H8264	Sigma Aldrich
L-glutamine	A2916801	ThermoFisher
NucBlue^{TM} Live ReadyProbes^{TM} Reagent (Hoechst 33342)	R37605	ThermoFisher
Penicillin-streptomycin	15140148	ThermoFisher
Phosphate-buffered saline	10010001	ThermoFisher
PrestoBlue^{TM} cell viability reagent	A13262	ThermoFisher
Propidium Iodide	P1304MP	ThermoFisher
Triton X-100	9036-19-5	Sigma Aldrich
Trypan Blue solution, 0.4%, liquid	T8154	Sigma Aldrich
Trypsin-EDTA (0.05%), phenol red	25300062	ThermoFisher
Zombie NIR^{TM} Fixable Viability Kit	423105	BioLegend

5.1.2 *C. elegans* Maintenance Components

Material	Code	Supplier
Agar	A1296	Sigma Aldrich
Agarose	A9539	Honeywell
Calcium Chloride Dihydrate ($CaCl_2.2H_2O$)	C3306	Sigma Aldrich
Cholesterol	C8667	Sigma Aldrich
Ethanol	12857182	ThermoFisher
Lysogeny broth powder	L3022	Sigma Aldrich
Magnesium Sulfate ($MgSO_4$)	M2643	Sigma Aldrich
Peptone	P5905	Sigma Aldrich

(Continued)

Material	Code	Supplier
Potassium Phosphate Dibasic (K_2HPO_4)	P3786	Sigma Aldrich
Potassium Phosphate Monobasic (KH_2PO_4)	P5655	Sigma Aldrich
Sodium Chloride (NaCl)	S9888	Sigma Aldrich
Sodium Hydroxide (NaOH)		
Sodium Hypochlorite (NaClO)	7681-52-9	Honeywell
Sodium Phosphate Dibasic (Na_2HPO_4)	S9763	Sigma Aldrich

5.1.3 Biological Strains

Table 5.1: All components were purchased from the Caenorhabditis Genetics Centre, University of Minnesota.

Name	Species	Genotype
N2	*C. elegans*	*C. elegans* wild isolate
CE1255		cep-1(ep347) I
FAS46		his-72 (uge30[gfp::his-72]) III
OP50	*Escherichia coli*	*E. coli*

5.1.4 Consumables

Material	Code	Supplier
25 cm^2 Cell Culture Flask	430639	Corning
75 cm^2 Cell Culture Flasks	156499	ThermoFisher
175 cm^2 Cell Culture Flasks	159910	ThermoFisher

(Continued)

Material	Code	Supplier
225cm^2 Cell Culture Flask	353138	Corning
Cell Culture-Treated, Flat-Bottom Microplate, 96-well	3596	Corning
Cell Culture-Treated, Flat-Bottom Microplate, 24-well	3524	Corning
Cell Culture-Treated, Flat-Bottom Microplate, 12-well	3513	Corning
Cell Culture-Treated, Flat-Bottom Microplate, 6-well	3516	Corning
Non-Treated, Flat-Bottom Microplate, 96-Well	351172	ThermoFisher
1,000 μl graduated Filter Tip	S1122-1830	StarLab
200 μl graduated Filter Tip	S1120-8810	StarLab
20 μl Filter Tip	BER-0REF-S96	Elkay Laboratory Products
10 μl graduated Filter Tip	S1121-3810	StarLab
50 mL Centrifuge Tube	SLS8106	SLS
15mL Centrifuge Tubes	431470	Corning
100 kDa Amicon® ultra centrifugal filter	UFC510024	Sigma Aldrich
2 mL Internal Threaded Cryogenic Vial	8672	Corning
Syringe Filter, Pore Size 0.22 μm	16541	Sartorius
Petri Dish (100 x 15 mm)	351029	SLS
Reusable Glass Media Bottles	15476113; 15486113; 15406123	ThermoFisher
Quartz microscope slide, 50.8 × 25.4 × 1.0mm	042297.KG	ThermoFisher

5.1.5 Other Reagents

Material	**Code**	**Supplier**
Dielectric ink - polymer dielectric grey for screen printing	902497	Sigma Aldrich
Gold nanoparticles, 100 nm diameter, stabilized suspension in citrate buffer	742031	Sigma Aldrich
Polypyrrole, conductivity 10-50 S/cm (pressed pellet)	577030	Sigma Aldrich
Potassium ferricyanide ($K_3[Fe(CN)_6]$) (> 98% for analysis)	196785000	Alfa Aesar
Potassium ferrocyanide trihydrate ($K_4[Fe(CN)_6]\cdot(H_2O)_3$) (> 99% for analysis)	211095000	ThermoFisher
Pyrrole (Reagent grade, 98%)	131709	Sigma Aldrich
Silica nanoparticle dispersion, non-porous, 5 % (w/w) in water	914843	Sigma Aldrich
Zinc oxide nanoparticle dispersion, 20 wt. % in H_2O	721077	Sigma Aldrich

5.1.6 Equipment

Instrument name	Manufacturer
Avance III^{TM} HD 600 MHz	Bruker Scientific Instruments
Avance III^{TM} HD 800 MHz	Bruker Scientific Instruments
Cary 3500 UV-Vis	Agilent Technologies Ltd
Cary 630 FTIR spectrometer	Agilent Technologies Ltd
EVOS M5000	ThermoFisher

(Continued)

Instrument	Manufacturer
Heraeus Multifuge 3S Centrifuge	Marshall Scientific
Heratherm^{TM} Compact Microbiological Incubators	ThermoFisher
LabRAM HR upright microscope	Horiba Ltd.
XploRA INV	Horiba Ltd.
ID7000^{TM} Spectral Cell Analyzer	Sony
Infinite 2000	TECAN
inovitro^{TM} Laboratory Research System	Novocure Ltd.
2000 FX TEM	Jeol, Ltd.
Zetasizer Nano-ZS	Malvern Instruments
MCO-18AC CO_2 Incubator	Sanyo Electric Co., Ltd.
ECLIPSE Ti Inverted Microscope	Nikon Instruments Inc.
Classic 126 Extended Portable Autoclave	Prestige Medical
RS PRO AFG-21225 Function Generator	RS Group plc
Scanning Electron Microscopy Field Emission Gun 7100F FEG-SEM	Jeol, Ltd.

5.1.7 Locations

Company	Location
Agar Scientific	Rotherham, UK
Agilent Technologies Ltd	Santa Clara, CA, USA
Alfa Aesar	Haverhill, MA, USA
Biolegend	San Diego, CA, USA
Bruker Scientific Instruments	Billerica, MA, USA

(Continued)

Company	Location
Corning	Corning, NY, USA
Electron Microscopy Sciences	Morgantown, WV, US
Elkay Laboratory Products	Sheffield, UK
EM Resolutions	Keele, UK
Greiner Bio-One	Kremsmünster, Austria
Honeywell	Charlotte, NC, USA
Horiba Instruments	Kyoto, Japan
Jeol, Ltd.	Tokyo, Japan
Malvern Instruments	Worcestershire, UK
Marshall Scientific	Hampton, NH, USA
Nikon Instruments Ltd.	Tokyo, Japan
Novocure Ltd.	Haifa, Israel
Prestige Medical	Lancashire, UK
RS Group plc	London, UK
Sanyo Electric Co., Ltd.	Osaka, Japan
Sartorius	Göttingen, Germany
Scientific Laboratory Supplies (SLS)	Nottingham, UK
Sigma Aldrich	St. Louis, MO, USA
StarLab	Milton Keynes, UK
ThermoFisher Scientific	Waltham, MA, USA

5.2 Cell Culture

5.2.1 Routine Cell Culture

GIN and GCE cells

'Glioma INvasive margin' (**GIN**) 28 & 31 cells were isolated from the 5-aminolevulinic acid fluorescence positive margin and 'Glioma Core Enhanced' (**GCE**) 28 & 31 cells were isolated from the core central region of a glioblastoma (**GBM**) patient at the Queen's Medical Centre, University of Nottingham (Nottingham, UK) using the method described by Smith *et al.* [30]. Clinical and molecular features are listed in Table 5.2.

Table 5.2: **Clinical and molecular features of GIN and GCE 28/ 31 cell pairs.** IDH and MGMT both refer to the histological mutations associated with GBM. RT = radiotherapy; CT = chemotherapy; WT = wild type; BSC = best support care; TMZ = temozolomide [31].

Clinical and Molecular Features	Sample Number	
	28	**31**
Date of Surgery	21/01/16	09/03/16
IDH-1	WT	WT
MGMT Status (% methylated)	0	0
Tumour Site	Right frontal	Right temporal
Resection Status (%)	99	100
Treatment (RT/ CT)	BSC	60/ TMZ
Survival (months)	3.1	16.1
Age (years)	71	57
Sex	M	F

Cells were maintained in Dulbecco's Modified Eagle Medium (**DMEM**) supplemented with 10% (v/v) foetal bovine serum (**FBS**), 100 U/ mL penicillin, 100 μg/ mL streptomycin, 0.25 μg/ mL Amphotericin B and 2 mM L-glutamine. The cells were grown with 12 mL of supplemented medium in a T75 cell culture-treated flasks and kept in an incubator at 37℃ and 5% CO_2.

Culture medium was changed every 3-4 days to maintain adequate nutrition and cells were passaged when confluent (80%) using the following procedure: old media was removed from the flask and cells were washed with sterile phosphate-buffered saline (**PBS**) (8 mL) to remove any remaining media. This was then removed, trypsin-ethylenediaminetetraacetic acid (**EDTA**) (3 mL) was added and the flask was incubated at 37℃ for 5 minutes. Gentle tapping of the flask helped aid cell detachment. Fresh supplemented media (9 mL) was added to deactivate the trypsin-EDTA, and the cells were collected by centrifugation at 300 $\times$ g for 5 minutes. The supernatant was removed and the cell pellet was resuspended in 5 mL of fresh supplemented medium. 1 mL of this stock was then transferred into a sterile falcon tube which was made up to 12 mL to perform a 1:5 split ratio.

Cells used were between passages 30 - 40.

D425 (Med Human Medulloblastoma) semi-adherent cells

D425 cells were maintained in DMEM supplemented with 10% FBS. The cells were grown with 5 mL of supplemented medium in a T25 cell culture-treated flasks and kept in an incubator at 37℃ and 5% CO_2. In the case of slow growing cells, the flask was put on its side with the lid facing upwards to allow suspension cells to settle for 5 minutes. 1 mL of cell culture medium was replaced with fresh supplemented medium. Cells were passaged when confluent (80%) using the following procedure: Suspension cells were first removed from the flask and placed in a centrifuge tube. The cells were then washed with

3 mL of Hank's Balanced Salt Solution (**HBSS**) to remove any remaining media. This was then removed, 2 mL trypsin-EDTA was added and the flask was incubated at 37℃ for 5 minutes. Gentle tapping of the flask helped aid cell detachment. Fresh supplemented media (2 mL) was added to deactivate the trypsin, and the cells were added to the falcon tube and collected by centrifugation at 123 $\times$ g for 5 minutes.

Cells used were between passages 30 - 40.

All cells used were tested monthly for mycoplasma where they were grown in antibiotic-free medium for one week before mycoplasma testing. All cells used were mycoplasma-free.

5.2.2 Routine Freezing and Revival of Cell Stocks

Freezing Cells

To freeze cells, cells were cultured in a T175 or T225 (with 40 - 50 mL cell culture medium) to grow sufficient numbers. Next they were trypsinised as in Section 5.2.1 using 10 - 12 mL PBS and 10 - 12 mL trypsin-EDTA, then counted in Section 5.2.3. Cells were diluted in supplemented medium containing 7.5% dimethylsulfoxide (**DMSO**) (freezing medium) to give a concentration of 2 - 4 x 10^6 cells/ mL. 1 mL of cells in freezing medium was added to each cryovial, before the vials were placed in a Mr Frosty in a -80℃ to slow the cooling rate to -1℃/ minute. Once fully frozen, cells were transferred to a cell storage box.

Cell Revival

To revive frozen cells, the cryovial was heated using a water bath for approximately 1 minute until just a small amount of ice was present in the vial to allow for rapid thawing of cells. Immediately, cells were carefully transferred dropwise to a tube containing 11 mL of warmed supplemented cell culture medium

and the suspension was gently mixed. This suspension was then added dropwise into a T75 flask before the flask was incubated at 37℃ and 5 % CO_2. After 24 hours, the medium was gently removed and replaced with fresh, warmed cell culture medium to remove dead cells and the remaining DMSO. Cells were left to become confluent before passaging as previously described in Section 5.2.1.

5.2.3 Trypan Blue Exclusion

To count the cells and determine the cell viability, trypan blue exclusion was used after cells had been trypsinised in Section 5.2.1, with the only difference to the above protocol being that the cell pellet was resuspended in 1 mL of medium instead of 5 mL. 25 μL of this cell stock was mixed with 25 μL of trypan blue and 14 μL of this mixture was then placed into a clean haemocytometer with a coverslip on top. The number of cells were counted in each of the four large corner squares, where cells on the line were counted if they were touching the bottom or right side. Cells were considered alive if they were white, while cells were considered dead if they were blue. The number of cells per square is 0.1 mm^3 so cell count/ mL was determined with Equation 5.1.

$$C_{cells} = \frac{\text{Live Cells}}{4} \times 10^4 \times \text{DF} \tag{5.1}$$

Where C_{cells} is the cell concentration (cells/ mL), live cells are the total live cells counted and DF is the dilution factor (this is always two if using the volumes of cells and trypan listed above).

Cell viability was always at least 90% and was determined using Equation 5.2, where total cells is the combined number of live and dead cells.

$$\text{Viability } \% = \frac{\text{Live Cells}}{\text{Total Cells}} \times 100 \tag{5.2}$$

5.2.4 Cell Seeding

After cells had been counted and the percentage viability determined as in Section 5.2.3, the desired volume of cells needed to make the required cell concentration was determined using Equation 5.3.

$$V_1 = \frac{C_2 V_2}{C_1} \tag{5.3}$$

Where V_1 is the unknown volume to take from the cell stock, C_2 is the desired final concentration of cells and V_2 is the total volume of solution to be prepared and C_1 is the starting concentration determined using Equation 5.1.

The appropriate volume of diluted cell stock was then added to the different well plates or flasks as listed in Table 5.3 unless explicitly stated elsewhere. The plate/ flask was then incubated for 24 hours at 37℃ and 5% CO_2 to allow for cell attachment.

Table 5.3: Volume of cell stock added to different culture plates or flasks. * 0.2 mL for semi-adherent cells.

Plate/ Flask	Volume (mL)
12-well	1
24-well	0.5
96-well	0.1*
T25	3-5
T75	12
T175	30
T225	45

5.2.5 Presto Blue^{TM} Cell Viability Assay

Cell metabolism was assessed using the resazurin-based PrestoBlue (**PB**) assay. To prepare the reagent, PB was diluted 1:10 in fresh, warmed, supplemented media.

Adherent Cells: Cell culture media in the plate was then removed and replaced with the diluted PB reagent. For a 96-well plate, 100 μL of PB reagent was used. The plate was incubated for was incubated at 37℃ for 2 hours, or until the negative control (live cells) had changed to pink/ purple in colour. To prevent air bubbles from being transferred to the black well plate, which can affect accuracy of measurements, 90 μL of the media containing PB was transferred to an opaque black 96-well plate and the fluorescence was measured using a plate reader (λ_{ex} = 560 nm, λ_{em} = 590 nm). Results were normalised by subtracting the average fluorescence value of PrestoBlue^{TM} from the fluorescence values of PrestoBlue^{TM} in the presence of cells and converted to percentage metabolism by setting the negative control as 100% as described in equations 5.4 and 5.5.

$$x_N = x - \bar{R} \tag{5.4}$$

$$\mathrm{M}\% = (\frac{x_N - \bar{p}}{\bar{n}}) \times 100 \tag{5.5}$$

Where x_N is the sample normalised to PrestoBlue^{TM}, x is the sample fluorescence, $\bar{R}$ is the average fluorescence of the PrestoBlue^{TM} control, M% is the relative metabolism of the cells, $\bar{p}$ is the average of the normalised positive (dead) control and $\bar{n}$ is the average of the normalised negative (live) control.

Semi-Adherent Cells: To prevent suspended cells from being removed, 10% PB was added directly to each well. In the case of a 96-well plate, 22 μL of PB was added to give a total volume per well of 222 μL. The reagent was mixed by gently tapping the plate. The plate was incubated at 37℃ for 2 hours, or until the negative control (live cells) had changed to pink/ purple in colour. To prevent cells from being transferred, the plate was then centrifuged at 123 $\times$ g for 5 minutes to sediment any suspended cells. 90 μL of the supernatant was then transferred to a black 96-well plate and fluorescence was measured as for the adherent cells.

5.2.6 *In Vitro* Toxicity Studies

5.2.6.1 Live/ Dead Fluorescence Imaging

To carry out live/ dead fluorescence imaging, GIN and GCE 31 cells were first seeded in a 96-well clear tissue culture plate at a density of 5 $\times$ 10^4 cells/ mL in 100 μL and left to attach for 24 hours. The cell medium was replaced with the desired concentration of treatment as discussed in Section 5.2.6.2. Negative (live) and positive (dead; 3% Triton-X 100 in DMEM) controls were also prepared. Cells were incubated for 48 hours with the treatment. The plate was then spun at 200 $\times$ g for 5 minutes to prevent the accidental removal of floating dead cells. A master stain mix was prepared in PBS containing 1 μL/

mL calcein Am (live stain), 1 μL/ mL ethidium homodimer-1 (dead stain) and 2 drops/ mL Hoechst 33342 (nucleus stain). The cell media was replaced with this master mix and cells were incubated for 20 minutes. The cells were then imaged using a Nikon ECLIPSE Ti Inverted Microscope with the green fluorescent protein 'GFP' (510 nm; green), tdTomato (581 nm; red) and 4',6-diamidino-2-phenylindole 'DAPI' (460 nm; blue) laser channels.

5.2.6.2 Toxicity Curve

In all toxicity curves, cells were seeded at the desired concentration as discussed in Section 5.2.4. After 24 hours, cell medium was removed from each well and replaced with 100 μL of the treatment at the desired concentration (prepared in PBS via serial dilution), then the cells were incubated for either 24 or 48 hours. Relative cell metabolism was determined using PrestoBlue^{TM} (Section 5.2.5).

For the ferricyanide/ ferrocyanide toxicity study (Section 2.4.2): Ferricyanide (**FIC**) and ferrocyanide (**FOC**) toxicity was tested at the following concentrations: 0, 0.001, 0.01, 0.1, 1, 2, 5, 10, 25, 50 and 100 mM.

For the pyrrole toxicity study (Section 2.4.2): Pyrrole (**Py**) toxicity was tested at the following concentrations: 0, 0.001, 0.01, 0.1, 1, 2, 5, 10, 25, 50, 100 200 and 500 mM.

For the nanoparticle toxicity study (Section 4.4.4.2): Zinc oxide (**ZnO**), silica (**SiO_2**) and gold (**Au**) nanoparticle toxicity was tested at the following concentrations: 0, 0.1, 0.5, 1, 2, 5, 10, 20, 50 or 100, 200 μg/ mL.

5.2.7 Flow Cytometry for Apoptosis Study

This work was carried out with Dr David Onion (School of Life Sciences, University of Nottingham).

5.2.7.1 Sample Preparation

Cells were counted as described in Section 5.2.3, and then seeded in a 12-well plate as described in Section 5.2.4. Culture medium was replaced with a supplemented DMEM containing the treatment and incubated for the desired amount of time. After this, the supernatant was removed from the wells and added to a falcon tube. Cells were washed with phosphate buffer saline (PBS), and this wash was also added to the same falcon tube. Next, cells were trypsinised, and after a 3 minute incubation media was added to inhibit the trypsin. This solution was added to the supernatant previously collected. Samples were centrifuged at 300 x g for 5 minutes, then the supernatant was discarded. 500 μL PBS was added to disperse the pellet, then 2 drops of caspase 3/ 7 detection reagent and 0.5 μL of Zombie dye were added to each sample. Controls of cells with no caspase 3/ 7 reagent or Zombie dye, and either just caspase 3/ 7 reagent or Zombie dye were also prepared for gating the samples as shown in Table 5.4.

Table 5.4: List of controls for flow cytometry experiment.

Control	Caspase 3/ 7	Zombie-NIR
1	-	-
2	X	-
3	-	X
4	X	X

Cells were incubated at 37℃, 5% and CO_2 for 30 min. Samples were then centrifuged, the supernatant discarded and the pellet redispersed in PBS. This

washing step was repeated. The resulting suspensions were then transferred to Falcon^{TM} round-bottomed polystyrene test tubes and stored in the dark until analysis. Samples were measured using an iD7000^{TM} Spectral Flow Cytometer (Sony).

5.2.7.2 Gating for Percentage Apoptotic Cells

To select single cells, the events were sequentially gated. First, forward scatter (**FSC**) - Area (**A**) was plotted against side scatter (SSC) - A to identify cells and exclude debris. Following this, to remove duplicate events, cells were gated against SSC- Height (**H**) against SSC-A. Finally, cells were gated using a quadrant gate for Caspase 3/ 7 vs Zombie-NIR. This gating was dictated by the position of the cells stain with just Caspase 3/ 7, just Zombie-NIR and the treated negative control (**NC**) stained with both stains. This is shown in Figure 5.1. All gating was performed using FlowJo^{TM} 10.10.

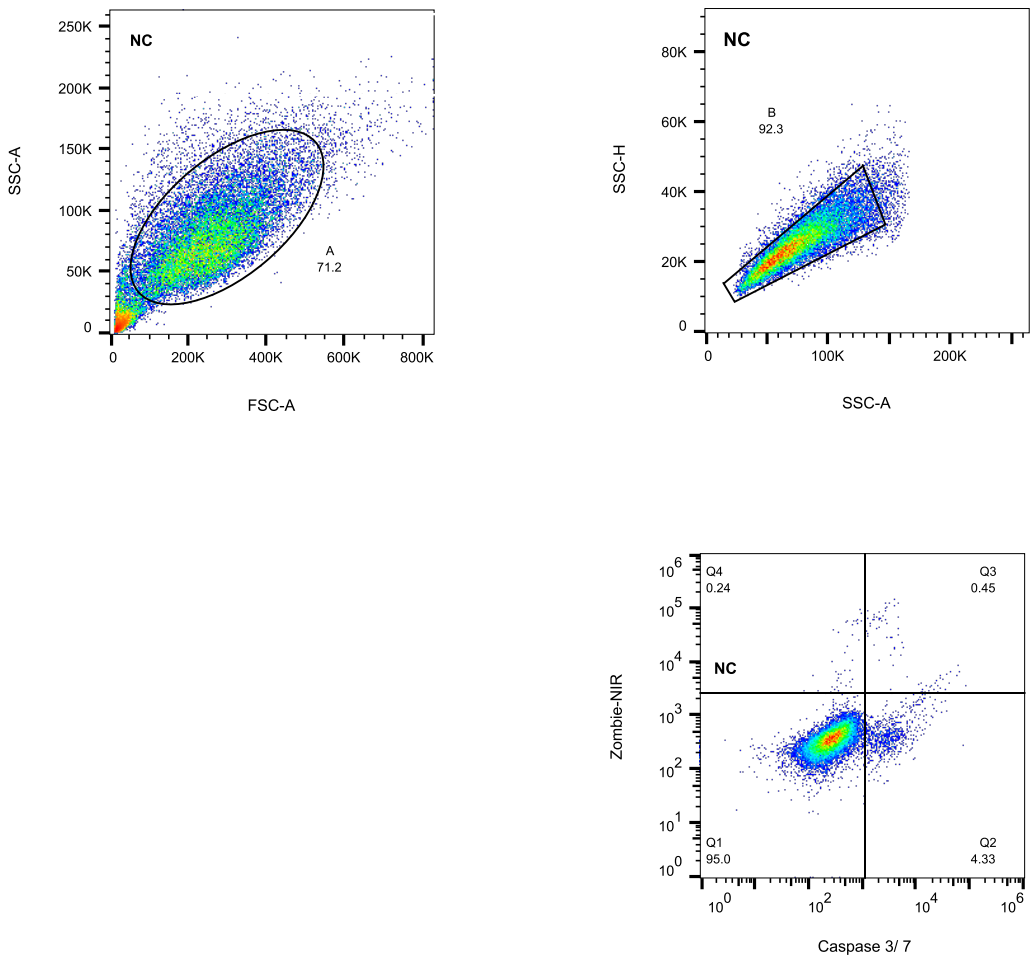


Figure 5.1: Gating strategy for negative control (NC) GCE 31 cells stained with both Caspase 3/7 and Zombie-NIR.
Cells were first gated based on physical parameters of cell size (Forward Scatter; FSC) and structural complexity (Side Scatter SSC). Next, cells were gated to remove duplicates by plotting SSC-Area (A) vs Height (H). Finally, cells were quadrant gated.

5.3 Cell-Induced Polymerisation

Cells were seeded in a tissue culture-treated T175 flask at a density of 6.5 x 10^6 cells per flask then incubated for 24 hours at 37°C and 5% CO_2 to attach. Py and FOC were added to supplemented DMEM to give final concentrations of 500 and 40 mM respectively. The cell-culture medium was replaced with 40 mL DMEM + Py + FOC, and left to incubate for 48 hours for the polymerisation to occur. This media was then removed and filtered through a

100 kDa Amicon® ultra centrifugal filter. The polypyrrole (**Ppy**) residue was then resuspended in dH_2O, then filtered and washed twice more. The final residue was resuspended in dH_2O and then snap frozen in liquid nitrogen and freeze-dried for analysis. Two chemically-synthesised Ppy controls were also prepared. Here, Py and FIC were added to either supplemented DMEM, or dH_2O to give final concentrations of 500 and 40 mM respectively, and a total volume of 40 mL. These solutions were incubated alongside the cell-mediated flask, and Ppy was isolated as above.

5.4 *Caenorhabditis elegans*

5.4.1 Preparation of Stock Solutions

Bacterial Food Source: Lysogeny broth (**LB**; also known as Luria Broth) was prepared by suspending 20 g of LB broth powder in 1 L of milliQ water. This was then autoclaved for 15 minutes at 121℃. One colony of *E. coli* 'OP50' was added to 50 mL of LB. Two tubes were prepared for every 1 L of Nematode Growth Medium (**NGM**). The tubes were incubated overnight at 37℃ to allow the bacterial food source to grow.

For experiments, the *E. coli* was prepared in the following way: After incubation in LB overnight, the bacteria solution was transferred to 15 mL centrifuge tubes, then spun at 4000 × *g* for 3 min. The supernatant was removed and the pellet resuspended in 10 mL M9 buffer. This was repeated twice more. Finally, the pellet was resuspended in M9 to give an optical density (**OD**) of 1 (measured using ultraviolet/ visible (**UV-Vis**) spectroscopy). This was used to dilute worm stocks to the desired concentration for worm seeding in Section 5.4.5.

Calcium chloride ($CaCl_2$) solution (1 M): 7.4 g of calcium chloride dihydrate ($CaCl_2 \cdot 2H_2O$) was weighed out then placed into a clean 250 mL borosilicate bottle. Approximately 50 mL of milliQ water was added to the bottle to make the concentration 1 M. This solution was swirled to fully dissolve the crystals. The lid was loosened, autoclave tape was added and this was autoclaved for 15 minutes. This was stored at 4℃. Before use, the solution was filter sterilised using a 0.22 μm filter.

Magnesium sulfate ($MgSO_4$) solution (1 M): 12.3 g of magnesium sulfate heptahydrate ($MgSO_4 \cdot 7H_2O$) was weighed out then placed into a clean 250 mL borosilicate bottle. Approximately 50 mL of milliQ water was added to the bottle to make the concentration 1 M. This solution was swirled to fully dissolve the crystals. The lid was loosened, autoclave tape was added and this was autoclaved for 15 minutes. This was stored at 4℃. Before use, the solution was filter sterilised using a 0.22 μm filter.

Potassium phosphate buffer (KPO_4) solution (1 M): 54.2 g of monopotassium phosphate (KH_2PO_4) (also known as potassium phosphate monobasic) was weighed out then placed into a clean 500 mL borosilicate bottle. 17.8 g of dipotassium phosphate (K_2HPO_4) (also known as potassium phosphate dibasic) was added. Next, 500 mL of milliQ water was added to the bottle and this solution was shaken vigorously to fully dissolve the crystals. The pH was checked using pH paper to ensure it was between 5.8 - 6.0. The lid was loosened, autoclave tape was added and this was autoclaved for 15 minutes. This was stored at room temperature. Before use, the solution was filter sterilised using a 0.22 μm filter.

Cholesterol in ethanol solution (5 mg/ mL): 10 mg of cholesterol was placed in a clean glass vial and 2 mL of ethanol was added and the vial was

shaken to mix. This was made each time NGM was prepared. It was not autoclaved before use.

M9 Buffer: 1.8 g KH_2PO_4, 3.6 g Na_2HPO_4 and 3 g NaCl were added to a 1 L borosilicate bottle and 600 mL of milliQ water was added. The lid was loosened, autoclave tape was added and this was autoclaved for 15 minutes. After the solution was cooled to approximately 50℃, 0.6 mL of $MgSO_4$ (1 M) was added and the solution mixed by swirling. This was stored at 4℃.

Sodium Hydroxide (NaOH) Solution (5 N): 50 g of NaOH was added to a clean container and milliQ water was added to make the total volume 250 mL. This was stored at room temperature.

5.4.2 Preparation of Growth Media

In this work, *C. elegans* were grown on NGM agar in 100 mm petri dishes to ensure large quantities of worms for experiments. These plates were prepared in the following manner:

NaCl (1.5 g), agar (8.5 g) and peptone (1.25 g) were added to a 1 L borosilicate glass bottle with an autoclavable lid. 488 mL milliQ water was added, the lid was loosely placed on the bottle with autoclave tape and this was autoclaved for 50 minutes. The bottle was then transferred to a sink filled with cold water to cool the contents to approximately 50℃ to prevent the salts from precipitating out when added.

A flame was setup to ensure an aseptic environment. 1 mL each of sterile $CaCl_2$ (1 M) and $MgSO_4$ (1 M) were added to the bottle, along with 1 mL of cholesterol in ethanol (5 mg/ mL) and 25 mL of KPO_4 buffer (1 M). This solution was then swirled to mix. The NGM solution was then poured into

petri plates using sterile procedures, filling each plate approximately 2/ 3 full. The plates were then left at room temperature for 2 - 3 days to allow excess moisture to evaporate from the plates.

To each plate, approximately 400 μL of *E. coli* OP50 in LB was added. This was spread over the plate using a sterile L-shaped spreader, ensuring the lawn was not spread to the very edge of the plate to prevent worms crawling up the plate, drying out and dying. Plates were incubated at 37℃ overnight, or until a visibly thick lawn was observed. The NGM plates were the stored upside down in an airtight container at 4℃ until needed.

5.4.3 Culturing *C. elegans*

Transferring worms on NGM plates: To quickly transfer worms from an old plate devoid of a bacteria lawn to a fresh plate, a 1 $\times$ 1 cm chunk of agar was cut from the old plate using a sterilised scalpel. This chunk was transferred to the fresh plate, ensuring the chunk was flipped so that the worms were able to crawl onto the new agar.

Cleaning Contaminated Plates: To remove bacterial or mould contaminants from plates, worms were first removed by washing the plate with sterile H_2O using a pipette. This was done twice to loosen any worms or eggs that were stuck in the contaminant. The liquid was transferred to a centrifuge tube and spun at 2000 $\times$ g for 2 minutes to settle the worms. The supernatant was removed and 3.5 mL sterile H_2O was added to re-suspend the worms. 0.5 mL NaOH (5N) was mixed with 1 mL sodium hypochlorite then this was added to the tube. The tube was shaken well for a few seconds every 2 minutes for a total of 10 minutes, or until the worms had broken down to release eggs as identified under a brightfield microscope. The tube was spun at 1500 $\times$ g for 1

minute to pellet the eggs. The supernatant was removed and sterile H_2O was added to re-suspend the eggs in 5 mL total volume. The tube was shaken then centrifuged as before. This wash step was repeated for a total of two washes. The supernatant was removed, then the pelleted eggs were transferred to a clean plate using a sterile pipette.

5.4.4 Synchronising the Worm Life Cycle

To synchronise the worm life cycle, eggs were obtained using the same method described in Section 5.4.3 "Cleaning Contaminated Plates", using NaOH and bleach to harvest eggs from adult worms. The eggs were divided between an appropriate number of plates and left to reach the desired stage in the life cycle. See below for timings for larval (**L**) stage 1 and adult worms.

To obtain larval (L1) worms: The plates were incubated at 20℃ for 60 hours to allow two cycles of the life cycle to occur. To isolate the L1 larvae, the worms were washed off the agar plate using dH_2O and passed through 2 $\times$ nylon 20 μm filters. 50 mL dH_2O was passed through the filters to ensure all L1 larvae had passed through. The larvae were then spun at 1500 $\times$ g for 2 minutes to pellet the worms. There were then counted as in Section 5.4.5 below.

To obtain adult worms: The plates were incubated at 20℃ for 52 hours to let the worms reach the adult stage in the life cycle, before egg laying had begun.

5.4.5 Counting *C. elegans*

Two 20 μm mesh filters were placed in a clean funnel and wetted using sterile dH_2O. Plates containing the synced worms previously described in Section 5.4.4 were washed with approximately 30 mL sterile dH_2O, and this liquid was then transferred to the filter to trap adult worms. Approximately 30 mL more dH_2O was passed through the filter to wash through any smaller worms or contaminants. The adult worms were washed off the filter with less than 10 mL dH_2O into a clean 15 mL centrifuge tube, before being spun at 1500 $\times$ g for 2 minutes to pellet the worms. The supernatant was discarded then the worms resuspended in dH_2O to make a total volume of 1 mL. 20 μL of this suspension was pipetted onto a microscope slide with grid marking using a wide tip to ensure the worms would fit through the tip end. The number of worms in 20 μL was counted then the concentration of worms was determined using Equation 5.6.

$$C_{worm} = N_{20} \times 50 \tag{5.6}$$

Where C_{worm} is the number of worms per mL (concentration) and N_{20} is the number of worms in 20 μL.

The stock solution of worms was then diluted with a mixture of *E. coli* in M9 at an OD of approximately 1 to achieve the desired number of worms per 100 μL. This was then added to 96-well plates with 100 μL of the worm suspension per well, ensuring that a tip with a wide end was used (cut using a scalpel if necessary) to ensure all worms could pass through intact. The exact number of worms per well was recorded, making note of both live and dead worms.

5.4.6 Imaging *C. elegans*

Two slides were wrapped in a single layer of masking tape to create a slightly raised platform and allow a thin agarose platform to be created. These were placed on either side of a clean microscope slide. A droplet of 5% agarose gel was placed in the middle of the microscope slide, then another clean slide was placed perpendicular to the first slide over the droplet and the gel was left to harden slightly (approximately 30 seconds). The top slide was removed, leaving the spread droplet on a single slide. 5 μL of worms were added to the droplet, and immobilised by the addition of levamisole (5 μL). Excess liquid was removed by blotting using a low-lint tissue, taking care to not disturb the worms or damage the gel. Finally, a coverslip was placed over the slide, which could then be inverted and imaged using the brightfield setting on an EVOS microscope. The preparation of agarose slides is depicted in Figure 5.2.

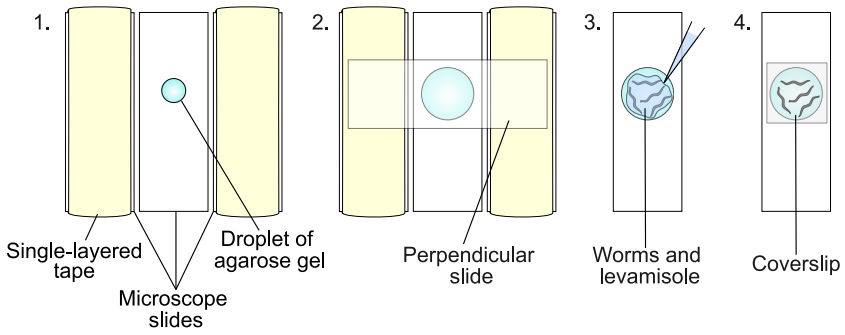


Figure 5.2: Graphical illustration of preparing agarose slides for imaging nematodes.
(1) Two slides wrapped in a single layer of masking tape were placed on either side of a clean microscope slide. A droplet of 5% agarose gel was placed in the middle of the slide. (2) A clean slide was placed perpendicular to the first slide over the droplet and the gel was left to harden. The slide was then removed. (3) Worms were added to the droplet, and immobilised with levamisole. Excess liquid was removed. (4) A coverslip was placed over the droplet before imaging.

5.4.7 *C. elegans* Life Cycle Study

Three NGM plates were used per mutant as biological repeats. Eggs were obtained using the method described in Section 5.4.3 "Cleaning Contaminated Plates". Briefly, the plates were washed with dH_2O and NaOH and sodium hypochlorite were added as previously described. After vortexing/ shaking regularly for 10 minutes, the tubes were spun at 2000 $\times$ g for 1 minute, the supernatant was removed, fresh dH_2O was added to wash the eggs and the tubes were spun again at 2000 $\times$ g for 1 minute. Worms were seeded on fresh NGM plates, with approximately 100 eggs added per plate.

The plates were imaged using an EVOS brightfield microscope immediately, then every three hours for a total of nine hours. In between imaging, the plates were incubated at 20℃.

5.4.8 *In vivo* Toxicity Study

Potassium ferricyanide (FIC), potassium ferrocyanide (FOC) and pyrrole (Py) serial dilutions were made up in M9 buffer to make concentrations of 0.002, 0.02, 0.2, 2, 4, 10, 20, 50, 100, 200, [400, 1000 - pyrrole only] mM.

Worms were plated as described in Section 5.4.5 to give approximately 15 worms per 100 μL per well in a 96-well plate. 100 μL of chemical concentration was added in triplicate to the worms to give final concentrations of 0.001, 0.01, 0.1, 1, 2, 5, 10, 25, 50, 100, [200, 500 - pyrrole only] mM. A negative control of 100 μL M9, and a positive control of 100 μL of ethanol were added in triplicate, ensuring the positive control was on a different plate to the other conditions due to the ethanol vapour toxicity that has previously been recorded [347]. The number of live and dead worms per well was recorded immediately.

Plates were then incubated for 24 and 48 hours at 20℃, with the number of live and dead worms counted every 24 hours. Images of the worms in the wells were also obtained using an EVOS brightfield microscope.

5.4.9 Nematode Length Measurements

When the number of live/ dead worms was counted in Section 5.4.8, brightfield images of the worms were taken. These were then processed using ImageJ with the plugin Wormsizer [256] to determine the length of the worms. The magnifications used in the plugin were recorded in a spreadsheet as: 4 | 1 | 1.582278481 and 10 | 1 | 0.782013685. The threshold used was 'IsoData'. This approach only worked when worms were well separated; for overlapping worms, manual measurements were taken using the 'segmented' line tool down the central 'spine' of the worm. These values were then plotted using a violin plot.

5.4.10 *In vivo* Polymerisation of Pyrrole

5.4.10.1 Polymerisation for Visual Microscopy Analysis

Nematodes were first synced as described in Section 5.4.4 to obtain a synchronous adult population, then counted and added to a 96-well plate as described in Section 5.4.5. Approximately 10 worms were plated per well in dH_2O. Worms were either treated with polypyrrole (100 μg/ mL), pyrrole (500 mM), FIC (40 mM) or FOC (40 mM) as shown in Table 5.5. The plate was then incubated for 24 or 48 hours before wells were imaged using an EVOS brightfield microscope.

Table 5.5: Treatments of *C. elegans* for *in situ* polymeristaion of pyrrole. *Sample 1 = negative control i.e. untreated. Ppy = polypyrrole; Py = pyrrole; FIC = potassium ferricyanide; FOC = potassium ferrocyanide.

Sample	Ppy (100 μg/ mL)	Py (500 mM)	FIC (40 mM)	FOC (40 mM)
1*	-	-	-	-
2	X	-	-	-
3	-	X	X	-
4	-	-	-	X
5	-	X	-	-
6	-	X	-	X

5.4.10.2 Polymerisation for Raman Analysis

Nematodes were first synced as described in Section 5.4.4 to obtain a synchronous adult population, then counted as described in Section 5.4.5 and nematodes were added to a 1.5 mL Eppendorf tube so that the total volume with the treatment was 1 mL containing either 1000 nematodes (for the Ppy, FIC, FOC or Py samples) or 3000 nematodes (for the $Py_{500}FOC_{40}$ sample). The treatments given are shown in Table 5.5, with an additional treatment of just FIC (40 mM) also given. The tubes were incubated at 20℃ for 48 hours, then spun at 2000 $\times$ g for 2 minutes. Worms were washed with dH_2O three times, resuspending and then pelleting the worms between each wash to remove any treatment not internalised.

5.5 Tumour Treating Fields

5.5.1 Initial Well Plate Layout

GIN and GCE 31 cells were counted as described in Section 5.2.3 then seeded in a tissue culture-treated 12-well or 24-well plate at a density of either 0.7 or 0.09 x 10^5 cells per well respectively and incubated at 25℃ and 5% CO_2. A control of cells without TTFields was also seeded at the same time.

5.5.2 High Throughput 96-Well Design

5.5.2.1 TTField Experiments using the High Throughput System:

Cells were seeded in a cell culture-treated 96-well plate and incubated for 24 hours at 37℃ and 5% CO_2 to allow for cell attachment. Cell medium was replaced with complete DMEM, and the plate lid replaced with the TTField-modified lid. Cells were incubated at 25℃ for 4, 24 or 48 hours with electrical stimulation at 300 kHz and 3 V/ cm. After stimulation for the desired length of time, cell media was replaced with 10% PrestoBlue™ and incubated at 25℃ for 3 hours before being transferred to an opaque black 96-well plate. The fluorescence was recorded using the method in Section 5.2.5.

5.5.2.2 TTField Enhancement with Nanoparticles (Adherent Cells):

Cells were seeded in a cell culture-treated 96-well plate and incubated for 24 hours at 37℃ and 5% CO_2 to allow for cell attachment. Cell media was then replaced with media containing 5 μg/ mL ZnO NPs and incubated for 4

hours at 37℃ and 5% CO_2 to allow for cellular uptake. Media was replaced with complete DMEM and cells were electrically stimulated as described in the above section for 48 hours, then metabolic activity was determined as in Section 5.2.5.

5.5.2.3 TTField Enhancement with Nanoparticles (Semi-Adherent Cells):

Cells were seeded as above and incubated for 24 hours to allow for partial adherence. To prevent the removal of adherent cells, the plate was first spun at 123 × g for 5 min. The supernatant was then replaced with media containing 5 μg/ mL ZnO NP and cells were incubated as above. After 4 hours, the plate was spun at 123 × g for 5 min and the media was replaced with supplemented DMEM. Cells were electrically stimulated as described previously. After 48 hours, 10% PrestoBlue^{TM} was added to each well to determine the relative metabolic activity.

5.5.2.4 Combined Therapy - TTField and 'Reverse Prodrug':

Cells were seeded as above and incubated for 24 hours to allow for cell attachment. Cell media was then replaced with media containing either Ppy (5 μg/ mL), or Py (10 or 20 mM) and FOC (2 mM). Immediately, cells were electrically stimulated as described in above for 48 hours, then metabolic activity was determined as in Section 5.2.5. The full list of conditions is shown in Table 5.6

Table 5.6: Conditions used for tumour treating fields and 'reverse pro-drug' combined study. EF = electric field stimulation; TTField = tumour treating field.

	No EF	**+ TTField**	**+ Current**
No Treatment	X	X	X
Ppy (5 μg/ mL)	X	X	X
Py10FOC2	X	X	X
Py20FOC2	X	X	X

5.5.3 Tumour Treating Field Enhancement with Nanoparticles

5.5.3.1 System Setup:

The equipment used for this experiment are shown in Figure 5.3. Briefly, this consisted of a TTField generator, a base plate capable of housing eight ceramic dishes and lids. The base plate was connected to the generator using a flat rainbow cable, and the system was connected to a computer, where the TTField parameters could be adjusted.

5.5.3.2 TTField Enhancement with Nanoparticles:

Cells were counted on a haemocytometer using trypan blue exclusion and then seeded on tissue culture-treated coverslips (22 mm diameter) housed in a 6-well plate at a density of 0.02 x 10^6 cells/ mL (24-hour treatment time) or 0.04 x 10^6 cells/ mL (48-hour treatment time) in 500 μL supplemented DMEM. Cells were incubated for 24 hours at 37°C and 5% CO_2 to attach.

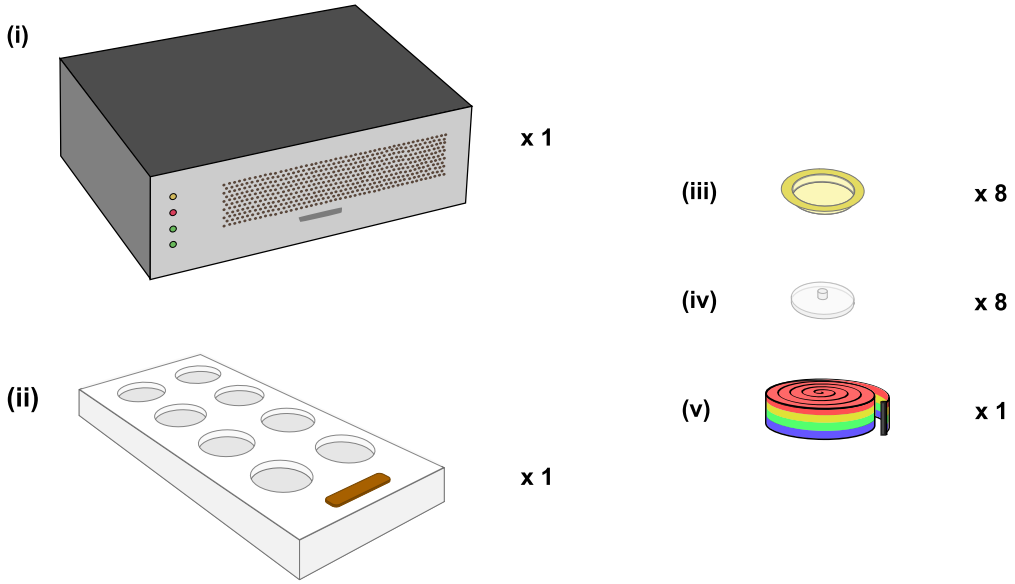


Figure 5.3: Novocure® Plate Layout.
(i) Generator; (ii) Inovitro™ base plate; (iii) ceramic dish and (iv) dish lid; (v) rainbow cable. Number of each components also shown.

ZnO, SiO_2, and Au NP suspensions were prepared in PBS and then added to supplemented DMEM to give a final concentration of 5 μg/ mL. The media on the coverslips was removed using a micropipette, the edges of the coverslip dried on a low-lint tissue, then the media was replaced with 400 μL of the nanoparticle-containing medium and the cells were incubated for 4 hours to allow for cellular nanoparticle uptake. This is illustrated in Figure 5.4.

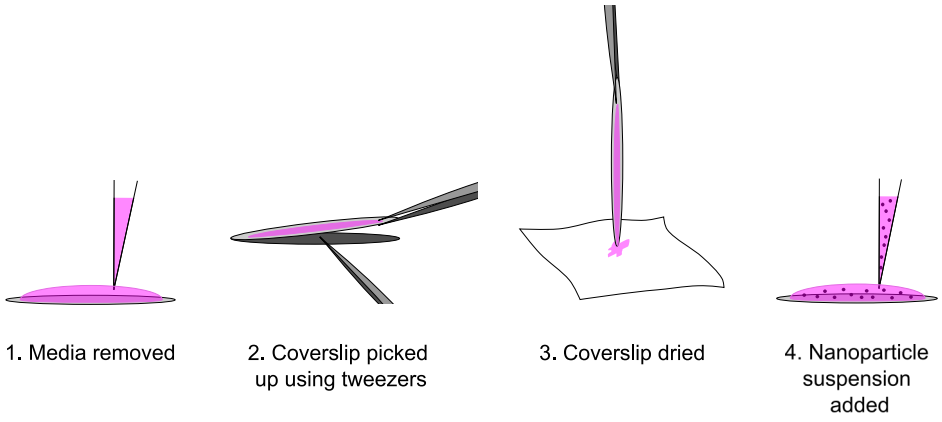


Figure 5.4: Schematic for the removal and NP replacement for cells on a coverslip.

The ceramic dishes and lids (Figure 5.3 (iii) and (iv)) were cleaned with 70% industrial methylated spirit then sterilised using UV for 15 minutes prior to use. The base plate was also wiped using 70% industrial methylated spirit just before use, then the ceramic dishes were mounted into the base plate.

After NP incubation was complete, the coverslips were removed from the 6-well plates using tweezers and transferred to the ceramic inovitro^{TM} dish. 1.5 mL of warmed, supplemented media was added to each dish to cover the cell-coated coverslips. A lid was placed on each dish and the plate was placed in an incubator set at 25℃ and 5% CO_2. Cells for the negative control (no TTFields or NPs) also had the media removed from the coverslip and 1.5 mL new media added to replicate the conditions of the TTField plate. This is illustrated in Figure 5.5). This plate was also added to the low temperature incubator. The rainbow cable was added to connect the inovitro^{TM} base plate to the generator, then the generator was switched on. The frequency was set to 300 kHz and 3 V/ cm. Cells were electrically stimulated for either 24 or 48 hours, with the culture medium replaced after 24 hours with 1.5 mL fresh, warmed, supplemented media to limit effects of media evaporation.

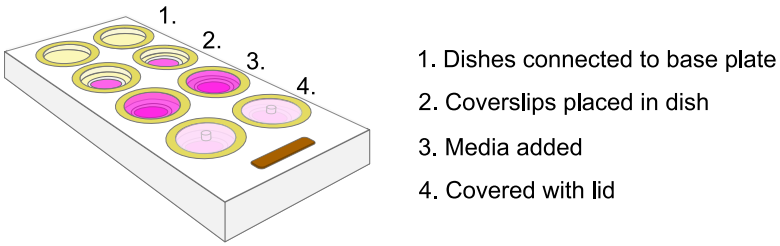


Figure 5.5: Schematic for using the ceramic dishes with the base plate and coverslips.

After the desired stimulation time, the generator was turned off and the base plate was disconnected. The media in each dish was removed, the edge of the coverslips were dried, then the coverslips were placed cell-side up into a sterile 6-well plate. Relative metabolism was determined as in Section 5.2.5, with minor adjustments. Cells were incubated with 400 μL diluted PrestoBlue^{TM} for 30 minutes, then the media was removed and mixed thoroughly in an Eppendorf before 100 μL was added to an opaque black 96-well plate in triplicate for each sample. Fluorescence measurements and calculations were performed as described previously. The conditions tested are shown in Table 5.7.

Table 5.7: Conditions tested for tumour treating field (TTField)-enhancement study.
Sample 1 was the negative (untreated) control.

Sample	TTField	Nanoparticle
1	-	-
2	X	-
3	X	X

5.6 Analytical Methods

5.6.1 Fourier Transform Infra-Red Spectroscopy

Crystalline samples were first ground into a fine powder using a pestle and mortar. Nanoparticles were air dried at 25℃ for 48 hours before measurement. The crystal of the Cary 360 Fourier transform infra-red spectrophotometer (Agilent Technologies Ltd.) was cleaned with an Azo 70% isopropyl alcohol wipe and left to dry. A background measurement was recorded before the samples were placed on the crystal and the transmittance was measured between 4000 to 400 cm^{-1}.

5.6.2 Ultraviolet-Visible Spectroscopy

Suspensions or solutions of the sample were made up in an appropriate medium, either deionised water or PBS as appropriate. The concentration of the solution was such that the maximum absorbance of the sample was 1 to fall within the limits of the Beer-Lambert law. Samples were added to a microcuvette (maximum volume of 1.5 mL) and the absorbance was measured against a blank of the same medium used to disperse the solution using a Cary 3500 UV-Vis (Agilent Technologies Ltd).

5.6.3 Dynamic Light Scattering

The hydrodynamic diameter (h_d) was measured on a Malvern Zetasizer Nano-ZS (Malvern Instruments, UK). The disposable folded capillary cell (DTS1070) was rinsed three times with diH_2O then dried using compressed air. The solution of interest was added to the cuvette using a syringe, avoiding bubble formation. The cuvette was inserted into the sample holder and the sample measured using the following parameters: Dispersant - water; temperature - 25℃; equilibration time = 120 s; measurement angle - 173° backscatter; automatic measurement duration; three measurements; 0 s between measurements.

5.6.4 Zeta Potential

The cuvette was prepared and sample filled as in Section 5.6.3. The cuvette was inserted into the sample holder and the sample measured using the following parameters: Dispersant - water; F(Ka) model - Smoluchowski; temperature - 25℃; equilibration time = 120 s; automatic measurement duration; three measurements; 0 s between measurements.

5.6.5 Solid State Nuclear Magnetic Resonance

This work was carried out with Dr Huw Williams (School of Chemistry, University of Nottingham). Samples were either analysed on a Bruker Advance III HD 600 MHz or 800 MHz spectrophotometer at room temperature. Spectra were calibrated to adamantane, with all signals referenced to the downfield carbonyl peak at 173.5 ppm. For samples run using the 600 MHz spectrophotometer, a Larmor frequency of 150.8 MHz using a 3.2 mm probe at a spin rate of 15 kHz was employed. The ^{13}C $\pi/2$ pulse duration was 4.0 μs, spectral width was 45.4 kHz, acquisition time was 18 ms, and 90112 scans were run. For samples run using the 600 MHz spectrophotometer, a Larmor frequency of 201.3 MHz using a 2.5 mm MAS probe at a spin rate of 18 kHz was used. the ^{13}C $\pi/2$ pulse duration was 3.6 μs, spectral width was 82 kHz, acquisition time was 38 ms, and 32768 scans were run.

5.6.6 Raman Spectroscopy

This work was carried out with Dr Graham Rance (Nanoscale and Microscale Research Centre, University of Nottingham). Spectra were acquired with either a HORIBA LabRAM HR upright microscope with 200 μm hole and a grating of 300 lines/ mm between 410 and 1800 cm^{-1} or a HORIBA XploRA INV inverted microscope with a 300 μm hole and a grating of 600 lines/ mm between 200 - 3600 cm^{-1}. A 785 nm laser was used with a grating of 300 lines/ mm. Before measurements were obtained, the instruments were calibrated using the Rayleigh line at 0 cm^{-1} and a standard Si (100) reference band at 520.7 cm^{-1}. A laser power of 0.1 - 100% was used. Samples were placed on a quartz microscope slide and left to dry for 48 hours prior to imaging. Toxic samples were imaged through a glass vial.

Intensity maps were carried out using the HORIBA XploRA INV inverted microscope with a grating of 600 lines/ mm using a 785 nm laser. Spectra were collected between 200 and 2600 cm^{-1} over an area of 10 $\times$ 10 μm with a grid spacing of 1 μm steps along both the x and y axes for a total of 121 spectra per map. Each spectrum was collected for four seconds and was repeated once to give a total acquisition time of approximately 17 minutes. The height intensity of the desired bands and corresponding intensity ratios were determined within the mapped cross-sectional area. Representative spectra were extracted for comparison. This was run at 100% laser power.

To map the location of Ppy across the surface of a nematode, the intensity of a known Ppy band was plotted in one of two ways. The first way was using univariate analysis (**UVA**), where intensity was plotted as a function of spatial location. The second way was using multivariate analysis (**MVA**), specifically multivariate curve resolution (**MCR**), where a two component model was applied to the optical image. The first loading corresponded to the Ppy, and the second loading to the background substrate. The combined loading scores were then normalised to 100% to generate individual maps. These were then overlaid onto an optical image of the nematode, and a heat map showing maximum signal intensity of Ppy was produced. Raman spectroscopic analysis was carried out at 785 nm and 0.1% power. A grating of 600 lines/ mm was used with a 200 μm slit and 300 μ hole. The spectra were taken at 20 $\times$ magnification, with a four second acquisition time over a 80 $\times$ 180 μm grid in 2 μm steps for a total of 3731 images. Total acquisition time was approximately 4 hours and 30 minutes.

5.6.7 Scanning Electron Microscopy

This work was carried out with Lorelei Robertson (Nanoscale and Microscale Research Centre, University of Nottingham). One drop of filtered Ppy solution was placed in a stub and left to air dry for 48 hours. This was then sputter coated with 10 μm Iridium using a turbo sputter and carbon coater (Quorum Q150TES), before imaging the sample using a 7100F FEG-SEM scanning electron microscope (Jeol Ltd.) with a 5 kV power supply.

5.6.8 Transmission Electron Microscopy

This work was carried out with Dr Michael Fay (Nanoscale and Microscale Research Centre, University of Nottingham). The stock nanoparticle solution was diluted 1:10 with dH_2O, then 10 μL of the sample was combined with 40 μL dH_2O and ultrasonicated 3 minutes to disperse particles and decreases agglomeration. 3 μL was then drop dispersed onto an appropriate grid (See Table 5.8). After five seconds, excess liquid was wicked off using filter paper. The sample was pre-pumped for five minutes to ensure it was completely dry before loading into a JEOL 2100 Plus transmission electron microscope (Jeol, Ltd.). Average particle diameter was measured using ImageJ.

Table 5.8: Grids used for TEM analysis of nanoparticles.

NP	Grid	Code	Company
Au	Carbon-coated copper (400 mesh)	AGS160	Agar Scientific
SiO_2	Amorphous Carbon (300 mesh)	C300Cu25	EM Resolutions
ZnO	Graphene Oxide on Holey Carbon (300 mesh)	GOHC300Cu50	Electron Microscopy Sciences

5.7 Statistical Analysis

All analysis was carried out using GraphPad Prism 10.3.1, with an appropriate statistical test used. Tests used: One-way ANOVA, two-way ANOVA and T-test. Significance was confirmed and represented by the following values: *P = 0.0332; **P = 0.0021; ***P = 0.0002; ****P < 0.0001.

5.8 Software

All graphs were plotted using using GraphPad Prism 10.3.1. Image analysis was performed using FIJI 2.16.0, an image processing package distribution of ImageJ2. All graphics were produced with Inkscape 1.0.2-2 or BioRender.com. The thesis was written using LaTeX.

Chapter 6

Future Work and Perspectives

This thesis has laid the foundation for investigating the combination of cell-induced polymerisation with tumour treating field (**TTFields)** stimulation as a dual approach to treat cancer. To first achieve this, polypyrrole (**Ppy**) was synthesised *in situ* and characterised using an *in vitro* model. Following this, polymer synthesis in an *in vivo* model was explored, showing the formation of Ppy in *Caenorhabditis elegans* (***C. elegans***) for the first time. Lastly, coupling this with TTFields was examined, and a combination approach of electric field (**EF**) stimulation with the 'reverse prodrug' had a significant effect on cell behaviour. Concluding remarks of each chapter and future directions of research are discussed in the next sections.

6.1 Polypyrrole Can Be Synthesised Using Adherent Cells

The aim of this chapter was to better understand the 'reverse prodrug' approach. This is where a toxic monomer is given to cells, inducing cell death then subsequently being inactivated to a biocompatible polyomer.

The first objective was to identify the most suitable analytical techniques for Ppy analysis in what is an inherently uncontrolled system. By utilising a range of different methods of purification and characterisation, solid state nuclear magnetic resonance (**NMR**) was found to be the most suitable approach. The formation of Ppy was successfully demonstrated by combining one of two adherent cell lines, 'Glioma INvasive margin' (**GIN**) 31 and 'Glioma Core Enhanced' (**GCE**) 31 with the inactive Fe (II) complex potassium ferrocyanide (**FOC**) and the monomer pyrrole. While this mechanism is not fully understood, this is hypothesised to be initiated by components in cellular exudate that converts Fe (II) to Fe (III), driving the polymerisation reaction.

The second objective was to investigate the toxicity of the starting materials on the two cell types. From this, optimum concentrations were determined: a non-toxic range of FOC was selected, and a concentration of pyrrole that induced some toxicity was chosen as hypothesised to initiate the polymerisation.

The toxicity was further evaluated using flow cytometry to explore the mechanism of cell death through either apoptosis or necrosis. Differences in the response to treatment were seen between the two cell lines, highlighting the potential to optimise this treatment to target different cells.

Combining both pyrrole and FOC induced less toxicity than the monomer alone suggesting that a 'reverse prodrug' approach is possible. This approach is where the toxic monomer can be polymerised to a biocompatible polymer. Future work should focus on optimising the parameters of this polymerisation reaction to more effectively treat the cancer cells remaining after surgical resection.

As the 'reverse prodrug' approach also relies on the inactivation of pyrrole as it is converted to Ppy, it is important to investigate the best ratio of pyrrole to FOC (Fe (II)). To initiate the polymerisation, Fe (II) must first be oxidised to Fe (III), with this conversion potentially limiting the rate of polymerisation [348]. As such, future work should first focus on understanding the rate of oxidation of Fe (II) in glioblastoma cells in both the presence and absence of pyrrole. Previous work in the Rawson Group has used linear sweep voltammetry to identify the concentration of iron in both the (II) and (III) oxidation states. Therefore, it is recommended that this technique is used to shed more light onto the changes in the ratios between these two oxidation states [348, 349].

Once the maximum concentration of Fe (III) in the system has been determined, future work should then be carried out to assess the most-suitable concentration of pyrrole and the rate of this reaction using ^{1}H NMR as described by Tan *et al.* [130]. Both of these features are important to know as they dictate the amount of polymer formed and the optimum treatment time for this cell-mediated polymerisation approach.

To answer questions about the internalisation of the resulting Ppy within living cells, impedance of the cells should be assessed to identify any decrease in current resistivity, which would indicate the conductive material is located within the cells [350]. Determining if conductive material is internalised would

also assist with understanding how TTFields could be combined with cell-induced polymerisation as a dual approach to treat cancer.

6.2 *C. elegans* Can Generate Polypyrrole *In Situ*

Following on from the cell-induced polymerisation approach, the application of this in an *in vivo* setting was assessed using *C. elegans* as a model organism. While there has been some research investigating the polymerisation of other materials within *C. elegans*, this is the first time Ppy has been made *in situ* in these nematodes.

In this work, the methods for analysing polymer formation were optimised, within initial observations using a brightfield microscope showing distinct morphological differences across different samples of nematodes treated first with the individual starting materials. From this, evidence of toxicity was seen at high concentrations of pyrrole (500 mM), causing the breakdown of lipid-containing fat deposits and disruption of other internal organs such as the intestinal tract. Lower concentrations of pyrrole also influenced nematodes, resulting in changed patterns of movement, such as body twitches and slowed locomotion at a concentration of greater than or equal to 10 mM. Changes to the morphology or locomotion of worms treated with FOC (Fe (II)) up to 100 mM were not observed.

In a previous study, Ppy nanoparticles were imaged within the intestinal tract of the nematodes [244]. The study provided the template for the imaging of internalised polymer in this work, here showing that non-formulated Ppy can be observed within the nematodes. While polymer was visible here, it was

only found in the posterior region of the nematode, indicating that within 24 hours the polymer had already passed through much of the intestine.

To improve characterisation of the polymer formed, Raman spectroscopy was chosen due to its compatibility with *C. elegans* [245]. This work showed the distribution of iron (II) and (III) varied significantly within the nematodes, with Fe (III) far more homogeneous across the sample, while Fe (II) only appeared in highly localised pockets. Within the Fe (III) sample, evidence of reduced Fe (II) was observed in the Raman spectrum, indicating the redox capabilities of the *in vivo* model without external stimuli.

To study the potential for *C. elegans*-initiated redox of iron, future work could investigate using a time-based study to map the intensity of Fe (II) and Fe (III) peaks following treatment. The ratio of Fe (II) to Fe (III) could then be plotted to see changes to the oxidation states *in situ*. This would provide a mechanistic understanding into the conversion of the inactive iron initiator to the active form before the polymerisation occurs. It is hypothesised that the iron initiator should be given before the monomer to allow for internalisation and oxidation to Fe (III), encouraging polymerisation within the nematode. By studying the length of time for the maximum conversion of Fe (II) to Fe (III), the optimum time between dosing with Fe (II) and pyrrole could also be identified.

After identifying the toxicity of the starting materials, a lower concentration of pyrrole and FOC (Fe (II)) were chosen to investigate the polymerisation using viable living nematodes. Thus, concentrations of 20 mM pyrrole and 2 mM FOC (in line with the concentrations identified in Chapter 2) were selected. Despite there being no significant change in the percentage of worm survival, those treated with pyrrole were smaller, indicating some developmental arrest. Before characterisation of the polymer within *C. elegans* using Raman is pos-

sible, it will be necessary to first optimise the ratio of iron to pyrrole, as any pyrrole not polymerised has been shown to fluoresce and mask the presence of any Raman peaks attributed to Ppy.

Another parameter to assess the polymerisation of pyrrole within *C. elegans* is to monitor changes to the impedance of the worms. This approach was previously carried out by Chen *et al.* to identify the stage of the nematode in the lifecycle based on the alterations in impedance caused by different worm lengths [351]. As Ppy is a conductive material, the hypothesis of this approach is that nematodes containing the polymer will have a reduced impedance compared to negative control worms allowing for change in the conductivity of the worms to indicate the presence of the polymer formed.

To investigate the use of *C. elegans* as a model organism for optimising cancer therapies, two mutants were selected due to their relevance to cancer (*TP53* homologue, *cep-1*, knockout and H3.3 mutation, *his-72*). Changes to the development and acute toxicity were assessed over 48 hours to as an indication for the toxicity of the starting materials on the mutant models. This work showed that, as with the Bristol N2 wild type nematodes, there was no significant effect on the proportion of viable worms over 48 hours, but that development was once again inhibited by the presence of pyrrole at a concentration of 20 mM. As the *TP53* homologue in nematodes, *cep-1*, causes changes in response to non-ionising radiation, given that this treatment was not used here there, effects due to the mutation would not be observed. It is therefore of interest to identify changes to the genome for the wild-type and mutant worms in response to the *in-situ* polymerisation. The ultimate aim for this cell or organism-induced polymerisation was to couple it with the tumour treating fields as a dual approach to treat cancer. Therefore, future work should also investigate changes to the gene expression in nematodes treated with TTFields

in the presence and absence of both pre-formulated and synthesised polymer *in situ*.

6.3 Tumour Treating Fields Can Be Enhanced

In this chapter, the overarching objective was to identify approaches to enhance the effects of TTFields, either using inorganic nanoparticles or the 'reverse prodrug' polymer.

First, the design of a TTField platform was investigated. An initial setup was prepared using blunted electrodes coated in a dielectric ink to insulate the wire. While evidence of an effect on cell viability could be observed, high intra-experiment variability led to the decision to investigate using a more robust system to generate TTFields. A modified setup consisting of fixed electrode position within each well reduced the potential for electrodes to move during the experiment, and electrode variation was limited to the thickness of the epoxy resin at the tip of each copper wire insulated electrode.

Initial experiments testing the efficacy of the system on adherent cells showed no difference in cell viability after 4 - 48 hours TTF application time. It was hypothesised that the lack of effect was because there could be a small number of cells in the correct orientation. To test this hypothesis, the semi-adherent medulloblastoma cell line, D425, was used. Here the metabolic activity greatly increased when TTFields were applied, but decreased when conductive electrodes were used, allowing the movement of ions within the system.

This work highlights the importance of designing a system that can target the more of the cell population, and so a dual electrode pair setup is preferred

for TTField stimulation. As the optimum frequency of the electric fields has a pronounced effect on the efficacy of the system, to improve this system it would be necessary to carry out a frequency scan, testing the cytotoxicity of increasing frequency between 100 - 400 kHz. The intensity applied could also be easily investigated between 1 - 4 V/ cm.

It was hypothesised that the dual approach of TTFields and cell-induced polymerisation may enhance the effects seen by TTFields. To test this, cells were treated with either no electrical stimulation, electric fields or electric currents and either no treatment, commercial Ppy or the starting materials of the cell-induced polymerisation in Chapter 2. No significant difference was observed when using the commercial polymer with either TTField or current stimulation. There was also no observed effect of the lower concentration of 'reverse prodrug' when combined with either TTFields or currents. However, when the higher concentration of pyrrole and FOC (Fe (II)) were combined with electric currents, there was a significant decrease in metabolic activity compared to currents or starting material treatment alone. This shows that the combined treatment had a significant effect on the cells. As this effect was not seen when electric fields were applied, the cause must be attributed to the movement of conductive materials within the culture medium and cells.

To further evaluate this hypothesis, there are a few different avenues to investigate. Firstly, a positive polymer control of Ppy nanoparticles should be used as a treatment method. This will allow for effects from internalised polymer combined with electric field or current application to be more easily assessed and compared to the 'reverse prodrug'. It is unclear from this work whether the effects are from the formation of the polymer extracellularly or intracellularly. To test for this, the cells should be first treated with the cell-mediated polymerisation starting materials, then after a period of incubation to allow

for the polymerisation to occur, the culture medium should be replaced prior to electrical stimulation. By removing any material outside of the cells effects due to material internalisation could be investigated.

To better understand the mechanism of action of TTFields, inorganic nanoparticles were used as TTField enhancers. A range of conductivities and charges were required, so as such, three nanoparticles with varying physicochemical properties were selected (gold - conductive, negatively charged; zinc oxide - semi-conductive, negatively charged; silicon dioxide - insulator, positively charged). When all three particles were used at a non-toxic concentration with TTFields, there was a significant decrease in metabolic activity of the cells. This shows that nanoparticles can be enhance the effect of TTFields. It is hypothesised that this is due to dipole alignment and dielectrophoresis. The effect was amplified when a higher concentration of gold nanoparticles was used.

To better understand how both the organic *in situ*-generated Ppy and the inorganic NPs influence TTFields, computational modelling using a multiphysics software such as COMSOL Multiphysics® should be used. This could be coupled with the experimental data generated in this work to provide clarity on changes in electric field strength when enhancing TTFields.

While this work suggests that in an *in vitro* model TTFields can be enhanced using nanoparticles, it is important to consider this in the context of clinical delivery of the therapy. In clinic, TTFields are always given alongside the chemotherapeutic temozolomide (TMZ) [66]. Therefore, this enhancement needs to be compared to using TMZ both with and without TTFields to assess its potential as a clinical treatment to enhance TTFields.

6.4 Final Conclusions

This thesis has investigated a combined cell-mediated polymerisation of pyrrole with TTField as a potential dual-approach to treat cancer.

The 'reverse prodrug' approach inactivating the toxic monomer to the biocompatible, conductive material, PPy, both *in vitro* in two adherent cell lines, and *in vivo* in a *C. elegans* model has been shown. From this work, understanding methods to characterise the polymer in complex environments has been determined, and effects of the starting material and 'reverse prodrug' on two glioblastoma cell lines have been established.

Significantly, the first known example of using *C. elegans* to generate Ppy has also been shown. This move to a simple model organism will allow for more research into the *in vivo* polymerisation instead of more complex systems with considerable ethical and experimental challenges. By utilising mutated *C. elegans* strains, there is opportunity to assess how this *in vivo* 'reverse prodrug' polymerisation could affect genetic pathways found in cancer. The cancer models could also provide valuable insight into ways that TTF enhancement could impact on the genetic profile of glioblastoma or other hard-to-treat-cancers.

This work has also investigated the enhancement of TTFields using inorganic nanoparticles and the organic Ppy synthesised through the above 'reverse prodrug' approach. A variety of routes could be employed that are either already approved by the United States Food and Drug Administration, or could be used as a new therapeutic modality in the treatment of cancer.

By identifying ways to enhance TTFields, specifically when combined with the 'reverse prodrug' approach, this work lays the foundations for further research into improving clinical treatments for cancer.

Appendix A

Introduction

The table on the following page (Table A.1) details a complete list of clinical trials between 2019 - 2024 (excluding trials that were withdrawn) that have used a device-based approach for treatment of glioblastoma (**GBM**).

Table A.1: **List of clinical trials (ClinicalTrials.gov) in the past five years using a device-based treatment for GBM.**

Treatment	Therapy	Drug	Description	Phase	Ref
Radiotherapy	GammaTile®	N/A	Caesium-131 seeds in a collagen tile permanently implanted at the tumour site.	IV	[352]
	TheraSphere GBM Y-90	N/A	Yttrium-90 glass microspheres used for targeted radiotherapy. 40 Gy ± 10%	I	[52]
Phototherapy	Intraoperative Photodynamic Therapy (**PDT**)	5-ALA HCl	PDT at 200 - 400 J/ cm^2	I/ II	[353]
			PDT at 400 - 800 J/cm^2	II	[354]
Thermotherapy	Laser Interstitial Thermal Therapy (**LITT**)	N/A	MR-Guided Laser Thermal ablation of brain lesions using the TRANBERG® Thermal Therapy System and TRANBERG® Thermoguide Workstation.	Pilot	[355]
		N/A	LITT followed by hypo-fractionated radiation therapy, 35 Gy/ 10 fractions.	Pilot	[356]
	NanoTherm® Therapy	Iron oxide nanoparticles (**NPs**)	Treatment with NPs and a variable magnetic field in induce hyperthermia of cancer cells.	N/A	[357]

Table A.1: **List of clinical trials (ClinicalTrials.gov) in the past five years using a device-based treatment for GBM.** (Continued)

Treatment	Therapy	Drug	Description	Phase	Ref
Ultrasound	SonoCloud-9 (SC9)	Liposomal doxorubicin + balstilimab + botensilimab	Ultrasound to induce blood-brain barrier (**BBB**) opening + cocomitant chemotherapeutic treatment.	II	[358]
		Albumin-bound paclitaxel + carboplatin		I/ II	[359]
		Carboplatin		III	[360]
	Exablate Model 4000	Carboplatin	Microbubbles and ultrasound used to dirsrupt BBB. Combined with chemotherapy.	I/II	[361, 362]
	CV011	5-ALA	Sonosensitiser used alongside ultrasound.	I	[363]
	NaviFUS	N/A	Combination of focused ultrasound with re-irradiation using stereotactic radiosurgery or conventional radiotherapy.	Pilot	[364]
		Bevacizumab	Microbubbles and ultrasound used to dirsrupt BBB. Combined with a targeted therapeutic.	II-III	[365–367]
	SonoFIRST	Temozolomide (**TMZ**)	Ultrasound to induce BBB opening and cocomitant chemotherapeutic treatment.	II	[368]

Table A.1: **List of clinical trials (ClinicalTrials.gov) in the past five years using a device-based treatment for GBM.** (Continued)

Treatment	Therapy	Drug	Description	Phase	Ref
Magnetic Fields	OncoMAGNETX	N/A	Exposure-time study using a portable non-invasive magnetic device.	Pilot	[369]
	Electromagnetic fields	N/A	Stupp protocol combined with radiofrequency electromagenetic field treatment (13.56 MHz).	N/A	[370]
Electric Fields	TDS-IM v 2.0 electroporation device	Personalized Neoantigen DNA vaccine + Retifanlimab	Immunotherapy given by electroporation-mediated intramuscular injection.	I	[371]
	ASCLU-300 Tumor Electric Fields Treatment System	N/A	Two pairs of electrodes worn for 19-22 h per day for 6 months to assess efficacy of TTFields on recurrent GBM.	I	[372]

Table A.1: **List of clinical trials (ClinicalTrials.gov) in the past five years using a device-based treatment for GBM.** (Continued)

Treatment	Therapy	Drug	Description	Phase	Ref
Electric Fields	Optune®	Tislelizumab/ pembrolizumab + TMZ	TTField treatment with chemotherapy and monoclonal antibodies.	II/ III	[96, 97]
		Pembrolizumab + lenvatinib	TTFields + immunotherapy + targeted cancer therapy.	I/ II	[98]
		Niraparib	TTFields + targeted cancer therapy.	II	[373]
		N/A	Preoperative/ preradiotherapy TTFields.	I	[99]
		N/A	TTFields + cocomitant radiotherapy.	II	[100]
		N/A	Increased number of ceramic discs to increase field intensity.	II	[374]

Appendix B

Cell-Induced Polymerisation

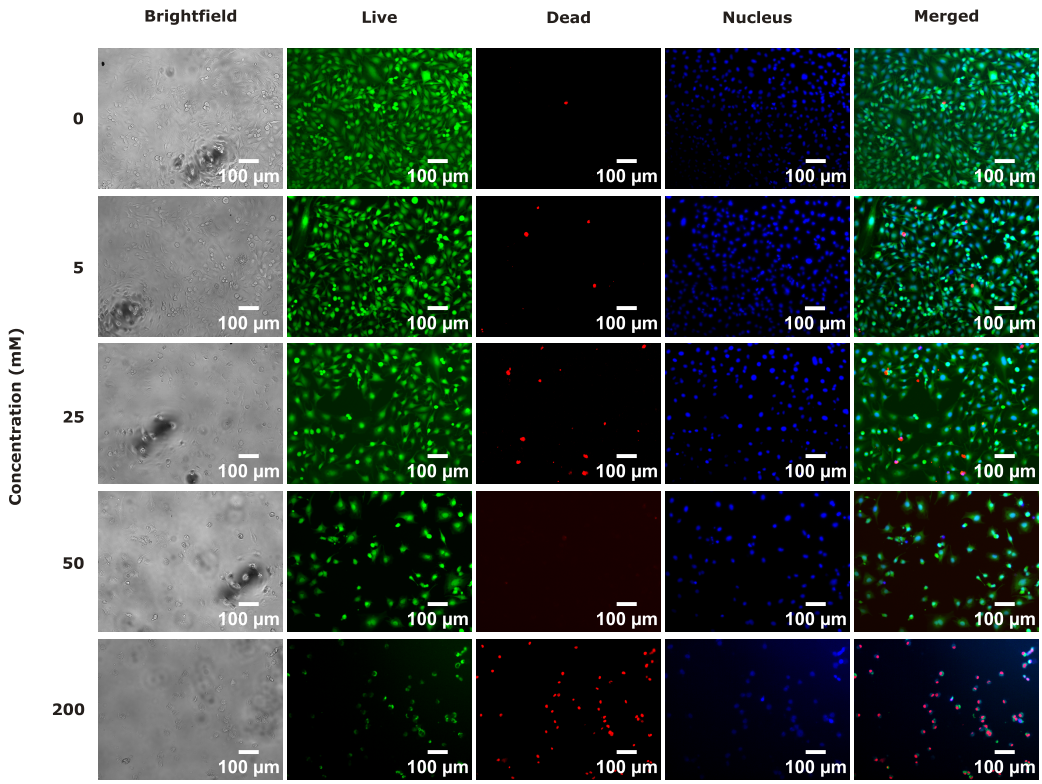


Figure B.1: Live/ dead staining of GIN 31 cells exposed to increasing concentrations of pyrrole.
Cell viability assessed 48-hours post-treatment. Scale bar 100 μm. Independent channels (brightfield, live, dead, nuclei shown separately and merged. Live (green fluorescence; Calcein AM), dead (red fluorescence; propidium iodide) and nuclei (blue fluorescence; Hoeschst 33342).

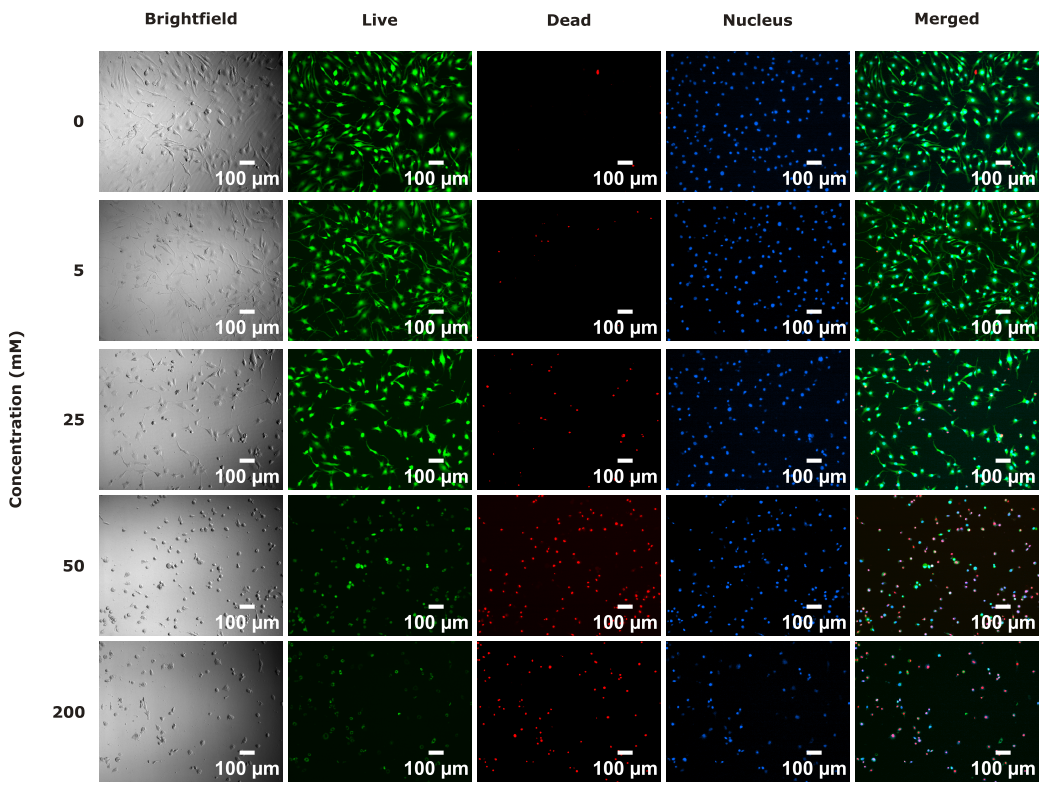


Figure B.2: Live/ dead staining of GCE 31 cells exposed to increasing concentrations of pyrrole.
Cell viability assessed 48-hours post-treatment. Scale bar 100 μm. Independent channels (brightfield, live, dead, nuclei shown separately and merged. Live (green fluorescence; Calcein AM), dead (red fluorescence; propidium iodide) and nuclei (blue flurescence; Hoechst 33342).

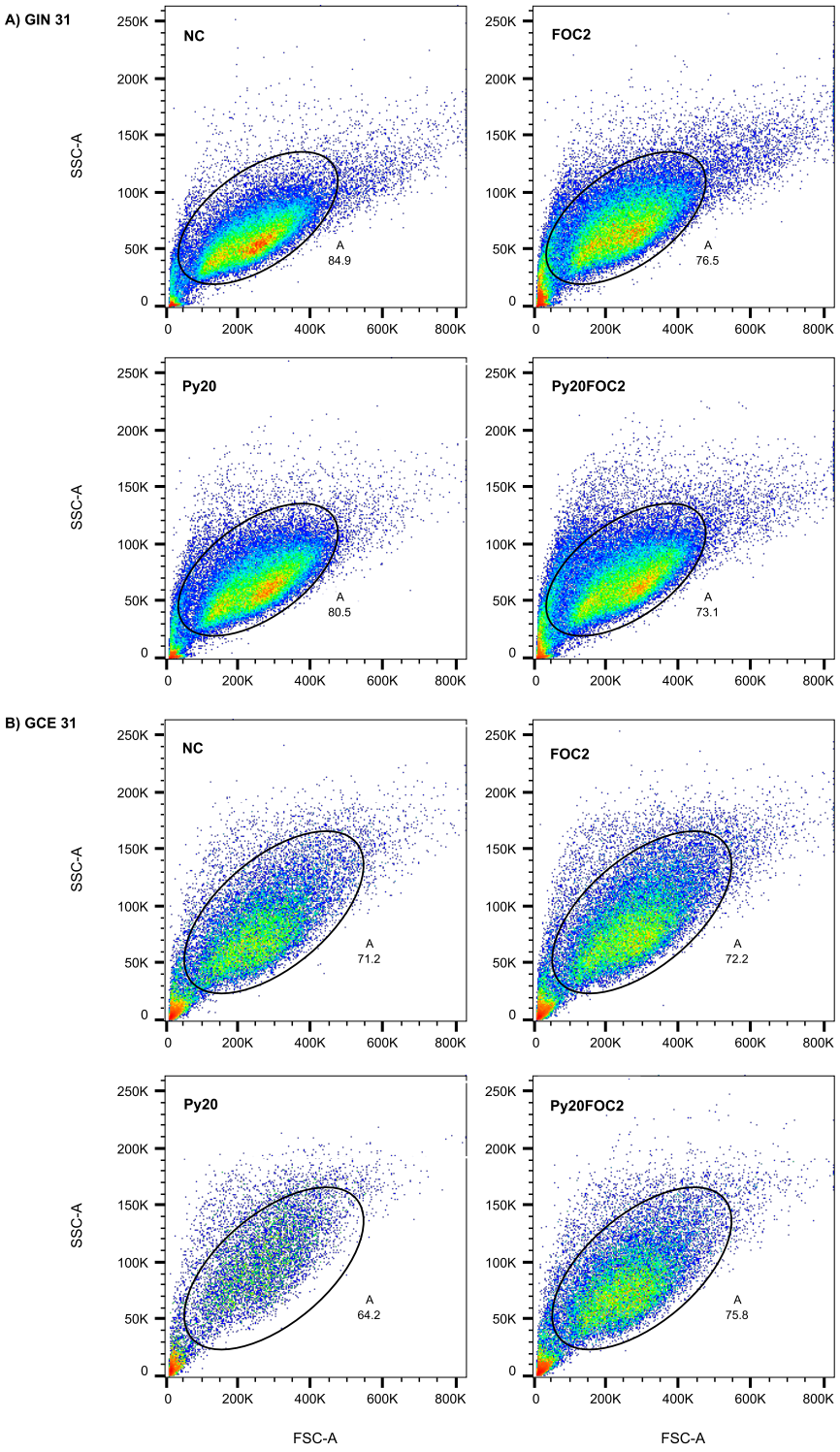


Figure B.3: Example flow cytometry gating of cell events (FSC v SSC). (A) GIN 31 and (B) GCE 31 gating.

Appendix C

Polymerisation of Pyrrole in Living Systems

Table C.1: Assignment of pyrrole Raman peaks from Figure 3.4

Wavenumber (cm^{-1})	Assignment
3135.78	C-H stretch
3107.57	C-H stretch
3054.57	C-H stretch
1468.68	C-H bend
1416.11	C–N stretch N–H bend (in plane)
1382.14	C-C stretch
1237.13	C–H bend (in plane)
1200.63	Ring breathing
1145.42	Ring breathing
1076.73	C–H bend (in plane)
1047.86	C–H bend (in plane)
868.51	Ring deformation
841.57	C–H bend (out of plane)
558.77	N–H bend (out of plane)

Table C.2: Assignment of ferrocyanide (Fe (II)) and ferricyanide (Fe (III)) Raman peaks from Figure 3.5. Values previously reported in brackets [272]; ** indicates only one band observed in this work.

Compound	Raman Shift (cm^{-1})		Vibration Mode
	Solid	Solution	
$Fe(CN)_6]^{4-}$	2065 (2131)	2058 (2129)	E_g
	2092 (2136)	2092 (2135)	A_{1g}
$Fe(CN)_6]^{3-}$	2126 (2063)	2130** (2062)	E_g
	2132 (2094)	2130** (2098)	A_{1g}

Table C.3: Assignment of *C. elegans* peaks in Figure 3.8.
Wavenumber in brackets from [277]. Structure: d, DNA/ RNA; l, lipid; p, protein.

Wavenumber (cm^{-1})	**Assignment**	**Structure**
664 (667)	G,T	d
721 (720)	Choline; A	l; d
780 (785)	U,T,C + (O-P-O)	d
820 (811)	O-P-O	d; l
855 (853)	Tyrosine	p
939 (936)	C-C	p
996 (1004)	Phenylalanine	p
1029 (1032)	Phenylalanine	p
1084 (1094, 1100)	PO_2^-	d
1120 (1125)	C-N; C-C	p; l
1315 (1300)	CH_2	l
1334 (1320)	G; CH deformation	d; p
1450 (1450)	CH deformation	p; l
1572 (1577)	A, G	d
1662 (1655∼1685)	Amide	p

Bibliography

[1] Cancer Research UK, "Brain, other CNS and intracranial tumours incidence statistics," 2024. [Online]. Available: https://www.cancerresearchuk.org/health-professional/cancer-statistics/statistics-by-cancer-type/brain-other-cns-and-intracranial-tumours/incidence

[2] A. Brodbelt, D. Greenberg, T. Winters, M. Williams, S. Vernon, and V. P. Collins, "Glioblastoma in England: 2007–2011," *European Journal of Cancer*, vol. 51, no. 4, pp. 533–542, 2015. [Online]. Available: https://doi.org/10.1016/j.ejca.2014.12.014

[3] Q. T. Ostrom, M. Price, C. Neff, G. Cioffi, K. A. Waite, C. Kruchko, and J. S. Barnholtz-Sloan, "CBTRUS Statistical Report: Primary Brain and Other Central Nervous System Tumors Diagnosed in the United States in 2015–2019," *Neuro-Oncology*, vol. 24, no. Supplement_5, pp. v1–v95, 2022. [Online]. Available: https://doi.org/10.1093/neuonc/noac202

[4] H. A. Wanis, H. Møller, K. Ashkan, and E. A. Davies, "The incidence of major subtypes of primary brain tumors in adults in England 1995-2017," *Neuro-Oncology*, vol. 23, no. 8, pp. 1371–1382, 2021. [Online]. Available: https://doi.org/10.1093/neuonc/noab076

[5] Q. T. Ostrom, M. Price, C. Neff, G. Cioffi, K. A. Waite, C. Kruchko, and J. S. Barnholtz-Sloan, "CBTRUS Statistical Report: Primary Brain and Other Central Nervous System Tumors Diagnosed in the United States in 2016—2020," *Neuro-Oncology*, vol. 25, no. Supplement_4, pp. iv1–iv99, 2023. [Online]. Available: https://doi.org/10.1093/neuonc/noad149

[6] D. Hanahan, "Hallmarks of Cancer: New Dimensions," *Cancer Discovery*, vol. 12, no. 1, pp. 31–46, 2022. [Online]. Available: https://doi.org/10.1158/2159-8290.cd-21-1059

[7] D. S. Noroxe, H. S. Poulsen, and U. Lassen, "Hallmarks of glioblastoma: a systematic review," *ESMO Open*, vol. 1, no. e000144, pp. 1–9, 2017. [Online]. Available: https://doi.org/10.1136/esmoopen-2016-000144

[8] L. M. Coussens and Z. Werb, "Inflammation and cancer," *Nature*, vol. 420, no. 6917, pp. 860–867, 2002. [Online]. Available: https://doi.org/10.1038/nature01322

[9] H. E. Marei, A. Althani, N. Afifi, A. Hasan, T. Caceci, G. Pozzoli, A. Morrione, A. Giordano, and C. Cenciarelli, "p53 signaling in cancer progression and therapy," *Cancer Cell International*, vol. 21, no. 1, pp. 1–15, 2021. [Online]. Available: https://doi.org/10.1186/s12935-021-02396-8

[10] M. Hollstein, D. Sidransky, B. Vogelstein, and C. C. Harris, "p53 mutations in human cancers," *Science*, vol. 253, no. 5015, pp. 49–53, 1991. [Online]. Available: https://doi.org/10.1126/science.1905840

[11] H. Saman, S. S. Raza, S. Uddin, and K. Rasul, "Inducing Angiogenesis, a Key Step in Cancer Vascularization, and Treatment Approaches," *Cancers*, vol. 12, no. 5, p. 1172, 2020. [Online]. Available: https://doi.org/10.3390/cancers12051172

[12] D. Hanahan and Robert, "Hallmarks of Cancer: The Next Generation," *Cell*, vol. 144, no. 5, pp. 646–674, 2011. [Online]. Available: https://doi.org/10.1016/j.cell.2011.02.013

[13] J. D. Henson, A. A. Neumann, T. R. Yeager, and R. R. Reddel, "Alternative lengthening of telomeres in mammalian cells," *Oncogene*, vol. 21, no. 4, pp. 598–610, 2002. [Online]. Available: https://doi.org/10.1038/sj.onc.1205058

[14] M. A. Blasco, "Telomeres and human disease: ageing, cancer and beyond," *Nature Reviews Genetics*, vol. 6, no. 8, pp. 611–622, 2005. [Online]. Available: https://doi.org/10.1038/nrg1656

[15] Z. E. Stine, Z. T. Schug, J. M. Salvino, and C. V. Dang, "Targeting cancer metabolism in the era of precision oncology," *Nature Reviews Drug Discovery*, vol. 21, no. 2, pp. 141–162, 2021. [Online]. Available: https://doi.org/10.1038/s41573-021-00339-6

[16] M. Neagu, C. Constantin, I. D. Popescu, D. Zipeto, G. Tzanakakis, D. Nikitovic, C. Fenga, C. A. Stratakis, D. A. Spandidos, and A. M. Tsatsakis, "Inflammation and metabolism in cancer cell—mitochondria key player," *Frontiers in Oncology*, vol. 9, no. 348, 2019. [Online]. Available: https://doi.org/10.3389/fonc.2019.00348

[17] S. K. Kim and S. W. Cho, "The Evasion Mechanisms of Cancer Immunity and Drug Intervention in the Tumor Microenvironment," *Frontiers in Pharmacology*, vol. 13, 2022. [Online]. Available: https://doi.org/10.3389/fphar.2022.868695

[18] D. Hanahan and R. A. Weinberg, "The hallmarks of cancer," *Cell*, vol. 100, no. 1, pp. 57–70, 2000. [Online]. Available: https://doi.org/10.1016/s0092-8674(00)81683-9

[19] C. C. Harris, "p53 tumor suppressor gene: From the basic research laboratory to the clinic - An abridged historical perspective," *Carcinogenesis*, vol. 17, no. 6, pp. 1187–1198, 1996. [Online]. Available: https://doi.org/10.1093/carcin/17.6.1187

[20] J. M. Adams and S. Cory, "The Bcl-2 apoptotic switch in cancer development and therapy," *Oncogene*, vol. 26, no. 9, pp. 1324–1337, 2007. [Online]. Available: https://doi.org/10.1038/sj.onc.1210220

[21] R. Stupp, W. P. Mason, M. J. van den Bent, M. Weller, B. Fisher, M. J. Taphoorn, K. Belanger, A. A. Brandes, C. Marosi, U. Bogdahn, J. Curschmann, R. C. Janzer, S. K. Ludwin, T. Gorlia, A. Allgeier, D. Lacombe, J. G. Cairncross, E. Eisenhauer, and R. O. Mirimanoff, "Radiotherapy plus Concomitant and Adjuvant Temozolomide for Glioblastoma," *New England Journal of Medicine*, vol. 352, no. 10, pp. 987–996, 2005. [Online]. Available: https://doi.org/10.1056/nejmoa043330

[22] R. Stupp, M. E. Hegi, W. P. Mason, M. J. van den Bent, M. J. Taphoorn, R. C. Janzer, S. K. Ludwin, A. Allgeier, B. Fisher, K. Belanger, P. Hau, A. A. Brandes, C. Gijtenbeek, Johanna Marosi, K. Vecht, Charles J Mokhtari, S. Wesseling, Pieter Villa, E. Eisenhauer, T. Gorlia, M. Weller, D. Lacombe, J. G. Cairncross, and R.-O. Mirimanoff, "Effects of radiotherapy with concomitant and adjuvant temozolomide versus radiotherapy alone on survival in glioblastoma in a randomised phase III study: 5-year analysis of the EORTC-NCIC trial," *The Lancet Oncology*, vol. 10, no. 5, pp. 459–466, 2009. [Online]. Available: https://doi.org/10.1016/s1470-2045(09)70025-7

[23] M. Weller, M. Van Den Bent, J. C. Tonn, R. Stupp, M. Preusser, E. Cohen-Jonathan-Moyal, R. Henriksson, E. L. Rhun, C. Balana, O. Chinot, M. Bendszus, J. C. Reijneveld, F. Dhermain, P. French, C. Marosi, C. Watts, I. Oberg, G. Pilkington,

B. G. Baumert, M. J. B. Taphoorn, M. Hegi, M. Westphal, G. Reifenberger, R. Soffietti, and W. Wick, "European Association for Neuro-Oncology (EANO) guideline on the diagnosis and treatment of adult astrocytic and oligodendroglial gliomas," *The Lancet Oncology*, vol. 18, no. 6, pp. e315–e329, 2017. [Online]. Available: https://doi.org/10.1016/s1470-2045(17)30194-8

[24] S. S. Agarwala and J. M. Kirkwood, "Temozolomide, a Novel Alkylating Agent with Activity in the Central Nervous System, May Improve the Treatment of Advanced Metastatic Melanoma," *The Oncologist*, vol. 5, no. 2, pp. 144–151, 2000. [Online]. Available: https://doi.org/10.1634/theoncologist.5-2-144

[25] P. Reidenberg, P. Statkevich, I. Judson, S. Moore, D. Cutler, V. Batra, M. Dugan, and M. Brada, "Effect of food on the oral bioavailability of temozolomide, a new chemotherapeutic agent." *Clinical Pharmacology and Therapeutics*, vol. 59, no. 2, pp. 199–199, 1996. [Online]. Available: https://doi.org/10.1038/sj.clpt.1996.295

[26] S. Y. Lee, "Temozolomide resistance in glioblastoma multiforme," *Genes and Diseases*, vol. 3, no. 3, pp. 198–210, 2016. [Online]. Available: https://doi.org/10.1016/j.gendis.2016.04.007

[27] National Cancer Institute, "Possible Side Effects of Temozolomide," National Cancer Institute, Bethseda, Maryland, Tech. Rep., 2023. [Online]. Available: https://ctep.cancer.gov/protocolDevelopment/docs/sideeffects/SideEffects-Temozolomide.docx

[28] M. C. Chamberlain, "Radiographic patterns of relapse in glioblastoma," *Journal of Neuro-Oncology*, vol. 101, no. 2, pp. 319–323, 1 2011. [Online]. Available: https://doi.org/10.1007/s11060-010-0251-4

[29] C. Neftel, J. Laffy, M. G. Filbin, T. Hara, M. E. Shore, G. J. Rahme, A. R. Richman, D. Silverbush, M. L. Shaw, C. M. Hebert, J. Dewitt, S. Gritsch, E. M. Perez, L. N. G. Castro, X. Lan, N. Druck, C. Rodman, D. Dionne, A. Kaplan, M. S. Bertalan, J. Small, K. Pelton, S. Becker, D. Bonal, Q.-D. Nguyen, R. L. Servis, J. M. Fung, R. Mylvaganam, L. Mayr, J. Gojo, C. Haberler, R. Geyeregger, T. Czech, I. Slavc, B. V. Nahed, W. T. Curry, B. S. Carter, H. Wakimoto, P. K. Brastianos, T. T. Batchelor, A. Stemmer-Rachamimov, M. Martinez-Lage, M. P. Frosch, I. Stamenkovic, N. Riggi, E. Rheinbay, M. Monje, O. Rozenblatt-Rosen, D. P. Cahill, A. P. Patel, T. Hunter, I. M. Verma, K. L. Ligon, D. N. Louis, A. Regev, B. E. Bernstein, I. Tirosh, and M. L. Suva, "An Integrative Model of Cellular States, Plasticity, and Genetics for Glioblastoma," *Cell*, vol. 178, no. 4, pp. 835–849, 2019. [Online]. Available: https://doi.org/10.1016/j.cell.2019.06.024

[30] S. Smith, M. Diksin, S. Chhaya, S. Sairam, M. Estevez-Cebrero, and R. Rahman, "The Invasive Region of Glioblastoma Defined by 5ALA Guided Surgery Has an Altered Cancer Stem Cell Marker Profile Compared to Central Tumour," *International Journal of Molecular Sciences*, vol. 18, no. 11, p. 2452, 2017. [Online]. Available: https://doi.org/10.3390/ijms18112452

[31] S. J. Smith, J. Rowlinson, M. Estevez-Cebrero, D. Onion, A. Ritchie, P. Clarke, K. Wood, M. Diksin, A. Lourdusamy, R. G. Grundy, and R. Rahman, "Metabolism-based isolation of invasive glioblastoma cells with specific gene signatures and tumorigenic potential," *Neuro-Oncology Advances*, vol. 2, no. 1, pp. 1–12, 2020. [Online]. Available: https://doi.org/10.1093/noajnl/vdaa087

[32] L. E. Gaspar, B. J. Fisher, D. R. Macdonald, D. V. Leber, E. C. Halperin, S. C. Schold, and J. G. Cairncross, "Supratentorial malignant glioma: Patterns of recurrence and implications for external beam local treatment," *International Journal of Radiation Oncology, Biology, Physics*, vol. 24, no. 1, pp. 55–57, 1992. [Online]. Available: https://doi.org/10.1016/0360-3016(92)91021-e

[33] G. J. Baker, V. N. Yadav, S. Motsch, C. Koschmann, A.-A. Calinescu, Y. Mineharu, S. I. Camelo-Piragua, D. Orringer, S. Bannykh, W. S. Nichols, A. C. deCarvalho, T. Mikkelsen, M. G. Castro, and P. R. Lowenstein, "Mechanisms of Glioma Formation: Iterative Perivascular Glioma Growth and Invasion Leads to Tumor Progression, VEGF-Independent Vascularization, and Resistance to Antiangiogenic Therapy," *Neoplasia*, vol. 16, no. 7, pp. 543–561, 2014. [Online]. Available: https://doi.org/10.1016/j.neo.2014.06.003

[34] S. Watkins, S. Robel, I. F. Kimbrough, S. M. Robert, G. Ellis-Davies, and H. Sontheimer, "Disruption of astrocyte–vascular coupling and the blood–brain barrier by invading glioma cells," *Nature Communications*, vol. 5, no. 1, pp. 1–15, 2014. [Online]. Available: https://doi.org/10.1038/ncomms5196

[35] A. L. Stensjoen, O. Solheim, K. A. Kvistad, A. K. Håberg, O. Salvesen, and E. M. Berntsen, "Growth dynamics of untreated glioblastomas in vivo," *Neuro-Oncology*, vol. 17, no. 10, pp. 1402–1411, 2015. [Online]. Available: https://doi.org/10.1093/neuonc/nov029

[36] O. Okolie, J. R. Bago, R. S. Schmid, D. M. Irvin, R. E. Bash, C. R. Miller, and S. D. Hingtgen, "Reactive astrocytes potentiate tumor aggressiveness in a murine glioma resection and recurrence model," *Neuro-Oncology*, vol. 18, no. 12, pp. 1622–1633, 2016. [Online]. Available: https://doi.org/10.1093/neuonc/now117

[37] S. L. Gerson, "MGMT: its role in cancer aetiology and cancer therapeutics," *Nature Reviews Cancer*, vol. 4, no. 4, pp. 296–307, 2004. [Online]. Available: https://doi.org/10.1038/nrc1319

[38] M. Kapalczynska, T. Kolenda, W. Przybyla, M. Zajaczkowska, A. Teresiak, V. Filas, M. Ibbs, R. Blizniak, L. Luczewski, and K. Lamperska, "2D and 3D cell cultures - a comparison of different types of cancer cell cultures," *Archives of Medical Science*, vol. 14, no. 4, pp. 910–919, 2018. [Online]. Available: https://doi.org/10.5114/aoms.2016.63743

[39] K. Von Der Mark, V. Gauss, H. Von Der Mark, and P. Müller, "Relationship between cell shape and type of collagen synthesised as chondrocytes lose their cartilage phenotype in culture," *Nature*, vol. 267, pp. 531–532, 1977. [Online]. Available: https://doi.org/10.1038/267531a0

[40] M. Allen, M. Bjerke, H. Edlund, S. Nelander, and B. Westermark, "Origin of the U87MG glioma cell line: Good news and bad news," *Science Translational Medicine*, vol. 8, no. 354, p. 354re3, 2016. [Online]. Available: https://doi.org/10.1126/scitranslmed.aaf6853

[41] R. Daneman and A. Prat, "The Blood–Brain Barrier," *Cold Spring Harbor Perspectives in Biology*, vol. 7, no. 1, p. a020412, 2015. [Online]. Available: https://doi.org/10.1101/cshperspect.a020412

[42] C. A. Lipinski, F. Lombardo, B. W. Dominy, and P. J. Feeney, "Experimental and computational approaches to estimate solubility and permeability in drug discovery and development settings," *Advanced Drug Delivery Reviews*, vol. 23, no. 1-3, pp. 3–25, 1997. [Online]. Available: https://doi.org/10.1016/s0169-409x(96)00423-1

[43] W. A. Banks, "Characteristics of compounds that cross the blood-brain barrier," *BMC Neurology*, vol. 9, no. Suppl. 1, pp. 1–5, 2009. [Online]. Available: https://doi.org/10.1186/1471-2377-9-S1-S3

[44] United States Food and Drug Administration, "Drug Approval Package: Gliadel Wafer," 2003. [Online]. Available: https://www.accessdata.fda.gov/drugsatfda_docs/nda/2003/20-637s016_Gliadel.cfm

[45] J. Beith, J. Hartley, J. Darling, and R. Souhami, "DNA interstrand cross-linking and cytotoxicity induced by chloroethylnitrosoureas and cisplatin in human glioma cell lines which vary in cellular concentration of O6-alkylguanine-DNA alkyltransferase," *British Journal of Cancer*, vol. 75, no. 4, pp. 500–505, 1997. [Online]. Available: https://doi.org/10.1038/bjc.1997.87

[46] Z. Z. Xiao, Z. F. Wang, T. Lan, W. H. Huang, Y. H. Zhao, C. Ma, and Z. Q. Li, "Carmustine as a Supplementary Therapeutic Option for Glioblastoma: A Systematic Review and Meta-Analysis," *Frontiers in Neurology*, vol. 11, 2020. [Online]. Available: https://doi.org/10.3389/fneur.2020.01036

[47] T. Kadota, R. Saito, T. Kumabe, J. Mizusawa, H. Katayama, M. Sumi, H. Igaki, M. Kinoshita, T. Komori, K. Ichimura, Y. Narita, and R. Nishikawa, "A multicenter randomized phase III study for newly diagnosed maximally resected glioblastoma comparing carmustine wafer implantation followed by chemoradiotherapy with temozolomide with chemoradiotherapy alone; Japan Clinical Oncology Group Study JCOG1703 (MACS study)," *Japanese Journal of Clinical Oncology*, vol. 49, no. 12, pp. 1172–1175, 2019. [Online]. Available: https://doi.org/10.1093/jjco/hyz169

[48] S. J. Smith, B. M. Tyler, T. Gould, G. J. Veal, N. Gorelick, J. Rowlinson, R. Serra, A. Ritchie, P. Berry, A. Otto, J. Choi, N. Skuli, M. Estevez-Cebrero, K. M. Shakesheff, H. Brem, R. G. Grundy, and R. Rahman, "Overall survival in malignant glioma is significantly prolonged by neurosurgical delivery of etoposide and temozolomide from a thermo-responsive biodegradable paste," *Clinical Cancer Research*, vol. 25, no. 16, pp. 5094–5106, 2019. [Online]. Available: https://doi.org/10.1158/1078-0432.ccr-18-3850

[49] M. H. Cohen, Y. L. Shen, P. Keegan, and R. Pazdur, "FDA Drug Approval Summary: Bevacizumab (Avastin®) as Treatment of Recurrent Glioblastoma Multiforme," *The Oncologist*, vol. 14, no. 11, pp. 1131–1138, 2009. [Online]. Available: https://doi.org/10.1634/theoncologist.2009-0121

[50] A. S. Pasciak, S. Manupipatpong, F. K. Hui, L. Gainsburg, R. Krimins, M. C. Zink, C. F. Brayton, M. Morris, J. Sage, D. R. Donahue, M. R. Dreher, D. L. Kraitchman, and C. R. Weiss, "Yttrium-90 radioembolization as a possible new treatment for brain cancer: proof of concept and safety analysis in a canine model," *EJNMMI Research*, vol. 10, no. 1, p. 96, 2020. [Online]. Available: https://doi.org/10.1186/s13550-020-00679-1

[51] R. Salem and K. G. Thurston, "Radioembolization with 90Yttrium Microspheres: A State-of-the-Art Brachytherapy Treatment for Primary and Secondary Liver Malignancies: Part 1: Technical and Methodologic Considerations," *Journal of Vascular and Interventional Radiology*, vol. 17, no. 8, pp. 1251–1278, 2006. [Online]. Available: https://doi.org/10.1097/01.rvi.0000233785.75257.9a

[52] S. Linda and F. Basarabescu, "NCT05303467: A Feasibility Study to Evaluate the Safety of the TheraSphere Glioblastoma (GBM) Device in Patients With Recurrent GBM (FRONTIER)," 2022. [Online]. Available: https://clinicaltrials.gov/study/NCT05303467

[53] K. Mahmoudi, K. L. Garvey, A. Bouras, G. Cramer, H. Stepp, J. G. Jesu Raj, D. Bozec, T. M. Busch, and C. G. Hadjipanayis, "5-Aminolevulinic Acid Photodynamic Therapy for the Treatment of High-Grade Gliomas," *Journal of Neuro-Oncology*, vol. 141, no. 3, pp. 595–607, 2 2019. [Online]. Available: https://doi.org/10.1007/s11060-019-03103-4

[54] B. J. Quirk, G. Brandal, S. Donlon, J. C. Vera, T. S. Mang, A. B. Foy, S. M. Lew, A. W. Girotti, S. Jogal, P. S. LaViolette, J. M. Connelly, and H. T. Whelan,

"Photodynamic therapy (PDT) for malignant brain tumors – Where do we stand?" *Photodiagnosis and Photodynamic Therapy*, vol. 12, no. 3, pp. 530–544, 2015. [Online]. Available: https://doi.org/10.1016/j.pdpdt.2015.04.009

[55] A. M. Hersh, M. Bhimreddy, C. Weber-Levine, K. Jiang, S. Alomari, N. Theodore, A. Manbachi, and B. M. Tyler, "Applications of Focused Ultrasound for the Treatment of Glioblastoma: A New Frontier," *Cancers*, vol. 14, no. 19, p. 4920, 2022. [Online]. Available: https://doi.org/10.3390/cancers14194920

[56] L. H. Treat, N. McDannold, N. Vykhodtseva, Y. Zhang, K. Tam, and K. Hynynen, "Targeted delivery of doxorubicin to the rat brain at therapeutic levels using MRI-guided focused ultrasound," *International Journal of Cancer*, vol. 121, no. 4, pp. 901–907, 2007. [Online]. Available: https://doi.org/10.1002/ijc.22732

[57] R. R. Baker, C. Payne, Y. Yu, M. Mohseni, J. J. Connell, F. Lin, I. F. Harrison, P. Southern, U. S. Rudrapatna, D. J. Stuckey, T. L. Kalber, B. Siow, L. Thorne, S. Punwani, D. K. Jones, M. Emberton, Q. A. Pankhurst, and M. F. Lythgoe, "Image-Guided Magnetic Thermoseed Navigation and Tumor Ablation Using a Magnetic Resonance Imaging System," *Advanced Science*, vol. 9, no. 12, p. 2105333, 2022. [Online]. Available: https://doi.org/10.1002/advs.202105333

[58] Y. Liu, Q. Tang, Q. Tao, H. Dong, Z. Shi, and L. Zhou, "Low-frequency magnetic field therapy for glioblastoma: Current advances, mechanisms, challenges and future perspectives," *Journal of Advanced Research*, 2024. [Online]. Available: https://doi.org/10.1016/j.jare.2024.03.024

[59] C. Cobbs, E. McClay, J. P. Duic, L. B. Nabors, D. Morgan Murray, and S. Kesari, "An early feasibility study of the Nativis Voyager device in patients with recurrent glioblastoma: First cohort in US," *CNS Oncology*, vol. 8, no. 1, 2019. [Online]. Available: https://doi.org/10.2217/cns-2018-0013

[60] D. S. Baskin, M. A. Sharpe, L. Nguyen, and S. A. Helekar, "Case Report: End-Stage Recurrent Glioblastoma Treated With a New Noninvasive Non-Contact Oncomagnetic Device," *Frontiers in Oncology*, vol. 11, 2021. [Online]. Available: https://doi.org/10.3389/fonc.2021.708017

[61] National Institute for Health and Care Excellence, "IPG446: Electrochemotherapy for metastases in the skin from tumours of non-skin origin and melanoma," Manchester, Tech. Rep., 2013. [Online]. Available: https://www.nice.org.uk/guidance/ipg446

[62] D. Miklavčič, B. Mali, B. Kos, R. Heller, and G. Serša, "Electrochemotherapy: from the drawing board into medical practice," *BioMedical Engineering OnLine*, vol. 13, 2014. [Online]. Available: https://doi.org/10.1186/1475-925X-13-29

[63] R. V. Davalos, L. M. Mir, and B. Rubinsky, "Tissue Ablation with Irreversible Electroporation," *Annals of Biomedical Engineering*, vol. 33, pp. 223–231, 2005. [Online]. Available: https://doi.org/10.1007/s10439-005-8981-8

[64] O. Rominiyi, A. Vanderlinden, S. J. Clenton, C. Bridgewater, Y. Al-Tamimi, and S. J. Collis, "Tumour treating fields therapy for glioblastoma: current advances and future directions," *British Journal of Cancer*, vol. 124, no. 4, pp. 697–709, 2021. [Online]. Available: https://doi.org/10.1038/s41416-020-01136-5

[65] M. K. Ramirez-Fort, A. Naveh, S. Mcclelland, C. K. Gilman, M. Fort, M. Mendez, J. Matta, Z. Bomzon, and C. S. Lange, "Computational simulations establish a novel transducer array placement arrangement that extends delivery of therapeutic TTFields to the infratentorium of patients with brainstem gliomas," *Reports of Practical Oncology and Radiotherapy*, vol. 26, no. 6, pp. 1045–1050, 2021. [Online]. Available: http://doi.org/10.5603/rpor.a2021.0132

[66] R. Stupp, S. Taillibert, A. Kanner, W. Read, D. M. Steinberg, B. Lhermitte, S. Toms, A. Idbaih, M. S. Ahluwalia, K. Fink, F. Di Meco, F. Lieberman, J.-J. Zhu, G. Stragliotto, D. D. Tran, S. Brem, A. F. Hottinger, E. D. Kirson, G. Lavy-Shahaf, U. Weinberg, C.-Y. Kim, S.-H. Paek, G. Nicholas, J. Bruna, H. Hirte, M. Weller, Y. Palti, M. E. Hegi, and Z. Ram, "Effect of Tumor-Treating Fields Plus Maintenance Temozolomide vs Maintenance Temozolomide Alone on Survival in Patients With Glioblastoma," *Journal of the American Medical Association*, vol. 318, no. 23, pp. 2306–2316, 2017. [Online]. Available: https://doi.org/10.1001/jama.2017.18718

[67] S. A. Toms, C. Y. Kim, G. Nicholas, and Z. Ram, "Increased compliance with tumor treating fields therapy is prognostic for improved survival in the treatment of glioblastoma: a subgroup analysis of the EF-14 phase III trial," *Journal of Neuro-Oncology*, vol. 141, no. 2, pp. 467–473, 2019. [Online]. Available: https://doi.org/10.1007/s11060-018-03057-z

[68] United States Food and Drug Administration, "NovoTTF- IOA System, PMA: P100034 Approval Order," 2011. [Online]. Available: https://www.accessdata.fda.gov/cdrh_docs/pdf10/P100034A.pdf

[69] United States Food and Drug Administration., "Summary of Safety and Effectiveness Data (SSED): Tumor Treatment Fields," Portsmouth, NH, 2015. [Online]. Available: https://www.accessdata.fda.gov/cdrh_docs/pdf10/P100034S013b.pdf

[70] A. Chaudhry, L. Benson, M. Varshaver, O. Farber, U. Weinberg, E. Kirson, and Y. Palti, "NovoTTF™-100A System (Tumor Treating Fields) transducer array layout planning for glioblastoma: a NovoTAL™ system user study," *World Journal of Surgical Oncology*, vol. 13, no. 1, pp. 1–7, 2015. [Online]. Available: https://doi.org/10.1186/s12957-015-0722-3

[71] A. Kinzel, M. Ambrogi, M. Varshaver, and E. D. Kirson, "Tumor Treating Fields for Glioblastoma Treatment: Patient Satisfaction and Compliance With the Second-Generation Optune® System," *Clinical Medicine Insights: Oncology*, vol. 13, 2019. [Online]. Available: https://doi.org/10.1177/1179554918825449

[72] M. E. Lacouture, M. Elizabeth Davis, G. Elzinga, N. Butowski, D. Tran, J. L. Villano, L. DiMeglio, A. M. Davies, and E. T. Wong, "Characterization and Management of Dermatologic Adverse Events With the NovoTTF-100A System, a Novel Anti-mitotic Electric Field Device for the Treatment of Recurrent Glioblastoma," *Seminars in Oncology*, vol. 41, no. Suppl. 4, pp. s1–s14, 6 2014. [Online]. Available: https://doi.org/10.1053/j.seminoncol.2014.03.011

[73] E. D. Kirson, Z. Gurvich, R. Schneiderman, E. Dekel, A. Itzhaki, Y. Wasserman, R. Schatzberger, and Y. Palti, "Disruption of cancer cell replication by alternating electric fields," *Cancer Research*, vol. 64, no. 9, pp. 3288–3295, 2004. [Online]. Available: https://doi.org/10.1158/0008-5472.can-04-0083

[74] E. D. Kirson, V. Dbaly, F. Tovarys, J. Vymazal, J. F. Soustiel, A. Itzhaki, D. Mordechovich, S. Steinberg-Shapira, Z. Gurvich, R. Schneiderman, Y. Wasserman, M. Salzberg, B. Ryffel, D. Goldsher, E. Dekel, and Y. Palti, "Alternating electric fields arrest cell proliferation in animal tumor models and human brain tumors," *Proceedings of the National Academy of Sciences*, vol. 104, no. 24, pp. 10 152–10 157, 2007. [Online]. Available: https://doi.org/10.1073/pnas.0702916104

[75] E. Chang, C. B. Patel, C. Pohling, C. Young, J. Song, T. A. Flores, Y. Zeng, L. M. Joubert, H. Arami, A. Natarajan, R. Sinclair, and S. S. Gambhir, "Tumor treating fields increases membrane permeability in glioblastoma cells," *Cell Death Discovery*, vol. 4, no. 1, 2018. [Online]. Available: https://doi.org/10.1038/s41420-018-0130-x

[76] A. A. Aguilar, M. C. Ho, E. Chang, K. W. Carlson, A. Natarajan, T. Marciano, Z. Bomzon, and C. B. Patel, "Permeabilizing cell membranes with electric fields," *Cancers*, vol. 13, no. 9, p. 2283, 2021. [Online]. Available: https://doi.org/10.3390/cancers13092283

[77] E. Salvador, A. F. Kessler, D. Domröse, J. Hörmann, C. Schaeffer, A. Giniunaite, M. Burek, C. Tempel-Brami, T. Voloshin, A. Volodin, A. Zeidan, M. Giladi, R.-I. Ernestus, M. Löhr, C. Y. Förster, and C. Hagemann, "Tumor Treating Fields (TTFields) Reversibly Permeabilize the Blood–Brain Barrier In Vitro and In Vivo," *Biomolecules*, vol. 12, no. 10, 2022. [Online]. Available: https://doi.org/10.3390/biom12101348

[78] M. Iv, L. Naya, S. Sanan, S. L. Van Buskirk, S. Nagpal, R. P. Thomas, L. D. Recht, and C. B. Patel, "Tumor treating fields increases blood-brain barrier permeability and relative cerebral blood volume in patients with glioblastoma," *Neuroradiology Journal*, vol. 37, no. 1, pp. 107–118, 2024. [Online]. Available: https://doi.org/10.1177/19714009231207083

[79] B. R. Zetter, "Angiogenesis and tumor metastasis," *Annual Review of Medicine*, vol. 49, pp. 407–424, 1998. [Online]. Available: https://doi.org/10.1146/annurev.med.49.1.407

[80] E. H. Kim, H. S. Song, S. H. Yoo, and M. Yoon, "Tumor treating fields inhibit glioblastoma cell migration, invasion and angiogenesis," *Oncotarget*, vol. 7, no. 40, pp. 65 125–65 136, 2016. [Online]. Available: https://doi.org/10.18632/oncotarget.11372

[81] J. Y. Oh, Y. J. Lee, and E. H. Kim, "Tumor-Treating Fields Inhibit the Metastatic Potential of Osteosarcoma Cells," *Technology in Cancer Research and Treatment*, vol. 19, 2020. [Online]. Available: https://doi.org/10.1177/1533033820947481

[82] M. Giladi, M. Munster, R. S. Schneiderman, T. Voloshin, Y. Porat, R. Blat, K. Zielinska-Chomej, P. Hååg, Z. Bomzon, E. D. Kirson, U. Weinberg, K. Viktorsson, R. Lewensohn, and Y. Palti, "Tumor treating fields (TTFields) delay DNA damage repair following radiation treatment of glioma cells," *Radiation Oncology*, vol. 12, no. 1, 2017. [Online]. Available: https://doi.org/10.1186/S13014-017-0941-6

[83] N. K. Karanam, K. Srinivasan, L. Ding, B. Sishc, D. Saha, and M. D. Story, "Tumor-Treating fields elicit a conditional vulnerability to ionizing radiation via the downregulation of BRCA1 signaling and reduced DNA double-strand break repair capacity in non-small cell lung cancer cell lines," *Cell Death and Disease*, vol. 8, no. 3, 2017. [Online]. Available: https://doi.org/10.1038/cddis.2017.136

[84] A. Shteingauz, Y. Porat, T. Voloshin, R. S. Schneiderman, M. Munster, E. Zeevi, N. Kaynan, K. Gotlib, M. Giladi, E. D. Kirson, U. Weinberg, A. Kinzel, and Y. Palti, "AMPK-dependent autophagy upregulation serves as a survival mechanism in response to Tumor Treating Fields (TTFields)," *Cell Death and Disease*, vol. 9, no. 11, 2018. [Online]. Available: https://doi.org/10.1038/s41419-018-1085-9

[85] E. H. Kim, Y. Jo, S. Sai, M. J. Park, J. Y. Kim, J. S. Kim, Y. J. Lee, J. M. Cho, S. Y. Kwak, J. H. Baek, Y. K. Jeong, J. Y. Song, M. Yoon, and S. G. Hwang, "Tumor-treating fields induce autophagy by blocking the Akt2/miR29b axis in glioblastoma cells," *Oncogene*, vol. 38, no. 39, pp. 6630–6646, 2019. [Online]. Available: https://doi.org/10.1038/s41388-019-0882-7

[86] E. D. Kirson, M. Giladi, Z. Gurvich, A. Itzhaki, D. Mordechovich, R. S. Schneiderman, Y. Wasserman, B. Ryffel, D. Goldsher, and Y. Palti, "Alternating electric fields (TTFields) inhibit metastatic spread of solid tumors to the lungs," *Clinical and Experimental Metastasis*, vol. 26, no. 7, pp. 633–640, 2009. [Online]. Available: https://doi.org/10.1007/s10585-009-9262-y

[87] Y. Lan, S. Zhang, Y. Pan, M. Wang, and G. Chen, "Research Progress on the Mechanism of Anti-Tumor Immune Response Induced by TTFields," *Cancers*, vol. 15, no. 23, 2023. [Online]. Available: https://doi.org/10.3390/cancers15235642

[88] J. I. Park, K. H. Song, S. Y. Jung, J. Ahn, S. G. Hwang, J. Kim, E. H. Kim, and J. Y. Song, "Tumor-Treating Fields Induce RAW264.7 Macrophage Activation Via NK-kB/MAPK Signaling Pathways," *Technology in Cancer Research and Treatment*, vol. 18, 2019. [Online]. Available: https://doi.org/10.1177/1533033819868225

[89] J. Branter, M. Estevez-Cebrero, M. Diksin, M. Griffin, M. Castellanos-Uribe, S. May, R. Rahman, R. Grundy, S. Basu, and S. Smith, "Genome-Wide Expression and Anti-Proliferative Effects of Electric Field Therapy on Pediatric and Adult Brain Tumors," *International Journal of Molecular Sciences*, vol. 23, no. 4, p. 1982, 2022. [Online]. Available: https://doi.org/10.3390/ijms23041982

[90] C. Wenger, P. C. Miranda, R. Salvador, A. Thielscher, Z. Bomzon, M. Giladi, M. M. Mrugala, and A. R. Korshoej, "A Review on Tumor-Treating Fields (TTFields): Clinical Implications Inferred From Computational Modeling," *IEEE Reviews in Biomedical Engineering*, vol. 11, pp. 195–207, 2018. [Online]. Available: https://doi.org/10.1109/rbme.2017.2765282

[91] Z. Ram, C.-Y. Kim, A. F. Hottinger, A. Idbaih, G. Nicholas, and J.-J. Zhu, "Efficacy and Safety of Tumor Treating Fields (TTFields) in Elderly Patients with Newly Diagnosed Glioblastoma: Subgroup Analysis of the Phase 3 EF-14 Clinical Trial," *Frontiers in Oncology*, vol. 11, 2021. [Online]. Available: https://doi.org/10.3389/fonc.2021.671972

[92] NovoCure Limited, "Form S-1 Registration Statement Under the Securities Act of 1933," 2015. [Online]. Available: https://www.sec.gov/Archives/edgar/data/1645113/000119312515308245/d940664ds1.htm

[93] Novocure GmbH, "QSD-QR-704 US(EN) Commercial Optune Gio INE_PIOM Rev07," Tech. Rep., 2023. [Online]. Available: https://assets.novocure.biz/patient/QSD-QR-704%20US%28EN%29%20Commercial%20Optune%20Gio%20INE_PIOM%20Rev07.pdf

[94] Novocure GmbH., "Novocure Announces Reimbursement of Optune for the Treatment of Newly Diagnosed Glioblastoma in France," Tech. Rep., 2023. [Online]. Available: https://www.novocure.com/novocure-announces-reimbursement-of-optune-for-the-treatment-of-newly-diagnosed-glioblastoma-in-france/

[95] T. Voloshin, N. Kaynan, S. Davidi, Y. Porat, A. Shteingauz, R. S. Schneiderman, E. Zeevi, M. Munster, R. Blat, C. T. Brami, S. Cahal, A. Itzhaki, M. Giladi, E. D. Kirson, U. Weinberg, A. Kinzel, and Palti Yoram, "Tumor-treating fields (TTFields) induce immunogenic cell death resulting in enhanced antitumor efficacy when combined with anti-PD-1 therapy," *Cancer Immunology, Immunotherapy*, vol. 69, no. 7, pp. 1191–1204, 2020. [Online]. Available: https://doi.org/10.1007/s00262-020-02534-7

[96] Jiangsu Healthy Life Innovation Medical Technology Co. Ltd, "NCT06353360: TTField in Combination With Temozolomide and Tislelizumab in The Treatment of Newly Diagnosed Glioblastoma," *ClinicalTrials.gov*, 2024. [Online]. Available: https://clinicaltrials.gov/study/NCT06353360

[97] NovoCure GmbH, "NCT06556563: EF-41//KEYNOTE D58: Phase 3 Study of Optune Concomitant With Temozolomide Plus Pembrolizumab in Newly Diagnosed Glioblastoma (EF-41)," *ClinicalTrials.gov*, 2024. [Online]. Available: https://clinicaltrials.gov/study/NCT06556563

[98] Tel Aviv Medical Center, "NCT05973903: Lenvatinib, Pembrolizumab, and Tumor Treating Fields (TTFields) for Second-line Treatment of Glioblastoma," *ClinicalTrials.gov*, 2023. [Online]. Available: https://clinicaltrials.gov/study/NCT05973903

[99] The Christie NHS Foundation Trust, "NCT06136611: Preoperative Preradiotherapy TTFields (PORTRAIT)," *ClinicalTrials.gov*, 2023. [Online]. Available: https://clinicaltrials.gov/study/NCT06136611

[100] Zhongnan Hospital, "NCT04902586: Effect of Radiotherapy Concurrent of TTFields in Patients With Glioblastoma (ECTG001)," *ClinicalTrials.gov*, 2021. [Online]. Available: https://clinicaltrials.gov/study/NCT04902586

[101] Y. Matsumura and H. Maeda, "A New Concept for Macromolecular Therapeutics in Cancer Chemotherapy: Mechanism of Tumoritropic Accumulation of Proteins and the Antitumor Agent Smancs," *Cancer Research*, vol. 46, no. 12, pp. 6387–6392, 1986. [Online]. Available: http://aacrjournals.org/cancerres/article-pdf/46/12_Part_1/6387/2424185/cr04612p16387.pdf

[102] S. D. Perrault, C. Walkey, T. Jennings, H. C. Fischer, and W. C. W. Chan, "Mediating Tumor Targeting Efficiency of Nanoparticles Through Design," *Nano Letters*, vol. 9, no. 5, pp. 1909–1915, 2009. [Online]. Available: https://doi.org/10.1021/nl900031y

[103] E. J. Chung, Y. Cheng, R. Morshed, K. Nord, Y. Han, M. L. Wegscheid, B. Auffinger, D. A. Wainwright, M. S. Lesniak, and M. V. Tirrell, "Fibrin-binding, peptide amphiphile micelles for targeting glioblastoma," *Biomaterials*, vol. 35, no. 4, pp. 1249–1256, 2014. [Online]. Available: https://doi.org/10.1016/j.biomaterials.2013.10.064

[104] Y. N. Yoon, D.-S. Lee, H. J. Park, and J.-S. Kim, "Barium Titanate Nanoparticles Sensitise Treatment-Resistant Breast Cancer Cells to the Antitumor Action of Tumour-Treating Fields," *Scientific Reports*, vol. 10, no. 2560, pp. 1–9, 2020. [Online]. Available: https://doi.org/10.1038/s41598-020-59445-x

[105] N. Kumar, "Electric Current," in *Comprehensive Physics XII*. Delhi: Laxmi Publications, 2004, ch. 4.

[106] S. Morab, M. M. Sundaram, and A. Pivrikas, "Review on Charge Carrier Transport in Inorganic and Organic Semiconductors," *Coatings*, vol. 13, no. 9, p. 1657, 2023. [Online]. Available: https://doi.org/10.3390/coatings13091657

[107] A. M. Bryan, L. M. Santino, Y. Lu, S. Acharya, and J. M. D'Arcy, "Conducting Polymers for Pseudocapacitive Energy Storage," *Chemistry of Materials*, vol. 28, no. 17, pp. 5989–5998, 2016. [Online]. Available: https://doi.org/10.1021/acs.chemmater.6b01762

[108] A. G. Atanasov, S. B. Zotchev, V. M. Dirsch, The International Natural Product Sciences Taskforce, and C. T. Supuran, "Natural products in drug discovery: advances and opportunities," *Nature Reviews Drug Discovery*, vol. 20, no. 3, pp. 200–216, 2021. [Online]. Available: https://doi.org/10.1038/s41573-020-00114-z

[109] J. Clayden, N. Greeves, and S. Warren, "Delocalization and Conjugation," in *Organic Chemistry*, 2nd ed. New York: Oxford University Press, 2012, ch. 7, pp. 141–162.

[110] W. Cao, X. Zhou, N. C. McCallum, Z. Hu, Q. Z. Ni, U. Kapoor, C. M. Heil, K. S. Cay, T. Zand, A. J. Mantanona, A. Jayaraman, A. Dhinojwala, D. D. Deheyn, M. D. Shawkey, M. D. Burkart, J. D. Rinehart, and N. C. Gianneschi, "Unraveling the structure and function of melanin through synthesis," *Journal of the American Chemical Society*, vol. 143, no. 7, pp. 2622–2637, 2021. [Online]. Available: https://doi.org/10.1021/jacs.0c12322

[111] N. B. Roberts, S. A. Curtis, A. M. Milan, and L. R. Ranganath, "The Pigment in Alkaptonuria Relationship to Melanin and Other Coloured Substances: A Review of Metabolism, Composition and Chemical Analysis," *JIMD Reports*, vol. 24, pp. 51–66, 2015. [Online]. Available: https://doi.org/10.1007/8904_2015_453

[112] R. L. Haining and C. Achat-Mendes, "Neuromelanin, one of the most overlooked molecules in modern medicine, is not a spectator," *Neural Regeneration Research*, vol. 12, no. 3, pp. 372–375, 2017. [Online]. Available: https://doi.org/10.4103/1673-5374.202928

[113] J. B. Mistry, M. Bukhari, and A. M. Taylor, "Alkaptonuria," *Rare Diseases*, vol. 1, p. e27475, 2013. [Online]. Available: https://doi.org/10.4161/rdis.27475

[114] E. P. Magennis, F. Fernandez-Trillo, C. Sui, S. G. Spain, D. J. Bradshaw, D. Churchley, G. Mantovani, K. Winzer, and C. Alexander, "Bacteria-instructed synthesis of polymers for self-selective microbial binding and labelling," *Nature Materials*, vol. 13, no. 7, pp. 748–755, 2014. [Online]. Available: https://doi.org/10.1038/nmat3949

[115] R. Qi, H. Zhao, X. Zhou, J. Liu, N. Dai, Y. Zeng, E. Zhang, F. Lv, Y. Huang, L. Liu, Y. Wang, and S. Wang, "In Situ Synthesis of Photoactive Polymers on a Living Cell Surface via Bio-Palladium Catalysis for Modulating Biological Functions," *Angewandte Chemie International Edition*, vol. 60, no. 11, pp. 5759–5765, 2021. [Online]. Available: https://doi.org/10.1002/anie.202015247

[116] J. Yang, J. Li, X. Wang, X. Li, N. Kawazoe, and G. Chen, "Single mammalian cell encapsulation by in situ polymerization," *Journal of Materials Chemistry B*, vol. 4, no. 47, pp. 7662–7668, 2016. [Online]. Available: https://doi.org/10.1039/c6tb02491b

[117] J. L. Lilly, G. Romero, W. Xu, H. Y. Shin, and B. J. Berron, "Characterization of Molecular Transport in Ultrathin Hydrogel Coatings for Cellular Immunoprotection," *Biomacromolecules*, vol. 16, no. 2, pp. 541–549, 2015. [Online]. Available: https://doi.org/10.1021/bm501594x

[118] G. Romero, J. J. Lilly, N. S. Abraham, H. Y. Shin, V. Balasubramaniam, T. Izumi, and B. J. Berron, "Protective Polymer Coatings for High-Throughput, High-Purity Cellular Isolation," *ACS Applied Materials and Interfaces*, vol. 7, no. 32, pp. 17 598–17 602, 2015. [Online]. Available: https://doi.org/10.1021/acsami.5b06298

[119] J. Niu, D. J. Lunn, A. Pusuluri, J. I. Yoo, M. A. O'Malley, S. Mitragotri, H. T. Soh, and C. J. Hawker, "Engineering live cell surfaces with functional polymers via cytocompatible controlled radical polymerization," *Nature Chemistry*, vol. 9, no. 6, pp. 537–545, 2017. [Online]. Available: https://doi.org/10.1038/nchem.2713

[120] Q. Shen, Y. Huang, Y. Zeng, E. Zhang, F. Lv, L. Liu, and S. Wang, "Intracellular Radical Polymerization of Paclitaxel-Bearing Acrylamide for Self-Inflicted Apoptosis of Cancer Cells," *ACS Materials Letters*, vol. 3, no. 9, pp. 1307–1314, 2021. [Online]. Available: https://doi.org/10.1021/acsmaterialslett.1c00357

[121] N. Lv, X. Yin, Z. Yang, T. Ma, H. Qin, B. Xiong, H. Jiang, and J. Zhu, "Electrostatically Controlled ex Situ and in Situ Polymerization of Diacetylene-Containing Peptide Amphiphiles in Living Cells," *ACS Macro Letters*, vol. 11, no. 2, pp. 223–229, 2022. [Online]. Available: https://doi.org/10.1021/acsmacrolett.1c00735

[122] A. Wang, H. Li, H. Feng, H. Qiu, R. Huang, Y. Wang, S. Ji, H. Liang, X.-C. Shen, and B.-P. Jiang, "In Situ Polymerization of Aniline Derivative in Vivo for NIR-II Phototheranostics of Tumor," *ACS Applied Materials & Interfaces*, vol. 15, no. 4, pp. 5870–5882, 2023. [Online]. Available: https://doi.org/10.1021/acsami.2c19927

[123] C. Liu, B. Xianyu, Y. Dai, S. Pan, T. Li, and H. Xu, "Intracellular Hyperbranched Polymerization for Circumventing Cancer Drug Resistance," *ACS Nano*, vol. 17, no. 12, pp. 11 905–11 913, 2023. [Online]. Available: https://doi.org/10.1021/acsnano.3c03512

[124] M. Li and R. K. Anand, "High-Throughput Selective Capture of Single Circulating Tumor Cells by Dielectrophoresis at a Wireless Electrode Array," *Journal of the American Chemical Society*, vol. 139, no. 26, pp. 8950–8959, 7 2017. [Online]. Available: https://pubmed.ncbi.nlm.nih.gov/28609630/

[125] G. Qi, X. Liu, L. Shi, M. Wu, J. Liu, and B. Liu, "Enzyme-Mediated Intracellular Polymerization of AIEgens for Light-Up Tumor Localization and Theranostics," *Advanced Materials*, vol. 34, no. 5, 2022. [Online]. Available: https://doi.org/10.1002/adma.202106885

[126] Q. L. Zhang, D. Zheng, X. Dong, P. Pan, S.-M. Zeng, F. Gao, S.-X. Cheng, and X.-Z. Zhang, "A Strategy Based on the Enzyme-Catalyzed Polymerization Reaction of Asp-Phe-Tyr Tripeptide for Cancer Immunotherapy," *Journal of the American Chemical Society*, vol. 143, no. 13, pp. 5127–5140, 2021. [Online]. Available: https://doi.org/10.1021/jacs.1c00945

[127] Y. Dai, T. Li, Z. Zhang, Y. Tan, S. Pan, L. Zhang, and H. Xu, "Oxidative Polymerization in Living Cells," *Journal of the American Chemical Society*, vol. 143, no. 28, pp. 10 709–10 717, 2021. [Online]. Available: https://doi.org/10.1021/jacs.1c04821

[128] H. G. Sherman, J. M. Hicks, A. Jain, J. J. Titman, C. Alexander, S. Stolnik, and F. J. Rawson, "Mammalian Cell-driven Polymerisation of Pyrrole," *ChemBioChem*, vol. 20, no. 8, pp. 1008–1013, 2019. [Online]. Available: https://doi.org/10.1002/cbic.201800630

[129] J. Rautio, N. A. Meanwell, L. Di, and M. J. Hageman, "The expanding role of prodrugs in contemporary drug design and development," *Nature Reviews Drug Discovery*, vol. 17, no. 8, pp. 559–587, 2018. [Online]. Available: https://doi.org/10.1038/nrd.2018.46

[130] Y. Tan and K. Ghandi, "Kinetics and mechanism of pyrrole chemical polymerization," *Synthetic Metals*, vol. 175, pp. 183–191, 2013. [Online]. Available: https://doi.org/10.1016/j.synthmet.2013.05.014

[131] B. Blad and B. Baldetorp, "Impedance spectra of tumour tissue in comparison with normal tissue; a possible clinical application for electrical impedance tomography," *Physiological measurement*, vol. 17, no. Suppl. 4A, pp. A105–A115, 1996. [Online]. Available: https://doi.org/10.1088/0967-3334/17/aA/015

[132] E. T. Wong and E. Lok, "Body Fluids Modulate Propagation of Tumor Treating Fields," *Advances in Radiation Oncology*, vol. 9, no. 1, p. 101316, 2024. [Online]. Available: https://doi.org/10.1016/j.adro.2023.101316

[133] E. Stavrinidou, R. Gabrielsson, E. Gomez, X. Crispin, O. Nilsson, D. T. Simon, and M. Berggren, "Electronic plants," *Science Advances*, vol. 1, no. 10, 2015. [Online]. Available: https://doi.org/10.1126/sciadv.1501136

[134] G. Dufil, D. Parker, J. Y. Gerasimov, T. Q. Nguyen, M. Berggren, and E. Stavrinidou, "Enzyme-assisted in vivo polymerisation of conjugated oligomer based conductors," *Journal of Materials Chemistry B*, vol. 8, no. 19, pp. 4221–4227, 2020. [Online]. Available: https://doi.org/10.1039/d0tb00212g

[135] D. Parker, Y. Daguerre, G. Dufil, D. Mantione, E. Solano, E. Cloutet, G. Hadziioannou, T. Näsholm, M. Berggren, E. Pavlopoulou, and E. Stavrinidou, "Biohybrid plants with electronic roots via in vivo polymerization of conjugated oligomers," *Materials Horizons*, vol. 8, no. 12, pp. 3295–3305, 2021. [Online]. Available: https://doi.org/10.1039/d1mh01423d

[136] S. M. Richardson-Burns, J. L. Hendricks, and D. C. Martin, "Electrochemical polymerization of conducting polymers in living neural tissue," *Journal of Neural Engineering*, vol. 4, 2007. [Online]. Available: https://doi.org/10.1088/1741-2560/4/2/l02

[137] X. Strakosas, H. Biesmans, T. Abrahamsson, K. Hellman, M. S. Ejneby, M. J. Donahue, P. Ekström, F. Ek, M. Savvakis, M. Hjort, D. Bliman, M. Linares, C. Lindholm, E. Stavrinidou, J. Y. Gerasimov, D. T. Simon, R. Olsson, and M. Berggren, "Metabolite-induced in vivo fabrication of substrate-free organic bioelectronics," *Science*, vol. 379, no. 6634, pp. 795–802, 2023. [Online]. Available: https://doi.org/10.1126/science.adc9998

[138] S. K. Verma, A. Nandi, A. Sinha, P. Patel, S. Mohanty, E. Jha, S. Jena, P. Kumari, A. Ghosh, I. Jerman, R. S. Chouhan, A. Dutt, S. K. Samal, Y. K. Mishra, R. S. Varma, P. K. Panda, N. K. Kaushik, D. Singh, and M. Suar, "The posterity of Zebrafish in paradigm of in vivo molecular toxicological profiling," *Biomedicine and Pharmacotherapy*, vol. 171, 2024. [Online]. Available: https://doi.org/10.1016/j.biopha.2024.116160

[139] J. Liu, Y. S. Kim, C. E. Richardson, A. Tom, C. Ramakrishnan, F. Birey, T. Katsumata, S. Chen, C. Wang, X. Wang, L.-M. Joubert, Y. Jiang, H. Wang, L. E. Fenno, J. B.-H. Tok, S. P. Paşca, K. Shen, Z. Bao, and K. Deisseroth, "Genetically targeted chemical assembly of functional materials in living cells, tissues, and animals," *Science*, vol. 367, no. 6484, pp. 1372–1376, 2020. [Online]. Available: https://doi.org/10.1126/science.aay4866

[140] M. D. Larrañaga, R. J. Sr. Lewis, and R. A. Lewis, "Pyrrole," in *Hawley's Condensed Chemical Dictionary, Sixteenth Edition*, M. D. Larrañaga, Ed. Wiley, 2016, p. 3008. [Online]. Available: https://doi.org/10.1002/9781119312468.ch16

[141] J. McMurry and D. Tully, "Heterocyclic Amines," in *Organic Chemistry: A Tenth Edition*, 10th ed., D. Tully, Ed. OpenStax, 2023, ch. 24.9. [Online]. Available: https://ncstate.pressbooks.pub/organicchem/chapter/heterocyclic-amines/

[142] V. Bhardwaj, D. Gumber, V. Abbot, S. Dhiman, and P. Sharma, "Pyrrole: A resourceful small molecule in key medicinal hetero-aromatics," *RSC Advances*, vol. 5, no. 20, pp. 15 233–15 266, 2015. [Online]. Available: https://doi.org/10.1039/c4ra15710a

[143] A. Domagala, T. Jarosz, and M. Lapkowski, "Living on pyrrolic foundations – Advances in natural and artificial bioactive pyrrole derivatives," *European Journal of Medicinal Chemistry*, vol. 100, pp. 176–187, 2015. [Online]. Available: https://doi.org/10.1016/j.ejmech.2015.06.009

[144] R. I. Sugimoto, K. Yoshino, and S. Hayashi, "Preparation and Properties of Conducting Heterocyclic Polymer Films by Chemical Method," *Japanese Journal of Applied Physics*, vol. 23, no. 12, pp. L899–L900, 1984. [Online]. Available: https://doi.org/10.1143/jjap.23.l899

[145] A. F. Diaz, K. K. Kanazawa, and G. P. Gardini, "Electrochemical polymerization of pyrrole," *Journal of the Chemical Society, Chemical Communications*, no. 14, pp. 635–636, 1979. [Online]. Available: https://doi.org/10.1039/c39790000635

[146] P. G. Pickup and R. A. Osteryoung, "Electrochemical Polymerization of Pyrrole and Electrochemistry of Polypyrrole Films in Ambient Temperature Molten Salts," *Journal of the American Chemical Society*, vol. 106, no. 8, pp. 2294–2299, 1984. [Online]. Available: https://doi.org/10.1021/ja00320a014

[147] C. K. Baker and J. R. Reynolds, "A quartz microbalance study of the electrosynthesis of polypyrrole," *Journal of Electroanalytical Chemistry and Interfacial Electrochemistry*, vol. 251, no. 2, pp. 307–322, 1988. [Online]. Available: https://doi.org/10.1016/0022-0728(88)85192-1

[148] S. Sadki, P. Schottland, N. Brodie, G. Sabouraud, S. Sa¨ıd, and S. Dr, "The mechanisms of pyrrole electropolymerization," *Chemical Society Reviews*, vol. 29, pp. 283–293, 2000. [Online]. Available: https://doi.org/10.1039/a807124a

[149] X. Wang, X. Gu, C. Yuan, S. Chen, P. Zhang, T. Zhang, J. Yao, F. Chen, and G. Chen, "Evaluation of biocompatibility of polypyrrole in vitro and in vivo," *Journal of Biomedical Materials Research - Part A*, vol. 68, no. 3, pp. 411–422, 2004. [Online]. Available: https://doi.org/10.1002/jbm.a.20065

[150] I. Uzieliene, A. Popov, R. Vaiciuleviciute, G. Kirdaite, E. Bernotiene, and A. Ramanaviciene, "Polypyrrole-based structures for activation of cellular functions under electrical stimulation," *Bioelectrochemistry*, vol. 155, p. 108585, 2024. [Online]. Available: https://doi.org/10.1016/j.bioelechem.2023.108585

[151] F. Yin, D. Wang, Z. Zhang, C. Zhang, and Y. Zhang, "Synthesis of mesoporous hollow polypyrrole spheres and the utilization as supports of high loading of Pt nanoparticles," *Materials Letters*, vol. 207, pp. 225–229, 2017. [Online]. Available: https://doi.org/10.1016/j.matlet.2017.07.074

[152] V. Vinothkumar, G. Kesavan, and S. M. Chen, "Graphitic carbon nitride nanosheets incorporated with polypyrrole nanocomposite: A sensitive metal-free electrocatalyst for determination of antibiotic drug nitrofurantoin," *Colloids and Surfaces A: Physicochemical and Engineering Aspects*, vol. 629, 2021. [Online]. Available: https://doi.org/10.1016/j.colsurfa.2021.127433

[153] Y. Cong, S. Liu, and H. Chen, "Fabrication of conductive polypyrrole nanofibers by electrospinning," *Journal of Nanomaterials*, 2013. [Online]. Available: https://doi.org/10.1155/2013/148347

[154] X. Yang, L. Cao, J. Wang, and L. Chen, "Sandwich-like Polypyrrole/Reduced Graphene Oxide Nanosheets Integrated Gelatin Hydrogel as Mechanically and Thermally Sensitive Skinlike Bioelectronics," *ACS Sustainable Chemistry and Engineering*, vol. 8, no. 29, pp. 10 726–10 739, 2020. [Online]. Available: https://doi.org/10.1021/acssuschemeng.0c01998

[155] D. Esrafilzadeh, J. M. Razal, S. E. Moulton, E. M. Stewart, and G. G. Wallace, "Multifunctional conducting fibres with electrically controlled release of ciprofloxacin," *Journal of Controlled Release*, vol. 169, no. 3, pp. 313–320, 2013. [Online]. Available: https://doi.org/10.1016/j.jconrel.2013.01.022

[156] S. Jiang, Y. Sun, X. Cui, X. Huang, Y. He, S. Ji, W. Shi, and D. Ge, "Enhanced drug loading capacity of polypyrrole nanowire network for controlled drug release," *Synthetic Metals*, vol. 163, no. 1, pp. 19–23, 2013. [Online]. Available: https://doi.org/10.1016/j.synthmet.2012.12.010

[157] C. E. Schmidt, V. R. Shastri, J. P. Vacanti, and R. Langer, "Stimulation of neurite outgrowth using an electrically conducting polymer," *Proceedings of the National Academy of Sciences of the United States of America*, vol. 94, no. 17, pp. 8948–8953, 1997. [Online]. Available: https://doi.org/10.1073/pnas.94.17.8948

[158] B. Weng, X. Liu, R. Shepherd, and G. G. Wallace, "Inkjet printed polypyrrole/collagen scaffold: A combination of spatial control and electrical stimulation of PC12 cells," *Synthetic Metals*, vol. 162, no. 15-16, pp. 1375–1380, 2012. [Online]. Available: https://doi.org/10.1016/j.synthmet.2012.05.022

[159] J. G. Hardy, M. K. Villancio-Wolter, R. C. Sukhavasi, D. J. Mouser, D. Aguilar, S. A. Geissler, D. L. Kaplan, and C. E. Schmidt, "Electrical Stimulation of Human Mesenchymal Stem Cells on Conductive Nanofibers Enhances their Differentiation toward Osteogenic Outcomes," *Macromolecular Rapid Communications*, vol. 36, no. 21, pp. 1884–1890, 2015. [Online]. Available: https://doi.org/10.1002/marc.201500233

[160] R.-B. Song, Y. Wu, Z.-Q. Lin, J. Xie, C. H. Tan, J. S. C. Loo, B. Cao, J.-R. Zhang, J.-J. Zhu, and Qichun Zhang, "Living and Conducting Coating Individual Bacterial Cells with In Situ Formed Polypyrrole," *Angewandte Chemie International Edition*, vol. 56, no. 35, pp. 10 516–10 520, 2017. [Online]. Available: https://doi.org/10.1002/anie.201704729

[161] Y. Y. Yu, H. L. Chen, Y. C. Yong, D.-H. Kim, and H. Song, "Conductive artificial biofilm dramatically enhances bioelectricity production in Shewanella-inoculated microbial fuel cells," *Chemical Communications*, vol. 47, no. 48, pp. 12 825–12 827, 2011. [Online]. Available: https://doi.org/10.1039/c1cc15874k

[162] A. Ramanavicius, E. Andriukonis, A. Stirke, L. Mikoliunaite, Z. Balevicius, and A. Ramanaviciene, "Synthesis of polypyrrole within the cell wall of yeast by redox-cycling of [Fe(CN)6]3-/[Fe(CN)6]4-," *Enzyme and Microbial Technology*, vol. 83, pp. 40–47, 2016.

[163] J. D. Ly and A. Lawen, "Transplasma membrane electron transport: enzymes involved and biological function," *Redox Report*, vol. 8, no. 1, pp. 3–21, 2003. [Online]. Available: https://doi.org/10.1179/135100003125001198

[164] V. M. Chauhan, G. Orsi, A. Brown, D. I. Pritchard, and J. W. Aylott, "Mapping the pharyngeal and intestinal pH of Caenorhabditis elegans and real-time luminal pH oscillations using extended dynamic range pH-sensitive nanosensors," *ACS Nano*, vol. 7, no. 6, pp. 5577–5587, 2013. [Online]. Available: https://doi.org/10.1021/nn401856u

[165] W. L. Nicholas, E. C. Dougherty, and E. L. Hansen, "Axenic Cultivation Of Caenorharditis Briggsae (Nematoda: Rhabditidae) With Chemically Undefined Supplements; Comparative Studies With Related Nematodes," *Annals of the New York Academy of Sciences*, vol. 77, no. 2, pp. 218–236, 1959. [Online]. Available: https://doi.org/10.1111/j.1749-6632.1959.tb36902.x

[166] S. Brenner, "The Genetics of Caenorhabditis Elegans," *Genetics*, vol. 77, no. 1, pp. 71–94, 5 1974. [Online]. Available: https://dx.doi.org/10.1093/genetics/77.1.71

[167] Z. F. Altun and D. H. Hall, "Handbook of C. elegans Anatomy. In WormAtlas." 2024. [Online]. Available: http://www.wormatlas.org/hermaphrodite/hermaphroditehomepage.htm

[168] A. K. Corsi, B. Wightman, and M. Chalfie, "A Transparent window into biology: A primer on Caenorhabditis elegans," in *WormBook*, The C. elegans Research Community, Ed. WormBook, 2015, pp. 1–31. [Online]. Available: https://doi.org/10.1895/wormbook.1.177.1

[169] N. Fielenbach and A. Antebi, "C. elegans dauer formation and the molecular basis of plasticity," *Genes and Development*, vol. 22, no. 16, pp. 2149–2165, 2008. [Online]. Available: https://doi.org/10.1101/gad.1701508

[170] D. L. Riddle, T. Blumenthal, B. J. Meyer, and J. R. Priess, "The Dauer State," 1997. [Online]. Available: https://www.ncbi.nlm.nih.gov/books/NBK20053/

[171] A. Pandey and G. K. Pandey, *The UNC-53-mediated Interactome*, ser. SpringerBriefs in Neuroscience. Cham: Springer International Publishing, 2014. [Online]. Available: https://doi.org/10.1007/978-3-319-07827-4

[172] W. M. S. Russell and R. L. Burch, "The Principles of Replacement," in *The Principles of Humane Experimental Technique*. Wheathampstead, UK: Universities Federation for Animal Welfare, 1992, pp. 1–11. [Online]. Available: https://caat.jhsph.edu/wp-content/uploads/2023/08/22.-The-Principles-of-Replacement.pdf

[173] "Animals (Scientific Procedures) Act 1986," London, UK, 1986. [Online]. Available: https://www.legislation.gov.uk/ukpga/1986/14

[174] N. P. Long, J. S. Kang, and H. M. Kim, "Caenorhabditis elegans: a model organism in the toxicity assessment of environmental pollutants," *Environmental Science and Pollution Research*, vol. 30, no. 14, pp. 39 273–39 287, 2023. [Online]. Available: https://doi.org/10.1007/s11356-023-25675-5

[175] P. R. Hunt, "The C. elegans model in toxicity testing," *Journal of Applied Toxicology*, vol. 37, no. 1, pp. 50–59, 1 2017. [Online]. Available: https://doi.org/10.1007/s11356-023-25675-5

[176] P. R. Hunt, N. Olejnik, K. D. Bailey, C. A. Vaught, and R. L. Sprando, "C. elegans Development and Activity Test detects mammalian developmental neurotoxins," *Food and Chemical Toxicology*, vol. 121, pp. 583–592, 2018. [Online]. Available: https://doi.org/10.1007/s11356-023-25675-5

[177] E. A. Engleman, K. B. Steagall, K. E. Bredhold, M. Breach, H. L. Kline, R. L. Bell, S. N. Katner, and B. S. Neal-Beliveau, "Caenorhabditis elegans show preference for stimulants and potential as a model organism for medications screening," *Frontiers in Physiology*, vol. 9, p. 346520, 2018. [Online]. Available: https://doi.org/10.3389/fphys.2018.01200

[178] S. Gao, W. Chen, Y. Zeng, H. Jing, N. Zhang, M. Flavel, M. Jois, J. D. J. Han, B. Xian, and G. Li, "Classification and prediction of toxicity of chemicals using an automated phenotypic profiling of Caenorhabditis elegans," *BMC Pharmacology and Toxicology*, vol. 19, no. 1, pp. 1–11, 2018. [Online]. Available: https://doi.org/10.1186/s40360-018-0208-3

[179] H. Xiong, C. Pears, and A. Woollard, "An enhanced C. elegans based platform for toxicity assessment," *Scientific Reports*, vol. 7, no. 1, pp. 1–11, 2017. [Online]. Available: https://doi.org/10.1038/s41598-017-10454-3

[180] L. D. Marroquin, D. Elyassnia, J. S. Griffitts, J. S. Feitelson, and R. V. Aroian, "Bacillus thuringiensis (Bt) Toxin Susceptibility and Isolation of Resistance Mutants in the Nematode Caenorhabditis elegans," *Genetics*, vol. 155, no. 4, pp. 1693–1699, 2000. [Online]. Available: https://doi.org/10.1093/genetics/155.4.1693

[181] J. Cerón, "Caenorhabditis elegans for research on cancer hallmarks," *Disease Models and Mechanisms*, vol. 16, no. 6, 2023. [Online]. Available: https://dx.doi.org/10.1242/dmm.050079

[182] C. H. Lai, C. Y. Chou, L. Y. Ch'ang, C. S. Liu, and W. C. Lin, "Identification of Novel Human Genes Evolutionarily Conserved in Caenorhabditis elegans by Comparative Proteomics," *Genome Research*, vol. 10, no. 5, pp. 703–713, 2000. [Online]. Available: https://doi.org/10.1101/gr.10.5.703

[183] K. S. Prabhu, F. Ahmad, S. Kuttikrishnan, R. Leo, T. A. Ali, M. Izadi, J. M. Mateo, M. Alam, A. Ahmad, A. S. A.-S. Akil, A. A. Bhat, J. Buddenkotte, E. Pourkarimi, M. Steinhoff, and S. Uddin, "Bortezomib exerts its anti-cancer activity through the regulation of Skp2/p53 axis in non-melanoma skin cancer cells and C. elegans," *Cell Death Discovery*, vol. 10, no. 1, pp. 1–13, 2024. [Online]. Available: https://doi.org/10.1038/s41420-024-01992-7

[184] Z. Zhou, K. Maxeiner, D. Y. W. Ng, and T. Weil, "Polymer Chemistry in Living Cells," *Accounts of Chemical Research*, vol. 55, no. 20, pp. 2998–3009, 2022. [Online]. Available: https://doi.org/10.1021/acs.accounts.2c00420

[185] N. A. A. Rossi, I. Constantinescu, D. E. Brooks, M. D. Scott, and J. N. Kizhakkedathu, "Enhanced Cell Surface Polymer Grafting in Concentrated and Nonreactive Aqueous Polymer Solutions," *Journal of the American Chemical Society*, vol. 132, no. 10, pp. 3423–3430, 2010. [Online]. Available: https://doi.org/10.1021/ja909174x

[186] J. A. Prescher, D. H. Dube, and C. R. Bertozzi, "Chemical remodelling of cell surfaces in living animals," *Nature*, vol. 430, pp. 873–877, 2004. [Online]. Available: https://doi.org/10.1038/nature02791

[187] Y. Teramura and H. Iwata, "Cell surface modification with polymers for biomedical studies," *Soft Matter*, vol. 6, no. 6, pp. 1081–1091, 2010. [Online]. Available: https://doi.org/10.1039/b913621e

[188] J. Geng, W. Li, Y. Zhang, N. Thottappillil, J. Clavadetscher, A. Lilienkampf, and M. Bradley, "Radical polymerization inside living cells," *Nature Chemistry*, vol. 11, no. 6, pp. 578–586, 2019. [Online]. Available: https://dx.doi.org/10.1038/s41557-019-0240-y

[189] A. Tanaka, Y. Fukuoka, Y. Morimoto, T. Honjo, D. Koda, M. Goto, and T. Maruyama, "Cancer cell death induced by the intracellular self-assembly of an enzyme-responsive supramolecular gelator," *Journal of the American Chemical Society*, vol. 137, no. 2, pp. 770–775, 2015. [Online]. Available: https://doi.org/10.1021/ja510156v

[190] L.-L. Li, S. L. Qiao, W. J. Liu, Y. Ma, D. Wan, J. Pan, and H. Wang, "Intracellular construction of topology-controlled polypeptide nanostructures with diverse biological functions," *Nature Communications*, vol. 8, no. 1, 2017. [Online]. Available: https://doi.org/10.1038/s41467-017-01296-8

[191] Y. Wang, X. Hu, J. Weng, J. Li, Q. Fan, Y. Zhang, and D. Ye, "A Photoacoustic Probe for the Imaging of Tumor Apoptosis by Caspase-Mediated Macrocyclization and Self-Assembly," *Angewandte Chemie International Edition*, vol. 58, no. 15, pp. 4886–4890, 2019. [Online]. Available: https://doi.org/10.1002/anie.201813748

[192] A. J. Robinson, A. Jain, H. G. Sherman, R. J. M. Hague, R. Rahman, P. Sanjuan-Alberte, and F. J. Rawson, "Toward Hijacking Bioelectricity in Cancer to Develop New Bioelectronic Medicine," *Advanced Therapeutics*, vol. 4, no. 3, 2021. [Online]. Available: https://doi.org/10.1002/adtp.202000248

[193] Q. Ding, X. Xu, Y. Yue, C. Mei, C. Huang, S. Jiang, Q. Wu, and J. Han, "Nanocellulose-Mediated Electroconductive Self-Healing Hydrogels with High Strength, Plasticity, Viscoelasticity, Stretchability, and Biocompatibility toward Multifunctional Applications," *ACS Applied Materials and Interfaces*, vol. 10, no. 33, pp. 27 987–28 002, 2018. [Online]. Available: https://doi.org/10.1021/acsami.8b09656

[194] J. John and S. Jayalekshmi, "Polypyrrole with appreciable solubility, crystalline order and electrical conductivity synthesized using various dopants appropriate for device applications," *Polymer Bulletin*, vol. 80, no. 6, pp. 6099–6116, 2023. [Online]. Available: https://doi.org/10.1007/s00289-022-04354-4

[195] K. R. Reddy, B. C. Sin, K. S. Ryu, J. Noh, and Y. Lee, "In situ self-organization of carbon black–polyaniline composites from nanospheres to nanorods: Synthesis, morphology, structure and electrical conductivity," *Synthetic Metals*, vol. 159, no. 19-20, pp. 1934–1939, 2009. [Online]. Available: https://doi.org/10.1016/j.synthmet.2009.06.018

[196] F. Khadem, M. Pishvaei, M. Salami-Kalajahi, and F. Najafi, "Morphology control of conducting polypyrrole nanostructures via operational conditions in the emulsion polymerization," *Journal of Applied Polymer Science*, vol. 134, no. 15, 2017. [Online]. Available: https://doi.org/10.1002/app.44697

[197] M. A. Chougule, S. G. Pawar, P. R. Godse, R. N. Mulik, S. Sen, and V. B. Patil, "Synthesis and Characterization of Polypyrrole (PPy) Thin Films," *Soft Nanoscience Letters*, vol. 01, no. 01, pp. 6–10, 2011. [Online]. Available: https://doi.org/10.4236/snl.2011.11002

[198] A. Yussuf, M. Al-Saleh, S. Al-Enezi, and G. Abraham, "Synthesis and Characterization of Conductive Polypyrrole: The Influence of the Oxidants and Monomer on the Electrical, Thermal, and Morphological Properties," *International Journal of Polymer Science*, vol. 2018, no. 1, p. 4191747, 2018. [Online]. Available: https://doi.org/10.1155/2018/4191747

[199] A. A. Bunaciu, V. D. Hoang, and H. Y. Aboul-Enein, "Applications of FT-IR Spectrophotometry in Cancer Diagnostics," *Critical Reviews in Analytical Chemistry*, vol. 45, no. 2, pp. 156–165, 2015. [Online]. Available: https://doi.org/10.1080/10408347.2014.904733

[200] S. K. Bopp and T. Lettieri, "Comparison of four different colorimetric and fluorometric cytotoxicity assays in a zebrafish liver cell line," *BMC Pharmacology*, vol. 8, 2008. [Online]. Available: https://doi.org/10.1186/1471-2210-8-8

[201] M. Xu, D. J. McCanna, and J. G. Sivak, "Use of the viability reagent PrestoBlue in comparison with alamarBlue and MTT to assess the viability of human corneal epithelial cells," *Journal of Pharmacological and Toxicological Methods*, vol. 71, pp. 1–7, 1 2015. [Online]. Available: https://doi.org/10.1016/j.vascn.2014.11.003

[202] Invitrogen, "PrestoBlue Cell Viability Reagent," 2019. [Online]. Available: https://assets.thermofisher.com/TFS-Assets/LSG/manuals/MAN0018370-PrestoBlueCellViabilityReagent-PI.pdf

[203] A. Ramanaviciene, A. Kausaite, S. Tautkus, and A. Ramanavicius, "Biocompatibility of polypyrrole particles: an in-vivo study in mice," *Journal of Pharmacy and Pharmacology*, vol. 59, no. 2, pp. 311–315, 2007. [Online]. Available: https://doi.org/10.1211/jpp.59.2.0017

[204] M. Younes, P. Aggett, F. Aguilar, R. Crebelli, B. Dusemund, M. Filipič, M. J. Frutos, P. Galtier, D. Gott, U. Gundert-Remy, G. G. Kuhnle, C. Lambré, J. C. Leblanc, I. T. Lillegaard, P. Moldeus, A. Mortensen, A. Oskarsson, I. Stankovic, I. Waalkens-Berendsen, M. Wright, A. Di Domenico, H. Van Loveren, A. Giarola, Z. Horvath, F. Lodi, and R. A. Woutersen, "Re-evaluation of sodium ferrocyanide (E 535), potassium ferrocyanide (E 536) and calcium ferrocyanide (E 538) as food additives," *EFSA Journal*, vol. 16, no. 7, p. e05374, 2018. [Online]. Available: https://doi.org/10.2903/j.efsa.2018.5374

[205] O. Toussaint, V. Royer, M. Salmon, and J. Remacle, "Stress-induced premature senescence and tissue ageing," *Biochemical Pharmacology*, vol. 64, no. 5-6, pp. 1007–1009, 2002. [Online]. Available: https://doi.org/10.1016/s0006-2952(02)01170-x

[206] M. C. Willingham, "Cytochemical methods for the detection of apoptosis," *Journal of Histochemistry and Cytochemistry*, vol. 47, no. 9, pp. 1101–1109, 1999. [Online]. Available: https://doi.org/10.1177/002215549904700901

[207] S. Budavari, "1H-Pyrrole," in *The Merck Index : An Encyclopedia of Chemicals, Drugs, and Biologicals*, 15th ed., M. J. O'Neil, P. E. Heckelman, P. H. Dobbelaar, and K. J. Roman, Eds. Cambridge, UK: The Royal Society of Chemistry, 2013, p. 8131.

[208] C. He, Y. Hu, L. Yin, C. Tang, and C. Yin, "Effects of particle size and surface charge on cellular uptake and biodistribution of polymeric nanoparticles," *Biomaterials*, vol. 31, no. 13, pp. 3657–3666, 2010. [Online]. Available: https://10.1016/j.biomaterials.2010.01.065

[209] Q. Xia, J. Huang, Q. Feng, X. Chen, X. Liu, X. Li, T. Zhang, S. Xiao, H. Li, Z. Zhong, and K. Xiao, "Size- and cell type-dependent cellular uptake, cytotoxicity and in vivo distribution of gold nanoparticles," *International Journal of Nanomedicine*, vol. 14, 2019. [Online]. Available: https://doi.org/10.2147/ijn.s214008

[210] R. Cruz-Silva, E. Amaro, A. Escamilla, M. E. Nicho, S. Sepulveda-Guzman, L. Arizmendi, J. Romero-Garcia, F. F. Castillon-Barraza, and M. H. Farias, "Biocatalytic synthesis of polypyrrole powder, colloids, and films using horseradish peroxidase," *Journal of Colloid and Interface Science*, vol. 328, no. 2, pp. 263–269, 2008. [Online]. Available: https://doi.org/10.1016/j.jcis.2008.09.021

[211] ASTM Standards, "ASTM E2490-09 (8.9.1)," Tech. Rep., 2021. [Online]. Available: https://www.astm.org/e2490-09r21.html

[212] Institute for Reference Materials and Measurements, T. P. J. Linsinger, G. Roebben, D. Gilliland, L. Calzolai, F. Rossi, N. Gibson, and C. Klein, "Requirements on measurements for the implementation of the European Commission definition of the term 'nanomaterial'," Publications Office of the European Union, Tech. Rep., 2012. [Online]. Available: https://doi.org/10.2787/63490

[213] J. L. Bredas, J. C. Scott, K. Yakushi, and G. B. Street, "Polarons and bipolarons in polypyrrole: Evolution of the band structure and optical spectrum upon doping," *Physical Review B*, vol. 30, no. 2, pp. 1023–1025, 1984. [Online]. Available: https://doi.org/10.1103/physrevb.30.1023

[214] S. Okur and U. Salzner, "Theoretical modeling of the doping process in polypyrrole by calculating UV/vis absorption spectra of neutral and charged oligomers," *Journal of Physical Chemistry A*, vol. 112, no. 46, pp. 11 842–11 853, 2008. [Online]. Available: https://doi.org/10.1021/jp8063257

[215] M. H. Chakrabarti and E. P. L. Roberts, "Analysis of Mixtures of Ferrocyanide and Ferricyanide using UV-Visible Spectroscopy for Characterisation of a Novel Redox Flow Battery," *Journal of The Chemical Society of Pakistan*, vol. 30, no. 6, pp. 817–823, 2008. [Online]. Available: https://jcsp.org.pk/ArticleUpload/553-2340-1-CE.pdf

[216] Metrohm AG, "AN-SEC-003: UV-Vis spectroelectrochemical cell for conventional electrodes," Metrohm AG, Ionenstrasse, Tech. Rep., 2023. [Online]. Available: https://www.metrohm.com/fr_fr/applications/application-notes/dropsens-applikationen-andropsens/an-sec-003.html

[217] J. Ojeda, C. A. Arrell, L. Longetti, M. Chergui, and J. Helbing, "Charge-transfer and impulsive electronic-to-vibrational energy conversion in ferricyanide: ultrafast photoelectron and transient infrared studies," *Physical Chemistry Chemical Physics*, vol. 19, pp. 17 052–17 062, 2017. [Online]. Available: https://doi.org/10.1039/c7cp03337k

[218] R. M. Jay, J. Norell, S. Eckert, M. Hantschmann, M. Beye, B. Kennedy, W. Quevedo, W. F. Schlotter, G. L. Dakovski, M. P. Minitti, M. C. Hoffmann, Ankush Mitra, S. P. Moeller, D. Nordlund, W. Zhang, H. W. Liang, K. Kunnus, K. Kubiček, S. A. Techert, M. Lundberg, Philippe Wernet, K. Gaffney, M. Odelius, and A. Föhlisch, "Disentangling Transient Charge Density and Metal-Ligand Covalency in Photoexcited Ferricyanide with Femtosecond Resonant Inelastic Soft X-ray Scattering," *Journal of Physical Chemistry Letters*, vol. 9, no. 12, pp. 3538–3543, 2018. [Online]. Available: https://doi.org/10.1021/acs.jpclett.8b01429

[219] Y. Fu, Y.-S. Su, and A. Manthiram, "Sulfur-Polypyrrole Composite Cathodes for Lithium-Sulfur Batteries," *Journal of The Electrochemical Society*, vol. 159, no. 9, pp. A1420–A1424, 2012.

[220] N. F. Antariksa, T. Yamada, and N. Kimizuka, "High seebeck coefficient in middle-temperature thermocell with deep eutectic solvent," *Scientific Reports*, vol. 11, no. 1, pp. 1–7, 2021. [Online]. Available: https://doi.org/10.1038/s41598-021-91419-5

[221] N. V. Blinova, J. Stejskal, M. Trchová, J. Prokeš, and M. A. Omastová, "Polyaniline and polypyrrole: A comparative study of the preparation," *European Polymer Journal*, vol. 43, no. 6, pp. 2331–2341, 2007. [Online]. Available: https://doi.org/10.1016/j.eurpolymj.2007.03.045

[222] Z. Ahmad, M. A. Choudhary, A. Mehmood, R. Wakeel, T. Akhtar, and M. A. Rafiq, "Synthesis of polypyrrole nano/microspheres using cobalt(III) as an oxidizing agent and its ammonia sensing behavior," *Macromolecular Research*, vol. 24, no. 7, pp. 596–601, 2016. [Online]. Available: https://dx.doi.org/10.1007/s13233-016-4081-x

[223] M. Tanzifi, Z. Taghipour Kolaeib, M. Kolbadi nezhadc, and M. Roushan, "Characterization of Polypyrrole Hydroxyethyl Cellulose/TiO2 Nanocomposite: Thermal Properties and AFM Analysis," *IJE Transactions B: Applications*, vol. 28, pp. 654–661, 2015. [Online]. Available: https://www.researchgate.net/publication/282060743

[224] NIST Mass Spectrometry Data Center and W. E. Wallace, "Infrared Spectra," in *NIST Chemistry WebBook, NIST Standard Reference Database Number 69*, P. J. Linstrom and W. G. Mallard, Eds. Gaithersburg MD: National Institute of Standards and Technology, 2023, vol. 20899. [Online]. Available: https://doi.org/10.18434/t4d303

[225] M. Forsyth and V. T. Truong, "Structural characterization of conducting polypyrrole using 13C cross-polarization/ magic-angle spinning solid-state nuclear magnetic resonance spectroscopy," *Polymer*, vol. 35, no. 8, pp. 1593–1601, 1994. [Online]. Available: https://doi.org/10.1016/0032-3861(94)90832-x

[226] G. B. Street, T. C. Clarke, M. Krounbi, K. Kanazawa, V. Lee, P. Pfluger, J. C. Scott, and G. Weiser, "Preparation and Characterization of Neutral and Oxidized Polypyrrole Films," *Molecular Crystals and Liquid Crystals*, vol. 83, pp. 1–12, 1982. [Online]. Available: https://doi.org/10.1080/00268948208072174

[227] F. Devreux, G. Bidan, A. A. Syed, and C. Tsintavis, "Solid state 13C NMR in conducting polymers," *Journal de Physique*, vol. 46, no. 9, pp. 1595–1601, 1985. [Online]. Available: http://dx.doi.org/10.1051/jphys:019850046090159500

[228] K. K. Zborowski and J. Poater, "Pyrrole and Pyridine in the Water Environment—Effect of Discrete and Continuum Solvation Models," *ACS Omega*, vol. 6, no. 38, pp. 24 693–24 699, 2021. [Online]. Available: https://doi.org/10.1021/acsomega.1c03437

[229] C. Yuan, J. Gao, J. Guo, L. Bai, C. Marshall, Z. Cai, L. Wang, and M. Xiao, "Dimethyl Sulfoxide Damages Mitochondrial Integrity and Membrane Potential in Cultured Astrocytes," *PLOS ONE*, vol. 9, no. 9, p. 107447, 2014. [Online]. Available: https://doi.org/10.1371/journal.pone.0107447

[230] J. L. Hanslick, K. Lau, K. K. Noguchi, J. W. Olney, C. F. Zorumski, S. Mennerick, and N. B. Farber, "Dimethyl Sulfoxide (DMSO) Produces Widespread Apoptosis in the Developing Central Nervous System," *Neurobiology of Disease*, vol. 34, no. 1, pp. 1–10, 4 2009. [Online]. Available: https://doi.org/10.1016/j.nbd.2008.11.006

[231] C. Zhang, Y. Deng, H. Dai, W. Zhou, J. Tian, G. Bing, and L. Zhao, "Effects of dimethyl sulfoxide on the morphology and viability of primary cultured neurons and astrocytes," *Brain Research Bulletin*, vol. 128, pp. 34–39, 2017. [Online]. Available: https://doi.org/10.1016/j.brainresbull.2016.11.004

[232] A. Casado, M. Mora, M. L. Sagrista, S. Rello-Varona, P. Acedo, J. C. Stockert, M. Cañete, and A. Villanueva, "Improved selectivity and cytotoxic effects of irinotecan via liposomal delivery: A comparative study on Hs68 and HeLa cells," *European Journal of Pharmaceutical Sciences*, vol. 109, pp. 65–77, 11 2017. [Online]. Available: https://doi.org/10.1016/j.ejps.2017.07.024

[233] B. H. Neufeld, J. B. Tapia, A. Lutzke, and M. M. Reynolds, "Small Molecule Interferences in Resazurin and MTT-Based Metabolic Assays in the Absence of Cells," *Analytical Chemistry*, vol. 90, no. 11, pp. 6867–6876, 2018. [Online]. Available: https://doi.org/10.1021/acs.analchem.8b01043

[234] W. L. He, Y. Feng, X. L. Li, Y. Y. Wei, and X. E. Yang, "Availability and toxicity of Fe(II) and Fe(III) in Caco-2 cells," *Journal of Zhejiang University: Science B*, vol. 9, no. 9, pp. 707–712, 2008. [Online]. Available: https://doi.org/10.1631/jzus.b0820023

[235] S. Chamnongpol, W. Dodson, M. J. Cromie, Z. L. Harris, and E. A. Groisman, "Fe(III)-mediated cellular toxicity," *Molecular Microbiology*, vol. 45, no. 3, pp. 711–719, 2002. [Online]. Available: https://doi.org/10.1046/j.1365-2958.2002.03041.x

[236] R. J. Cavanagh, S. Baquain, C. Alexander, O. A. Scherman, and R. Rahman, "Supramolecular hydrogels enable co-delivery of chemotherapeutics with synergistic efficacy against patient-derived glioblastoma cells and spheroids," *RSC Pharmaceutics*, no. 4, 2024. [Online]. Available: https://doi.org/10.1039/d4pm00177j

[237] S. Elmore, "Apoptosis: A Review of Programmed Cell Death," *Toxicologic Pathology*, vol. 35, no. 4, pp. 495–516, 2007. [Online]. Available: https://doi.org/10.1080/01926230701320337

[238] S. L. Fink and B. T. Cookson, "Apoptosis, Pyroptosis, and Necrosis: Mechanistic Description of Dead and Dying Eukaryotic Cells," *Infection and Immunity*, vol. 73, no. 4, pp. 1907–1916, 2005. [Online]. Available: https://doi.org/10.1128/iai.73.4.1907-1916.2005

[239] A. Gielecińska, M. Kciuk, E. B. Yahya, T. Ainane, S. Mujwar, and R. Kontek, "Apoptosis, necroptosis, and pyroptosis as alternative cell death pathways induced by chemotherapeutic agents?" *Biochimica et Biophysica Acta (BBA) - Reviews on Cancer*, vol. 1878, no. 6, p. 189024, 2023. [Online]. Available: https://doi.org/10.1016/j.bbcan.2023.189024

[240] S.-K. Hsu, C.-Y. Li, I.-L. Lin, W.-J. Syue, Y.-F. Chen, K.-C. Cheng, Y.-N. Teng, Y.-H. Lin, C.-H. Yen, and C.-C. Chiu, "Inflammation-related pyroptosis, a novel programmed cell death pathway, and its crosstalk with immune therapy in cancer treatment," *Theranostics*, vol. 11, no. 18, pp. 8813–8835, 2021. [Online]. Available: http://doi.org/10.7150/thno.62521

[241] S. Du, H. Liang, L. Zhou, C. Chen, R. Sun, J. Zhang, X. Meng, and A. Gao, "Effect of doramectin on programmed cell death pathway in glioma cells," *Clinical and Translational Oncology*, vol. 25, no. 10, pp. 2871–2883, 2023. [Online]. Available: https://doi.org/10.1007/s-023-03147-z

[242] J. Stejskal, M. Kohl, M. Trchová, Z. Kolská, M. Pekárek, I. Křivka, and J. Prokeš, "Conversion of conducting polypyrrole nanostructures to nitrogen-containing carbons and its impact on the adsorption of organic dye," *Materials Advances*, vol. 2, no. 2, pp. 706–717, 2021. [Online]. Available: https://doi.org/10.1039/d0mA00730g

[243] European Medicines Agency (EMA), "Guideline on the principles of regulatory acceptance of 3Rs (replacement, reduction, refinement) testing approaches," European Medicines Agency, London, Tech. Rep., 2016. [Online]. Available: https://www.ema.europa.eu/en/documents/scientific-guideline/guideline-principles-regulatory-acceptance-3rs-replacement-reduction-refinement-testing-approaches_en.pdf

[244] S. Y. Srinivasan, P. A. Illera, D. Kukhtar, N. Benseny-Cases, J. Cerón, J. Álvarez, R. I. Fonteriz, M. Montero, and A. Laromaine, "Arrhythmic Effects Evaluated on Caenorhabditis elegans: The Case of Polypyrrole Nanoparticles," *ACS Nano*, vol. 17, no. 17, pp. 17 273–17 284, 2023. [Online]. Available: http://doi.org/10.1021/acsnano.3c05245

[245] W.-W. Chen, G. A. Lemieux, C. H. Camp, T.-C. Chang, K. Ashrafi, and M. T. Cicerone, "Spectroscopic coherent Raman imaging of Caenorhabditis elegans reveals lipid particle diversity," *Nature Chemical Biology*, vol. 16, no. 10, pp. 1087–1095, 2020. [Online]. Available: https://doi.org/10.1038/s41589-020-0565-2

[246] K. Delaney, J. Mailler, J. M. Wenda, C. Gabus, and F. A. Steiner, "Differential Expression of Histone H3.3 Genes and Their Role in Modulating Temperature Stress Response in Caenorhabditis elegans," *Genetics*, vol. 209, no. 2, pp. 551–565, 2018. [Online]. Available: https://doi.org/10.1534/genetics.118.300909

[247] K. Delaney, M. Strobino, J. M. Wenda, A. Pankowski, and F. A. Steiner, "H3.3K27M-induced chromatin changes drive ectopic replication through misregulation of the JNK pathway in C. elegans," *Nature Communications*, vol. 10, no. 1, 2019. [Online]. Available: https://doi.org/10.1038/s41467-019-10404-9

[248] B. Schumacher, K. Hofmann, S. Boulton, and A. Gartner, "The C. elegans homolog of the p53 tumor suppressor is required for DNA damage-induced apoptosis," *Current Biology*, vol. 11, no. 21, pp. 1722–1727, 2001. [Online]. Available: https://doi.org/10.1016/s0960-9822(01)00534-6

[249] W. B. Derry, A. P. Putzke, and J. H. Rothman, "Caenorhabditis elegans p53: Role in apoptosis, meiosis, and stress resistance," *Science*, vol. 294, no. 5542, pp. 591–595, 2001. [Online]. Available: https://doi.org/10.1126/science.1065486

[250] A. M. Saratsis, T. Knowles, A. Petrovic, and J. Nazarian, "H3K27M mutant glioma: Disease definition and biological underpinnings," *Neuro-Oncology*, vol. 26, no. Suppl 2, pp. S92–S100, 2024. [Online]. Available: https://doi.org/10.1093/neuonc/noad164

[251] T. d. l. R. Corrales, M. Losada-Pérez, and S. Casas-Tintó, "JNK Pathway in CNS Pathologies," *International Journal of Molecular Sciences*, vol. 22, no. 8, p. 3883, 2021. [Online]. Available: https://doi.org/10.3390/ijms22083883

[252] J. Kopecká, M. Mrlík, R. Olejník, D. Kopecký, M. Vř Nata, J. Prokeš, P. Bober, Z. Morávková, M. Trchová, and J. Stejskal, "Polypyrrole Nanotubes and Their Carbonized Analogs: Synthesis, Characterization, Gas Sensing Properties," *Sensors*, vol. 16, no. 11, 2016. [Online]. Available: https://doi.org/10.3390/s16111917

[253] G. C. Arteaga, M. A. del Valle, M. Antilén, M. Romero, A. Ramos, L. Hernández, M. C. Arévalo, E. Pastor, and G. Louarn, "Nucleation and Growth Mechanism of Electro-synthesized Poly(pyrrole) on Steel," *International Journal of Electrochemical Science*, vol. 8, no. 3, pp. 4120–4130, 2013. [Online]. Available: https://doi.org/10.1016/s1452-3981(23)14458-0

[254] M. Trchová and J. Stejskal, "Resonance Raman Spectroscopy of Conducting Polypyrrole Nanotubes: Disordered Surface versus Ordered Body," *Journal of Physical Chemistry A*, vol. 122, no. 48, pp. 9298–9306, 2018. [Online]. Available: https://doi.org/10.1021/acs.jpca.8b09794

[255] J. R. Hellinga, J. Krucken, H. Schulenburg, and G. von Samson-Himmelstjerna, "Use of Viscous medium to study anthelmintic drug action in Caenorhabditis elegans," *Scientific Reports*, vol. 14, no. 1, pp. 1–11, 2024. [Online]. Available: https://doi.org/10.1038/s41598-024-63090-z

[256] B. T. Moore, J. M. Jordan, and L. R. Baugh, "WormSizer: high-throughput analysis of nematode size and shape," *PLOS One*, vol. 8, no. 2, 2013. [Online]. Available: https://doi.org/10.1371/journal.pone.0057142

[257] K. I. Lawas, S. Doliente, R. Carpio, V. Migo, and C. Alfafara, "Parametric study of corn cob biochar (CCBc) yield via microwave pyrolysis," *MATEC Web of Conferences*, vol. 268, no. 04005, 2019. [Online]. Available: https://doi.org/10.1051/matecconf/201926804005

[258] J. Yochem, "Nomarski images for learning the anatomy, with tips for mosaic analysis," in *WormBook*, The C. elegans Research Community, Ed. WormBook, 2006. [Online]. Available: https://doi.org/10.1895/wormbook.1.100.1

[259] R. M. McKay, J. P. McKay, L. Avery, and J. M. Graff, "C. elegans: A model for exploring the genetics of fat storage," *Developmental Cell*, vol. 4, no. 1, pp. 131–142, 2003. [Online]. Available: https://doi.org/10.1016/s1534-5807(02)00411-2

[260] S. Q. Zheng, A. J. Ding, G. P. Li, G. S. Wu, and H. R. Luo, "Drug Absorption Efficiency in Caenorhbditis elegans Delivered by Different Methods," *PLOS ONE*, vol. 8, no. 2, p. e56877, 2013. [Online]. Available: https://doi.org/10.1371/journal.pone.0056877

[261] J. Chen and E. P. Caswell-Chen, "Facultative Vivipary is a Life-History Trait in Caenorhabditis elegans," *Journal of Nematology*, vol. 36, no. 2, pp. 107–113, 2004. [Online]. Available: https://pmc.ncbi.nlm.nih.gov/articles/instance/2620758/pdf/107.pdf

[262] C. Trent, N. Tsuing, and H. R. Horvitz, "Egg-Laying Defective Mutants of the Nematode Caenorhabditis Elegans," *Genetics*, vol. 104, no. 4, pp. 619–647, 1983. [Online]. Available: https://doi.org/10.1093/genetics/104.4.619

[263] V. Sant'anna, W. de Souza, and R. C. Vommaro, "Anthelmintic effect of herbicidal dinitroanilines on the nematode model Caenorhabditis elegans," *Experimental Parasitology*, vol. 167, pp. 43–49, 2016. [Online]. Available: https://doi.org/10.1016/j.exppara.2016.04.017

[264] X. Zhang, R. Bai, and Y. W. Tong, "Selective adsorption behaviors of proteins on polypyrrole-based adsorbents," *Separation and Purification Technology*, vol. 52, no. 1, pp. 161–169, 2006. [Online]. Available: https://doi.org/10.1016/j.seppur.2006.04.001

[265] B. Saoudi, N. Jammul, M.-L. Abel, M. M. Chehimi, and G. Dodin, "DNA adsorption onto conducting polypyrrole," *Synthetic Metals*, vol. 87, no. 2, pp. 97–103, 1997. [Online]. Available: https://doi.org/10.1016/s0379-6779(96)03812-x

[266] M. Q. Cárdenas, A. Oliveira-Menezes, and R. M. Lanfredi, "Effects of albendazole on Litomosoides chagasfilhoi (Nematoda: Filarioidea) females in vivo," *Parasitology Research*, vol. 107, no. 4, pp. 817–826, 2010. [Online]. Available: https://doi.org/10.1007/s00436-010-1934-7

[267] J. D. Popham and J. M. Webster, "Ultrastructural changes in Caenorhabditis elegans (nematoda) caused by toxic levels of mercury and silver," *Ecotoxicology and Environmental Safety*, vol. 6, no. 2, pp. 183–189, 1982. [Online]. Available: https://doi.org/10.1016/0147-6513(82)90007-0

[268] J. G. Ibanez, M. E. Rincón, S. Gutierrez-Granados, M. Chahma, O. A. Jaramillo-Quintero, and B. A. Frontana-Uribe, "Conducting Polymers in the Fields of Energy, Environmental Remediation, and Chemical-Chiral Sensors," *Chemical reviews*, vol. 118, no. 9, pp. 4731–4816, 2018. [Online]. Available: https://doi.org/10.1021/acs.chemrev.7b00482

[269] B. I. Łydzba-Kopczyńska, K. B. Beć, J. Tomczak, and J. P. Hawranek, "Optical constants of liquid pyrrole in the infrared," *Journal of Molecular Liquids*, vol. 172, pp. 34–40, 2012. [Online]. Available: https://doi.org/10.1016/j.molliq.2012.05.009

[270] G. Panczer, D. De Ligny, C. Mendoza, M. Gaft, A.-M. Seydoux-Guillaume, and X. Wang, "Raman and fluorescence," in *European Mineralogical Union Notes in Mineralogy*, J. Dubessy, M.-C. Caumon, and F. Rull, Eds. European Mineralogical Union, 2012, vol. 12, ch. 2, pp. 1–22. [Online]. Available: https://doi.org/10.1180/emu-notes.12

[271] C. Korzeniewski, M. W. Severson, P. P. Schmidt, S. Pons, and M. Fleischmann, "Theoretical analysis of the vibrational spectra of ferricyanide and ferrocyanide adsorbed on metal electrodes," *Journal of Physical Chemistry*, vol. 91, no. 22, pp. 5568–5573, 1987. [Online]. Available: https://doi.org/10.1021/j100306a015

[272] M. Fleischmann, P. R. Graves, and J. Robinson, "The raman spectroscopy of the ferricyanide/ferrocyanide system at gold, β-palladium hydride and platinum electrodes," *Journal of Electroanalytical Chemistry*, vol. 182, no. 1, pp. 87–98, 1985. [Online]. Available: https://doi.org/10.1016/0368-1874(85)85442-3

[273] A. Habekost, "Combining Optical and Raman Spectroscopy with Electrochemistry: The Ferricyanide and Ferrocyanide System-Experiments for Undergraduates," *World Journal of Chemical Education*, vol. 12, no. 1, pp. 30–38, 2024. [Online]. Available: https://doi.org/10.12691/wjce-12-1-5

[274] S. J. Vigmond, V. Ghaemmaghami, and M. Thompson, "Raman and resonance-Raman spectra of polypyrrole with application to sensor - gas probe interactions," *Canadian Journal of Chemistry*, vol. 73, pp. 1711–1718, 1995. [Online]. Available: https://doi.org/10.1139/v95-209

[275] F. Chen, G. Shi, M. Fu, L. Qu, and X. Hong, "Raman spectroscopic evidence of thickness dependence of the doping level of electrochemically deposited polypyrrole film," *Synthetic Metals*, vol. 132, no. 2, pp. 125–132, 2003. [Online]. Available: https://doi.org/10.1016/s0379-6779(02)00197-2

[276] A. A. Nekrasov, O. D. Iakobson, and O. L. Gribkova, "Raman spectroelectrochemical study of pyrrole electropolymerization in the presence of sulfonated polyelectrolytes," *Electrochimica Acta*, vol. 390, p. 138869, 2021. [Online]. Available: https://doi.org/10.1016/j.electacta.2021.138869

[277] R. Poorna, W. W. Chen, P. Qiu, and M. T. Cicerone, "Toward Gene-Correlated Spatially Resolved Metabolomics with Fingerprint Coherent Raman Imaging," *Journal of Physical Chemistry B*, vol. 127, no. 25, pp. 5576–5587, 2023. [Online]. Available: https://doi.org/10.1021/acs.jpcb.3c01446

[278] S. F. Kettle, G. L. Aschero, E. Diana, R. Rossetti, and P. L. Stanghellini, "The vibrational spectra of the cyanide ligand revisited: Terminal cyanides," *Inorganic Chemistry*, vol. 45, no. 13, pp. 4928–4937, 2006. [Online]. Available: https://doi.org/10.1021/ic0514041

[279] D. Weidinger, G. M. Sando, and J. C. Owrutsky, "Vibrational dynamics of metal cyanides," *Chemical Physics Letters*, vol. 489, no. 4-6, pp. 169–174, 2010. [Online]. Available: https://doi.org/10.1016/j.cplett.2010.02.070

[280] G. McColl, S. A. James, S. Mayo, D. L. Howard, C. G. Ryan, R. Kirkham, G. F. Moorhead, D. Paterson, M. D. de Jonge, and A. I. Bush, "Caenorhabditis elegans maintains highly compartmentalized cellular distribution of metals and steep concentration gradients of manganese," *PLOS ONE*, vol. 7, no. 2, 2012. [Online]. Available: https://doi.org/10.1371/journal.pone.0032685

[281] S. Valentini, F. Cabreiro, D. Ackerman, M. M. Alam, M. B. Kunze, C. W. Kay, and D. Gems, "Manipulation of in vivo iron levels can alter resistance to oxidative stress without affecting ageing in the nematode C. elegans," *Mechanisms of Ageing and Development*, vol. 133, no. 5, pp. 282–290, 2012. [Online]. Available: https://doi.org/10.1016/j.mad.2012.03.003

[282] Y.-O. Hu, Y. Wang, B.-P. Ye, and D.-Y. Wang, "Phenotypic and Behavioral Defects Induced by Iron Exposure Can Be Transferred to Progeny in Caenorhabditis elegans 1," *Biomedical and Environmental Sciences*, vol. 21, pp. 467–473, 2008. [Online]. Available: https://doi.org/10.1016/s0895-3988(09)60004-0

[283] P. Chen, E. J. Martinez-Finley, J. Bornhorst, S. Chakraborty, and M. Aschner, "Metal-induced neurodegeneration in C. elegans," *Frontiers in Aging Neuroscience*, vol. 5, 2013. [Online]. Available: https://doi.org/10.3389/fnagi.2013.00018

[284] B. Blume, V. Schwantes, M. Witting, H. Hayen, P. Schmitt-Kopplin, P. O. Helmer, and B. Michalke, "Lipidomic and Metallomic Alteration of Caenorhabditis elegans after Acute and Chronic Manganese, Iron, and Zinc Exposure with a Link to Neurodegenerative Disorders," *Journal of Proteome Research*, vol. 22, no. 3, pp. 837–850, 2023. [Online]. Available: https://doi.org/10.1021/acs.jproteome.2c00578

[285] S. Moyson, R. M. Town, K. Vissenberg, and R. Blust, "The effect of metal mixture composition on toxicity to C. elegans at individual and population levels," *PLOS ONE*, vol. 14, no. 6, p. e0218929, 2019. [Online]. Available: https://doi.org/10.1371/journal.pone.0218929

[286] M. R. Lackner, R. M. Kindt, P. M. Carroll, K. Brown, M. R. Cancilla, C. Chen, H. de Silva, Y. Franke, B. Guan, T. Heuer, T. Hung, K. Keegan, J. M. Lee, V. Manne, C. O'Brien, D. Parry, J. J. Perez-Villar, R. K. Reddy, H. Xiao, H. Zhan, M. Cockett, G. Plowman, K. Fitzgerald, M. Costa, and P. Ross-Macdonald, "Chemical genetics identifies Rab geranylgeranyl transferase as an apoptotic target of farnesyl transferase inhibitors," *Cancer Cell*, vol. 7, no. 4, pp. 325–336, 2005. [Online]. Available: https://doi.org/10.1016/j.ccr.2005.03.024

[287] M. T. Ballo, P. Conlon, G. Lavy-Shahaf, A. Kinzel, J. Vymazal, and A. M. Rulseh, "Association of Tumor Treating Fields (TTFields) therapy with survival in newly diagnosed glioblastoma: a systematic review and meta-analysis," *Journal of Neuro-Oncology*, vol. 164, no. 1, pp. 1–9, 2023. [Online]. Available: https://doi.org/10.1007/s11060-023-04348-w

[288] M. Giladi, R. S. Schneiderman, T. Voloshin, Y. Porat, M. Munster, R. Blat, S. Sherbo, Z. Bomzon, N. Urman, A. Itzhaki, S. Cahal, A. Shteingauz, A. Chaudhry, E. D. Kirson, U. Weinberg, and Y. Palti, "Mitotic Spindle Disruption by Alternating

Electric Fields Leads to Improper Chromosome Segregation and Mitotic Catastrophe in Cancer Cells," *Scientific Reports*, vol. 5, no. 1, 2015. [Online]. Available: https://doi.org/10.1038/srep18046

[289] J. A. Tuszynski, C. Wenger, D. E. Friesen, and J. Preto, "An Overview of Sub-Cellular Mechanisms Involved in the Action of TTFields," *International Journal of Environmental Research and Public Health*, vol. 13, no. 11, 2016. [Online]. Available: https://doi.org/10.3390/ijerph13111128

[290] Novocure, "Launch of the inovitro™ Laboratory Research System," New York, NY, 2013. [Online]. Available: https://www.novocure.com/launch-of-the-inovitro-laboratory-research-system/

[291] Y. Porat, M. Giladi, R. S. Schneiderman, R. Blat, A. Shteingauz, E. Zeevi, M. Munster, T. Voloshin, N. Kaynan, O. Tal, E. D. Kirson, U. Weinberg, and Y. Palti, "Determining the Optimal Inhibitory Frequency for Cancerous Cells Using Tumor Treating Fields (TTFields)," *Journal of Visualized Experiments*, no. 123, 2017. [Online]. Available: https://doi.org/10.3791/55820

[292] A. R. Smothers, J. R. Henderson, J. J. O'Connell, J. M. Stenbeck, D. Dean, T. G. Harvey, and B. W. Booth, "Efficacy and selectivity of tumor-treating field therapy for triple-negative breast cancer cells via in-house delivery device," *Discover Oncology*, vol. 14, no. 1, 2023. [Online]. Available: https://doi.org/10.1007/s12672-023-00647-w

[293] M. Giladi, R. S. Schneiderman, Y. Porat, M. Munster, A. Itzhaki, D. Mordechovich, S. Cahal, E. D. Kirson, U. Weinberg, and Y. Palti, "Mitotic disruption and reduced clonogenicity of pancreatic cancer cells in vitro and in vivo by tumor treating fields," *Pancreatology*, vol. 14, no. 1, pp. 54–63, 2014. [Online]. Available: https://doi.org/10.1016/j.pan.2013.11.009

[294] R. Ravin, T. X. Cai, R. H. Pursley, M. Garmendia-Cedillos, T. Pohida, R. Z. Freidlin, H. Wang, Z. Zhuang, A. J. Giles, N. H. Williamson, M. R. Gilbert, and P. J. Basser, "A Novel In Vitro Device to Deliver Induced Electromagnetic Fields to Cell and Tissue Cultures," *Biophysical Journal*, vol. 119, no. 12, pp. 2378–2390, 2020. [Online]. Available: https://doi.org/10.1016/j.bpj.2020.11.002

[295] Y. Jo, J. Sung, H. Jeong, S. Hong, Y. K. Jeong, E. H. Kim, and M. Yoon, "Effectiveness of a Fractionated Therapy Scheme in Tumor Treating Fields Therapy," *Technology in Cancer Research and Treatment*, vol. 18, 2019. [Online]. Available: https://doi.org/10.1177/1533033819845008

[296] E. Iredale, A. Deweyert, D. A. Hoover, J. Z. Chen, S. Schmid, M. O. Hebb, T. M. Peters, and E. Wong, "Optimization of multi-electrode implant configurations and programming for the delivery of non-ablative electric fields in intratumoral modulation therapy," *Medical Physics*, vol. 47, no. 11, pp. 5441–5454, 2020. [Online]. Available: https://doi.org/10.1002/mp.14496

[297] E. Iredale, A. Elsaleh, H. Xu, P. Christiaans, A. Deweyert, J. Ronald, S. Schmid, M. O. Hebb, T. M. Peters, and E. Wong, "Spatiotemporally dynamic electric fields for brain cancer treatment: an in vitro investigation," *Physics in Medicine and Biology*, vol. 68, no. 8, p. 85012, 2023. [Online]. Available: https://doi.org/10.1088/1361-6560/acc308

[298] H. Nguyen, K. E. Schubert, C. Pohling, E. Chang, V. Yamamoto, Y. Zeng, Y. Nie, S. van Buskirk, R. W. Schulte, and C. B. Patel, "Impact of glioma peritumoral edema, tumor size, and tumor location on alternating electric fields (AEF) therapy in realistic 3D rat glioma models: a computational study," *Physics in Medicine and Biology*, vol. 69, no. 8, 2024. [Online]. Available: https://doi.org/10.1088/1361-6560/ad2e6c

[299] L. Berkelmann, A. Bader, S. Meshksar, A. Dierks, G. H. Majernik, J. K. Krauss, K. Schwabe, D. Manteuffel, and A. Ngezahayo, "Tumour-treating fields (TTFields): Investigations on the mechanism of action by electromagnetic exposure of cells in telophase/cytokinesis," *Scientific Reports*, vol. 9, no. 7362, pp. 1–11, 2019. [Online]. Available: https://dx.doi.org/10.1038/s41598-019-43621-9

[300] C. Wenger, M. Giladi, Z. Bomzon, R. Salvador, P. J. Basser, and P. C. Miranda, "Modeling Tumor Treating Fields (TTFields) application in single cells during metaphase and telophase," in *Annual International Conference of the IEEE Engineering in Medicine and Biology Society*. Milan, Italy: IEEE, 2015, pp. 6892–6895. [Online]. Available: https://doi.org/10.1109/embc.2015.7319977

[301] S. K. Libutti, G. F. Paciotti, A. A. Byrnes, H. R. Alexander, W. E. Gannon, M. Walker, G. D. Seidel, N. Yuldasheva, and L. Tamarkin, "Phase I and Pharmacokinetic Studies of CYT-6091, a Novel PEGylated Colloidal Gold-rhTNF Nanomedicine," *Clinical Cancer Research*, vol. 16, no. 24, pp. 6139–6149, 2010. [Online]. Available: https://doi.org/10.1158/1078-0432.ccr-10-0978

[302] S. C. Gad, K. L. Sharp, C. Montgomery, J. D. Payne, and G. P. Goodrich, "Evaluation of the Toxicity of Intravenous Delivery of Auroshell Particles (Gold–Silica Nanoshells)," *International Journal of Toxicology*, vol. 31, no. 6, pp. 584–594, 2012. [Online]. Available: https://dx.doi.org/10.1177/1091581812465969

[303] P. Sanjuan-Alberte, A. Jain, A. J. Shaw, S. A. Abayzeed, R. F. Domínguez, M. E. Alea-Reyes, M. Clark, M. R. Alexander, R. J. M. Hague, L. Pérez-García, and F. J. Rawson, "Wireless Nanobioelectronics for Electrical Intracellular Sensing," *ACS Applied Nano Materials*, vol. 2, no. 10, pp. 6397–6408, 2019. [Online]. Available: https://doi.org/10.1021/acsanm.9b01374

[304] A. N. Kharlamov, A. E. Tyurnina, V. S. Veselova, O. P. Kovtun, V. Y. Shur, and J. L. Gabinsky, "Silica-gold nanoparticles for atheroprotective management of plaques: Results of the NANOM-FIM trial," *Nanoscale*, vol. 7, no. 17, pp. 8003–8015, 2015. [Online]. Available: https://doi.org/10.1039/c5nr01050k

[305] United States Food and Drug Administration, "182.8991 Zinc Oxide," 2024. [Online]. Available: https://www.ecfr.gov/current/title-21/chapter-I/subchapter-B/part-182/subpart-I/section-182.8991

[306] S. R. Choudhury, J. Ordaz, C. L. Lo, N. P. Damayanti, F. Zhou, and J. Irudayaraj, "From the Cover: Zinc oxide Nanoparticles-Induced Reactive Oxygen Species Promotes Multimodal Cyto- and Epigenetic Toxicity," *Toxicological Sciences*, vol. 156, no. 1, pp. 261–274, 2017. [Online]. Available: https://doi.org/10.1093/toxsci/kfw252

[307] S. Anjum, M. Hashim, S. A. Malik, M. Khan, J. M. Lorenzo, B. H. Abbasi, and C. Hano, "Recent Advances in Zinc Oxide Nanoparticles (ZnO NPs) for Cancer Diagnosis, Target Drug Delivery, and Treatment," *Cancers*, vol. 13, no. 18, p. 4570, 2021. [Online]. Available: https://doi.org/10.3390/cancers13184570

[308] C. Hanley, J. Layne, A. Punnoose, K. M. Reddy, I. Coombs, A. Coombs, K. Feris, and D. Wingett, "Preferential killing of cancer cells and activated human T cells using ZnO nanoparticles," *Nanotechnology*, vol. 19, no. 29, p. 295103, 2008. [Online]. Available: https://doi.org/10.1088/0957-4484/19/29/295103

[309] H. Wang, D. Wingett, M. H. Engelhard, K. Feris, K. M. Reddy, P. Turner, J. Layne, C. Hanley, J. Bell, D. Tenne, C. Wang, and A. Punnoose, "Fluorescent dye encapsulated ZnO particles with cell-specific toxicity for potential use in biomedical applications," *Journal of Materials Science: Materials in Medicine*, vol. 20, no. 1, pp. 11–22, 2009. [Online]. Available: https://doi.org/10.1007/s10856-008-3541-z

[310] K. Patel, S. Angelos, W. R. Dichtel, A. Coskun, Y. W. Yang, J. I. Zink, and J. F. Stoddart, "Enzyme-responsive snap-top covered silica nanocontainers," *Journal of the American Chemical Society*, vol. 130, no. 8, pp. 2382–2383, 2008. [Online]. Available: https://doi.org/10.1021/ja0772086

[311] Z. Li, Y. Mu, C. Peng, M. F. Lavin, H. Shao, and Z. Du, "Understanding the mechanisms of silica nanoparticles for nanomedicine," *Wiley Interdisciplinary Reviews. Nanomedicine and Nanobiotechnology*, vol. 13, no. 1, 2021. [Online]. Available: https://doi.org/10.1002/wnan.1658

[312] A. Jain, I. Jobson, M. Griffin, R. Rahman, S. Smith, and F. J. Rawson, "Electric field responsive nanotransducers for glioblastoma," *Bioelectronic Medicine*, vol. 8, no. 17, pp. 1–9, 2022. [Online]. Available: https://doi.org/10.1186/s42234-022-00099-7

[313] C. E. Vasey, R. J. Cavanagh, V. Taresco, C. Moloney, S. Smith, R. Rahman, and C. Alexander, "Polymer pro-drug nanoparticles for sustained release of cytotoxic drugs evaluated in patient-derived glioblastoma cell lines and in situ gelling formulations," *Pharmaceutics*, vol. 13, no. 2, pp. 1–17, 2021. [Online]. Available: https://doi.org/10.3390/pharmaceutics13020208

[314] R. T. Nitta, E. J. Luo, M. Lim, and G. Li, "Can tumor treating fields induce DNA damage and reduce cell motility in medulloblastoma cell lines?" *Journal of Neurosurgery. Pediatrics*, vol. 30, no. 6, pp. 555–566, 2022. [Online]. Available: https://doi.org/10.3171/2022.8.peds22300

[315] M. D. Cahalan, "How to STIMulate Calcium Channels: Two studies reveal the reciprocal regulation of two different calcium channels," *Science*, vol. 330, no. 6000, pp. 43–44, 2010. [Online]. Available: https://doi.org/10.1126/science.1196348

[316] M. R. Cho, H. S. Thatte, M. T. Silvia, and D. E. Golan, "Transmembrane calcium influx induced by ac electric fields," *The Federation of American Societies for Experimental Biology Journal*, vol. 13, no. 6, pp. 677–683, 1999. [Online]. Available: https://doi.org/10.1096/fasebj.13.6.677

[317] R. P. Trueman, O. Guillemot-Legris, H. T. Lancashire, A. S. Mehta, J. Tropp, R. E. Daso, J. Rivnay, A. B. Tabor, J. B. Phillips, and B. C. Schroeder, "Aligned Bioelectronic Polypyrrole/Collagen Constructs for Peripheral Nerve Interfacing," *Advanced Engineering Materials*, vol. 26, no. 6, 2024. [Online]. Available: https://doi.org/10.1002/adem.202301488

[318] H. Cindric, B. Kos, and D. Miklavcic, "Irreversible electroporation as a novel method for soft tissue ablation: review and challenges in clinical practice," *Slovenian Medical Journal*, vol. 90, no. 1-2, pp. 38–53, 2021. [Online]. Available: https://doi.org/10.6016/zdravvestn.2954

[319] A. Moore, J. Mercer, G. Dutina, C. J. Donahue, K. D. Bauer, J. P. Mather, T. Etcheverry, and T. Ryll, "Effects of temperature shift on cell cycle, apoptosis and nucleotide pools in CHO cell batch cultues," *Cytotechnology*, vol. 23, no. 1-3, p. 47, 1997. [Online]. Available: https://doi.org/10.1023/a:1007919921991

[320] S. C. C. van der Lubbe and P. Canepa, "Modeling the effects of salt concentration on aqueous and organic electrolytes," *npj Computational Materials*, vol. 9, no. 1, 2023. [Online]. Available: https://doi.org/10.1038/s41524-023-01126-0

[321] C. S. Widodo, H. Sela, and D. R. Santosa, "The effect of NaCl concentration on the ionic NaCl solutions electrical impedance value using electrochemical impedance spectroscopy methods," in *The 8th Annual Basic Science International Conference*. East Jaya, Indonesia: AIP Conference Proceedings, 2018. [Online]. Available: https://doi.org/10.1063/1.5062753

[322] M. T. Zahoor, G. A. Khan, M. B. Nawaz, S. Farouk, Z. Imran, and W. Ahmed, "Rapid dielectrophoresis-assisted deposition of highly concentrated ZnO nanowires for enhanced performance of humidity sensors," *Sensors and Actuators A: Physical*, vol. 362, 2023. [Online]. Available: https://doi.org/10.1016/j.sna.2023.114651

[323] T. Pfeifer, L. Bai, J. Gladkich, W. Gross, L. Liu, I. Herr, and M. Schaefer, "Therapy of pancreatic cancer with alternating electric fields: Limitations of the method," *Bioelectrochemistry*, vol. 141, 2021. [Online]. Available: https://doi.org/10.1016/j.bioelechem.2021.107881

[324] A. Pirzkall, C. McGue, S. Saraswathy, S. Cha, R. Liu, S. Vandenberg, K. R. Lamborn, M. S. Berger, S. M. Chang, and S. J. Nelson, "Tumor regrowth between surgery and initiation of adjuvant therapy in patients with newly diagnosed glioblastoma," *Neuro-Oncology*, vol. 11, no. 6, pp. 842–852, 2009. [Online]. Available: https://doi.org/10.1215/15228517-2009-005

[325] K. Petrecca, M. C. Guiot, V. Panet-Raymond, and L. Souhami, "Failure pattern following complete resection plus radiotherapy and temozolomide is at the resection margin in patients with glioblastoma," *Journal of Neuro-Oncology*, vol. 111, no. 1, pp. 19–23, 2013. [Online]. Available: https://doi.org/10.1007/s11060-012-0983-4

[326] S. Kim, W. K. Oh, Y. S. Jeong, J. Y. Hong, B. R. Cho, J. S. Hahn, and J. Jang, "Cytotoxicity of, and innate immune response to, size-controlled polypyrrole nanoparticles in mammalian cells," *Biomaterials*, vol. 32, no. 9, pp. 2342–2350, 2011. [Online]. Available: https://doi.org/10.1016/j.biomaterials.2010.11.080

[327] A. R. Sarhan, B. B. Yousif, N. F. F. Areed, and S. S. Obaya, "Modeling of Fiber Optic Gold SPR Sensor Using Different Dielectric Function Models: A Comparative Study," *Plasmonics*, vol. 15, no. 6, pp. 1699–1707, 2020. [Online]. Available: https://doi.org/10.1007/s11468-020-01179-7

[328] S. V. Vegesna, V. J. Bhat, D. Bürger, J. Dellith, I. Skorupa, O. G. Schmidt, and H. Schmidt, "Increased static dielectric constant in ZnMnO and ZnCoO thin films with bound magnetic polarons," *Scientific Reports*, vol. 10, no. 1, pp. 1–11, 2020. [Online]. Available: https://doi.org/10.1038/s41598-020-63195-1

[329] K. Dutta and S. K. De, "Electrical conductivity and dielectric properties of SiO2 nanoparticles dispersed in conducting polymer matrix," *Journal of Nanoparticle Research*, vol. 9, no. 4, pp. 631–638, 2007. [Online]. Available: https://doi.org/10.1007/s11051-006-9184-4

[330] W. Haiss, N. T. Thanh, J. Aveyard, and D. G. Fernig, "Determination of size and concentration of gold nanoparticles from UV-Vis spectra," *Analytical Chemistry*, vol. 79, no. 11, pp. 4215–4221, 2007. [Online]. Available: https://doi.org/10.1021/ac0702084

[331] V. Amendola and M. Meneghetti, "Size evaluation of gold nanoparticles by UV-vis spectroscopy," *Journal of Physical Chemistry C*, vol. 113, no. 11, pp. 4277–4285, 2009. [Online]. Available: https://doi.org/10.1021/jp8082425

[332] NanoComposix, "Gold Nanoparticles," NanoComposix, San Diego, Tech. Rep. [Online]. Available: https://nanocomposix.com/pages/knowledge-base

[333] R. Khokhra, B. Bharti, H. N. Lee, and R. Kumar, "Visible and UV photo-detection in ZnO nanostructured thin films via simple tuning of solution method," *Scientific Reports*, vol. 7, no. 1, pp. 1–14, 2017. [Online]. Available: https://doi.org/10.1038/s41598-017-15125-x

[334] A. Fouda, S. EL-Din Hassan, S. S. Salem, and T. I. Shaheen, "In-Vitro cytotoxicity, antibacterial, and UV protection properties of the biosynthesized Zinc oxide nanoparticles for medical textile applications," *Microbial Pathogenesis*, vol. 125, pp. 252–261, 2018. [Online]. Available: https://doi.org/10.1016/j.micpath.2018.09.030

[335] K. Talreja, I. Chauhan, A. Ghosh, A. Majumdar, and B. S. Butola, "Functionalization of silica particles to tune the impact resistance of shear thickening fluid treated aramid fabrics," *RSC Advances*, vol. 7, no. 78, pp. 49 787–49 794, 2017. [Online]. Available: https://doi.org/10.1039/c7ra09834k

[336] Y. Wang, Y. Sun, J. Wang, Y. Yang, Y. Li, Y. Yuan, and C. Liu, "Charge-Reversal APTES-Modified Mesoporous Silica Nanoparticles with High Drug Loading and Release Controllability," *ACS Applied Materials and Interfaces*, vol. 8, no. 27, pp. 17 166–17 175, 2016. [Online]. Available: https://doi.org/10.1021/acsami.6b05370

[337] E. Blanco, H. Shen, and M. Ferrari, "Principles of nanoparticle design for overcoming biological barriers to drug delivery," *Nature Biotechnology*, vol. 33, no. 9, p. 941, 2015. [Online]. Available: https://doi.org/10.1038/nbt.3330

[338] D. Zhang, L. Wei, M. Zhong, L. Xiao, H. W. Li, and J. Wang, "The morphology and surface charge-dependent cellular uptake efficiency of upconversion nanostructures revealed by single-particle optical microscopy," *Chemical Science*, vol. 9, no. 23, pp. 5260–5269, 2018. [Online]. Available: https://doi.org/10.1039/c8sc01828f

[339] T. L. Moore, L. Rodriguez-Lorenzo, V. Hirsch, S. Balog, D. Urban, C. Jud, B. Rothen-Rutishauser, M. Lattuada, and A. Petri-Fink, "Nanoparticle colloidal stability in cell culture media and impact on cellular interactions," *Chemical Society Reviews*, vol. 44, no. 17, pp. 6287–6305, 2015. [Online]. Available: https://doi.org/10.1039/c4cs00487f

[340] V. R. Patel and Y. K. Agrawal, "Nanosuspension: An approach to enhance solubility of drugs," *Journal of Advanced Pharmaceutical Technology and Research*, vol. 2, no. 2, p. 81, 2011. [Online]. Available: https://doi.org/10.4103/2231-4040.82950

[341] A. Rostek, D. Mahl, and M. Epple, "Chemical composition of surface-functionalized gold nanoparticles," *Journal of Nanoparticle Research*, vol. 13, no. 10, pp. 4809–4814, 2011. [Online]. Available: https://doi.org/10.1007/s11051-011-0456-2

[342] M. Bonora, S. Patergnani, A. Rimessi, E. de Marchi, J. M. Suski, A. Bononi, C. Giorgi, S. Marchi, S. Missiroli, F. Poletti, M. R. Wieckowski, and P. Pinton, "ATP synthesis and storage," *Purinergic Signalling*, vol. 8, no. 3, pp. 343–357, 2012. [Online]. Available: https://doi.org/10.1007/s11302-012-9305-8

[343] B. D. Chithrani and W. C. Chan, "Elucidating the mechanism of cellular uptake and removal of protein-coated gold nanoparticles of different sizes and shapes," *Nano Letters*, vol. 7, no. 6, pp. 1542–1550, 2007. [Online]. Available: https://doi.org/10.1021/nl070363y

[344] A. J. Robinson, A. Jain, R. Rahman, S. Abayzeed, R. J. Hague, and F. J. Rawson, "Impedimetric Characterization of Bipolar Nanoelectrodes with Cancer Cells," *ACS Omega*, vol. 6, no. 44, pp. 29 495–29 505, 2021. [Online]. Available: https://doi.org/10.1021/acsomega.1c03547

[345] P. Sanjuan-Alberte, E. Saleh, A. J. Shaw, N. Lacalendola, G. Willmott, J. Vaithilingam, M. R. Alexander, R. J. M. Hague, and F. J. Rawson, "Remotely Controlled in Situ Growth of Silver Microwires Forming Bioelectronic Interfaces," *ACS Applied Materials and Interfaces*, vol. 11, no. 9, pp. 8928–8936, 2019. [Online]. Available: https://doi.org/10.1021/acsami.8b22075

[346] J. Cottet, O. Fabregue, C. Berger, F. Buret, P. Renaud, and M. Frénéa-Robin, "MyDEP: A New Computational Tool for Dielectric Modeling of Particles and Cells," *Biophysical Journal*, vol. 116, no. 1, pp. 12–18, 2019. [Online]. Available: https://doi.org/10.1016/j.bpj.2018.11.021

[347] C. Jee and E. Batsaikhan, "JNK Signaling Positively Regulates Acute Ethanol Tolerance in C. elegans," *International Journal of Molecular Sciences*, vol. 25, no. 12, p. 6398, 2024. [Online]. Available: https://doi.org/10.3390/ijms25126398

[348] M. R. Bennett, A. Jain, K. Kovacs, P. J. Hill, C. Alexander, and F. J. Rawson, "Engineering bacteria to control electron transport altering the synthesis of non-native polymer †," *ACS Advances*, vol. 12, pp. 451–457, 2022. [Online]. Available: https://doi.org/10.1039/d1ra06403g

[349] H. G. Sherman, C. Jovanovic, S. Stolnik, and F. J. Rawson, "Electrochemical System for the Study of Trans-Plasma Membrane Electron Transport in Whole Eukaryotic Cells," *Analytical Chemistry*, vol. 90, no. 4, pp. 2780–2786, 2018. [Online]. Available: https://doi.org/10.1021/acs.analchem.7b04853

[350] K. Astanina, Y. Simon, C. Cavelius, S. Petry, A. Kraegeloh, and A. K. Kiemer, "Superparamagnetic iron oxide nanoparticles impair endothelial integrity and inhibit nitric oxide production," *Acta Biomaterialia*, vol. 10, no. 11, pp. 4896–4911, 2014. [Online]. Available: https://doi.org/10.1016/j.actbio.2014.07.027

[351] W. Chen, B. Tian, J. Lan, D. Chen, and Z. Zhu, "Using microfluidic impedance cytometry to identify the life stages of C. elegans nematodes," *19th International Conference on Solid-State Sensors, Actuators and Microsystems (TRANSDUCERS)*, pp. 1628–1631, 2017. [Online]. Available: https://www.beitongtian.com/uploads/TRANSDUCERS2017.pdf

[352] E. Dunbar, D. McCracken, A. Nowlan, K. Dusenbery, C. Ferreira, S. Lee, M. S. Peach, R. Corns, and C. Chen, "GESTALT (GammaTile Enhanced Stupp Alternative): Feasibility Study of Resection and GammaTile Followed by Concomitant External Beam Radiation Therapy (EBRT)/Temozolomide (TMZ) and Adjuvant TMZ in Newly Diagnosed Glioblastoma (GBM) (P13-13.001)," *Neurology*, vol. 100, no. 17_supplement_2, 4 2023. [Online]. Available: https://doi.org/10.1212/wnl.0000000000204100

[353] A. Mequignon, "NCT05736406: A Dose-escalation Clinical Study of Intraoperative Photodynamic Therapy of Glioblastoma," *ClinicalTrials.gov*, 2023. [Online]. Available: https://clinicaltrials.gov/study/NCT05736406

[354] N. Reyns and M. Vermandel, "NCT04391062: Dose Finding for Intraoperative Photodynamic Therapy of Glioblastoma (DOSINDYGO)," *ClinicalTrials.gov*, 2021. [Online]. Available: https://clinicaltrials.gov/study/NCT04391062

[355] P. Siesjo, "NCT05296122: Safety and Feasibility of MR-guided Laser Thermal Ablation of Brain Lesions," *ClinicalTrials.gov*, 2022. [Online]. Available: https://clinicaltrials.gov/study/NCT05296122

[356] M. Mishra and M. A. Camara, "NCT04181684: LITT Followed by Hypofractionated RT for Recurrent Gliomas (GCCC 19140)," *ClinicalTrials.gov*, 2020. [Online]. Available: https://clinicaltrials.gov/study/NCT04181684

[357] S. Michalak and J. Moskal, "NCT06271421: NanoTherm In Adjuvant Therapy of Glioblastoma Multiforme (ANCHIALE)," *ClinicalTrials.gov*, 2024. [Online]. Available: https://clinicaltrials.gov/study/NCT06271421

[358] C. Amidei, "NCT05864534: Phase 2a Immune Modulation With Ultrasound for Newly Diagnosed Glioblastoma," *ClinicalTrials.gov*, 2023. [Online]. Available: https://clinicaltrials.gov/study/NCT05864534

[359] C. Amidei and R. Stupp, "NCT04528680: Ultrasound-based Blood-brain Barrier Opening and Albumin-bound Paclitaxel and Carboplatin for Recurrent Glioblastoma (SC9/ABX)," *ClinicalTrials.gov*, 2020. [Online]. Available: https://www.clinicaltrials.gov/study/NCT04528680

[360] C. Desseaux, "NCT05902169: Sonocloud-9 in Association With Carboplatin Versus Standard-of-Care Chemotherapies (CCNU or TMZ) in Recurrent GBM (SONOBIRD)," *ClinicalTrials.gov*, 2023. [Online]. Available: https://clinicaltrials.gov/study/NCT05902169

[361] S. Nagpal, C. Patel, and G. Li, "NCT04417088: Exablate Blood-Brain Barrier Disruption for the Treatment of rGBM in Subjects Undergoing Carboplatin Monotherapy," *ClinicalTrials.gov*, 2020. [Online]. Available: https://clinicaltrials.gov/study/NCT04417088

[362] InSightec Ltd., "NCT04440358: Exablate Blood-Brain Barrier Disruption With Carboplatin for the Treatment of rGBM," *ClinicalTrials.gov*, 2020. [Online]. Available: https://clinicaltrials.gov/study/NCT04440358

[363] Alpheus Medical Inc., "NCT05362409: Study to Evaluate 5-ALA Combined With CV01 Delivery of Ultrasound in Recurrent High Grade Glioma," *ClinicalTrials.gov*, 2022. [Online]. Available: https://clinicaltrials.gov/study/NCT05362409

[364] S.-T. Fung, "NCT04988750: Evaluate the Safety and Preliminary Efficacy of the Combination of NaviFUS System With Re-irradiation for rGBM Patients," *ClinicalTrials.gov*, 2021. [Online]. Available: https://clinicaltrials.gov/study/NCT04988750

[365] NaviFUS Corporation, "NCT04446416: Efficacy and Safety of NaviFUS System add-on Bevacizumab (BEV) in Recurrent GBM Patients," *ClinicalTrials.gov*, 2020. [Online]. Available: https://clinicaltrials.gov/study/NCT04446416

[366] NaviFUS Corporation., "NCT06496971: A Prospective Pivotal Study to Evaluate the Efficacy and Safety of Avastin Bevacizumab (BEV) With or Without Microbubble-mediated Focused Ultrasound (FUS-MB) Using NaviFUS System in Recurrent Glioblastoma Multiforme Patients," *ClinicalTrials.gov*, 2024. [Online]. Available: https://clinicaltrials.gov/study/NCT06496971

[367] NaviFUS Corporation, "NCT06329570: Safety and Efficacy of Bevacizumab in Combination With NaviFUS System for the Treatment of Recurrent Glioblastoma Multiforme (rGBM)," *ClinicalTrials.gov*, 2024. [Online]. Available: https://clinicaltrials.gov/study/NCT06329570

[368] Assistance Publique - Hopitaux de Paris, "NCT04614493: Innovative SonoCloud-9 Device for Blood Brain Barrier Opening in First Line Temozolomide Glioblastoma Patients. (SonoFIRST)," *ClinicalTrials.gov*, 2020. [Online]. Available: https://clinicaltrials.gov/study/NCT04614493

[369] BioTex Inc., "NCT06533163: Low-Intensity Oscillatory Magnetic Therapy in Patients With Newly Diagnosed Glioblastoma Multiforme (GBM) - An Exposure-time Escalation Pilot Trial (OMX-EFS-01)," *ClinicalTrials.gov*, 2024. [Online]. Available: https://clinicaltrials.gov/study/NCT06533163

[370] P. Ghadjar and D. Kaul, "NCT06140875: Amplitude Modulated Radiofrequency Electromagnetic Field Treatment Combined With Radiochemotherapy and Maintenance Chemotherapy in Patients With Glioblastoma (Brain-RF)," *ClinicalTrials.gov*, 2023. [Online]. Available: https://clinicaltrials.gov/study/NCT06140875

[371] T. M. Johanns, "NCT05743595: Neoantigen-based Personalized DNA Vaccine With Retifanlimab PD-1 Blockade Therapy in Patients With Newly Diagnosed, Unmethylated Glioblastoma," *ClinicalTrials.gov*, 2023. [Online]. Available: https://clinicaltrials.gov/study/NCT05743595

[372] Xiangya Hospital of Central South University, "NCT04417933: Tumor Electric Fields Treatment System for Glioblastoma," *ClinicalTrials.gov*, 2020. [Online]. Available: https://clinicaltrials.gov/study/NCT04417933

[373] University of Pennsylvania, "NCT04221503: Niraparib/ TTFields in GBM," *ClinicalTrials.gov*, 2019. [Online]. Available: https://clinicaltrials.gov/study/NCT04221503

[374] NovoCure GmbH, "NCT04492163: Open-Label Pilot Study of OPTUNE With High Density Transducer Arrays for the Treatment of Recurrent GBM," *ClinicalTrials.gov*, 2020. [Online]. Available: https://clinicaltrials.gov/study/NCT04492163